THESE

Présentée à

L'UNIVERSITE DES SCIENCES ET TECHNOLOGIES DE LILLE

Pour l'obtention du grade de

Docteur de l'université des sciences et technologies de Lille

Mention : Optiques et Lasers – Physico-Chimie – Atmosphère

Présentée par

Zuzanna PAWŁOWSKA

THE PHOTOPHYSICS OF PYRIDINIUM BETAINES STUDIED BY ULTRAFAST TRANSIENT ABSORPTION SPECTROSCOPY: FOCUS ON THE PHOTOINDUCED INTRAMOLECULAR CHARGE TRANSFER PROCESS

Soutenue le 18 janvier 2011 devant la commission d'examen :

Rapporteurs :   **Patrice BALDECK**, Directeur de recherche CNRS, Université Joseph Fourier, Grenoble 1
              Stefan HAACKE, Professeur, Université de Strasbourg

Examinateurs : **Stéphane ALOISE**, Maître de conférences, Université de Lille 1
              Thomas GUSTAVSSON, Directeur de recherche CNRS, CEA de Saclay
              Patrice JACQUES, Professeur, Université de Haute-Alsace
              Olivier POIZAT, Directeur de recherche CNRS, Université de Lille 1

Acknowledgements

The realization of this thesis would not have been possible for me if not the great help and the support of people around me.

First of all I would like to thank Dr. Stéphane Aloïse who has made available his support in a number of ways. With his enthusiasm, patience and great efforts to explain things clearly and simply he helped to accomplish this thesis in its shape and quality. I am also grateful for his help in everyday life, especially at the start – when I arrived to France. I would have been lost without him.

I owe my deepest gratitude to Dr. Olivier Poizat, who agreed to supervise this thesis, for his kind support, remarkable patience and meaningful criticism as well as for the trust he put on me. I am also grateful to Dr. Gotard Burdzinski, who first told me and encouraged me to apply for a PhD position at LASIR laboratory and helped me with many scientific, administrational and personal problems. I would like to thank also Prof. Jiro Abe for making his molecules available for my studies and all those people who helped me to develop studied subject: Dr. Aurélie Perrier-Pineau, Prof. Patrice Jacques, Dr. Jean-Pierre Malval, Dr. Eduard Fron, Dr. Stéphanie Dealbeare, Dr. Cyril Ruckebusch and many others...

My life and work would not have been so easy and pleasant if not all the people from the LASIR laboratory. In particular I would like to show my gratitude to its director – Dr. Guy Buntinx and to Dr. Michel Sliwa for many scientific discussions and help in solving problems. I would like to thank also all students, who have worked to develop subject of this thesis during their training periods.

Great support were also all my polish friends. I want to thank "Lejdis" – Kaczka (Karolina), Maja and Jagoda for long e-mails, phone-talks and adventuresome meetings as well as Wawrzek for long talks on many very important problems. The great thanks should go to my boyfriend Arek who had to deal with all my problems and moods during those three years. With his belief in me and his help in everyday life, there was always a sun in cloudy Lille.

Finally, I could not forget about my family. I would like to thank my parents for encouraging me to undertake the studies in Lille, believing in my success at every step of my scientific journey and being for me whenever I needed. I am also grateful to my sisters Ania and Ala for listening to all my crying and laughter and for long talks bringing me closer home which I missed.

Abstract

This work deals with the photophysics, in solution, of Pyridinium betaine, 2-Pyridin-1-yl-1H-benzimidazole (SBPa), and two derivatives substituted by mono- or bi-thiophene groups. It is based on a combination of steady-state and time-resolved absorption spectroscopic measurements, supported by PCM-(TD)DFT calculations.

SBPa was found to undergo ultrafast intramolecular charge transfer (ICT) upon light excitation, with a drastic change in dipole moment. Stationary absorption and emission as well as TDDFT results revealed a strongly solvatochromic CT absorption due to a $S_0 \rightarrow S_2(CT)$ transition and a non-solvatochromic emission due to $S_1 \rightarrow S_0$ transition. Comprehensive band shape analysis and innovative solvatochromic data treatment considering protic and aprotic solvents separately led to a detailed knowledge of the solvent effects and allowed estimating four relevant dipole moments.

From femtosecond transient absorption experiments, the photophysics of SBPa could be discussed in terms of two distinct CT states and a photophysical scheme was proposed: in parallel to the ultrafast production of the emissive S_1 state, an ultrafast ICT process occurs from the initially populated $S_2(CT)$ state to a new charge transfer $S_1(CT)$ state, reaction ranging from 300 fs – 12 ps depending on the solvent. Examining solvent effects, we found that the ICT process arises in the Marcus inverted region and is purely solvent controlled in aprotic media. Comparison with pre-twisted model molecule has excluded possibility of geometrical changes during ICT.

Similar study of the mono- and bi-thiophene substituted SBPa molecules revealed that the ICT process is still present but occurs in competition with a decay route involving the π-electron system localized in the thiophenic groups.

Résumé

Ce travail concerne la photophysique en solution de la Pyridinium betaine, 2-Pyridin-1-yl-1H-benzimidazole (SBPa), et de deux dérivés substitués par des groupes mono- ou bi-thiophéniques. Il repose sur un ensemble de mesures par spectroscopies stationnaires et par absorption résolue en temps, complétées par des calculs PCM-(TD)DFT.

Les données d'absorption/émission et de TDDFT révèlent pour SBPa une transition de transfert de charge intramoléculaire $S_0 \rightarrow S_2(CT)$ intense et fortement solvatochromique, accompagnée d'une considérable variation de moment dipolaire, et une transition d'émission $S_1 \rightarrow S_0$ dépourvue de solvatochromisme. L'analyse détaillée des formes de bandes et du solvatochromisme, en traitant les solvants protiques et aprotiques séparément, a conduit à une connaissance approfondie des effets de solvants et l'évaluation de quatre moments dipolaires impliqués.

A partir de mesures d'absorption femtoseconde, un schéma complet de la photophysique de SBPa a pu être établi, mettant en jeu deux états CT distincts : parallèlement à la formation d'un état S_1 fluorescent, un état $S_2(CT)$ provenant de la relaxation de la zone de Franck-Condon subit un processus ICT de l'ordre de 300 fs à 20 ps en fonction du solvant pour aboutir à un autre état de transfert de charge $S_1(CT)$. L'examen des effets de solvants suggère que le second processus ICT a lieu dans la région inverse de Marcus et est purement contrôlé par la dynamique du solvant en milieu aprotique. La comparaison de ces résultats avec une molécule modèle non-plane a permis d'exclure définitivement l'hypothèse d'un changement de géométrie durant l'ICT.

L'étude analogue des molécules substituées par des groupes mono et bi-thiophéniques montre que le processus de transfert de charge est préservé mais entre en compétition avec une autre voie de désactivation photophysique parallèle impliquant spécifiquement le système π localisé sur les substituants thiophéniques.

INDEX

CHAPTER I

Introduction

During the last two decades, organic molecules and materials owning photofunctional properties have became a major subject of worldwide research from highest academic preoccupation to industrial interest [1-9]. Ophthalmic glasses with variable transition [8, 9], optical memories [6], optoelectronic devices [10] are concrete illustrations of one very simple principle: macroscopic properties modulation upon light irradiation. The synthesis of photofunctional molecules itself as well as the design of related advanced materials (photofunctional molecules crystallized in solid state, embedded in polymer matrix, polymerized into thick film...) can be optimized through the thoughtful comprehension of the underlying elementary photophysical processes but also non desired competing mechanisms. Moreover, understanding the influence of the direct neighbourhood of the molecule upon the overall photophysics can be sometimes of major importance in view of application (a photofunctional property can be observed in solution but not in matrix polymer or in crystal for example).

From a molecular point of view, all photofunctional properties are first based on some type of molecular modification induced by the light absorption with varying degrees of complexity, such as a conformational change (cis-trans isomerization of azobenzene [11]), a breaking of covalent bond (ring-opening of chromene [12, 13]), a creation of covalent bond (electrocylization of diarylethene [14]), a hydrogen transfer (photoenolization of quinolic ketones [15]), a proton transfer (ESIPT [1] of salycideneaniline [16]), as few examples of the subject for which an exhaustive literature review would be hardly achievable. A class of elementary processes that does not necessarily involve a change of molecular geometry concerns the charge transfer (CT) reaction and more especially the intramolecular charge transfer (ICT) reaction: after irradiation, the charge is transferred from one part of the molecule to another part inducing a drastic change in magnitude (and direction eventually) of the excited state dipole moment. Such phenomenon is therefore used to photomodulate the macroscopic quantities related with the dipole moments as the hyperpolarizability, which is a quantity extensively used in non-linear optics (NLO) [17].

Among all the families of molecules exhibiting strong photoinduced ICT properties, that related to the (1- pyridinio)benzimidazolate molecule, abbreviated as **SBPa** (chart I.1), has been the object of numerous investigations initiated 15 years ago in the group of

---

[1] Excited State intramolecular Proton Transfer

Professor Jiro Abe [2] [18-21]. **SBPa** is characterized by a ground state with some zwitterionic character, with negative and positive charges expected to be localized on the betaine and pyridinium moieties, respectively.

Chart I.1 (1- pyridinio)benzimidazolate abbreviated as **SBPa**.
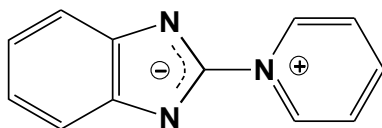
In the past, two preliminary studies pointed out the charge transfer properties of SBPa. First, Boyd et al. [22] demonstrated the excited state CT character of SBPa from the solvatochromic behaviour of the absorption spectra and suggested that a large change of dipole moment arises upon photoexcitation, as illustrated in chart I.2. Next, in the end of the eighties, Alcade et al. [23] measured a dipole moment of +10.33 D for SBPa in the ground state by conventional electrotechnics using a highly concentrated solution in the weakly polar solvent 1,4 dioxane (neglecting the dimerization ability of this molecule).

Chart I.2 Photoinduced dipole moment inversion in **SBPa**.
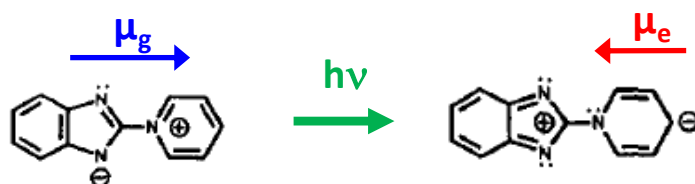
However, it is only in 1997 that J. Abe et al. [20] highlighted the potential interest of SBPa for non-linear optics with the determination, from hyper-Rayleigh scattering (HRS) measurements, of a negative first-order hyperpolarizability value of $|\beta|=(115\pm25)10^{-30}$ esu, which is 5 times larger than that of 4-nitroaniline in chloroform, a reference molecule in the field of NLO. A series of semi-empirical (ZINDO[3]) and *ab initio* calculations [21] predicted an excited S_1 state dipole moment of $\mu_e\sim-3$ D inverted relative to the ground state value, leading to a theoretical hyperpolarizability in satisfactory agreement with experiment.

---

[2] presently working in the department of Chemistry, School of Science and Engineering, Aoyama Gakuin University (Japan).
[3] Zerner's Intermediate Neglect of Differential Overlap

The betaine pyridinium: an interesting "unit" for photofunctional systems.
Convinced by the potentiality of SBPa molecule, Professor Abe's group explored the way
of utilizing the photoinduced dipole inversion property of SBPa for designing advanced
photofunctional materials in view of various applications. One of the objectives was to
insert the SBPa molecule within a polythiophenic chain as a photoactive unit allowing to
control by light the conductivity through the polymer chain (see for example chart I.3).

Chart I.3. photoinduced ICT in thiophenic substituted stilbenzodium pyridinium monomer
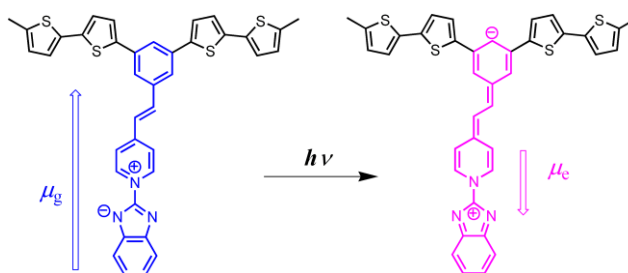
The underlying idea was that, while electron delocalization between the two
oligothiphenic π systems can occur through the central phenyl link in the ground state,
strong reduction of the electron mobility arises in the excited state. Indeed, as illustrated in
chart I.3 photoinduced ICT is expected to yield a molecular configuration characterized by
a negative charge on the carbon in position α to the thiophenic groups, and, consequently,
a lower π electron mobility due to coulombic repulsion. Unfortunately, preliminary
photoconductivity measurements (optoelectronic devices) made by the Japanese group
seem to indicate that the initial goal cannot be reached [24]. In order to figure out this
failure, the detailed knowledge of the photophysics of SBPa and related compounds is
highly desirable.

Another typical application under exploration in Professor Abe's group concerns the
field of optical memories based on photochromic materials, with an original concept of
non-destructive readout method. Numerous optical memories materials are based on
organic bistable photochromic molecules[4]. One light wavelength is used "to write" and
another one "to read" the information. However, the reading step also induces some back
reaction to the initial photochromic state of the material, which erases the recorded

---

[4] a photochromic reaction is the reversible transformation of a molecule between two stable isomers (**A**, **B**)
having different UV-Vis absorption spectra with distinct maxima of absorption λ_A and λ_B respectively. **A** is
converted to **B** by irradiation with λ_A light and the reverse reaction is caused by irradiation with λ_B light. In
general photochromic memory media, λ_A light is used as writing light and λ_B light as reading light, since **A**
does not absorb at this wavelength.

information after many readout processes (destructive readout). As an alternative, the group of Professor Abe has imagined to couple the stongly solvatochromic dye SBPa species to the photochromic entities (azobenzene for instance, see chart I.4) [25], in order to shift the reading wavelength out of the spectral region of the photochromic back reaction, which provides a way to read the information without erasing it.

Chart I.4 Example of molecular system envisaged for the concept of non-destructive optical memory readout

Solvatochromic unit

Photochromic unit
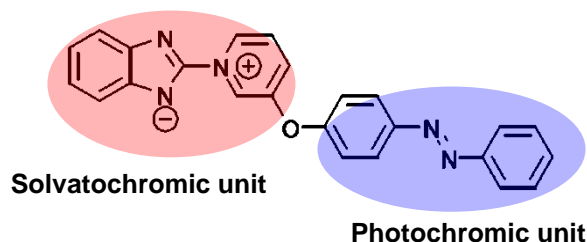
SBPa is thus clearly a very promising molecule for various potential applications in organic photofunctional materials. From evidence, for all these applications, a deep knowledge of the fundamental photophysics of SBPa is of crucial importance. It is particularly important to better understand the solvatochromic properties and the photoinduced ICT reaction mechanism. Some scarce steady state optical spectroscopic data on SBPa have been reported in the literature. However, the behaviour of this molecule upon light excitation remains mainly unexplored. In this respect, the main objective of the work presented in this manuscript was to provide a comprehensive investigation of the photophysical behaviour of SBPa in solution by using steady-state as well as time-resolved optical spectroscopic techniques. Particular attention has been given on i) the ICT reaction responsible for the charge distribution inversion in the excited state and ii) the role of the solvent and the solvatochromism effect induced by the ICT properties.

Photophysical studies of ICT reactions. "Reference" solvatochromic molecules. One of the most remarkable characteristics of CT excited states is undeniably the solvatochromism effect characterizing the absorption and/or emission bands involving these states, i.e., the shift of the band position with the solvent polarity [26-28].

This effect results from the different solvation of the ground and excited states that have very different polarities: the energy gap between the ground and excited CT states is strongly solvent dependent. Thorough analyses of the solvatochromism using methods such as the well known Lippert-Mataga approach [29-32], interpreted with the help of the

dipole solvation theory including Onsager model [33], can allow to estimate excited state dipole moments. The most famous solvatochromic molecule is the pyridinium-N-phenolate (or Reichardt betaine or betaine-30) abbreviated as B30, since the shift of its visible absorption band (CT transition) with polarity is one of the most important ever reported, ranging from λ_{max} = 810 nm in diphenylether to λ_{max} = 453 nm in water [27, 34]. From solvatochromic data analyses, an excited state dipole moment μ_e = 6.2 D was determined, more or less reproduced by theoretical calculations [35, 36], much weaker than the ground sate value of μ_g = 14.8 D estimated from dielectric constant measurements [34]. This change in dipole moment upon excitation is responsible for the blue shift of the absorption maximum in polar solvents (negative solvatochromism). Inversely, para-nitroaniline (PNA) shows a red shift of the absorption band upon increasing solvent polarity (positive solvatochromism), with an increase of dipole moment upon irradiation, $\mu_g \approx 6$ D $\rightarrow \mu_e \approx$ 14 D, conferring NLO properties to this molecule. Finally, para-N,N-dimethylaminobenzonitrile (DMABN) is a representative example of molecule characterized by a solvatochromic emission spectrum. DMABN, for which an extensive review has been published by Grabowski et al. [37], presents an unusual dual fluorescence signal in polar solutions explained by the existence of two different emissive singlet states, a localized excited (LE) state initially populated by light excitation and an intramolecular charge transfer (ICT) state. From an analysis of the solvatochromic stokes shift as a function of the solvent polarity for both emissions, distinct dipole moments could be assessed and compared to calculations [37].

Chart I.5 Solvatochromic Molecules

PNA   B30   DMABN
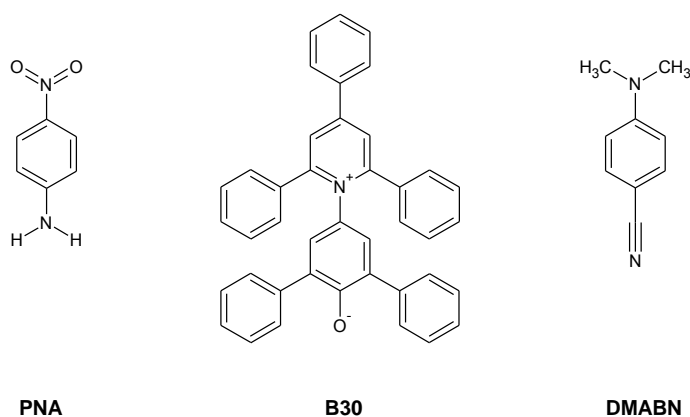
Therefore, for the three molecules B30, PNA and DMABN, but also in many other cases, steady-state spectroscopy has been clearly able to provide detailed information on

photoinduced ICT processes such as the nature of the involved electronic excited states, dipole moments, energy levels and vertical transitions.

On the other hand, time-resolved spectroscopy is able to inform on the real-time evolution of a system following light excitation and to visualize the photophysical relaxation pathways and related dynamics. The high time resolution available in the current transient optical absorption/emission experiments (few tens to few hundreds femtoseconds) allows one to expect capturing the temporal dynamics and the kinetics of the fastest photophysical events such as CT processes. Indeed, in the case of molecule B30, Kovalenko et al. could identify an ultrafast ICT reaction occurring with a characteristic time ranging from ~100 fs to ~2 ps depending on the solvent polarity or viscosity. In polar solvents, the CT dynamics follows the solvent relaxation The back CT reaction (bCT) is a slower process ranging from ~1 ps to ~10 ps depending also on the solvent characteristics [35, 38-44]. Similarly, PNA has been studied by the same group who succeeded to understand its overall dynamics in water: after solvation of the FC excited state (~100 fs), an ICT immediately takes places within ~120 fs governed by the twisting motion of the nitro group; then internal conversion (IC) leads to a hot ground state within ~250 fs, followed by a final relaxation dynamics longer than 3 ps [45, 46]. DMABN is characterized by longer characteristic times: an ICT occurs within 4 ps and the back reaction in a few ns [47-51]. The ICT dynamics varies depending on the molecules as the nature of the excited states, geometries, and elementary photophysical processes engaged in the CT reaction differ. This point will be discussed in more details in chapter IV.

Finally, because ICT reactions are quite complex processes with both solute and solvent contributions, advanced *ab initio* calculations are required to help interpreting experimental data from a quantitative point of view. Realistic prediction of the solute/solvent conformation through the Polarizable Continuum Model (PCM) [52] is obviously a major priority. For molecules with CT transitions, the choice between post Hartree-Fock (HF) methods or DFT can be difficult. Post HF methods are generally recommended for CT molecules [53] but are computationally expensive. At the same time, Time Dependent DFT (TD-DFT) calculations are less time consuming and, with PCM inclusion, are able to compute vertical transitions to Franck-Condon (FC) excited states and predict solvatochromic effects provided that great care is brought to the choice of the functional. Recent examples of conclusive calculations have been reported for DMABN

[50] and B30 [35]. Since a few years, TDDFT optimization of the excited state geometry from the FC configuration is even possible and, consequently, emissive transitions to the ground state can be predicted [54].

Thus, combining stationary and time-resolved spectroscopic techniques together with *ab inito* calculations is certainly a key strategy to get a comprehensive understanding of ultrafast photoinduced ICT reactions in solution. This is the approach adopted in this thesis for the investigation of the SBPa photophysical properties.

Thesis content. The presentation and discussion of the results are divided in five chapters and will be followed by a final section consecrated to the conclusion and perspectives.

Following the introduction, Chapter II is dedicated to the description of the experimental apparatus (stationary UV-vis absorption, fluorescence, and NMR experiments, nanosecond laser-flash photolysis, pump-probe subpicosecond time-resolved absorption) and procedures utilized in this work, as well as the methods of data treatment and analysis (global fitting method, advanced methods of data treatments based on chemometrics). Finally, the quantum chemical calculation (mainly DFT and TDDFT) strategy is briefly presented.

Within chapter III main background concepts and theories necessary for a good understanding of the charge transfer process will be reviewed. After introducing the basic concepts of CT reactions including the well known Marcus theory, the possible influence of the environment on the ICT process will be described through different experimental or empirical approaches. A special emphasis will be laid on the solvent influence.

Chapter IV is dedicated to the study by stationary optical spectroscopy and TDDFT calculations of the SBPa solvatochromic molecule. At the beginning, the experimental evidences for the presence of an ICT reaction are provided. Advanced band shape analysis is then performed to get a more quantitative insight in the ICT reaction and estimate some determinant parameters such as the transition moment, solvent and solute reorganization energies...etc. The main electronic states involved in the electronic transitions observed by steady-state absorption and emission are identified with the help of advanced TDDFT calculations. Finally, to better apprehend the influence of the solvent, an innovative

solvatochromic data treatment is applied and the dipole moments of four electronic states can be deduced and compared to those predicted by TDDFT.

Chapter V is totally devoted to a real time investigation of the photoinduced processes following laser pulse excitation of SBPa using pump-probe femtosecond absorption experiment. The main goal is to obtain a reliable photophysical scheme able to account for the results of the previous chapter and highlights the dynamics of the ICT reaction and other competitive processes. The influence of solvent polarity or viscosity on the ICT and back-CT reactions is then investigated. Finally, an attempt to determine whether the excited ICT state is twisted will be emphasized with the similar investigation of a pre-twisted SBPa analogue.

In Chapter VI are investigated by pump-probe femtosecond absorption two molecules derived from SBPa by substituting two mono- or bi-thiophene units symmetrically on the betaine phenyl ring. Our aim here is to understand in which extent the substituted groups modify the photophysics of the parent SPBa molecule and, in particular, check whether the photoinduced ICT properties are still present.

Finally, the main conclusions will be summarized at the end of this manuscript and some perspectives for future studies will be proposed.

CHAPTER II

Experimental techniques and computational methods

II.1 Introduction

As indicated in the introduction, the main goal of this thesis is to understand the photophysics of 2-Pyridin-1-yl-1H-benzimidazole (SBPa) and related molecules paying a special attention to a charge transfer (CT) process. The different experimental and theoretical techniques utilized to attain this goal will be presented in this chapter.

First, all molecules and abbreviated names used will be first displayed in subsection II.2. Second, the stationary spectroscopic methods employed to estimate the ground state electronic and geometric properties will be presented in subsection II.3. Then, two time-resolved absorption techniques applied for studying the fast and ultrafast photophysical processes, respectively, will be introduced in subsection II.4. These are the nanosecond laser flash photolysis, covering the 50 ns to 100 ms time domain (subsection II.4.1), and the pump probe femtosecond transient absorption experiment employed to probe the 100 fs to 1500 ps time window. Making experiments with such short time scales requires bearing special attention to spectral and kinetic signal treatments. In this regard, special effects such as group velocity dispersion and global fitting procedure will be presented (subsection II.4.3). Additionally, chemometric data treatment methods, which provide an advanced tool for the analysis of femtosecond transient absorption data, will be described.

Finally various *ab-initio* calculations were utilized at different stages of this work to help in the interpretation of the experimental data and provide a more quantitative understanding of the observed phenomena, all of them being based on the Density Functional Theory (DFT) and Time-Dependent DFT (TD-DFT) formalisms (taking solvent into account). Basis and functional will be given in subsection II.5 (see also appendix A).

II.2 Materials

All molecules studied in this thesis were synthesized by the group of Professor Jiro Abe in Japan and are presented in table II.1.

Table II.1. Schemes, names and molecular weights of investigated molecules

Name	Full name	Structural formulae	Mol.wt. (g.mol^{-1})	Ref.
SBPa	2-Pyridin-1-yl-1H-benzimidazole		195.22	[22] [23]
TwSBPa	2-(2,4,6-Triphenyl-1-pyridinio)benzimidazolate		423.51	[23]
Br$_2$SBPa	4,7-Dibromo-2-pyridin-1-yl-1H-benzimidazole		353.01	
Th$_2$SBPa	4,7-Dithiophen-1H-benzimidazol-2èyl-pyridinium		359.46	
Th$_4$SBPa	4,7-Bis(2,2'-bithiophebe)-1H-benzimidazol-2èyl-pyridinium		523.72	

All solvents (spectrophotometric grade) were used as received (Aldrich) Commercial compounds used as references and bought in Sigma Aldrich, TCI Europe and were used without further purification.

II.3 Stationary spectroscopic techniques

II.3.1   Stationary absorption

UV – visible stationary absorption spectra were recorded on CARY 100bio in transmission mode and two beams configuration (reference on pure solvent). Measurements were performed in ambient temperature using a 1 cm quartz cuvetts on solution of concentration ranging from 10^{-4} to 10^{-6} mol.L^{-1}.

II.3.2   Stationary fluorescence

The stationary fluorescence spectra – emission and excitation – were performed using a Jobin Yvon Div. FluoroMax 3 spectrometer. All spectra were corrected for the spectral sensitivity of the instrument. The optical density at the absorption maximum of all solutions was kept below 0.1 in a 1 cm cuvette. Note that fluorescence quantum yield was assessed for SBPa molecule, but due to very low and thus imprecise values $\Phi \approx 10^{-3}$ we did not focus on this value.

II.3.3   NMR spectroscopy

All ^{1}H NMR experiments were done with Bruker Avance 300 MHz and Avance 500 MHz spectrometers. ^{1}H NMR experiments were acquired on BRUKER AVANCE NMR spectrometers equipped with QNP or TXI probe, and operating at 300 MHz or 500 MHz for ^{1}H. Solutions of SBPa were prepared in methanol-d$_4$, acetonitrile-d$_3$, tetrahydrofuran-d$_8$, toluene-d$_8$ (concentration 10^{-2}-10^{-3}M).

II.4 Time resolved absorption experiments

Transient absorption spectroscopy is a powerful time-resolved spectroscopic technique that is widely used to investigate photoinduced chemical processes ranging from femtosecond to millisecond time scale. After photo-excitation a molecule in its singlet ground state (S_0) reaches usually an upper excited state (S_n). From this latter excited state S_n a recovery of the ground state is obtained by relaxing the excess of energy by different processes characterized by different time from femtosecond to millisecond time scale, as shown in the diagram of Jablonski (see figure II.1). Depending on the time scale, excited species can be observed according to two different techniques: (i) femtosecond transient absorption for time scale from femtosecond to nanosecond, (ii) nanosecond transient absorption for time scale further (named also laser flash photolysis). Indeed for ultrafast processes of characteristic time in the picosecond and sub-ps time domain, any electronic apparatus can follow signal variations and explain the existence of two different techniques.

Anyhow, both techniques require two irradiations: one irradiation, called the pump, to initiate the photoreaction and create the excited species and a second one, called probe, is use to probe those excited species.
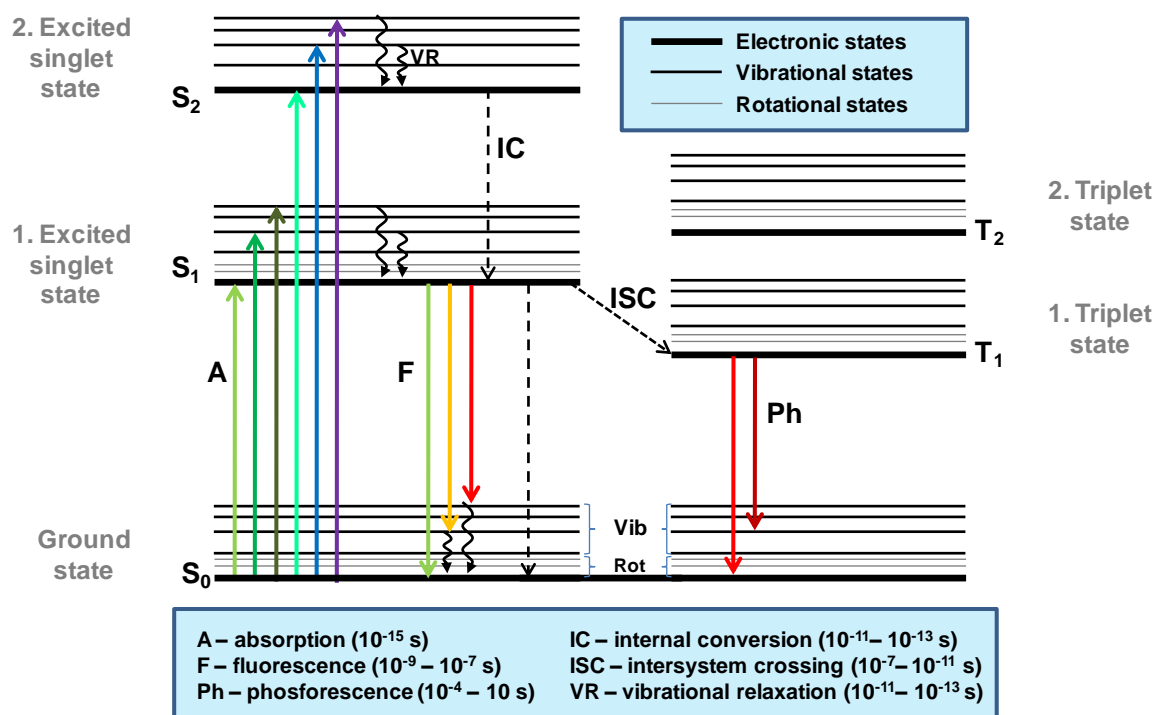
Figure II.1. Jablonski diagram.

II.4.1   Nanosecond Laser Flash photolysis

The scheme of experimental setup is presented in figure II.2. To create transient species the sample is first excited with a pump beam, from a nanosecond Nd:YAG laser (DIVA II, Thales Laser, 0 to 20 Hz, 7 − 8 ns pulses (FWHM)). Laser pulses, originally of 1064 nm, are doubled or tippled in frequency (266 or 355 nm) with non linear crystal of BBO to adjust to the absorption of the sample. The power of the pump beam is adjusted to 1 mJ with optical density filter. A Xenon (XBO 150W/CR OFR, OSRAM) continuous arc lamp, is used to probe the sample after excitation. The probe and pump beam are at 90° each other to avoid remaining pump beam in the probe signal. Emission intensity of this lamp can be strongly increased with an electric discharge delivered by an external module. Such discharge causing a significant increase in emitted photon flux provides a better signal to noise ratio. The intensity profile of such probe beam is fluctuating with time with the existence a characteristic plateau of 500 µs. Therefore this pulsing technique option can only be used during this plateau and limited to probe species with lifetime below 500 µs. The probe beam is focalized (lens L1) inside the measurement cell and a cylindrical lens (L2) is used to focus the pump beam. Samples are contained in a quartz cell (10×10 mm section) at a concentration adjusted (~10^{-4} mol.dm^{-3}) to get an OD value of about 1.0 at the pump excitation wavelength. The transmitted light is focused by a lens (L3), dispersed by a monochromator (Horiba Jobin-Yvon, iHR320) and analyzed with a photomultiplier (R1477-06, Hamamatsu) coupled to a digital oscilloscope (LeCroy 454, 500 MHz). The oscilloscope measures the variation of intensity for one wavelength of the probe beam after the excitation by the pump beam. The experiments are repeated for different wavelengths of the monochromator and transient spectra can be reconstructed.

The acquisition is controlled by a synchronizator box: a trigger signal is sent to the laser to get a single pump pulse and to the discharge controller to get a single probe pulse (the time between these two pulses is controlled by a delay generator DG 535 Stanford Research Systems). The acquisition of the oscilloscope is synchronized by a fast photodiode from a remaining signal from the pump laser pulse. The data from the oscilloscope is transferred to the computer. To emphasize the transient species created by the pump beam excitation, differential optical density is indeed measured. The differential optical density of the sample versus time for one wavelength is characterized by the transmitted intensity of the probe beam with and without pump beam.
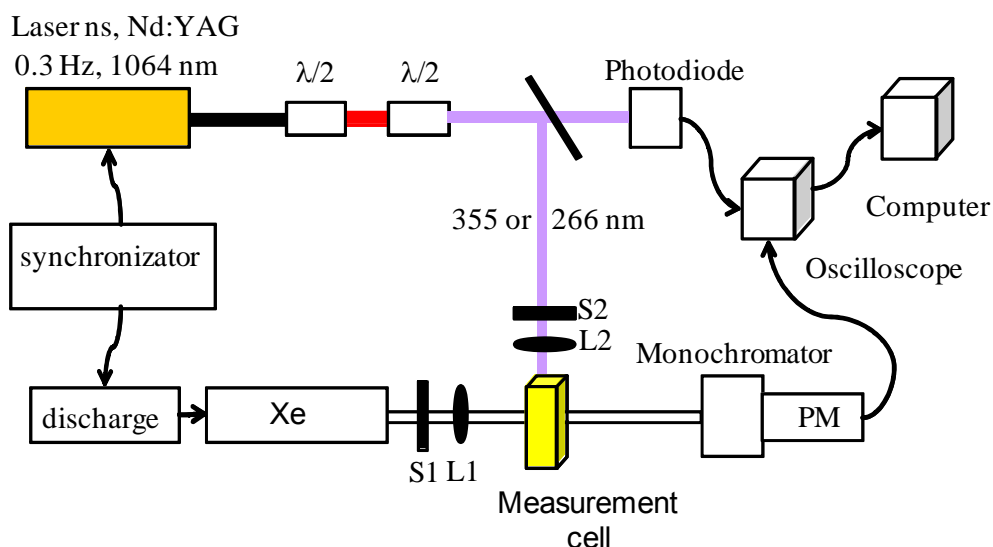
Figure II.2. Experimental setup for nanosecond flash photolysis experiment

Then the difference of optical density is derived from two alternative data measurements by controlling two shutters (S1 and S2) which are situated in the two optical pathways (pump and probe beam):

- Intensity after pump beam excitation: $I_{signal}(t)$ – intensity transmitted by the sample after nanosecond laser excitation (both shutters 1 and 2 are open)

- Intensity without pump beam excitation: $I_{ref}(t)$ – transmitted intensity without laser excitation (shutter 1 is closed and shutter 2 is open).

For each pair of the data sets the differential optical density is calculated using following formula:

$$\Delta[OD]_\lambda(t) = log\left(\frac{I_{signal}(t)}{I_{signal+pump}(t)}\right) \qquad (II.1)$$

Such kind of calculation assures better quality of the signal even if the plateau is not perfectly flat or noise of the system appears. Finally, while the signal is low and noisy one can accumulate more data and take the average of more than one measurement to increase signal to noise ratio. The ratio increases with a square root of the number of accumulation (Poisson statistics).

II.4.2 Optical pump probe Femtosecond transient absorption experiments

II.4.2.1 Principles

Femtosecond optical pump-probe configuration of transient absorption experiment needs two pulses. First monochromatic femtosecond pump pulse of high intensity, excites the sample and thus creates an initial excited states population at zero time (see figure II.3a). Subsequent excited state's evolutions are then followed threw absorption of a femtosecond white light continuum (WLC) probe pulse. The example in figure II.3 shows the initial excitation $S_0 \rightarrow S_n$ and transient absorption ($S_n \rightarrow S_m$) for two different delay times Δt_1 and Δt_2 probing two different excited species. So, to obtain dynamics of all processes which occur after photoexcitation one can step by step change the delay time Δt between pump and probe. It should be pointed here that in comparison to nanosecond transient absorption experiments, it is not possible to measure the evolution of the intensity of the probe beam with femtosecond time resolution. This is the reason to use two femtosecond pulses and to "take a picture" of the photo-dynamic at Δt, the delay between the pump and probe femtosecond pulse. The measurement is than repeated for different delays Δt to get the entire kinetic. After split of the fundamental beam the second, much less intense (a few micro joules) beam is focused in 1 mm CaF_2 plate and resulting from non-linear processes used to generate a white light continuum [55]. This beam of very broad spectral range (300 – 750 nm) is used as probe pulse.

As a particularity of a transient absorption spectrum, it can be either positive or negative. As already explained, positive signal is ascribed to absorption of excited states. Reversely, negative signal can be ascribed to bleaching process (depopulation of the ground state) or stimulated emission. The bleaching band appears at the same position (inverted) as the stationary absorption spectra (example – black solid line in graph in figure II.3b). This is easily explained because differential transient spectra are obtained after substraction from ground state absorbing species. The stimulated emission (SE) band is usually found in the same region as the stationary fluorescence spectra (example – black dashed line in graph in figure II.3b). Indeed, this is a WLC that induces the SE signal and so stimulated photons are added to the probe light photons what leads to negative signal after substraction of ground state absorption.
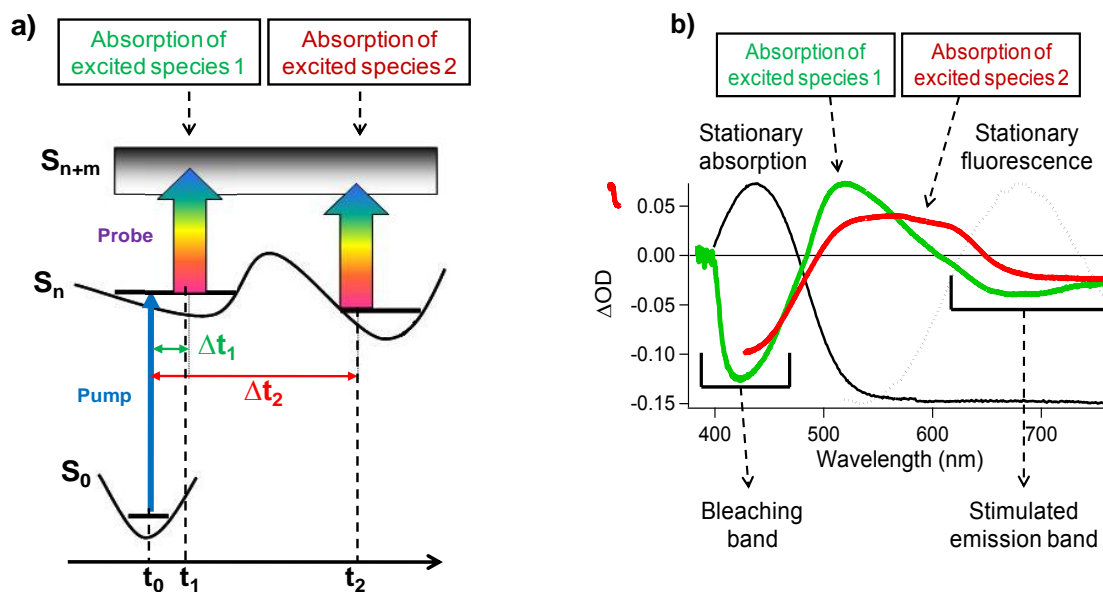
Figure II.3. a) Principle of time resolved absorption experiment, b) example of spectra obtained with femtosecond transient absorption

II.4.2.2   Experimental setup

To generate both pump and probe pulses a Ti:Sapphire amplified laser system is used (see figure II.4). Femtosecond oscillator – Coherent MIRA 900D is pumped with 5 W continuous laser Nd:YVO$_4$ (Millenia Vs. Spectra Physics) at 532 nm wavelength and delivers pulses characterized by time-duration of 100 fs (FWHM), energy of 10 nJ, repetition rate of 76 MHz and wavelength tunable in the 690 – 1050 nm spectral range. The pulses are next stretched, amplified with a regenerative amplifier (ALPHA 1000, B. M. Industries) and recompressed. The amplifier with a Ti:Sapphire active center is pumped with a 12 W / 1 kHz intracavity frequency doubled Nd:YLF laser (621D, B. M. Industries). Amplified pulse has following parameters: energy of 1 mJ, time duration of 120 fs (FWHM) determined by autocorrelation and 750 – 850 nm tunability. After amplification the beam is split in two beams – the majority (90%) of its energy is frequency doubled by generating second harmonic (SHG) in ta 0.5 mm thick β-barium borate (BBO) crystal. By this way pump pulse at wavelength chosen from 375 to 425 nm interval is generated[56]. It is possible summing frequencies of second harmonic and fundamental beam again in a BBO crystal of 0.5 mm thickness to generate pump beam of wavelength varying from 250 to 283 nm. The pump pulse energy at the sample is 6 µJ with a diameter of about 0.5 mm (3 mJ/cm^2).

The white light continuum probe beam is generated by focusing the second part of the fundamental beam in a 1 mm CaF$_2$ rotating plate. The pump-probe polarization

configuration is set at the magic angle (54.7°) and the probe pulse is delayed in time relative to the pump pulse using an optical delay line (Microcontrol Model, precision ± 0.1 μm). The white light continuum is split into a probe beam (with pump) and a reference beam (without pump). The transmitted light of the probe and reference beams is recorded on 2 different channels of a multichannel spectrograph equipped with a CCD camera (LN/CCD 1340/400 EB/1, Princeton Instrument) and the transient spectra (detailed below) are computed. The transient absorption measurement covers a 300 - 750 nm spectral range and a 0 - 5 ns temporal range. The optical density variation accuracy is ± 0.001 (before averaging) in the spectral range of the experiments. Sample diluted in organic solvent solution (absorbance of 0.1 – 0.8 at excitation wavelength $\sim 10^{-4} – 10^{-3}$ M) is circulating in a flow cell equipped with 1 mm thick CaF_2 entrance windows and characterized by a 2 mm optical path length. The transient absorption intensity is displayed as differential absorption and the spectral data at one time delay are measured between 3000 and 6000 times and averaged. All experiments are carried out at 294 ± 2 K.
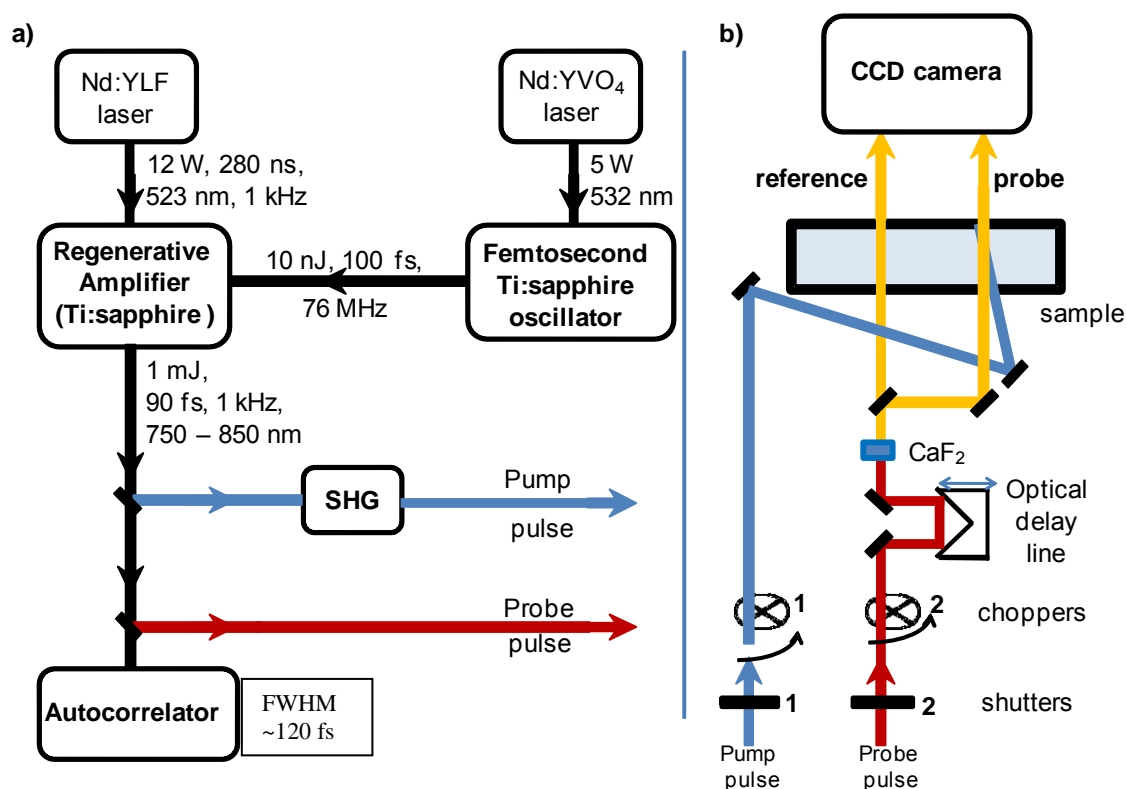
Figure II.4. Setup used for femtosecond transient absorption experiment.

II.4.2.3   Estimation of the temporal resolution

An estimation of the temporal resolution can be achieved from the time response of the stimulated Raman signal of the solvent molecules since this phenomenon appears only during the overlap time of the pump and probe laser pulses and provides therefore an indirect measure of the pump-probe cross correlation time.

As shown in figure II.5, for very short times between -1 and 0.7 ps, the stimulated Raman signal in ACN consists in three sharp negative peaks originating from methyl C-H stretching modes. Due to a chirp effect on the different wavelengths of the white light continuum, the position of the maximum of the Raman peak shifts with time. Therefore, a plot of the peak intensity of the Raman signal as a function of time presents Gaussian distribution that represents the pump-probe correlation function. As shown in figure II.5 c, by fitting with Gaussian functions we measure a FWHM (Full Width at the Half Maximum) value of 160 fs for ACN excited at 390 nm. From repeated this measurements we were able to estimate the temporal resolution of our experimental setup to $\leq$ 200 fs. The accuracy of this estimation is essential for ensuring a correct global fitting treatment (see hereafter).
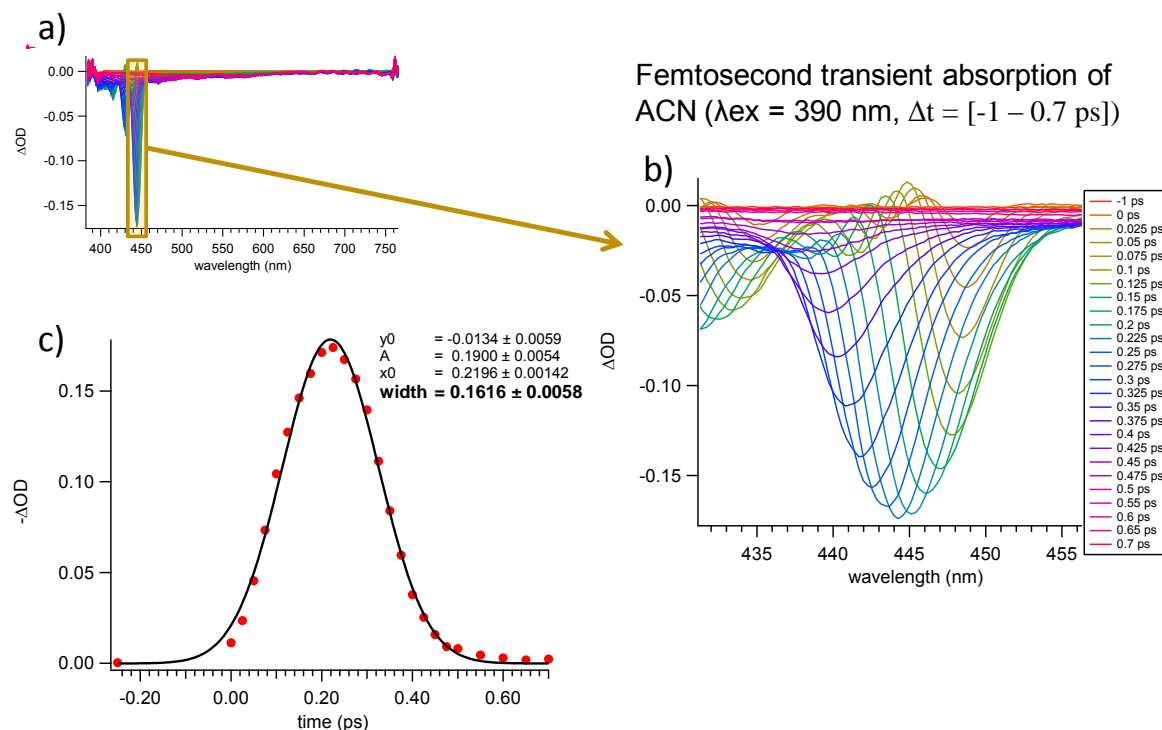
Figure II.5. Femtosecond transient absorption spectra of pure ACN (390 nm excitation) for delay between -1 and 0.7 ps showing three Raman peaks; 400-750 nm wavelength range (a) and zoom on one Raman peak between 430-460 nm (b). Estimation of the temporal resolution of our pump-probe transient absorption experiment from the most intense stimulated Raman signal (c).

II.4.2.4   Data acquisition

The CCD camera cannot acquire the data for each pulse (kHz). The CCD camera is synchronized with a chopper placed in the probe beam (chopper 2, figure II.4) to acquire integrated intensities of the probe beam and corresponding reference beam at the repetition rate of 66 Hz, i.e. 8 pulses for each acquisition. The differential absorption is obtained by adding another chopper (chopper 1) placed at pump beams optical path, synchronized with chopper 2 and modulated at half of its frequency − 33 Hz giving the opportunity to measure probe intensities with and without excitation.

Data registered with CCD camera are sent to the computer where data acquisition procedure is totally controlled with Winspec 32 software. The spectral variation of the optical density (OD) with and without pump excitation for a delay time Δt is given by the following formula:

$$\Delta OD(\lambda, \Delta t) = OD^{probe+pump} - OD^{probe} \qquad (II.2)$$

Taking:

$$OD = -log\left(\frac{I}{I_0}\right) \qquad (II.3)$$

Equation II.II.4 gives the details how each optical density (with and without pump) are calculated:

$$OD^{probe+pump} = -log\left(\frac{I^{probe}_{pump}(\lambda,\Delta t)-I^{em}(\lambda)}{I^{ref}_{pump}(\lambda)-I^{em}(\lambda)}\right) \ and \ OD^{probe} = -log\left(\frac{I^{probe}_0(\lambda,)-I^{stray}(\lambda)}{I^{ref}_0(\lambda)-I^{stray}(\lambda)}\right)(II.4)$$

Each intensity are the intensity acquired by the CCD camera for 8 pulses where:

- I^{probe}_0 and I^{ref}_0 are the intensities of the probe and reference pulses respectively while the pump pulse is stopped with chopper 1

- I^{probe}_{pump} and I^{ref}_{pump} are the intensities of the probe and reference respectively with pump pulse.

- I^{stray} is the intensity of the noise light measured when pump and probe/reference beams are stopped with choppers 1 and 2 respectively.

- I^{em} is the emission of the sample induced with the pump pulse; measured while pump and reference beams are blocked with chopper 2.

We get final equation II.5 for spectral variation of optical density:

$$\Delta OD(\lambda, \Delta t) = log \left[\frac{I_0^{probe}(\lambda) - I^{stray}(\lambda)}{I_0^{ref}(\lambda) - I^{stray}(\lambda)} \cdot \frac{I_{pump}^{ref}(\lambda) - I^{em}(\lambda)}{I_{pump}^{probe}(\lambda, \Delta t) - I^{em}(\lambda)} \right] \qquad (II.5)$$

The I^{stray} and I^{em} are measured at the beginning of each experiment. Such calculated optical density reflects variations of properties of investigated sample after photoexcitation while other changes of the continuum spectral distribution along the different optical paths are suppressed. The optical density variation accuracy is $\pm$ 0.001 (before averaging) in the spectral range of the experiments.

There is one specific issue which should be considered: we are using a white light continuum probe beam and the group velocity of the different wavelength is wavelength dependent. Therefore the group velocity will change differently when it propagate in dispersive media. This issue is known as Group velocity dispersion issue. Two problems are then found in femtosecond transient absorption experiments:

- the broadening of femtosecond pulse while propagating dispersive media and induce that the instrumental response function is wavelength dependent for the white light continuum probe beam.

- The determination of the time (Δt) of the transient spectra is defined by the difference of propagation optical pathway between pump and probe beam and control by the delay line. Therefore each wavelength of the probe beam has a different time zero.

These issues are important in the time scale below 1 ps and in the following section we will details how we consider it in our data treatment.

II.4.3   Femtosecond data processing

II.4.3.1   Group velocity dispersion:

The propagation of ultrafast light pulse in a dispersive media is perturbed by the effect of dispersion of the media refractive index. Normally, in optical materials, the refractive index constantly decreases with increasing wavelength [57]. In consequence, according to the group velocity formula:

$$v_g = c \left(n - \lambda \frac{dn}{d\lambda} \right)^{-1} \qquad (II.6)$$

the red portion of the pulse propagates faster than the blue one, in such a way that there is a time delay between the blue and red parts of the light pulse. This is the so-called group velocity dispersion effect (GVD). Thus, in a pump-probe experiment using a spectrally broad probe pulse (white light continuum), there will be a notable difference between the "time zero" (i.e., pump-probe coincidence) of the blue and red regions of the probe (see figure II.6)[5]. In our experiments we minimized as much as possible the dispersive media by using only mirrors for transporting the probe beam and very thin materials for generating the continuum light (1 mm thick CaF_2 plate) and for the sample cell entrance window (1 mm thick CaF_2 plate). However we cannot avoid some dispersion of the probe beam. There are two possible ways of correcting this effect: either the transmitted probe light is spectrally recompressed using a prism or a grating before being detected, or the dispersed probe light is mathematically corrected after its detection. In this thesis, we applied this second procedure, named as the GVD correction. It consists in adding some delay to the red part of the detected spectrum to compensate for the GVD temporal distortion.
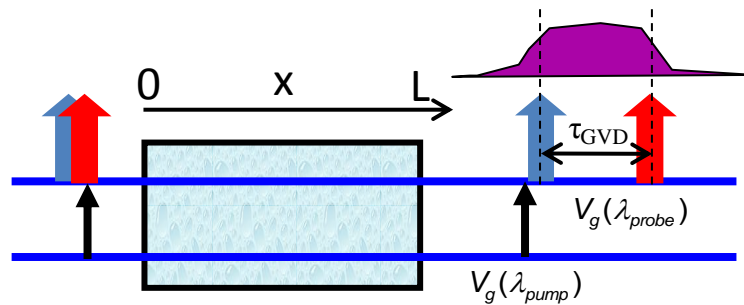
Figure II.6. The group velocity dispersion (GVD) effect

II.4.3.2   GVD correction with standard procedure

In femtosecond transient absorption spectroscopy, the Instrumental Response Function (IRF) can be estimated by measuring the cross-correlation signal between the pump and probe pulses [58, 59]. As explained above (subsection II.4.2.3) the IRF is well described in our experiments by a Gaussian shape and its width measured at half maximum provides a reliable estimate of the time resolution σ of the experiment (at 400 nm, Γ < 200 fs). The IRF can be measured also in a more classical manner, in a thin BK7 plate and in the pure solvent (non absorbing material for the pump beam). Due to group velocity dispersion, the

---

[5] The phenomenon where two optical pulses with different optical frequencies initially overlapping in time that no longer overlap after some propagation distance due to their different group velocities is known as group velocity mismatch phenomenon. However within this thesis we will use only GVD notation for both phenomena as they origin from the same physical behavior.

position of the maximum of the cross correlation, which can be accounted as time zero signal, is wavelength-dependent. However knowing the different time delay zero for each wavelength (maximum of each cross correlation Gaussian signal) it is easy to correct the GVD issue by a data pretreatment to reconstruct the "real" spectra shifting the time delay for every wavelength [58].

However the IRF measurement is not perfect because it cannot be measured for the sample (compounds + solvent). The GVD is in fact different for the solvent alone and the solution containing the solvent and the sample. For example indeed the pump and probe beam propagate through the entire cell (2 mm) for the solvent alone (no absorption of the pump beam) whereas the sample absorbs strongly the pump beam in few micrometer. Moreover it is very difficult to predict the refractive indexes (and dispersion of group velocity) for the solution containing the sample if someone wants to use equation II.6.

As we need to get the best kinetic evolution in the short time scale and be able to perform global analysis for all wavelengths (fitting all the data at the same time) we did not perform generally any GVD data pretreatment with the standard procedure. Instead, the kinetics for each wavelength were fitted convolving an analytical instrumental function which takes into account for different time zero for each wavelength (GVD effect) and propagation through an absorbing solution.

II.4.3.3 Theoretical model for GVD corrected fitting function.

As already mentioned femtosecond transient absorption experiments give transient spectra at different delay time and spectral data from several different time delays are needed to reconstruct the transient absorption kinetic traces at selected wavelength. To analyze these traces a kinetic model describing the observed processes should be chosen. Assuming that photophysical and photochemical processes in our case involve only relaxing of excited states (no photochemical reaction) the growth and decay of different transient species with time were fitted by a sum of n-mono-exponential function.

$$F(t) = y_0 + \sum_i a_i e^{-k_i t} \qquad (II.7)$$

The observed signal S(t) is in fact the convolution of the different transient species evolving signal (modelled by a sum of exponential and named as $S_{theor}(t)$ by the instrumental response function signal (G(t)).

$$S(t) = S_{theor}(t) \otimes G(t) = \int_0^\infty S_{theor}(t') G(t - t') dt' \qquad (II.8)$$

In femtosecond transient absorption experiments G(t) is characterized by the pump-probe cross-correlation function which can be approximated analytically by a Gaussian Instrumental response function (a Gaussian pulse is consider for pump and probe beam).

$$G(t) = G_0 exp\left(\frac{-t^2}{\tau^2}\right) \qquad (II.9)$$

where τ can be expressed using full width at half maximum (FWHM) of a Gaussian as follow:

$$\tau = \frac{\tau_{FWHM}}{2\sqrt{ln2}} \qquad (II.10)$$

and is usually slightly longer compare to full width at half maximum of the laser pulses.

Now the group velocity dispersion (GVD) correction for different zero time delay has to be introduced. Let us so consider a sample cell of thickness L in which two laser pulses are propagating: pump pulse with a wavelength λ_{pump} and probe pulse with a wavelength λ_{probe}, and $\lambda_{pump} \neq \lambda_{probe}$. It means that in the following layers of the sample the relative delay between two pulses will never be the same. $S_{GVD}(t)$ which is the transient absorption signal obtain after passing through the sample and measured at all relative delay times between pump and probe pulses can be expressed as:

$$S_{GVD}(t) = \frac{1}{L}\int_0^L S\big(t - \Delta t(x)\big)dx \qquad (II.11)$$

where x is chosen layer thickness and can vary from 0 to L and t is a relative delay between pump and probe at x = 0. $\Delta t(x)$ can be expressed as following

$$\Delta t(x) = \frac{x}{v_g(\lambda_{pump})} - \frac{x}{v_g(\lambda_{probe})} \qquad (II.12)$$

where $v_g(\lambda)$ is the group velocity at wavelength λ as given in equation II.6. $S_{GVD}(t)$ becomes

$$S_{GVD}(t) = \frac{1}{L}\int_0^L S\left(t - \frac{x}{L}\tau_{GVD}\right)dx \qquad (II.13)$$

where τ_{GVD} is the total time delay induce by the propagation through the dispersive media L. Finally the signal measured can be expressed using the convolution of theoretical signal (sum of exponential) and an IRF containing the GVD issue as a fit parameter

$$S_{GVD} = \frac{1}{L}\int_0^L \left(\int_0^\infty S_{theor}(t')G\left(t - \frac{x}{L}\tau_{GVD} - t'\right)dt'\right)dx \qquad (II.14)$$

In above equation only the IRF (G(t)) depends on the x parameter, so the equation can be rewritten as:

$$S_{GVD}(t) = G_{GVD}(t) \otimes S_{theor}(t) \qquad (II.15)$$

where

$$G_{GVD}(t) = \frac{1}{L}\int_0^L G\left(t - \frac{x}{L}\tau_{GVD}\right)dx \qquad (II.16)$$

Up to now the absorption of pump pulse has been neglected but when the absorbance of the sample is higher than $OD \geq 0.5$ the contribution of each layer to the overall signal will decrease with pulses propagation in the sample and should be reflected in final equation. Taking OD as an absorbance of the sample and making use of the error function definition and the equation (II.16 can be rewritten as:

$$G_{GVD}(t) = G_0 exp\left(\frac{2.3OD}{\tau_{GVD}}t\right) \times \left[erf\left(\frac{t}{\tau} - \frac{2.3OD}{\tau_{GVD}}\frac{\tau}{2}\right) - erf\left(\frac{t}{\tau} - \frac{2.3OD}{\tau_{GVD}}\frac{\tau}{2} - \frac{\tau_{GVD}}{\tau}\right)\right] \qquad (II.17)$$

where τ and τ_{GVD} are the only parameters describing GVD-modified cross-correlation function and erf function is defined by:

$$\int_0^x e^{-t^2}dt = \frac{\sqrt{\pi}}{2}erf(x) \qquad (II.18)$$

τ_{GVD} is:

- Medium – sensitive for normal refractive index dispersion – it increases with increasing wavelength difference between pump and probe

- Sample thickness sensitive – the greater the samples thickness the higher τ_{GVD}

Thus the final analytical function used for fitting the kinetics from femtosecond transient absorption experiment is:

$$F(t) = G_{GVD}(t, \tau, \tau_{GVD}, OD) \otimes \left(y_0 + \sum_i a_i e^{-k_i t}\right) \qquad (II.19)$$

II.4.3.4   Global fitting method including GVD correction

We will now present the procedure used in this thesis for fitting the femtosecond transient absorption data at different wavelengths i.e., the global fitting method. All data fittings were done using Igor Pro 5.05A program. Figure II.7 presents an example of transient absorption signal divided into two distinct temporal windows: [-1 – 1 ps] for the increase of the transient signal and [1.2 – 600 ps] for its decrease. One can recognize two negative bands corresponding to bleaching (between 360 and 450 nm) and stimulated emission (between 620 and 640 nm) as well as positive bands of excited state absorption (between 310 – 360 and 450 – 620 nm), see figure II.3 for explanation.

Observing carefully the very short time domain, as the 0.4 ps trace – thick black line in figure II.7a, one can notice that the excited state absorption band at lower wavelengths (330 nm) has already begun to increase (intensity of 0.045), while the band at longer wavelengths (490 nm) has not even started its growth. This is the consequence of the GVD effect.

Figures II.7c and d present examples of four kinetics extracted from the set of transient absorption spectra displayed in figure II.7a and (symbols) and their fit by using the global fitting procedure (full lines). In this procedure, instead of fitting kinetics at different wavelengths separately, all kinetics' are fitted together with the assumption that some fitting parameters should be the same at all wavelengths. The fitting function (equation II.19) is the final result of convolution between multi-exponential functions and a pump-probe correlation function approximated by a Gaussian (equation II.9) taking into account the GVD correction (equation II.17). The variables used in this fitting function are divided into two groups: the global variables, characterizing parameters that are common to all kinetics, and the local variables, for parameters dependent on the wavelength at which the kinetic is taken. All these parameters are presented in table II.2.

Table II.2 Global and local parameters of fitting function

	LOCAL parameters- varying with λ	**GLOBAL parameters –** do not depend on λ
GVD-modified cross-correlation function (equation II.17)	τ_{GVD}	**OD** of the sample.
		τ – the FWHM of pump-probe correlation
Multi-exponential function (equation II.7)	y_0 – the offset	τ_i – characteristic times
	a_i – pre-exponential factor	
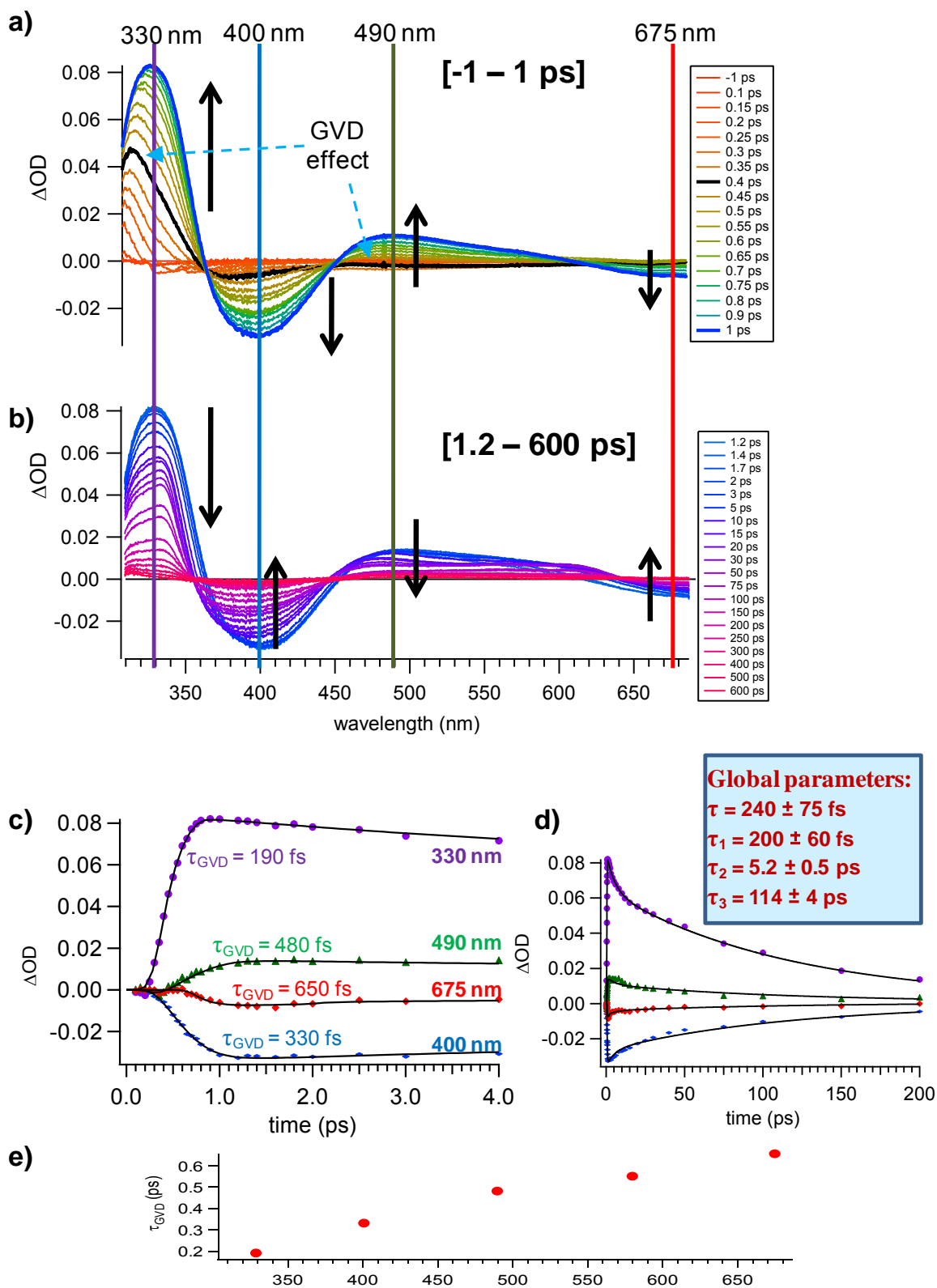
Figure II.7. Example of global fitting procedure. a) and b) – transient absorption signal of SBPa in ACN using excitation wavelength of 266 nm, for time intervals [-1 – 1 ps] and [1.2 – 600 ps] respectively; c) and d) – kinetics at different wavelengths fitted with the global fitting method using equation II.19 for the short and longer time ranges, respectively; e) increase of the τ_{GVD} value obtained from the global fit with kinetics wavelengths.

In the example presented above, we apply the global fitting method including three-exponential functions to four selected wavelengths. As shown by the vertical coloured lines in the spectra (figure II.7a and b) the four kinetics are taken at the extrema of all transient absorption bands. The GVD effect can be observed in the short time range of the kinetics (figure II.7c): the kinetics start with a time delay clearly increasing with increasing wavelength. To fit properly all wavelengths, taking into account these differences in their origin, a τ_{GVD} parameter was introduced in equation II.19 and was kept as a local variable in the fitting procedure

As one can see, the fit function reproduces perfectly the experimental kinetics for both short (figure II.7c) and long time delays (figureII.7d). As a result, three characteristic times of transient species with acceptable matching errors are obtained (indicated in the blue insert in figure II.7d). Moreover, values of τ_{GVD} are, as expected, higher for longer wavelengths, so one can observe an increase of its value with increasing wavelength, as shown in figure II.7e. Furthermore, the width of pump-probe correlation is of the same order of magnitude as the increase of the transient absorption signal characteristic time ($\tau = 240$ fs and $\tau_1 = 200$ fs respectively). The value found for τ is, therefore, in accordance with the experimental 200 fs time estimated from autocorrelation measurements or more precisely measured with the help of stimulated Raman signal [60]. The similarity of these two shortest times τ and τ_1 indicates that we managed to deconvolve the signal from the pump probe correlation function and therefore, could extract the pure characteristic time of signal appearance, not affected by the apparatus response function. However, taking into account the proximity of these two times, the later will not be considered quantitatively in this thesis and will serve only as a qualitative indicator of the order of magnitude of the associated kinetics.

II.4.3.5   Multivariate curve resolution

Data analysis is often a non-trivial task in ultrafast time-resolved spectroscopy and, besides global fit analysis; different approaches have been proposed in the literature quite recently, such as global and target analysis[61, 62], multivariate curve resolution[63, 64] and other chemometric methods[65]. These methods share a common objective which is to describe both the variation of the observed data in time and spectral domain. These methods rely on the assumption that the data are bilinear in nature, that is to say the properties of a multi-component system can be modelled as additive contributions the

spectroscopic properties of k components weighted by their concentration, as described in the following equation in matrix notation and illustrated figure II.8.

$$D = CS^T + E \qquad\qquad (II.20)$$

where $\mathbf{D}$, of dimensions $m \times n$, contains difference absorbance values corresponding to transient spectra collected at one of the m successive delay time points; each column of $\mathbf{D}$ represents a time decay trace at one of the n different wavelengths. The concentration matrix $\mathbf{C}$, of dimensions $m \times k$, contains time-dependent profiles of the k pure contributions at m delays and the matrix $\mathbf{S^T}$, of dimensions $k \times n$, the corresponding k transient spectra at n spectroscopic variables (wavelengths). In equation II.20, the error matrix $\mathbf{E}$, of dimensions $m \times n$, contains the residuals not explained by the k components.
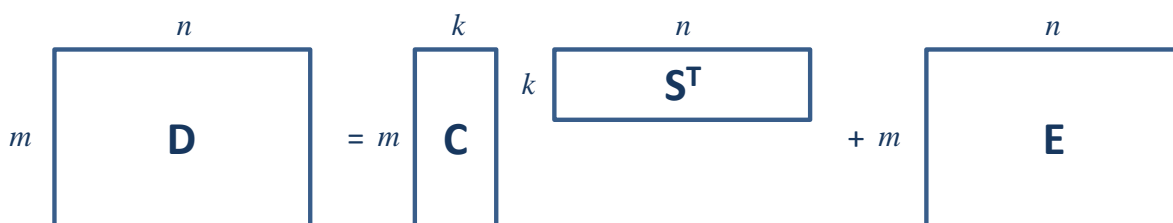
Figure II.8. Principle of decomposition of kinetic matrix D

MCR-ALS. In recent years, multivariate curve resolution-alternating least squares (MCR-ALS) [66] has been successfully applied to a wide range of evolutionary processes in chemistry. In time-resolved spectroscopy, the method aims at resolving the spectra probing the evolving multi-component system described by the observed absorbance changes into a small number of contributions defined by pure difference spectra and kinetic profiles. An example is given in figure II.9 for the case of ultrafast $S_1(\pi\pi^*) \rightarrow T_1(n\pi^*)$ ISC of benzophenone occurring within 10 ps [63]. The possibility to apply tailored constraints and the flexibility of the method to model multiset (multi-experiment) data are the most striking advantages of MCR-ALS. Another advantage of MCR-ALS is that a kinetic model is not required and can thus be applied for variety of processes. Among multiple developments, it is possible to implement chemical knowledge such as a known spectral fingerprint or a kinetic model [67] as constraints. The latter approach leads to a more rationalized description of the process investigated and is of great relevance in femtosecond absorption spectroscopy in order to gain a better description of the spectro-kinetic data.
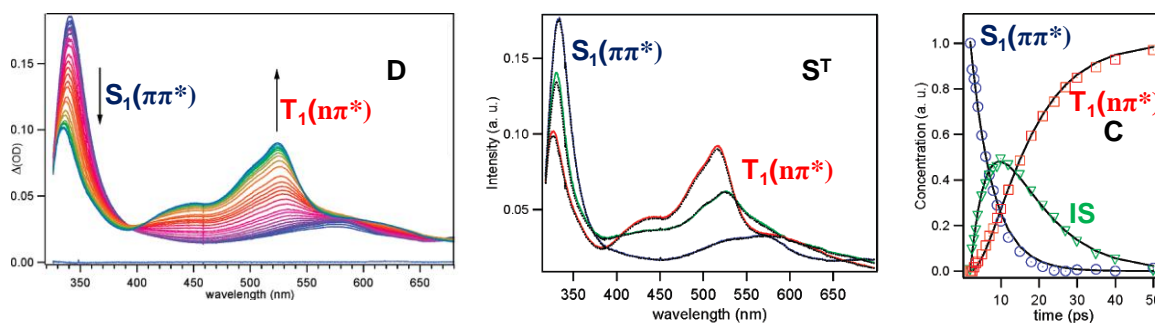
Figure II.9. Femtosecond time resolved absorption spectra of benzophenone in ACN for 267 nm excitation in the 0.8 – 50 ps temporal window allowing constructing the kinetic matrix **D.** Spectra (S^T) and corresponding time dependent concentrations (**C**) deduced from MCR-ALS decomposition (coloured lines and markers respectively) and from HS-MCR decomposition (black lines in both cases) with a kinetic model $S_1(\pi\pi^*) \rightarrow IS \rightarrow T_1(n\pi^*)$ (IS = intermediate state).

The full MCR-ALS procedure can be summarized in the following steps:

(1) Determination of the number of contributions to the experimental matrix **D** by means of singular value decomposition (SVD) or based on a priori knowledge.

(2) Construction of initial estimates of the profiles in **C** or spectra in S^T using chemometric methods and/or chemical insight.

(3) Given **D** and **C**, least-squares calculation of $S^T = C^+ D$ under suitable constraints (the notation C^+ defines the pseudo-inverse of **C**).

(4) Given **D** and S^T, least-squares calculation of $C = D (S^T)^+$ under suitable constraints .

(5) Reproduction of **D** using **C** and S^T calculated in steps (3) and (4). Go back to step (3) until convergence is achieved, i.e. the number of iterative cycle is achieved or the lack of fit between two consecutive iterations is below a selected threshold value.

HS-MCR. Hybrid MCR-ALS methods exist between soft and hard modelling, methods designed as hard-soft MCR (HS-MACR). Indeed, hard-modelling constraints can be included in the iterative soft modelling MCR-ALS to force the concentration profiles to satisfy a kinetic model. Within step (4) of the procedure, the soft-modelled kinetic profiles in C are used as input of a non-linear kinetic fitting, as described in de Juan et al. [67]. In the case of benzophenone it has been shown that triplet production mechanism can be described with an intermediate state IS i.e. $S_1(\pi\pi^*) \rightarrow IS \rightarrow T_1(n\pi^*)$ with two distinct constant rates $k_1 = 6$ ps^{-1} and $k_2 = 2$ ps^{-1}, respectively.

All the calculations for MCR-ALS were performed using MATLAB 7.0 (R14) (The Matworks Ltd., MA). The interface for soft-modelling MCR-ALS calculations is freely available [63].

II.5 Theoretical calculations

Different calculations were done to reproduce stationary absorption and emission spectra, all of them being based on the Density Functional Theory (DFT) and Time-Dependent DFT (TD-DFT) formalisms. At all stages of the procedure, solvent effects were introduced by using the Polarizable Continuum Model (PCM) [52] and all the geometry optimizations as well as the absorption and emission calculations have been carried out with essentially the PBE0 functional and basis set more or less extended depending on the calculations: from 6-31G+(d) (geometry optimization, vertical transitions, etc.) scheme to 6-311G++(2d,p) (NMR). The choice of PBE0 functional has been made after different tests attempting to reproduce the solvatochromic absorption spectrum of SBPa (see details in appendix A). All these calculations have been performed with the Gaussian03 and 09 programs.

In the case of vertical absorption transitions, the usual the three-step methodology is followed [68]: i) ground state geometries were optimized without any symmetry constraint in gas phase with DFT calculations; the corresponding state is named S_0 ii) vibrational spectra were computed to check that the optimized structures correspond to true minima on the potential energy surface; iii) the vertical transition energies and oscillator strengths to the first two excited states, S_1(FC) and S_2(FC), were computed with (PCM)TD-DFT (the first ten lowest-lying singlet states were actually computed).

In the case of vertical emission transitions, an optimization of the excited states was necessary[6]. Starting from the FC geometry, a complete optimization procedure was accomplished following the TD-DFT analytical gradients available in Gaussian09 software. During the exploration of the excited state potential energy surfaces, we used the equilibrium, Linear Response (LR) solvatation scheme [69]. True minima are validated by ensuring that no imaginary frequencies stand in the computed vibrational spectra. Starting from S_1(FC) and S_2(FC), we obtained two optimized structures, named respectively S_1(opt) and S_2(opt). For each optimized state, the emission to the final ground state was obtained by exploiting the corrected LR scheme [70]. Within the cLR approach, a "state-specific" correction to LR excitation energies is introduced by using a solvent reaction field created in response to the excited state charge distribution.

---

[6] All calculations of excited state were done by Aurélie Perrier-Pineau at Universite *Paris* Diderot

The emission wavelength is then simply deduced from the energy gap between the optimized excited state S_1(opt) and S_2(opt) and the corresponding lower vertical state, respectively abbreviated as S_0' and S_0". At this stage, the ground state energy is computed with non-equilibrium solvatation, at the excited state geometry and with the static solvatation reaction field from the excited state.

To analyse the charge transfer within the molecule, we used the Merz-Kollman (MK) charges [71].

CHAPTER III

Concepts and theories related with intramolecular charge transfer processes.

III.1 Introduction

In this chapter we propose to review the main background concepts and theories necessary for a good understanding of the charge transfer process in solution. It is worth to mention, that an exhaustive review is not possible due to the very large number of theories proposed in the literature concerning this subject.

So, in the following, we first present a basic theoretical background related to CT theories often extrapolated from the theories developed for electron transfer (ET): from the thermodynamical approach of Weller to the most advanced descriptions based on Marcus theory (such knowledge will be directly applied in chapter IV). Then, the influence of the environment on the ICT process will be reviewed through different experimental or empirical approaches. A special emphasis will be laid on the solvent influence. These background theories will be of special importance for the interpretation of our femtosecond transient absorption results in chapter V. Solvent reorganization and viscosity effects during ICT process will be discussed introducing fundamental concepts (solvation, power law) or theories (Kramers, Grote and Hynes, ...).

III.2   Theoretical background on charge transfer theories.

To derive a reliable photophysical scheme of ICT molecule not only the proper experimental techniques should be chosen. It is also important to apply proper theories describing processes after photoexcitation.

Electron transfer (ET) from a donor site D to an acceptor site A is one of the simplest chemical reactions as it does not imply any forming or breaking of chemical bonds. ET has been extensively studied – both theoretically and experimentally – since the 1940's [72]; however, due to the usually very fast ET rates, kinetic investigations were inaccessible until the development of fast measuring techniques (as laser pulsed spectroscopy).

Photoinduced electron transfer (PET) occurs when either D or A is excited to a higher energy state due to absorption of a photon. In the first case, an electron of D is excited to an unoccupied MO of high energy and can relax to an empty orbital of lower energy of A. In the second case, an electron of A is excited; leaving a vacancy in a ground state orbital that can be filled by an electron of D.
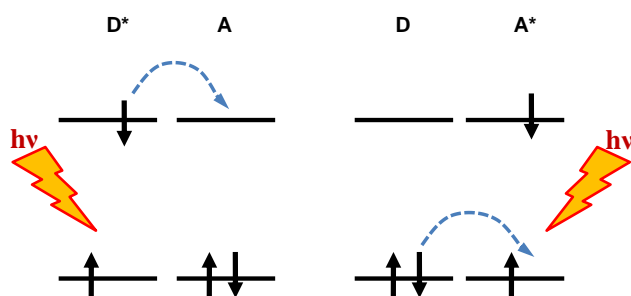
Figure III.1 Photoinduced electron transfer occurring while D (left) or A (right) excited.

As a generalization of PET, photoinduced CT transition[7] concerns the transfer of a fraction of elementary charge (e) from D to A

$$D + A + h\nu \longrightarrow D^{+|\delta|} + A^{-|\delta|} \qquad \text{(III.1)}$$

---
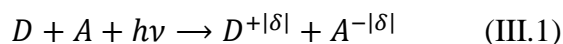
[7] IUPAC definition of CT transition: "An electronic transition in which a large fraction of an electronic charge is transferred from one region of a molecular entity, called the electron donor, to another, called the electron acceptor (intramolecular CT) or from one molecular entity to another (intermolecular CT). Typical for donor-acceptor complexes or multichromophoric molecular entities. In some cases the charge-transfer absorption band may be obscured by the absorption of the partners."

Photoinduced CT reactions can be classified as intramolecular CT (ICT) when D and A belong to the same molecule or intermolecular CT when D and A are distinct molecules. Note this thesis is concerned only with photoinduced ICT.

III.2.1 Weller equation

From a thermodynamic point of view, the PET efficiency is determined by the reaction free energy ΔG^0_{ET} which can be estimated by the Weller expression (equation III.2) [73]

$$\Delta G^0_{ET} = e[E_{ox}(D) - E_{red}(A)] - E_{00} + C + S \qquad (III.2)$$

where $E_{ox}(D)$ and $E_{red}(A)$ are the oxidation and reduction potential of the D and A species, respectively, in acetonitrile, which can be evaluated experimentally from electrochemical measurements; e is the elementary charge; E_{00} is the excited state energy $(0-0$ transition) of either A or D; C is the coulombic term representing electrostatic interactions between ions; finally, S is a corrective factor for solvents other than acetonitrile. Terms C and S can be evaluated from eqs. III.3 and III.4, respectively, where ε_S is the static dielectric constant of the solvent, ε_{ACN} is the static dielectric constant of acetonitrile, ε_0 is the permittivity in vacuum, d is the inter-ionic centre-to-centre distance and r_D^+ and r_A^- are the ionic radii of D and A, respectively.

$$C = \frac{1}{4\pi\varepsilon_0} \frac{-e^2}{\varepsilon_S d} \qquad (III.3)$$

$$S = \frac{1}{4\pi\varepsilon_0} \frac{-e^2}{2} \left(\frac{1}{r_D^+} + \frac{1}{r_A^-} \right) \left(\frac{1}{\varepsilon_{ACN}} - \frac{1}{\varepsilon_S} \right) \qquad (III.4)$$
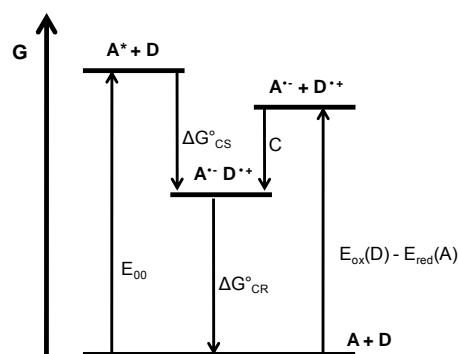
Figure III.2. Typical free energy level diagram for photoinduced ET.

Figure III.2 illustrates equation III.2 by showing the free energy levels of the reactants and products involved in the photoinduced CS and ensuing charge recombination (CR) processes. Here, A is photoexcited and the solvent effects are neglected. It can be seen that charge separation (CS) is not feasible if both D and A are in the ground state, as it would imply an increase of free energy (endergonic reaction, $\Delta G^0_{ET} > 0$). CS becomes exergonic (spontaneous reaction) in the excited state when ΔG^0_{ET} is negative. Furthermore, a high value of $-\Delta G°_{CS}$ (highly exergonic CS) implies a small value of $-\Delta G°_{CR}$ (weakly exergonic CR).

In the case of covalently bounded D-A molecules, to ensure that ICT reaction is thermodynamically allowed, i.e. $\Delta G^0_{ET} < 0$, an extrapolation of the Weller equation is often used [74, 75]. We will apply this equation for SBPa in subsection IV.2.2.

III.2.2 Marcus related theories

The dominant theory of electron transfer in chemistry is undeniably that developed by Rudolph A. Marcus (Nobel Prize in chemistry in 1992 [72]). Starting in 1956, to explain the rates of electron transfer reactions, it was originally formulated to address intermolecular electron transfer reactions [76], and next extended to intramolecular electron transfer reactions by Noel S. Hush [77] (Hush's formulation is known as Marcus-Hush theory). During the last decades, numerous more elaborated theories based on Marcus ideas were developed in order to better explain results from advanced experiments (time-resolved spectroscopy with increasing time resolution...).

In the following, the notion of adiabacity of a reaction is first explained and the main Marcus related theories are briefly presented.

III.2.2.1 Basic concepts and adiabacity

The transfer of a negative charge from D to A, leads to a redistribution of electron density relative to the reactant state. In consequence, both the geometry and solvation cage of D and A will have to adapt to the new electronic configuration. Thus, the reactant state (D + A) and product state (D$^+$ + A$^-$) can be represented by potential energy surfaces R and P, respectively, along a reaction coordinate Q containing the nuclear and solvent contributions. Depending on the extent of electronic coupling between the R and P states (V_{RP}), CT reactions can be classified as adiabatic or non-adiabatic [78].

Non-adiabatic CT process. In this case V_{RP} is small and both R and P can be presented as unperturbed potential energy surfaces, crossing at an intersection point of common energy and geometry/solvation, as presented in figure III.3. The CT process is thus, in the classical description, a jump from surface R to surface P through the intersection point that can be reached due to thermal fluctuations. At the intersection, the probability of R→P crossing depends on the electronic coupling between D and A. The time it takes for the electron to move from D to A limits the rate of non-adiabatic CT. The crossing probability is thus usually small.

On the other hand, from quantum mechanical point of view, crossing of the potential energy surface in non-adiabatic CT process is an isoenergetic non-radiative transition between two levels with sufficiently large Franck-Condon factor. In this case, the Franck-Condon principle can be applied to the non-adiabatic ET, as electron is a very light particle and nuclear and solvent coordinates do not have time to change during the R→P transition. ET can be thus compared with internal conversion process and the crossing can be treated by first order perturbation theory (according to Fermi golden rule). Therefore, the crossing probability depends on V^2_{RP} and the overall ET rate depends on both V^2_{RP} and the probability to reach the crossing point. An electron remains bound to the system during non-adiabatic ET and the spatial transition of negative charge from D to A occurs via tunnelling.
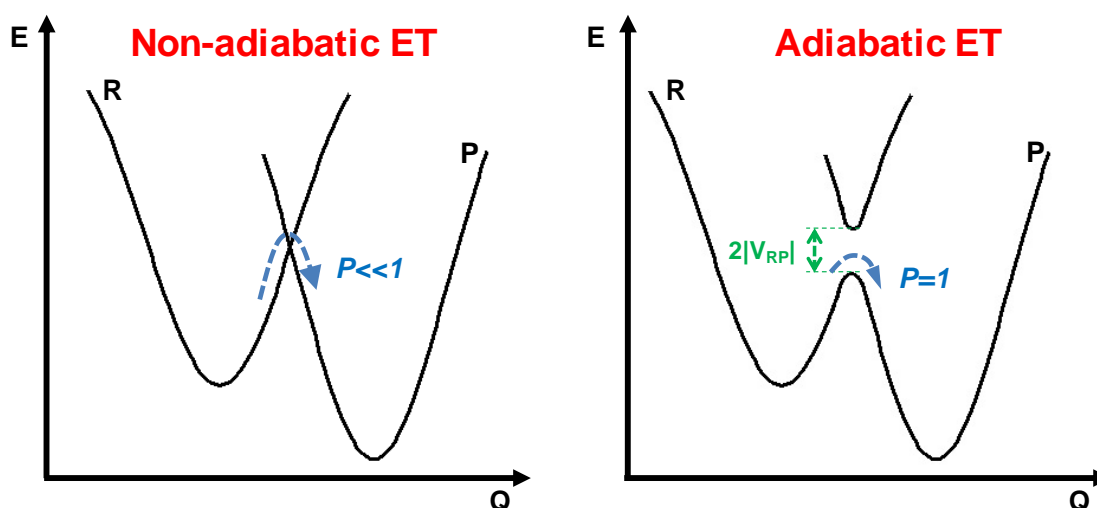
Figure III.3. Potential energy surfaces of reactant (R) and product (P) in non-adiabatic and adiabatic ET.

Adiabatic CT reaction. In this case, the potential energy surfaces of R and P are split by $2|V_{RP}|$ as presented in figure III.3. The lower energy surface consists of two wells

(representing R and P) separated by an activation barrier. Either thermal activation or tunnelling can occur in order to cross the activation barrier. Once the transition state is reached, the CT probability is close to one. The rate of an adiabatic CT is limited by the dynamics of nuclear and/or solvation rearrangement that are much slower than the electron jump from D to A.

III.2.2.2 The classical Marcus-Hush theory(non-adiabatic case)

This theory, for which numerous reviews can be found [72, 79, 80], relates the CT driving force (ΔG^0_{CT}) to its rate (k_{CT})[76, 77, 81-84]. It is based on a purely classical description of non-adiabatic ET, based on the transition state theory (TST[8]). Conditions of validity of this model are in general:

- electron transfer is non-adiabatic

- solvent relaxation is much faster than ET process.

- no excited vibrational levels are involved

- Reactants stay at a fixed distance during ET

The first assumption of the classical Marcus-Hush theory is that the thousands of reaction coordinates (normal modes of a solute, position of solvent molecules...) are summarized in one dimensional coordinate Q. While the vibrations of R and P are treated as harmonic oscillators, the solvent is considered as a dielectric continuum. Moreover, the system is in quasi-equilibrium during the ET process and with respect to conservation of energy and FC principle, transition can only occur at the intersection of two potential energy surfaces, considered to be a transition state (figure III.4).

---

[8] Transition-State Theory assumes that the reactants and the activated complex are in equilibrium and that the population of the other molecular and bath degrees of freedom may be characterized by a temperature T.
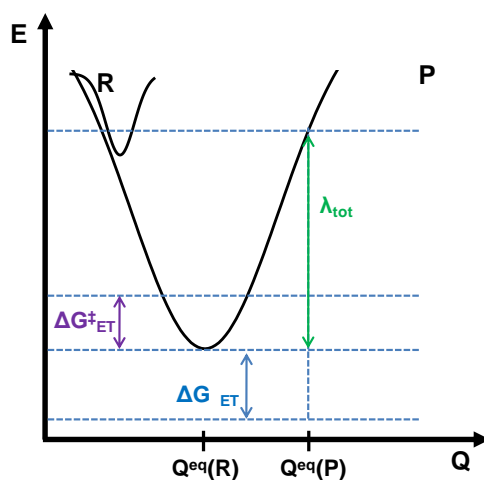
Figure III.4. Potential energy surfaces of reactant (R) and product (P) according to the classical Marcus-Hush theory.

Within this model, the rate of ET depends on two quantities [85]: i) the probability to reach the transition state from the bottom of the well, via random thermal fluctuations of the nuclear and/or solvent coordinates (nuclear factor); ii) on the rate to cross the transition state (an electronic factor depending on the electronic coupling between R and P potential curves (Landau-Zener expression)). It can be expressed by the Arrhenius equation (equation III.5) according to the transition state theory.

$$k_{ET} = A exp\left(\frac{-\Delta G_{ET}^{\ddagger}}{k_B T}\right) \qquad (III.5)$$

The $\Delta G_{ET}^{\ddagger}$ is the activation energy, k_B the Boltzmann constant, A a pre-exponential factor, and T the temperature. Figure III.4 shows the activation energy, free energy of reaction, and total reorganization energy (λ_{tot}) to get from the reactant to product equilibrium position on the reactant free energy surface. The activation energy can be thus expressed (by solving a quadratic expression at the intersection point of two parabolas) as:

$$\Delta G_{ET}^{\ddagger} = \frac{\left(-\Delta G_{ET}^{0} + \lambda_{tot}\right)^2}{4\lambda_{tot}} \qquad (III.6)$$

The total reorganization energy is a sum of the solvent reorganization energy (λ_s) and intramolecular reorganization energy (λ_i):

$$\lambda_{tot} = \lambda_s + \lambda_i \qquad (III.7)$$

The solvent reorganization energy can be evaluated using equation III.8, where Δq is the transferred charge, r_D^+ and r_A^- are the ionic radii of the reactants, r_{AD} is their centre-to-

centre distance, n and ε_s are the refractive index and static dielectric constant of the solvent, respectively.

$$\lambda_S = \frac{1}{4\pi\varepsilon_0}\Delta q^2 \left(\frac{1}{2r_D^+} + \frac{1}{2r_A^-} - \frac{1}{r_{AD}}\right)\left(\frac{1}{n^2} - \frac{1}{\varepsilon_s}\right) \qquad (III.8)$$

Treating the intramolecular modes as harmonic oscillators with force constants f_i, energy λ_i can be evaluated by equation III.9.

$$\lambda_i = \Sigma\left[\left(\frac{f_i(R)\cdot f_i(P)}{f_i(R)+f_i(P)}\right)(\Delta x_i)^2\right] \qquad (III.9)$$

where Δx_i is the displacement of vibrational mode i from the reactant equilibrium position to the product equilibrium position while $f_i(R)$ and $f_i(P)$ are the force constants of mode i in P and R, respectively.
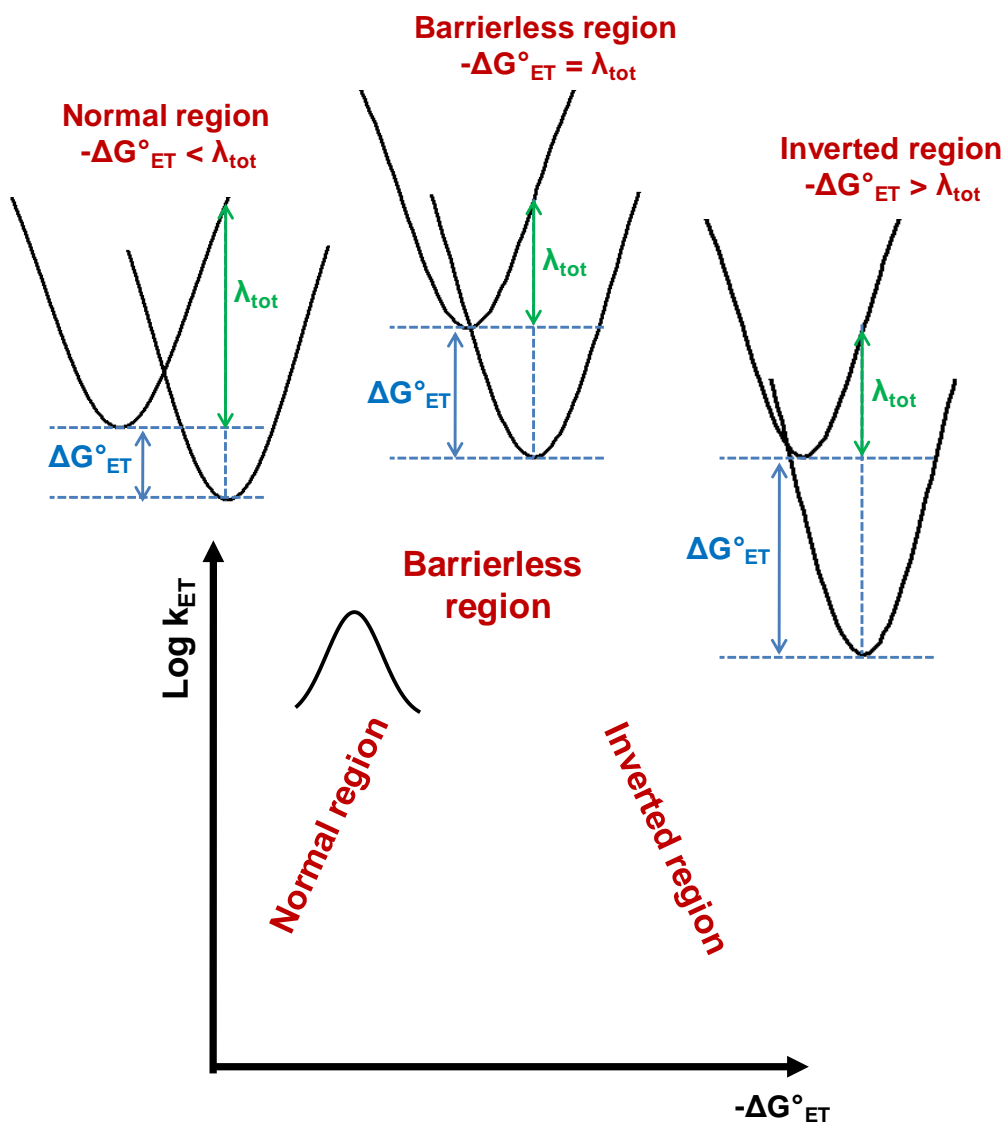
Figure III.5. The normal, barrierless and inverted Marcus regions.

The pre-exponential factor A in Arrhenius equation (equation III.5) is proportional to the probability of the electronic crossing from the reactant to the product free energy surface in the transition state region. Several expressions have been proposed to evaluate this parameter; however the most commonly used in non-adiabatic limit was proposed by Levich and Dogonadze [86] (see equation III.10).

$$A = \frac{2\pi}{\hbar} \frac{V_{RP}^2}{\sqrt{4\pi\lambda_s k_B T}} \qquad \qquad (III.10)$$

Finally, combining III.5, III.6 and III.10, a complete expression for the rate of electron transfer can be given:

$$k_{ET} = \frac{2\pi}{\hbar} \frac{V_{RP}^2}{\sqrt{4\pi\lambda_s k_B T}} exp\left(-\frac{\left(\Delta G_{ET}^0 + \lambda_{tot}\right)^2}{4\lambda_{tot} k_B T}\right) \qquad (III.11)$$

A plot of $\log(k_{ET})$ as a function of $-\Delta G_{ET}^0$ yields the bell-shape curve shown in figure III.5, where three characteristic regions can be distinguished:

- The normal region ($-\Delta G_{ET}^0 < \lambda_{tot}$) where the ET rate increases with exergonicity

- The barrierless region ($-\Delta G_{ET}^0 = \lambda_{tot}$) where there is no activation barrier and thus the ET rate reaches its maximum.

- The inverted region ($-\Delta G_{ET}^0 > \lambda_{tot}$) where the ET rate decreases with increasing driving force.

In chapter V, even if it appears as a challenging task, we will attempt to determine in which Marcus region the SBPa CT process arises.

III.2.2.3   The semiclassical Marcus theory (non-adiabatic case)

As the experimental techniques were improved, very high ET rates became measurable and the classical Marcus-Hush theory appeared no longer appropriate. One of the experimental indications pointing out the need of improvement of the existing theory was the observation of less pronounced inverted region than predicted. A generalized semiclassical Marcus theory was thus proposed that took into account the high frequency intramolecular quantum modes and the possibility of vibronic transitions (the ET reaction occurs from the vibrational ground state of R to an excited vibrational state of P – see figure III.6a) [87]. This model can be applied under the following conditions:

- Non-adiabatic ET process

- The relaxation of the solvent is much faster than ET process

- Excited vibrational levels are involved

- Reactants are at the fixed distance

Therefore, for each vibronic transition, there is a free energy of reaction ($\Delta G^0{}_{0\to n}$) and a coupling element ($V_{0\to n}$). The former term includes the vibrational energy of the excited vibrational mode (as presented in equation III.12) where v_i is a single vibrational frequency being the average of all existing quantum modes involved. The second term includes the purely electronic coupling and Franck-Condon overlap between the ground state of R and the nth excited vibronic state of P (see equation III.13). The rate constant related to each one of the vibronic transitions can be calculated from equation III.14 (see also eq. III.11)

$$\Delta G^0_{0\to n} = \Delta G^0_{ET} + nh\nu_i \qquad (III.12)$$

$$V^2_{0\to n} = V^2_{RP}|\langle 0|n\rangle|^2 \qquad (III.13)$$

$$k_{0\to n} = \frac{2\pi}{\hbar}\frac{V^2_{0\to n}}{\sqrt{4\pi\lambda_s k_B T}} exp\left(-\frac{\left(\Delta G^0_{ET}+nh\nu_i+\lambda_s\right)^2}{4\lambda_s k_B T}\right) \qquad (III.14)$$

Therefore, the overall ET rate constant is the sum of all individual $k_{0\to n}$ rates as presented in equation III.15 (note that in this case, the reorganization energy is solely given by the solvent reorganization energy)

$$k_{ET} = \frac{2\pi}{\hbar}\frac{V^2_{RP}}{\sqrt{4\pi\lambda_s k_B T}}\sum_n|\langle 0|n\rangle|^2 exp\left(-\frac{\left(\Delta G^0_{ET}+nh\nu_i+\lambda_s\right)^2}{4\lambda_s k_B T}\right) \qquad (III.15)$$

The important difference between the classical Marcus-Hush and semiclassical Marcus theories concerns the shape of inverted region. In semiclassical theory this region is flatter (see figure III.6b), which corresponds better to experimental observations [88-90].

a)   b)
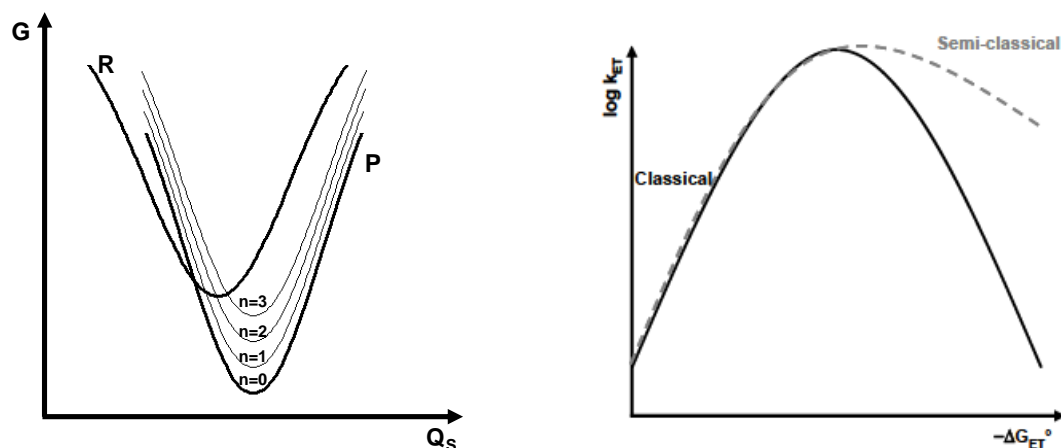
Figure III.6 a) potential energy surface involved in ET, including vibrational levels of P; b) Schematic driving force dependence of k_{ET} comparing classical and semi-classical Marcus theory [91].

III.2.2.4   From non-adiabatic to adiabatic ET.

As discussed previously for adiabatic ET (unlike for non-adiabatic ET) R and P lie on the same potential energy surface. Therefore, electronic crossing in the transition state appears with probability equal to one ($P = 1$). The rate of ET does not depend on the electronic coupling; instead, it depends on: i) the probability of the system to reach the transition state region, ii) the time it will take to cross this region and iii) the rate of dissipation of the energy to trap the system in the product well. The motion of the system along the reaction coordinate Q becomes thus very important.

Let us now discard for a moment intramolecular effects influencing the system and focus on the motion from R to P in terms of interactions with the highly irregular motion of large number of solvent molecules, leading to frictional and random forces. A first consequence of the existence of such forces is an exchange of energy in the form of heat between the system and its environment. Such exchange allows reaching the transition state, as well as relaxing into the product well. On the other hand, motion over the transition state is affected by interactions with solvent molecules. For non-adiabatic ET, it was assumed, that the system is in quasi-equilibrium with the environment, so that only static solvent interactions were considered. In case of adiabatic ET, when the rate of the process is of the same order of magnitude (or even faster) as solvent relaxation rate, the dynamical interactions with the solvent become important and should be taken into

consideration. The characteristic time used for the solvent relaxation in response to changes of charge distribution in D and A is the longitudinal relaxation time (τ_L)[9].

The ET rate is thus influenced by: the electronic coupling, motions along the reaction coordinate and the competition between the ET process and solvent relaxation dynamics [92]. Beyond that, adiabatic and non-adiabatic processes should be considered as limiting cases. The classical Landau–Zener theory can be adapted to ET in order to account for the adiabaticity and motion along the solvent coordinate.

The purely adiabatic limit case was treated by Kramers. This important theory is reviewed with more details later in this chapter.

III.2.2.5 The classical Marcus-Sumi Theory (adiabatic case).

For extremely fast adiabatic ET processes ($k_{ET} \gg 1/\tau_L$), the previously discussed theories are insufficient to explain experimental data. The Marcus-Sumi theory assumes that crossing over the ET activation barrier is driven by fast intramolecular vibrations [93-95]. This model can be applied in case of very different R and P equilibrium geometries. It is a bidimensional theory taking into account both nuclear coordinates (**q**) and solvent coordinates (**X**). The main assumptions for the Marcus-Sumi model are:

- Different time scales characterize motions along the q and X reaction coordinates
- ET is much faster than the reorganization of the solvent molecules
- No excited vibrational modes are involved
- Reactants are at the fixed distance

The ET reaction proceeds in this case along the solvent coordinate X, presenting slow Brownian diffusion as well as along the perpendicular intramolecular vibrational coordinate presenting fast geometrical changes. The difference between this model and the one-dimensional approaches is that for the later the R $\rightarrow$ P reaction appears at the

---

[9] Longitudinal relaxation time - represents a fraction of Debye time τ_D: $\tau_L = \frac{\varepsilon_\infty}{\varepsilon_0} \tau_D$ which is a setting of the polarization in dielectric putted in constant dielectric field (ε_0 is the static dielectric constant and ε_∞ is an optic dielectric constant, which at frequency ∞ is equal to n²). More detail will be given in chapter IV (subsection III.3.1)

transition state, which is a single point, whereas in the bi-dimensional approach it can occur along the whole region of intersection between the two potential surfaces.

Some limiting cases which can be defined in terms of the relation between $(1/\tau_L)$ and the rate $k(X)$ along the X coordinate or the relation between the solvent and intramolecular reorganization energies λ_S and λ_i, respectively:

- The slow reaction limit $(k(X) \ll 1/\tau_L)$: in this case the classical Marcus-Hush theory (non-adiabatic) applies as the system is in quasi-equilibrium with the solvent during ET and only static solvent effects are considered.

- The non-diffusing limit $(k(X) \gg 1/\tau_L)$: the solvent is "frozen" during the ET reaction. In this case, no diffusion along the X coordinate occurs and the solvent dynamics does not influence the reaction.

- The wide reaction window limit $(\lambda_S \ll \lambda_i)$: the activation energy depends only slightly on X and the reaction can occur over a wide range of solvent configurations. Again, the situation reduces to classical Marcus-Hush theory.

- The narrow reaction window limit $(\lambda_S \gg \lambda_i)$: the activation energy strongly depends on X and the reaction can occur only for a narrow range of solvent configurations. Solvent dynamics influence strongly the reaction.

In this manuscript we will be concerned to select appropriate CT theory to best interpret stationary (chapter IV) or time resolved data (chapter V).

III.3   Solvent influence on the ICT dynamics

III.3.1   Solvent reorganization during reaction dynamics.

The role of the dynamics of solvent reorganization which accompanies the formation of ion pairs or polar species in polar medium has been taken into account over thirty years ago [96], but solvent behaviour in polar medium was studied long before. Debye considered that the readjustment of the polarization of a dielectric put in a constant dielectric field occurs with an exponential kinetics with characteristic time τ_D. The longitudinal relaxation time of the solvent, τ_L, can be expressed as a function of τ_D as follow [97]:

$$\tau_L = \frac{\varepsilon_\infty}{\varepsilon_0} \tau_D \qquad\qquad (III.16)$$

Where ε_0 is the static dielectric constant and ε_∞ is an optic dielectric constant (which is equal to n^2 at frequency ∞). τ_D can be described as the time of dielectric relaxation of a constant charge. When the solvent is treated as a dielectric continuum, the CT time constant is proportional to the solvent longitudinal relaxation time τ_L.

It is known that the reorganization of solvent molecules around a charge or dipole takes place in different stages: the first ultrafast process (100 – 300 fs) is attributed to the initial response of solvent molecules in closest proximity of the charge, and then slower stages (often multi-exponential) are controlled by dielectric relaxation. The average of these components corresponds to average solvation time $\langle\tau\rangle_{solv}$ [98]:

$$\langle\tau\rangle_{solv} = \sum_i a_i \tau_i \qquad\qquad (III.17)$$

where a_i is the statistical weight associated with each relaxation time τ_i, respectively. Experimentally, Marconcelli et al. have investigated the Coumarin 153 in different organic solvents with high resolution time resolved florescence to measure the $\langle\tau\rangle_{solv}$ [99].

Theoretical studies on charge transfer reactions try to explain which factors are predominant during the electronic rearrangement through the molecule. If solvation is the only relevant coordinate, $(\langle\tau\rangle_{solv})^{-1}$ or $(\tau_L)^{-1}$ (if the solvent is considered as a dielectric continuum) are the higher limit for the characteristic time constant of the CT reaction which is barrierless [99]. On the other hand, in systems where the CT process is combined with some intramolecular reorganization of the solute, the theoretical model of Sumi-

Marcus (described in details in chapter I), in which both intramolecular (nuclear) and solvent coordinates are explicitly separated, shows that the CT process can be faster than $\langle\tau\rangle_{solv}$ or τ_L.

III.3.2   Effect of the viscosity of the solvent on the reaction dynamics.

Let us consider an intramolecular reaction (isomerization for example) occurring in a homogenous medium of given viscosity. At low values of the solvent friction, the reaction rate increases with increasing friction because collisions provide the energy needed to attain the threshold energy for reaction. In the opposite limit, when the friction or the collision frequency becomes very high, the collisions (or friction) impede the reaction and the rate decreases with increasing friction. This is this balance between "enhancement" and "impediment" induced by solute-solvent collisions that affects the ICT dynamics.

If the electron transfer process is combined with intramolecular reorganization of the solute, the friction of the surrounding solvent plays substantial role in the transfer dynamics. In Debye-Stokes-Einstein theory the friction of the solvent ζ is directly related to the rotational diffusion D of molecules[100]:

$$D = \frac{k_B T}{\zeta} = \frac{k_B T}{8\pi r3} \times \frac{1}{\eta} \qquad (III.18)$$

With $\zeta = 8\pi\eta r^3$, r is the spherical molecule radius, and η is the viscosity of the solvent. The role of the solvent viscosity on chemical reactions was first studied by Kramers [100, 101]. He described intramolecular reactions as a transition of the molecule through the potential barrier situated between two wells representing the reactant and the product. More recent studies by Grote and Hynes[100, 102] introduced the notion of time dependent friction of solvent molecules for predicting the reaction kinetics in solution.

III.3.2.1   Kramers model [100, 101].

Kramers treated the reactive motion as the escape of a particle over a potential barrier in one dimension (see figure III.7). The particle is initially bound in the potential well at point A. It must pass over a potential barrier of energy ΔE at point B to reach the product well at point C.
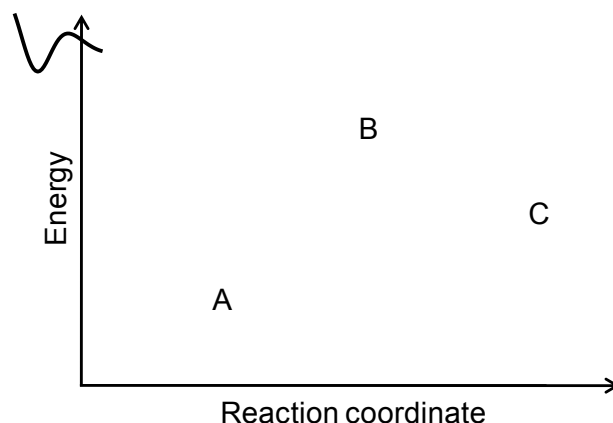
Figure III.7 One-dimensional potential surface for an activated barrier crossing[100].

Kramers described the dynamics of the particle as diffusion along the potential according to the following assumptions:

- the particle motion is driven by random forces

- $E_{01} \gg kT$ (the particle is in a quasi-stationary state in well A)

- Near A exists a Boltzmann distribution of velocities

- The potential is piecewise harmonic with a frequency ω_0 near A and ω_0' near B

- There is no back reaction.

He found that the rate constant is given by:

$$k_{Kr} = k_{TST} \left[\frac{\sqrt{1+(2\omega'\tau_v)^2}-1}{2\omega'\tau_v} \right] \qquad (III.19)$$

where τ_v is a characteristic time for the velocity distribution, $\tau_v = 1/\zeta$ is the velocity relaxation time, and k_{TST} is the transition-state theory (TST[10]) rate constant and can be calculated with:

$$k_{TST} = \frac{\omega'}{2\pi} exp\left(\frac{-\Delta G^{\neq}}{k_B T}\right) \qquad (III.20)$$

Where ω' is the frequency in the reactant potential well and $\Delta G^{\neq}$ is the activation energy of reaction. Crossing the reaction barrier proceeds with probability equal to 1, according the transition state theory. During reactions in solution solvent molecules can change the

---

[10] Transition-State Theory assumes that the reactants and the activated complex are in equilibrium and that the population of the other molecular and bath degrees of freedom may be characterized by a temperature T.

trajectory of the reactants and the probability of crossing the barrier becomes smaller than 1. In the time constant calculated by Kramers, we can separate two limit cases:

- Strong friction regime, where $k_{Kr} \sim 1/\zeta$
- Low friction regime, where $k_{Kr} \sim \zeta$

The study of the cis-trans isomerization of stilbene showed that the transition between these two limiting cases corresponds to the liquid/gas phase limit. In solution the rate of a reaction decreases while the solvent viscosity increases.

III.3.2.2   Grote and Hynes model [100, 102].

Kramers theory was refined by Grote and Hynes. They cancelled the first assumption of Kramers, that the movement of molecules in solution is driven by random forces. In their approach, friction forces depend on time according to the memory of the diffusion path through the solution (non-Markov process). The friction-dependent time is proportional to the average in space of the solvent movement correlation function. The correlation time of fluctuating forces exerted with a solvent can be compared with the time during which reactants cross the barrier. To describe the movement of the reactants into products, Grote and Hynes model bases on a generalized Langevin equation in which the friction exerted by a solvent on reactants is the time dependent term. The time constant calculated using this equation is as follows:

$$k_{GH} = \frac{\lambda}{\omega\prime} k_{TST} \qquad (III.21)$$

Where λ is determined from the self-consistent relation:

$$\lambda = \frac{\omega\prime^2}{\lambda + \xi(\lambda)} \qquad (III.22)$$

However, the direct use of those equations is not straightforward due to the unknown function $\xi(\lambda)$.

III.3.2.3   Power law [100].

A clear dependence of the reaction time constant on the viscosity of the surrounding solvent can be an indication that conformational changes appear within investigated system during this reaction. An empirical law was proposed after numerous theoretical and experimental studies to describe such conformational changes or isomerisation and evaluate the associated rate constants. The law can be written as follows:

$$k = \left(\frac{B}{\eta^\alpha}\right) exp\left(-\frac{E_{act}}{RT}\right) \qquad (III.23)$$

where E_{act} is the activation energy, B is a constant, and $0 \leq \alpha \leq 1$

The first term is a universal function of viscosity and represents the friction or dynamical effects exerted by the surrounding solvent opposing the motion of the parts of the molecule involved in the conformational change. The second term represents the barrier in the form of conformational changes process. At a particular temperature and in a class of solvents for which E_{act} remains more or less unchanged, it is possible to consider the exponential term as constant and eq.IV.8 can be rewritten as:

$$ln(k) = \alpha \; ln\left(\frac{1}{\eta}\right) + C \qquad (III.24)$$

A plot of ln(k) versus ln(1/η)should be a straight line with a positive slope of magnitude equal to α and a value at origin equal to constant C = ln(B) − E_{act}/RT. Depending on the magnitude of the slope, one can consider two cases:

- $\alpha \approx 1$ means that the process is barrierless

- $\alpha < 1$ means that an activation energy barrier has to be crossed along the reaction pathway

CHAPTER IV

Stationary spectroscopy results and theoretical

studies of SBPa

IV.1 Introduction

In the introduction, we pointed out the potential interest of the SBPa molecule related to the dipole moment inversion and subsequent hyperpolarizability enhancement in the excited state. In order to rationalize this effect, a series of *ab initio* (HF, CIS, MP2 levels of calculation) as well as semi-empirical calculations (ZINDO) of the $S_1(\pi,\pi^*)$ excited state structure have been performed by Professor Abe's group [18, 19]. An intramolecular charge transfer (ICT) character of S_1 has been identified, which involves a displacement of the π charge from the betaine (donor) to the pyridinium (acceptor) part of the molecule. Advanced MP2 calculations have successfully reproduced the experimental dipole moment value for the ground state, $\mu_g(\exp) = 10.33$ D [23]. In parallel, CIS calculations of the excited state have predicted the preservation of the ground state molecular symmetry group (namely C_{2V}) and an enhancement of the overall quinoid character of the molecule accompanied by a decrease and flip of the dipole moment, with a calculated value around $\mu_e \sim -3$ D. [18, 19]. However, only semi-empirical calculations have been able to reproduce approximately the absorption spectrum of the molecule, pointing out the difficulty to describe correctly the electronic cloud engaged in the CT reaction. Furthermore, theoretical implementation of the solvent has never been reported for this molecule.

Apart the refinement one can expect from advanced calculations, further experimental investigations are lacking to get a good understanding of the ICT process in SBPa, especially concerning the solvatochromism effect. Indeed, although it has been shown in the literature that experimental estimation of excited state dipole moments can be provided from analyses of the solvatochromism [26, 28, 103, 104], thoughtful solvatochromism study of SBPa has never been reported except for some sparse data [22]. Note furthermore that any emission data on SBPa has not been reported in the literature so far. Indeed, it is well known that investigations dealing with the changes for steady-state absorption and/or emission band maximum of a CT transition with solvent polarity, interpreted with the help of a dielectric continuum model, leads to a more or less accurate determination of μ_g and μ_e. In general, the procedure for analyzing solvatochromic data, first proposed by Lippert and Mataga [29-32], consists in evaluating $\Delta\mu$ through a plot of the Stokes shift as a function of a solvent polarity parameter and deducing μ_e from a second independent measurement of μ_g by conventional electrotechnics [23, 105]. However, great care has to be taken with regard to the different assumptions made in the theoretical treatment of the

solvatochromism, such as the choice of the solute polarizabilty and gas phase transition energy. [106, 107] It is worth mentioning here that the solute polarizability in both the ground and excited states, α_g and α_e, is *a priory* an important physical characteristics to be considered. Practically, it is a challenging task, much debated in the literature [103, 108, 109] .

Similarly, the band shape analysis [110] of solvatochromic absorption (emission) transitions can allow determining relevant quantities concerned with CT reactions like the transition moment, driving force, intramolecular or solvent reorganizations energies... This approach is made possible with the decisive contribution of Marcus who first derived an analytical expression for the extinction coefficient (fluorescence intensity) of a CT transition according to a semi-empirical approach. Note however that such advanced band shape analysis deals with a large number of parameters so that great care has to be taken concerning the significance of the results.

In the following, first evidences of ICT process based on electrochemistry measurements and solvatochromic effects will be discussed. At this point, three distinct approaches will be achieved. A band shape analysis of the solvatochromic absorption CT band will be performed to assess relevant energetically quantities dealing with the surrounding medium. Focusing then on the molecule itself, a comparison between absorption and emission solvatochromic data with the help of advanced PCM-TDDFT calculations will allow to get a thoughtful knowledge of the ground and excited states involved in the ICT process. Furthermore, from these calculations (which include excited states optimization), various dipole moment will be determined. Finally, an innovative data treatment of the observed absorption and emission solvatochromic data will be proposed with the final aim to deduce experimental values for the dipole moments of both the ground and excited states, allowing relevant comparison with (TD)DFT values.

IV.2   First evidences for a photoinduced ICT process in SBPa

We will now present the first experimental evidences for the CT character of the absorption transition of SBPa. In the beginning of the analysis, we will focus only on data in a few representative solvents and next we will undertake a more advanced analysis done for a larger set of solvents.

IV.2.1   Negative solvatochromism of the absorption band

To get a first evidence of the existence of an ICT process in SBPa, solvatochromic behaviour has been searched with the help of stationary absorption data. Figure IV.1a presents spectrum of SBPa in the $300 - 600$ nm region for four solvents of different polarities: methanol (MeOH), acetonitrile (ACN), tetrahydrofuran (THF), and toluene. To describe the solvent polarity, among the different parameters reported in the literature, we will chose the well-known $E_T(30)$ scale defined as [111]:

$$E_T(30)(kcal.M^{-1}) = \frac{28590}{\lambda(nm)} \qquad \textbf{\textit{(IV.1)}}$$

where λ refers to the maximum of absorption of the Richard's Betaine solvatochromic molecule. The absorption spectra in Fig IV.1a present one strong band showing a drastic hyspochromic shift of the maximum upon increasing the solvent polarity from MeOH ($E_T(30) = 55.4$; $\lambda_{max} = 385$ nm) to ACN ($E_T(30) = 45.6$; $\lambda_{max} = 393$ nm), THF ($E_T(30) = 37.4$; $\lambda_{max} = 421$ nm) and toluene ($E_T(30) = 33.9$; $\lambda_{max} = 446$ nm).

This strong negative solvatochromism is indicative of a much better stabilization by solvation of the ground state compared to the excited state in polar solvents. This reveals that SBPa is more polar in the ground state than in the excited state, as schematically shown in figure IV.1b. As the ground state has some zwitterionic character, such a polarity decrease between ground and excited state can be explained by a CT nature of the electronic transition, leading to a (partial) intramolecular charge recombination.

a)

b)
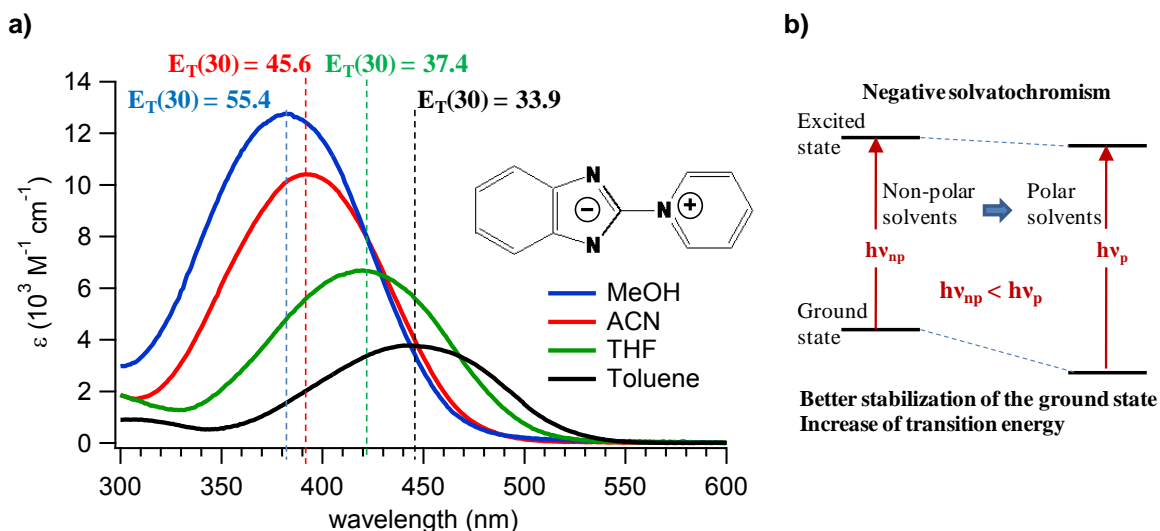
Figure IV.1. a) Stationary absorption spectra of SBPa in four solvents of different polarities; b) schematic explanation of the negative solvatochromism effect.

IV.2.2 Electrochemical measurements

From a thermodynamical point of view, the Weller expression, presented previously, gives the efficiency of photoinduced ET through the determination of the free energy of reaction (equation III.2). This equation in the case of ACN (representative case) reduces to equation IV.2:

$$\Delta G_{ET}^0(eV) = [E_{ox}(D) - E_{red}(A)] - E_{00} - 0.06 \qquad (IV.2)$$

In this equation, E_{00} is the pure electronic transition energy, generally deduced from the intersection of the absorption and emission spectra. As we will see, we cannot proceed by this way for SBPa since different excited states are involved in these two transitions. Consequently, E_{00} will be approximated as the average between the top and right footband positions of the absorption band; in ACN $E_{00} \approx 2.75$ eV. Moreover in the above equation, the value of E_{ox} - E_{red} can be determined from the cyclic voltammogram of SBPa which is depicted in figure IV.2. Such an electrochemical measurement[11] was performed at the "Institut de Science de Matériaux de Mulhouse" by Dr. Jean-Pierre Malval. The cathodic part of the voltammogram in figure IV.2 shows the irreversible reduction of SBPa. The corresponding potential has a value of ca. -1.39 V/SCE which is close to the reduction potential of the pyridium group [112] (-1.21 V/SCE). At high potential, SBPa shows an irreversible oxidation wave with a maximum located at 0.11 V/SCE which should be

---

[11] The cyclic voltammetry experiments (using a computer-controlled Princeton 263A potentiostat with a three-electrode single-compartment cell; a saturated calomel electrode used as a reference was placed in a separate compartment) were performed at 300 K, in Ar-degassed acetonitrile with a constant concentration (0.1 M) of n-Bu$_4$BF$_4$. Ferrocene was used as an internal reference.

ascribed to the oxidation of the anionic part of the chromophore (benzopyrazole moiety). Accordingly, a $E_{ox} - E_{red}$ value of 1.51 eV is estimated, which leads to a $\Delta G_{ET}^{0}(eV) = -1.3$ eV in ACN. This manifestly negative value reveals the exothermic character of the photoinduced charge transfer and confirms thus that the CT reaction occurs spontaneously in the excited state.
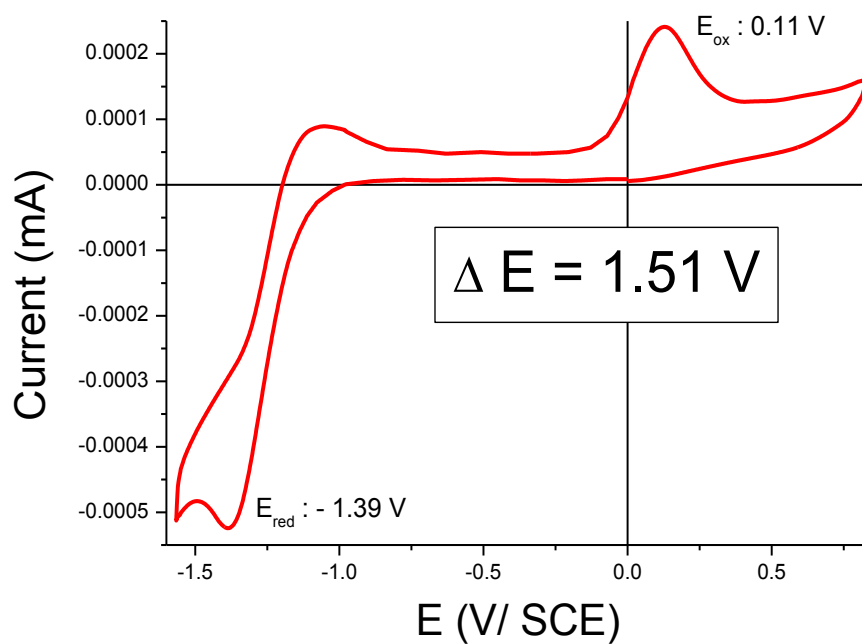
Figure IV.2. Cyclic voltamogram of SBPa in ACN ($\sim 10^{-3}$ M) with 0.1 M n-BuF$_4$ as electrolyte support.

IV.3 Transition moment and band shape analysis of the solvatochromic absorption band

Analysing the absorption band shape can provide a lot of valuable information about the photoinduced ICT process. First, from the band area, the transition dipole moment of the vertical transition related with ICT can be evaluated. Secondly, detailed band shape analysis based on the Marcus theory can deliver additional energetical parameters, as the intramolecular or solvent reorganization energies (see equations III.9 and III.8). Various examples of band shape analyses can be found in the literature [113, 114]. In this chapter, results obtained for 12 solvents are discussed.

IV.3.1 Transition dipole moment

For a quantitative analysis of the spectral intensity, the transition dipole moment M_{abs}, which describes the probability of transition between the ground and excited states, must be determined. This parameter can be deduced from the extinction coefficient integrated over the whole absorption CT band by using the following relation:

$$|M_{abs}|^2 = \frac{3ln10\varepsilon_0 hc}{2\pi v_{max}N_a} \int \varepsilon(v_a)dv_a \qquad (III.3)$$

where ε_0 is the vacuum permittivity, h the Planck constant, c the speed of light, v_{max} the maximum wavenumber of the absorption band, N_a the Avogadro constant, and the integral term the band area. The calculated M_{abs} values are reported in table IV.1.

Table IV.1 Transition dipole moment M_{abs} of SBPa in 12 solvents determined using equation III.3. Absorption band maximum λ_{max}, extinction coefficient $\varepsilon(\lambda_{max})$, as well as solvent polarity parameters are added.

		solvent	ε	$E_T(30)$ (kcal.M^{-1})	λ_{max} (nm)	$\varepsilon(\lambda_{max})$ (M^{-1}cm^{-1})	M_{abs} (D)
APROTIC	Alkylnitrile	ACN	35.94	45.6	392	10444.9	9.0
		Butyronitrile	24.83	42.5	403	11910.2	9.4
		Octanenitrile	13.60	41.1	413	11884.3	9.3
		Decanenitrile	10.60	-	389	3488.7	5.4
	Low Polar	THF	7.58	37.4	420	6622.5	7.7
		MeOAc	6.68	38.9	410	8853.1	8.9
		EtOAc	6.02	38.1	413	5313.7	6.4
		Toluene	2.38	33.9	443	3786.2	5.4
PROTIC		2-Pentanol	13.90	49.1	401	5722.2	6.5
		MeOH	32.66	55.4	382	12617.4	10.8
		EtOH	24.55	51.9	391	11747.1	9.4
		2-butanol	16.56	47.1	399	7456.3	7.4

Analysing the dependency of $|M_{abs}|$ on the solvent polarity parameter $E_T(30)$, see figure IV.3, reveals that all solvents do not follow the same tendency but, instead, can be divided into two groups: the aprotic solvents ($R^2 = 0.66$) and the protic solvents, ($R^2 = 0.82$). This distinction denotes clearly the influence of specific solvent-solute interactions due to hydrogen bonding. The presence of such H-bond interactions will be evidenced again later in other stationary and time-resolved spectroscopic data.
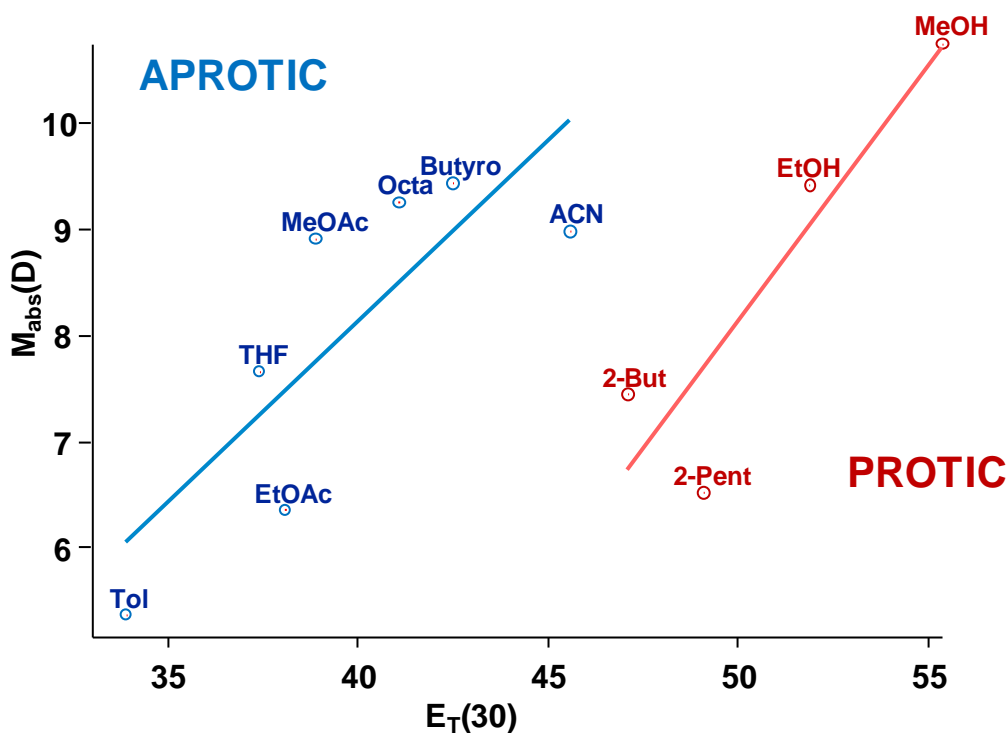
Figure IV.3. Evolution of the transition dipole moment (in Debye) as a function of the solvent polarity parameter $E_T(30)$ for aprotic (in blue) and protic (in red) solvents

IV.3.2   Band shape analysis according to Marcus theory

We aim to analyze the experimental absorption solvatochromic band described above (see figure IV.1a) in order to evaluate some relevant energetical parameters as the driving force of the CT process ($-\Delta G_0$) (see subsection III.2.2.3), as well as the solvent and intramolecular reorganization energies (equations III.8 and III.9). We will use an analytical expression based on the semi-classical Marcus theory with paying special attention to the physical relevancy of the fitted parameters. For this reason, some tests of validity are required and we will thus define additional validity equations. The methodology used to perform such a relevant band shape analysis will be briefly described and the results will be discussed.

IV.3.2.1 Analytical expression for the extinction coefficient

As demonstrated in 1980's by R. A. Marcus, the theoretical expression giving the absorption intensity associated to the excited state ET transition, as a function of frequency, $\varepsilon = f(\nu)$, is known to parallel the expression of the ET rate constant expressed as a function of the free energy, $k_{ET} = f(-\Delta G^0_{ET})$. The common point for both expressions is the FC parameter [115]. Basing on this analogy and applying semi-classical derivation of the FC parameter [87] (see subsection III.2.2.3) restricted to one vibrational harmonic mode, an analytical expression for the extinction coefficient $\varepsilon(\nu)$ of the CT band has been derived:

$$\frac{\varepsilon(\nu)}{n\nu} = \frac{8\pi^3}{3cln10} M_{abs}^2 \sum_{j=0} \frac{e^{-S}S^j}{j!} \sqrt{\frac{1}{4\pi\lambda_0 k_B T}} exp\left[-\frac{(jh\nu_i+\lambda_0-hc\nu+\Delta G_{CT})^2}{4\lambda_0 k_B T}\right] \qquad (IV.4)$$

Where k_B is the Boltzman constant, n is the solvent refractive index, S is the electron-vibration coupling constant:

$$S = \lambda_i/h\nu_i \qquad (IV.5)$$

and the other relevant quantities, which can be evaluated by the band shape analysis, are illustrated in figure IV.4:

- $h\nu_i$ is the harmonic mode energy, considered as identical in both D and A.
- λ_0 is the low frequency reorganization energy (intramolecular normal modes of low frequency as well as solvent modes of the first solvation shell).
- λ_i is the high frequency reorganization energy (stretching modes).
- ΔG_{CT} is the Gibbs free energy of the CT process.

As one can see in equation IV.4; the solvatochromic absorption band will be fitted with multi-Gaussian functions including five different variables ($k_B T$, $h\nu_i$, λ_0, λ_i, ΔG_{CT}). To ensure that the obtained values are physically correct, we employed some validity equations, following the procedure of Kapturkiewicz et al. [110].
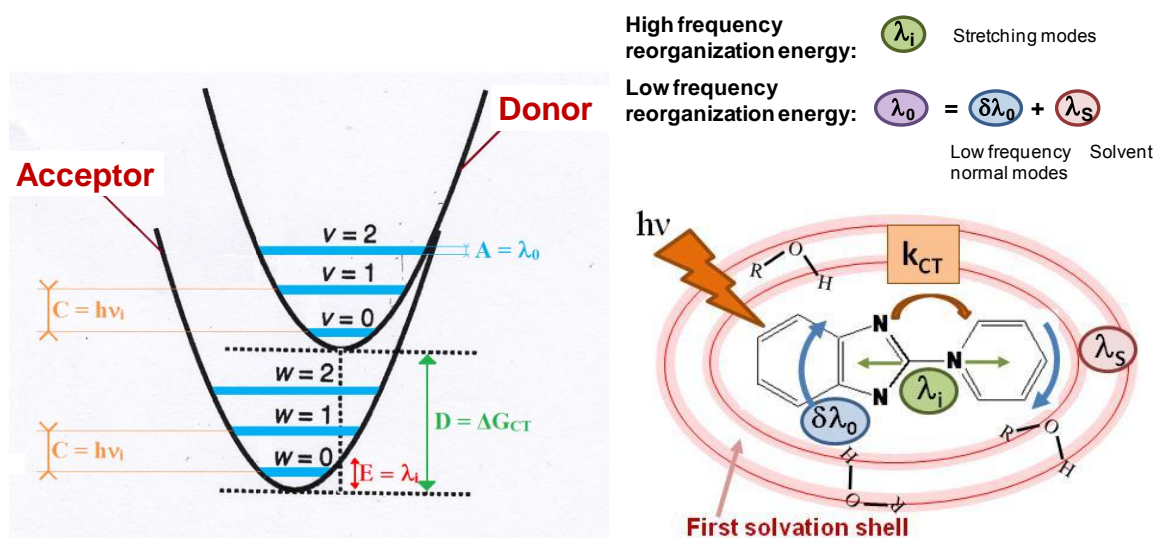
Figure IV.4. (left) Donor and acceptor harmonic potentials involved in the semi-classical Marcus approach; (right) illustration of the different quantities evaluated by band shape analysis:

IV.3.2.2   Validity equations used in the band shape analysis.

Because we are concerned by solvatochromic data, it is prudent to use analytical expressions for checking the solvent dependency of the fitted parameters. First, according to Onsager theory, the energy of solvation of a dipole is expressed as [33]:

$$\Delta G_{CT} = \Delta G_{CT}(vacuum) + \frac{\vec{\mu}_e^2 - \vec{\mu}_g^2}{a_0^{\,3}} f(\varepsilon) \qquad (IV.6)$$

where $\vec{\mu}_g$ and $\vec{\mu}_e$ are the dipole moments of the ground and excited states, a_0 is the Onsager cavity radius, and $f(\varepsilon)$ is the low frequency polarizability including the effect of molecular reorientations of the solvent molecules (occurring on a slower time scale):

$$f(\varepsilon) = \frac{\varepsilon - 1}{2\varepsilon + 1} \qquad (IV.7)$$

By plotting the values obtained for the free energy as a function of the low frequency polarizability parameter for different solvents, one should obtain a linear correlation with negative slope. Similarly, one can test the correctness of the chosen parameters by plotting the low frequency reorganization energy as a function of the orientational solvent polarizability [110]:

$$\lambda_0 = \delta\lambda_0 + \lambda_S = \delta\lambda_0 + \frac{\vec{\mu}_e^2 - \vec{\mu}_g^2}{a_0^{\,3}} \Delta f \qquad (IV.8)$$

where Δf is the orientational polarizability, i.e., the difference between the low frequency polarizability $f(\varepsilon)$, explained above, and high frequency polarizability $f(n)$ due to solvent

79

electron reorganization, which is essentially instantaneous and is a function of the refractive index, *n*

$$\Delta f = f(\varepsilon) - f(n) = \frac{\varepsilon - 1}{2\varepsilon + 1} - \frac{n^2 - 1}{2n^2 + 1} \qquad (IV.9)$$

and $\delta\lambda_0$ is related to the low frequency modes of the solute ($\sim$200 – 600 cm^{-1}). The plot of the low frequency reorganization energy as a function of the orientational polarizability should be a linear correlation of positive slope.

IV.3.2.3   Band shape analysis procedure.

To perform a reliable band shape analysis using equation IV.4 we have to use a multi-Gaussian function to deduce five parameters, namely $k_B T$, λ_0, λ_i, ΔG_{CT}, and $h\nu_i$. An example of spectral fit of the SBPa absorption band with 7 Gaussian functions is presented in figure IV.5a in order to show that the experimental band can be perfectly reproduced. Note that the spacing between individual Gaussian is given by $h\nu_i$ and one ensures to cover the full range spectra by choosing high enough number of Gaussian functions (typically 20 gaussians).

The most difficult task in the band shape analysis procedure is the proper choice, among the five parameters, of those to be set as variables and those as constants. To overcome this issue we will systematically use validity equations as explained above.

First, it was natural to consider all these parameters as variables, but no reliable results could be obtained (no linear correlation was found for equations IV.6 and IV.8 for a small set of solvents). Evidently, we first decided to fix the thermal energy parameter at room temperature (208 cm^{-1}), but the results were still not satisfying. By consequence, following suggestions of Kapturkiewicz et al. [110], we decided to fix $h\nu_i$ as a constant. To choose properly this value, a resonance Raman spectrum of SBPa in ACN was recorded. As one can see in figure IV.5b, the majority of the peaks are located between 1000 and 1500 cm^{-1} thus we have tested different values of $h\nu_i$ within this interval. It has been found that, for polar aprotic solvents, $h\nu_i$ = 1350 cm^{-1} led to the best results with respect to the two validity equations. This value is close to the position of Raman peak 12 (see figure IV.5b), corresponding to the C-N stretching mode. For protic solvents, an optimum $h\nu_i$ value of 1200 cm^{-1} was found. For non-polar aprotic solvents the results are not so good, suggesting some special behaviour such as solute-solute or solute-solvent stacking effects. This hypothesis will be discussed later in this chapter.

a)

b)
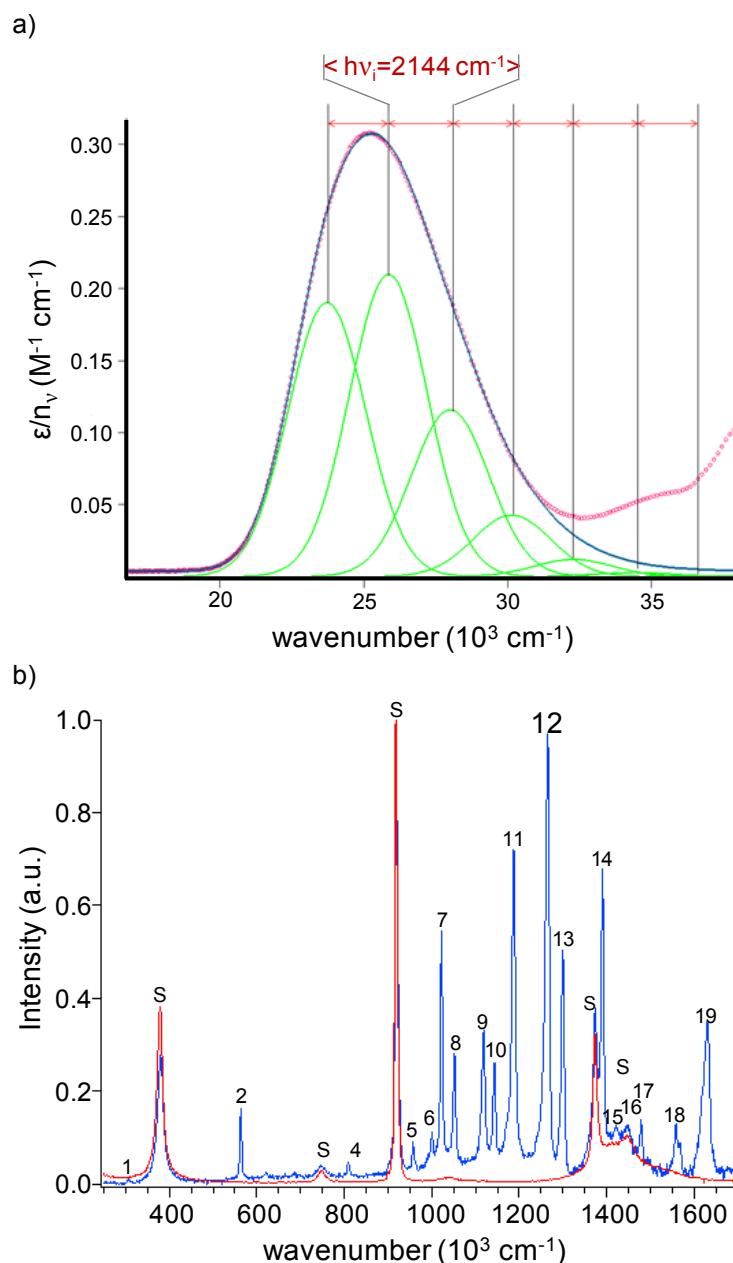
Figure IV.5 a) reduced molar extinction coefficient ($\varepsilon/n\nu$) of SBPa in ACN fitted with analytical function IV.4; all parameters being variables (7 gaussian functions); b) resonance Raman spectra of SBPa in ACN (in blue) and ACN alone (in red) for λ_{ex} = 488 nm (resolution 3.2 cm^{-1}). Raman picks are numbered, s = solvent pick.

Finally, introducing the fixed parameters $k_B T$ = 208 cm^{-1} and $h\nu_i$ = 1350/1200 cm^{-1} as constants in equation IV.4, reliable values of the other parameters were derived in all solvents. As shown in figure IV.6 a and b, the validity equations of λ_0 and ΔG_{CT} as a function of Δf and $f(\varepsilon)$, respectively (equations IV.6 and IV.8), show a good linear correlation.

First it is interesting to observe that for both quantities λ_0 and ΔG_{CT} we can distinguish between three distinct groups, namely: weakly polar aprotic, alkylnitriles (polar aprotic),

aprotic, and protic. Next, the reorganization solvent energy is markedly different comparing protic and aprotic cases i.e. λ_0(protic) $<$ λ_0(aprotic). As a matter of fact the hydrogen bond network around the solute is probably responsible for such results. Anyhow, one can predict some hydrogen bond effect during time resolved experiments. Furthermore, the values of ΔG_{CT} will be used later in chapter V to identify the Marcus region concerned by the CT process in SBPa.
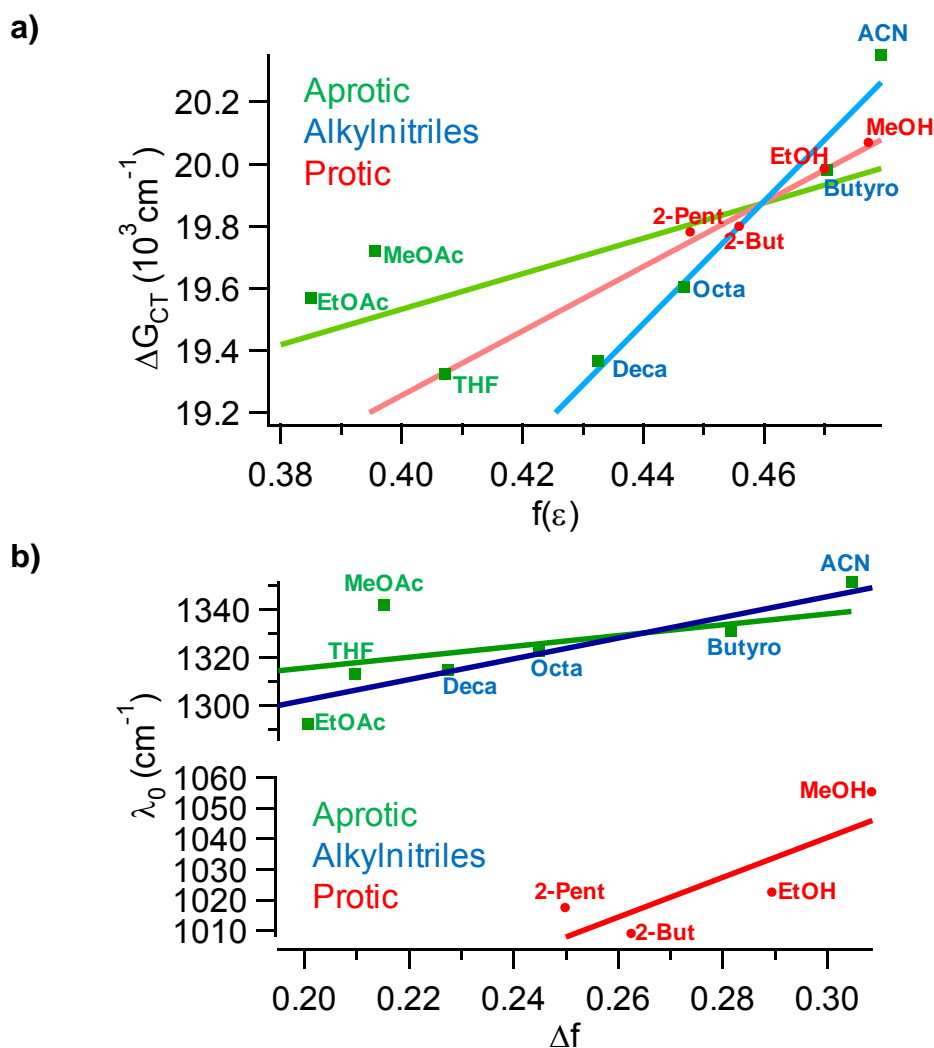
Figure IV.6 (a) ΔG_{CT} function of $f(\varepsilon)$ for alkylnirile (blue), aprotic (green) and protic (red) solvents (toluene point is not shown). . (b) λ_0 function of Δf for the same solvent groups.

IV.4 Stationary spectroscopy and (TD)DFT calculations – overall photophysics.

Up to now, reasonable evidences for a photoinduced ICT process were presented based on electrochemistry measurements as well as solvatochromism of the stationary absorption band of SBPa in solvents of different polarities.

At this point, we are concerned with the identification of the electronic states responsible for the solvatochromism. First, it appears significant to complete the stationary absorption data set with comparable data from emission measurements. Then, we will attempt to reproduce the absorption spectra by computing vertical electronic transitions with standard TDDFT calculations. Afterward, more advanced TDDFT calculations, requiring excited state geometry optimizations will be done to reproduce the emission spectra.

All the (TD)DFT computational strategy is detailed in chapter II (subsection II.5). Briefly, the ground state with optimized geometry will be abbreviated indifferently as S_0 or S_0(opt). Next, vertical excitation from S_0 to the Franck-Condon (FC) region of the first two excited potential curves gives rise to configurations labelled as S_1(FC) and S_2(FC), respectively, with the same geometry as in the ground state. Finally, geometry optimization of these two states leads to the corresponding true excited state minima abbreviated as S_1(opt) and S_2(opt). Additionally, vertical transitions from S_1(opt) and S_2(opt) to the ground state surface, on one hand, and to the other excited state surface, on the other hand, lead to new states named as S_0' and S_2' (transition from S_1(opt)), and S_0'' and S_1'' (transition from S_2(opt)).

Table IV.2 LR-PCM-TDDFT wavelengths and oscillator strengths (values in parentheses) for absorption and emission compared to the experimental data. Transition moment values are those previously deduced from the experimental absorption band analysis (Table III.3). The S_0 state dihedral angle (θ) values are deduced from: i) the comparison of experimental and PCM-DFT NMR chemical shifts (figure IV.9) ii) PCM-DFT geometry optimization for SBPa + 4 solvent molecules.

	θ (dihedral angle)		M_{ge} (D)	Absorption			Emission	
	PCM-DFT / NMR	PCM-DFT + 4 explicit molecules	exp	exp	TDDFT $S_0{\rightarrow}S_2$	TDDFT $S_0{\rightarrow}S_1$	exp	TDDFT $S_1{\rightarrow}S_0$
MeOH	35°	2°	10.8	385	397 *(0.4576)*	416 (0.0092)	665	-
ACN	22°	10°	9.0	393	406 *(0.4669)*	432 (0.0094)	687	714
THF	25°	3°	7.7	421	422 *(0.4815)*	453 (0.0091)	675	709
Toluene	-	-	5.4	446	462 *(0.5198)*	510 (0.0082)	669	703

IV.4.1 Solvent effect on the absorption and fluorescence spectra: participation of two S_1 and S_2 states

Figure IV.7 presents the steady-state absorption and fluorescence spectra of SBPa in Toluene, THF, ACN and MeOH, together with the TDDFT results (sticks of same colour code). The results are tabulated also in table IV.2. We will first focus on experimental data and comment theoretical results just after. Indeed, it is worth to observe that the already discussed negative solvatochromism that characterizes the experimental absorption band contrasts with a lack of such effect for the emission band lying in the $500 - 750$ nm domain. At first glance, the hypsochromic shift accompanied by a hyperchromic intensity effect noticed on the absorption band upon increasing the solvent polarity is not observed for the emission band, which shows only very moderate positive solvatochromism (λ_{max} 669, 675 and 687 nm for Toluene, THF, and ACN respectively). Note that, this result appears unusual because the reversed situation (solvatochromic emission / nonsolvatochromic absorption) is frequently reported in the literature [27, 28]. It suggests, anyhow, that the emissive transition does not involve the same excited state as the CT absorption transition. At this point, considering Kasha rules, the apparent non-solvatochromic emissive band is related to a first singlet state noticed in the whole manuscript as $S_1(E)$. A challenging task is therefore the thoughtful identification of $S_1(E)$. Comparison of these experimental data with theoretical results will help us to identify properly the CT and $S_1(E)$ states.

In figure IV.7, the TDDFT oscillator strength and wavelength of the first two vertical transitions $S_0 \rightarrow S_1(FC)$ and $S_0 \rightarrow S_2(FC)$ are indicated in the $300 - 550$ nm region for the four different solvents. Note that transitions above S_2 states (not shown) have negligible oscillator strengths and will not be considered. So for absorption, the results indicate that the two transitions of lowest energy are close together but only the $S_0 \rightarrow S_2(FC)$ transition has significant oscillator strength and can reasonably be ascribed to the observed absorption band. Furthermore, this assignment is supported by the high-quality agreement between the calculated and observed peak maxima in the four solvents and an excellent prediction of the experimental solvatochromic behaviour (see figure IV.7). Vertical absorption to the $S_1(FC)$ state is much less probable than that to $S_2(FC)$ due to symmetry restriction on the dipole moments, as it is explained in appendix B.

After a LR-PCM-TDDFT optimization of the first excited state, the vertical $S_1(opt) \rightarrow S_0'$ transition wavelength was calculated for three solvents (see table IV.2) but the

corresponding oscillator strength is not computable. The position predicted for this transition corresponds very well to that observed for the experimental emission band. Note that even the moderate positive solvatochromism of the emission band (λ_{max} 669, 675 and 687 nm for Toluene, THF, and ACN) is well reproduced by the calculation (703, 709 and 714 nm respectively). Accordingly, we can safely relate the emissive $S_1(E)$ state with the calculated $S_1(opt)$ state.

In summary experiment-TDDFT comparisons can be illustrated as:

- the solvatochromic absorption band $\Leftrightarrow S_0 \rightarrow S_2(FC)$ transition

- the emission from $S_1(E)$ state $\Leftrightarrow S_1(opt) \rightarrow S_0'$ transition

Later in this chapter, we will study in more details the electronic configuration, MO involved, and geometry of these excited states.
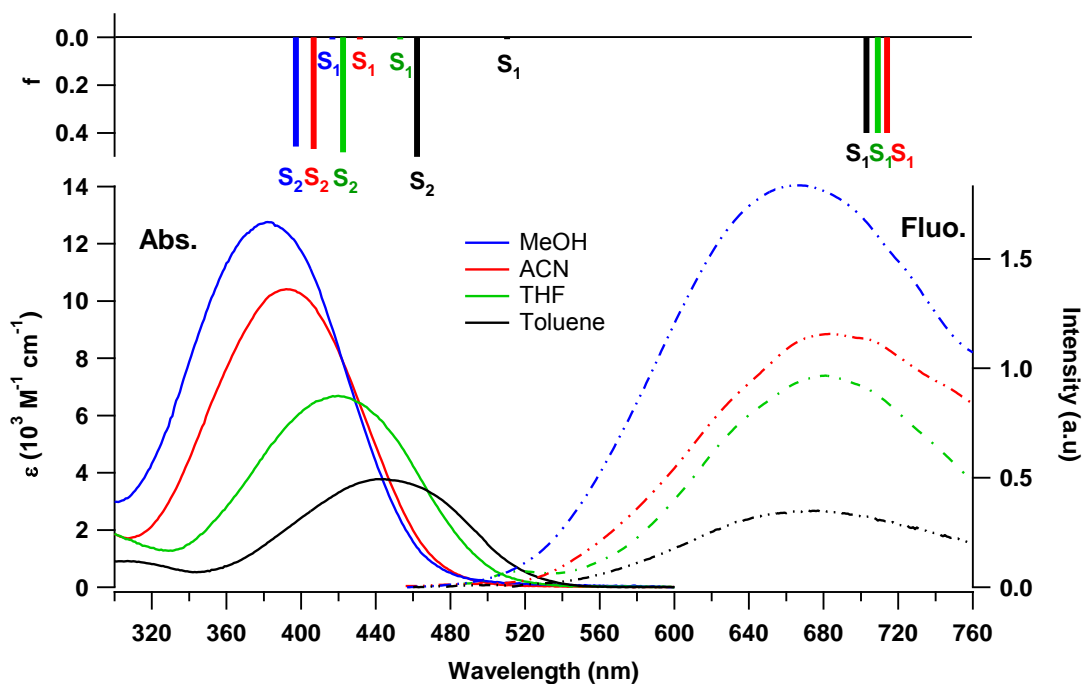
Figure IV.7. Stationary absorption and fluorescence spectra of SBPa in four different solvents: methanol (blue), ACN (red), THF (green) and toluene (black) with the corresponding TDDFT oscillator strengths and wavelengths of vertical transitions from S_0 to the first two excited states as well as the wavelength (oscillator strengths are not computable) of the vertical transition from $S_1(opt)$ to S_0 (same colour code).

IV.4.2 Excitation spectra - evidence for a dimerization effect in non-polar environment

The geometry of the ground state SBPa molecule is planar in the solid state with a near C_{2v} symmetry, as measured by X-ray spectroscopy by Alcalde et al. [23]. This planar configuration together with some zwitterionic character is responsible for strong stacking

effects. Indeed, head-to-tail dimeric enities have been identified by X-ray spectroscopy with a distance between monomers of d = 3.29 Å. In solution, experimental values measured for the dipole moment with conventional electrotechniques show a decrease with increasing concentration, giving some evidence for a dimerisation effect [23]. Moreover, the dimer conformation was confirmed by MM2/AM1 calculations that predict a satisfying distance of 3.4 Å between the planar monomeric units [116].

In solution, the tendency for dimerization can be also evidenced by comparing the absorption and excitation spectra (see figure IV.8): whereas the latter reproduces perfectly the absorption spectrum in polar solvents, a splitting of the band shape is found in the excitation spectra for the less polar solvents. According to the exciton theory [117, 118], the component of highest energy can be related to the monomer while the lowest energy one is ascribable to the dimer. It will be seen in the next section that such dimerization effects in nonpolar solvents can disturb the analysis of the solvatochromic effect.
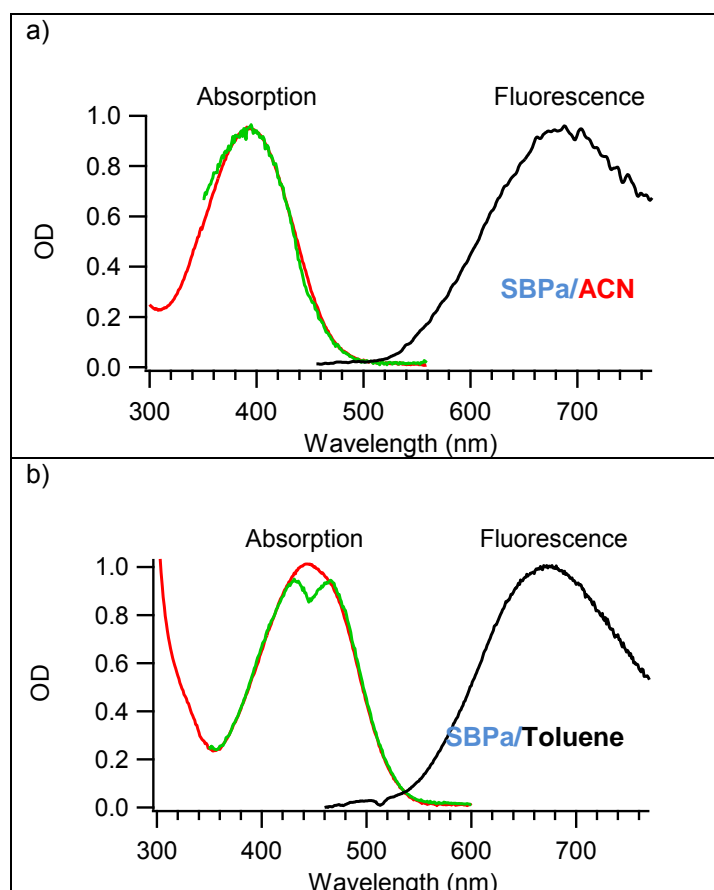
Figure IV.8. Normalized stationary absorption (red), fluorescence (black) and excitation (green) spectra of SBPa in ACN (a) and toluene (b). The emission wavelength for excitation spectra is set at the maximum of the fluorescence signal.

IV.5 Ground and excited states geometries and electronic properties.

IV.5.1 Ground state geometry: a planar molecule?

IV.5.1.1 NMR experiment-theory comparison

In order to assess the right ground state geometry of SBPa in solution, we will compare experimental NMR chemical shifts in MeOD, ACN, THF and Toluene (figure IV.9a) with those predicted from PCM-DFT calculations for various molecular geometries of SBPa. The full assignment has been obtained from 1D and 2D NMR experiments (1H, 13C, 1H-1H COSY, 1H-13C HSQC, 1H-13C HMBC). As expected, the proton H3, in ortho position with the pyridinium nitrogen, is always the most deshielded. Its chemical shift is increased on going from MeOD (9.72 ppm) to THF (10.15 ppm) via ACN (9.98 ppm). In contrast, the four other protons are more and more shielded, with always the couple of H6 (δ_{MeOD} = 7.58 ppm, δ_{ACN} = 7.52 ppm, δ_{THF} = 7.44 ppm) and H7 (7.10 /7.02 /6.88 ppm) at lower frequencies than the frequencies of H1 (8.62 /8.41 /8.39 ppm) and H2 (8.19 / 8.00 /8.02 ppm). Different is the behaviour in toluene solution where the protons H6 (δ_{Tol} = 8.10 ppm) and H7 (δ_{Tol} = 8.34 ppm) have higher values of chemical shifts than those observed for H1 (δ_{Tol} = 6.32 ppm) and H2 (δ_{Tol} = 6.03 ppm). Such an effect likely arises from the magnetic anisotropy induced by toluene molecules but can be enhanced also by a head-to-tail dimerization of SBPa molecules discussed above. Anyhow, both effects cannot be accounted within PCM approach and the toluene case is thus excluded from the experiment-theory comparison.

In parallel we did PCM-PBE0/6-311++G(2d,p) geometry optimization of SBPa followed by NMR chemical shift calculations [119] (same basis/functional) for its planar geometry (found as an optimum) and various geometries resulting from twisting the dihedral angle θ between the betaine and pyridinium parts (only θ is fixed as a constant during calculations while all other parameters are variable). As a first result, the linear correlation between the experimental and calculated data, appreciated by the least square parameter χ^2 as well as correlation coefficient R^2, is already excellent for a planar geometry but can be further improved for non-zero θ values. As indicated in table IV.2, slight optima are found for angles of 25°, 22°, and 35° in THF, ACN (figure IV.9b) and MeOH, respectively. However, this result has to be considered with caution as the potential

energy curve computed along θ is very flat and the difference of total energy between the planar and twisted geometries is less than the thermal energy (0.025 eV), indicating the probable existence of a distribution of molecules with various angles with relative populations obeying the Boltzmann law (figure IV.9c).
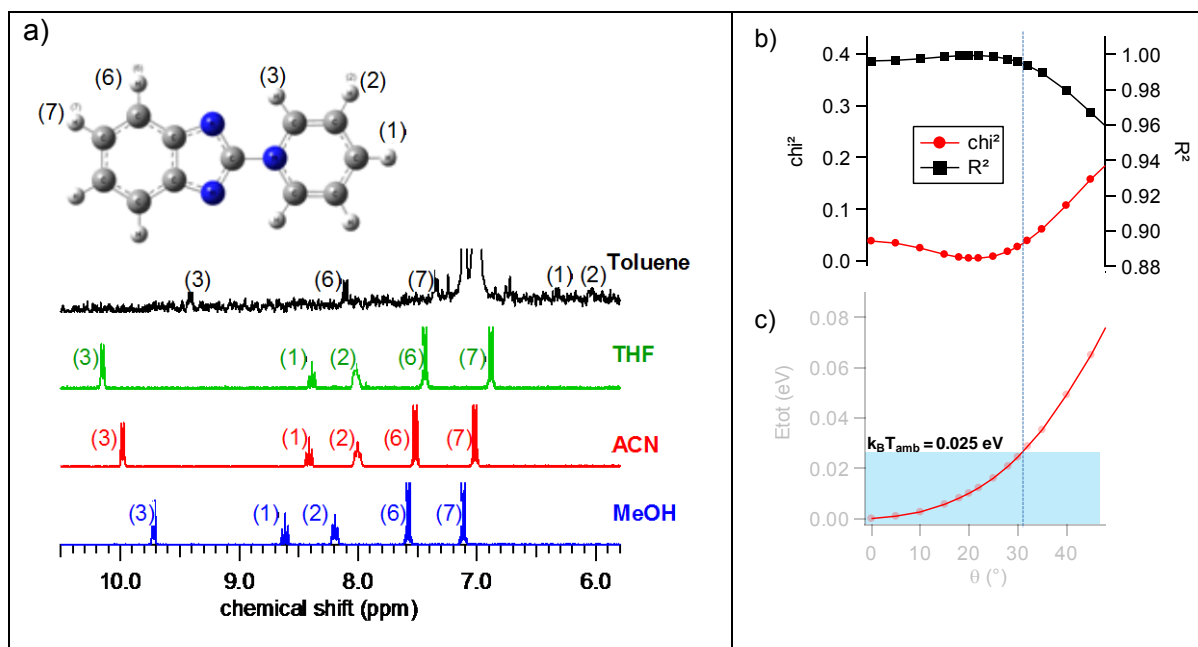
Figure IV.9. a)^{1}H- NMR spectra of SBPa in four different solvents. b) χ^2 and R^2 coefficients related to the linear correlation of the experimental and PCM-DFT NMR chemical shifts as a function of the dihedral angle θ for SBPa in ACN. c) PCM-DFT total energy as a function of θ (the thermal energy threshold is indicated by a blue area).

IV.5.1.2   Calculations including explicit solvent molecules
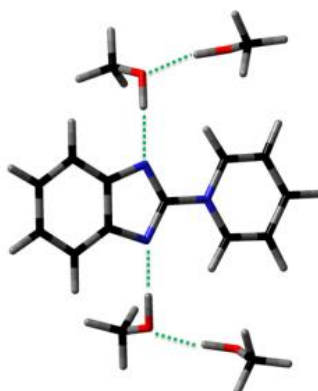
Figure IV.10. (SBPa + 4 MeOH) geometry optimized by PCM-DFT calculations. Hydrogen bonds are indicated with dotted lines.

To confirm the near-planar geometry of SBPa, additional PCM-DFT calculations performed with 4 explicit solvent molecules predict an angle between 2° and 10° (see table IV.2). Note that for the MeOH case displayed in figure IV.10, solute-solvent hydrogen

bonds can be considered while a distance N-H of 1.8Å is noticed [120]. In conclusion, it is probable that the SBPa conformation in solution deviates slightly from planarity, with a dihedral angle that is not correlated to the solvent polarity.

IV.5.2 Advanced calculations on electronic excited states

We will now present advanced calculation results to better characterize the excited states discussed above. All Computational details are given in chapter II. For each one of the $S_0/S_1(FC)/S_2(FC)$, $S_0'/S_1(opt)/S_2'$, and $S_0''/S_1''/S_2(opt)$ sets of states belonging to the same FC region (same geometry), the energies predicted in vacuum and in ACN, THF, and toluene are presented in the diagram displayed in figure IV.11.
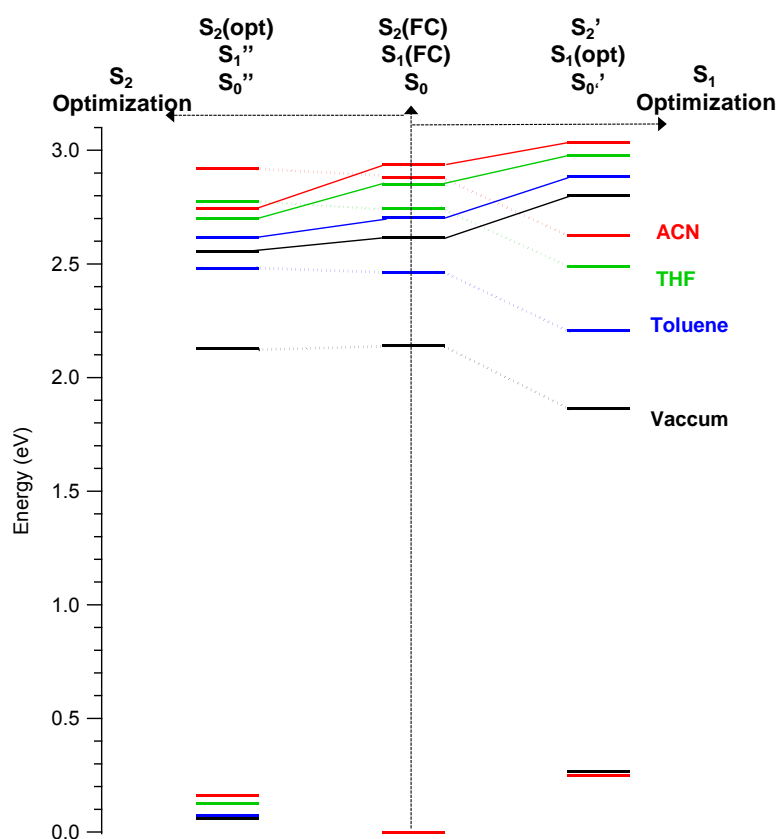
Figure IV.11. Relative LR-PCM-TD- PBE0/6-31G+(d)// PBE0/6-31G+(d) energy levels of the ground state S_0 and the first excited states S_1 and S_2 for three different geometries: $S_0(opt)$, $S_1(opt)$ and $S_2(opt)$. The calculations are performed in Vacuum (black), Toluene (blue), THF (green) and ACN (red). For each solvent, the reference energy corresponds to the $S_0(opt)$ state.

Although the optimization was feasible in all solvents, the situation can be complicated by possible state inversions during the optimization process. It is worth to notice that with increasing the solvent polarity, an inversion can occur between $S_2(opt)$ and S_1'' (see left side of diagram), suggesting the possibility of some avoided crossing between these two

states. This effect is not observed for S_1(opt) (right side of the diagram). For all these states, dipole moments were computed and listed in table IV.4

Molecular Orbitals. From a MO point of view, as shown in figure IV.12, the S_1(FC) state arises from HOMO $\rightarrow$ LUMO excitation while the S_2(FC) states arises from (HOMO-1) $\rightarrow$ LUMO excitation (red MOs). The contour plot of these three MOs and their energy calculated in toluene, THF and ACN are also shown in figure IV.12. It appears clearly that both transitions have charge transfer character, with notable electronic delocalization from the betaine to the pyridinium part. With the help of these results, we can easily rationalize the experimental negative solvatochromism of the CT absorption band. Indeed, upon increasing the solvent polarity, a similar blue shift of both the $S_0 \rightarrow$ S_2(FC) and $S_0 \rightarrow S_1$(FC) transitions is predicted (figure IV.7) as a consequence of the large and similar energy lowering of the HOMO-1 and HOMO together with a moderate destabilization of the LUMO (the energy gap of the CT transitions increase with solvent polarity.).

Table IV.4: Maximum of absorption, Oscillator strength and dipole moment of the S_0, S_1, and S_2 states in their optimized and FC configurations, as computed by PCM-(TD)- PBE0/6-31G+(d)// PBE0/6-31G+(d) calculations.

			Vacuum	Toluene	THF	ACN
	S₀(opt)	**μ(D)**	+8.23	+10.28	+11.65	+12.23
Absorption	**S₁(FC)**	**μ(D)**	-1.84	-3.70	-4.89	-5.28
		λ(nm)	579	504	450	428
		F	0.0040	0.0071	0.0079	0.0082
	S₂(FC)	**μ(D)**	+2.66	+0.52	-1.36	-2.10
		λ(nm)	474	457	421	404
		F	0.4234	0.5186	0.4807	0.4631
Emission	**S₁(opt)** **S₀'**	**μ(D)**	-1.41	-1.39	-1.45	-1.51
			+8.84	+10.58	+9.97	+9.61
		λ(nm)	776	703	709	714
	S₂(opt) **S₀''**	**μ(D)**	+2.66	+3.84	+4.62	+4.93
			+8.44	+9.98	+10.15	+10.23
		λ(nm)	497	460	443	436

Reversely, the strong solvatochromism expected for the $S_0 \rightarrow S_1$(FC) absorption contrasts surprisingly with the quasi lack of solvatochromism noticed for the experimental emission ascribed to S_1(E) state (figure IV.7). This disagreement clearly suggests that S_1(E) and S_1(FC) are two distinct states. With the help of advanced calculations, we succeeded to overcome this contradiction by computing MOs related to the optimized

excited state S_1(opt) (blue MOs in figure IV.12). It was found that the HOMO and LUMO of S_1(opt) state are predicted to be stabilized in the same way in polar solvents. Such situation is possible due to a reversion of the excited state dipole moment compared to the ground state S_0'.
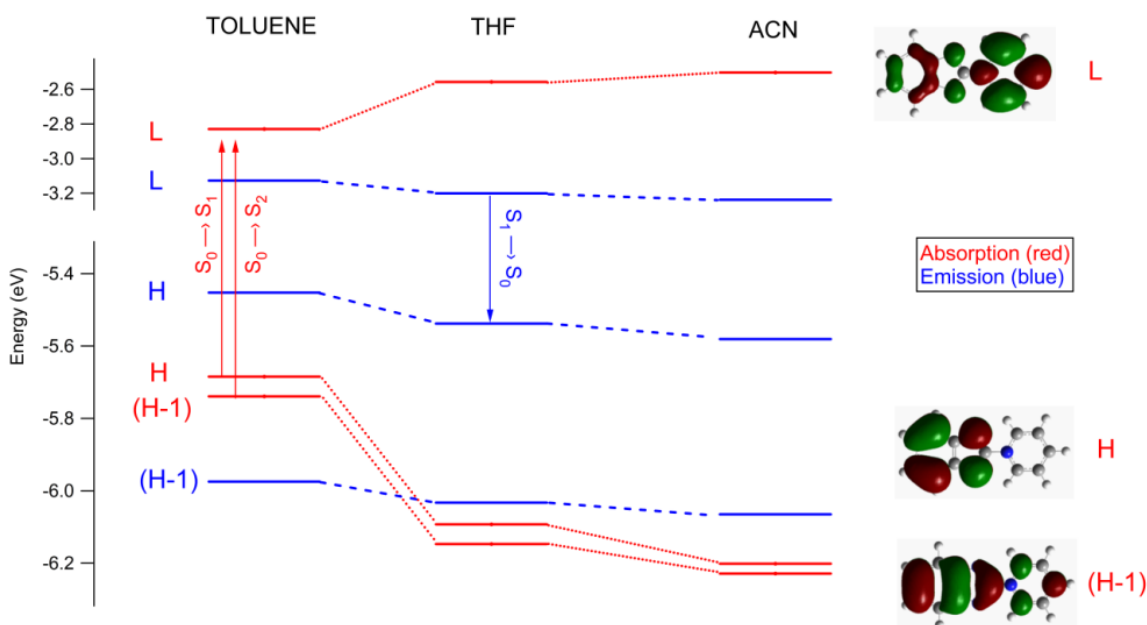
Figure IV.12 HOMO-1, HOMO and LUMO energies in toluene, THF and ACN. Red levels are those involved in the case of absorption (DFT optimization of the ground state) and correspond to the MO contour plots given on the right side. Blue levels are those involved in the case of emission (TDDFT optimization of the first excited state).

FC and Optimized states. Within the FC region, it has been found that both S_1(FC) and S_2(FC) are charge transfer states. However, a careful analysis of the charge distribution in the different states involved in these transitions indicates that they involve distinct parts of the molecule. Actually, one has to consider three different parts of the SBPa molecule rather than only the two pyridinium and betaine moieties: the benzene ring and the imidazole bridge N-C-N appear to be two distinct donor groups, while the pyridinium is the acceptor group (see figure IV.13). In fact, considering the MK computed charges, as shown in figure IV.13 the $S_0 \rightarrow S_2$(FC) transition corresponds to a CT of 0.2|e| from the benzene to the pyridinium group, the imidazole charge keeping a constant value. Similarly, the S_2(FC) $\rightarrow S_1$(FC) transition corresponds to a further CT of almost 0.2|e| from the imidazole group to pyridinium ring, the benzenic ring charge being not significantly modified. On the other hand, in vacuum, the CT character of the two FC excited states is maintained in the optimized configurations S_1(opt) and S_2(opt), but this is no longer true when solvent is taken into account.

Indeed, as seen in table IV.4, inclusion of the solvent induces a diminution of the dipole moment values predicted for the optimized excited states as compared to the FC state values. This effect is easily understood by considering that solvation will tend to maximize the charge delocalization over the entire molecule in order to take benefit of the electrostatic potential of the solvent shell. Finally, it is worth to notice that the S_2(opt) dipole moment is still sensitive to the solvent polarity, as its precursor configuration S_2(FC), in accordance with the solvatochromic behaviour of the S_0-S_2 absorption band. Reversely, it is found that the S_1(opt) dipole moment is nearly insensitive to the solvent polarity, which is consistent with the non solvatochromic behaviour of the emission band described above.

So, S_1(FC) and S_2(FC) as well as S_1(opt) and S_2(opt) have all their own CT characters. However between FC and relaxed configurations the later is of higher importance. For this reason we will use the new notations for relaxed states highlighting CT character:

$$S_1(opt) \Leftrightarrow S_1(CT) \text{ as well as } S_2(opt) \Leftrightarrow S_2(CT).$$
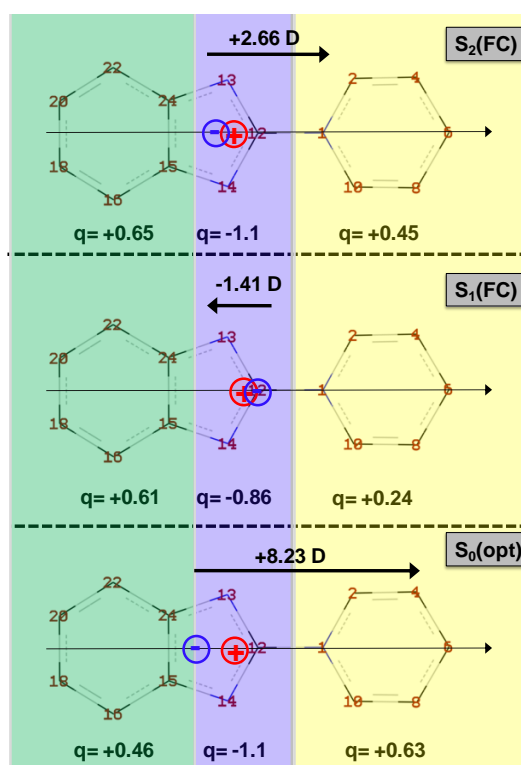
Figure IV.13 Computed MK charges, for the vacuum case, summed over three parts of SBPa, barycentric positions of positive and negative charges and dipole moment for S_0, S_1(FC) and S_2(FC) states.

Geometries. From a structural point of view, both S_1(opt) and S_2(opt) are predicted to have planar geometries with no drastic changes in bond length relative to the S_0 molecule. Figure IV.14 shows the variations of the interatomic distances on going from the ground state to S_1(opt) (blue) and S_2(opt) (red), in vacuum and in ACN (PCM optimization). A common point between the S_1(opt) and S_2(opt) geometries is clearly the comparable, weakly solvent dependent decrease of the pyridinium ring aromacity (N_1C_2 and C_4C_6 bond expansion and C_2C_4 bond shortening). Reversely, these two states differ by the degree of aromaticity of the benzenic ring that increases in S_1(opt) but decreases in S_2(opt) with respect to S_0. The effect of solvation is noticeably manifested by a contraction of the fundamental N_1C_{12} and an expansion of the imidazole N-C-N bonds as compared to the geometry predicted in vacuum.
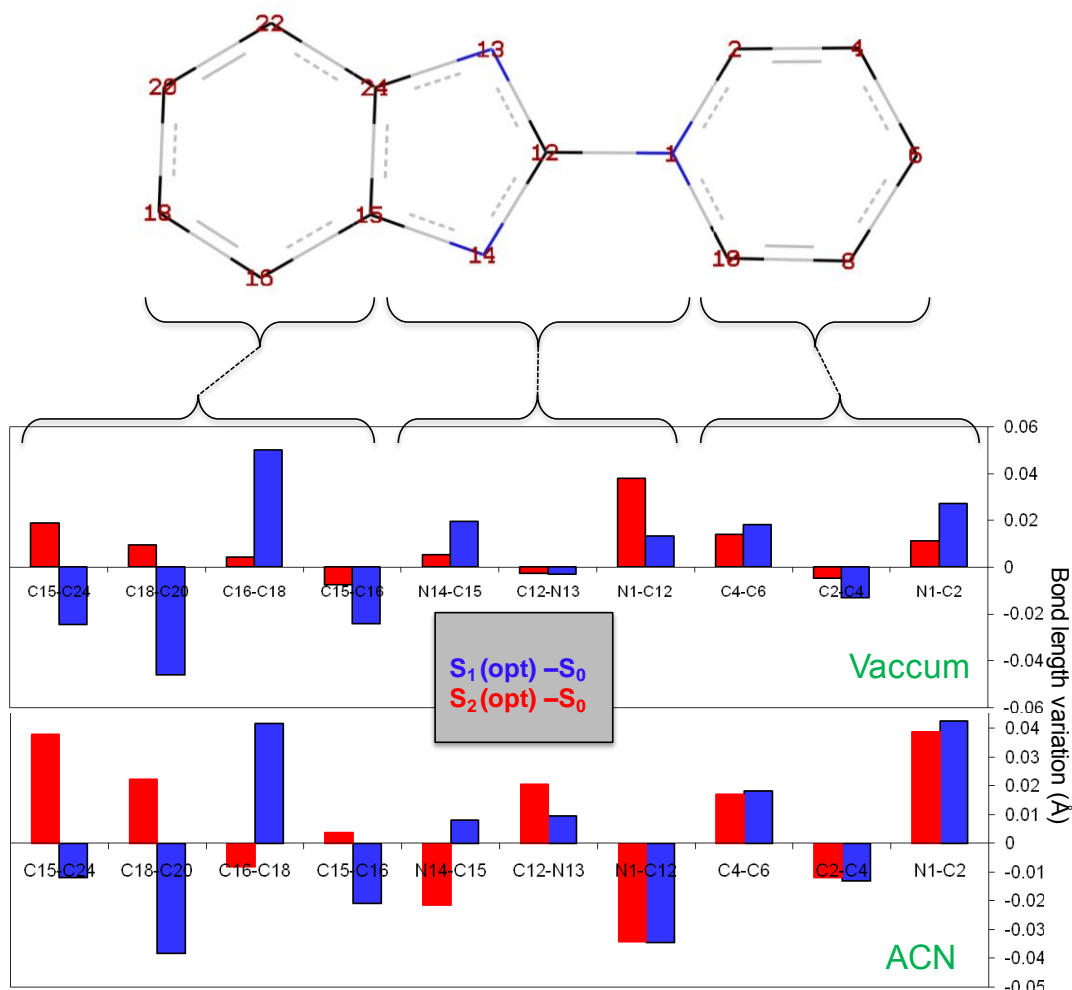
Figure IV.14 Variation of C-C and C-N bonds (Å) going from S_0(opt) to S_1(opt)(blue) and from S_0 to S_2(opt) (red). Both vacuum and ACN cases are indicated. The atom numbering is indicated above.

IV.6 Innovative solvatochromic treatment

We are now concerned with the quantitative treatment of solvatochromic data in order to evaluate the dipole moments involved in the photoinduced CT transition. The solvatochromic data characterizing the absorption and emission transitions in 19 different solvents are tabulated in table IV.5. As we have shown in a previous subsection that absorption and emission do not involve the same excited states, a safe treatment of solvatochromism based on the Stokes shifts, such as the Lippert-Mataga approach [29-32], cannot be done and an alternative approach has to be found in which absorption and fluorescence data must be considered separately.

Table IV.5 SBPa absorption and emission band energy and wavelength maxima and the corresponding Stokes shift ($\Delta\nu_{st}$) in different solvents. Solvent properties (dielectric constant ε, refractive index n, Dimroth-Reichardt $E_T(30)$ parameter, and Kamlet-Taft α, β, and π^* parameters) are also given.

n°	solvent	$E_T(30)$ (kcal.mol^{-1})	ε	n	α	β	π^*	λ_{ABS} (nm)	λ_{FLUO} (nm)	ν_{abs} (cm^{-1})	ν_{fluo} (cm^{-1})	$\Delta\nu_{st}$ (cm^{-1})
1	Toluene	33.9	2.38	1.4941	0	0.11	0.49	446	669	22421.5	14947.7	7473.8
2	Dioxane	36	2.21	1.4203	0	0.37	0.49	424	671	23584.9	14903.1	8681.8
3	Anisole	37.1	4.33	1.5143	0	0.32	0.7	429	674	23310.0	14836.8	8473.2
4	THF	37.4	7.58	1.405	0	0.55	0.55	421	675	23753.0	14814.8	8938.2
5	EtOAc	38.1	6.02	1.3698	0	0.45	0.45	415	680	24096.4	14705.9	9390.5
6	MeOAc	38.9	6.68	1.3589	0	0.42	0.49	412	683	24271.8	14641.3	9630.6
7	DCM	40.7	8.93	1.421	0.13	0.1	0.82	415	672	24096.4	14881.0	9215.4
8	HMPA	40.9	29.3	1.457	0	1	0.87	404	677	24752.5	14771.0	9981.4
9	Acetone	42.2	20.56	1.356	0.08	0.48	0.62	402	681	24875.6	14684.3	10191.3
10	Butyronitrile	42.5	24.83	1.382	0	0.45	0.63	405	680	24691.4	14705.9	9985.5
11	DMF	43.2	36.71	1.428	0	0.69	0.88	399	685	25062.7	14598.5	10464.1
12	ACN	45.6	35.94	1.341	0.19	0.4	0.66	393	687	25445.3	14556.0	10889.3
13	2-BuOH	47.1	16.56	1.3953	0.69	0.8	0.4	401	642	24937.7	15576.3	9361.3
14	1-propanol	50.7	20.45	1.3837	0.84	0.9	0.52	397	654	25188.9	15290.5	9898.4
15	EtOH	51.9	24.55	1.3594	0.86	0.75	0.54	393	662	25445.3	15105.7	10339.6
16	MeOH	55.4	32.66	1.3265	0.98	0.66	0.6	385	665	25974.0	15037.6	10936.4
17	TFE	59.8	26.67	1.2907	1.51	0	0.73	370	592	27027.0	16891.9	10135.1
18	H2O	63.1	78.36	1.3325	1.17	0.47	1.09	361	643	27700.8	15552.1	12148.7
19	HFIP	65.3	16.62	1.277	1.96	0	0.65	349	558	28653.3	17921.1	10732.1

By an appropriate solvatochromic treatment of absorption data, we can deduce the $\mu_g(S_0)$ and $\mu_e(S_2)$ dipole moments, while from fluorescence $\mu_e(S_1)$ and $\mu_g(S'_0)$ can be evaluated (see figure IV.15). With this approach, we will be able to compare experimental values with (TD)DFT values tabulated in table IV.4.
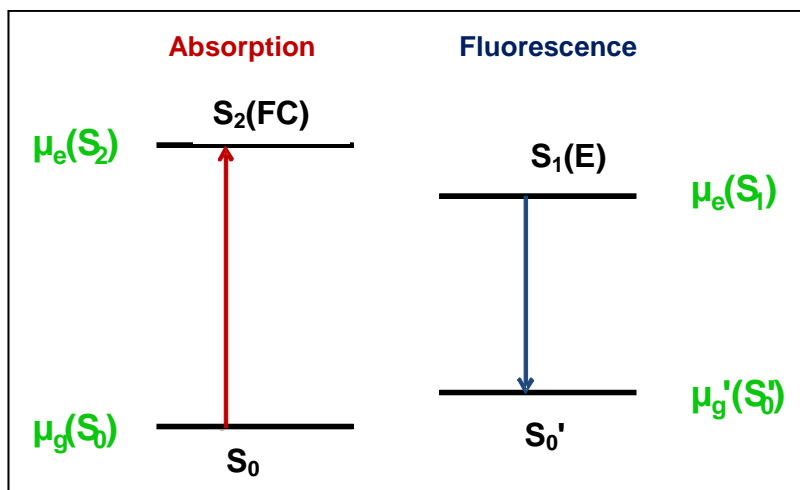
Figure IV.15. Dipole moments concerned by the solvatochromic effects

So, the main goal of this subsection is to derive an innovative solvatochromic data treatment allowing the deduction of the 4 dipole moments for chosen electrostatic solvents unable to develop specific interactions. For this reason, systematic Kamlet-Taft correlation will be applied on the solvent set under investigation.

In the following, we will plot solvatochromic data as a function of $E_T(30)$ values to define the solvent group relevant for this study. Kamlet-Taft correlation will be presented as well. Finally, after reviewing the solvatochromism theory, the innovative solvatochromism algorithm will be presented in details. Results and comparisons with theoretical results will end this section.

IV.6.1   Classification of solvatochromic data

IV.6.1.1   Solvatochromic data as a function of the polarity scale.

The analysis of the solvatochromic data cannot be done directly on the whole set of solvents but, instead, it appears crucial to distinguish different families of solvents depending on the type of interaction with the solute. In particular, great care has to be taken to consider separately solvents that undergo specific interactions. A preliminary evidence of the existence of this type of interaction is shown in figure IV.16 a and b where the absorption and fluorescence band maxima are plotted as a function of the solvent polarity index $E_T(30)$. Undeniably, a clear distinction appears between protic and aprotic solvents for both absorption and emission processes. The presence of solute-solvent hydrogen bonding interaction is confirmed from PCM-DFT geometry optimization performed for SBPa with 4 specific MeOH molecules added (figure IV.10). Two

symmetrical hydrogen bonds are predicted to arise between MeOH and the betaine nitrogen atoms whereas no interactions are engaged with pyridinium nitrogen. Concerning the fluorescence data, besides the separation between protic and aprotic solvents, we can distinguish in figure IV.16b two sub-groups of aprotic solvents depending whether they are weakly or strongly polar. We suggest that this partition results from the presence in the less polar solvents of dimerization effects, as discussed previously, which probably affect the emission.

a)
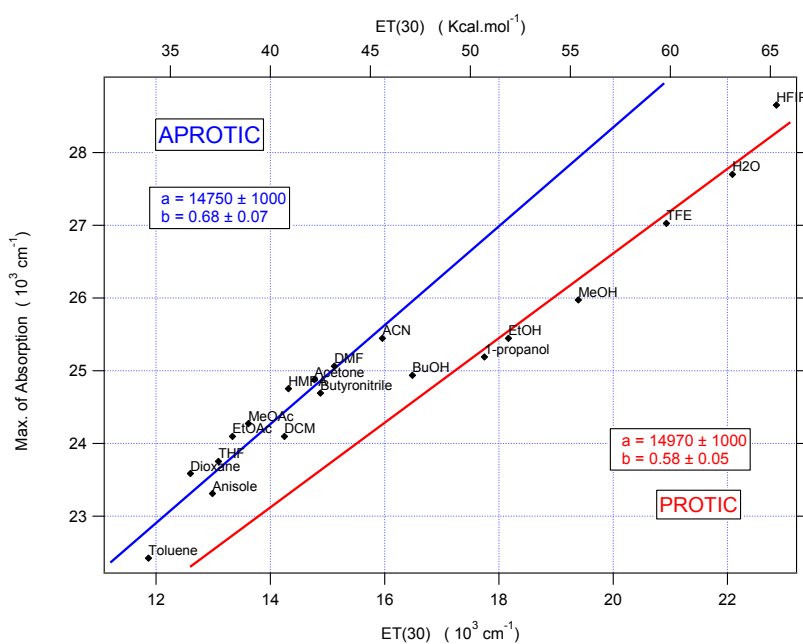
b)
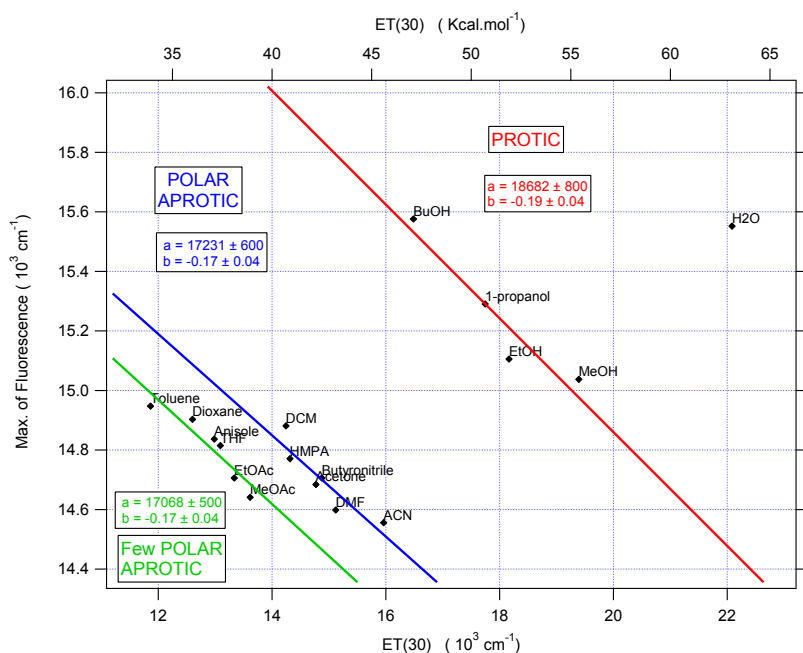
Figure IV.16. Solvatochromic plots for a) Absorption and b) Fluorescence as a function of the $E_T(30)$ polarity index. The slopes of linear correlations are indicated.

Clearly, with this representation, three distinct sets of solvents have been considered independently according to the numbering given in table IV.5:

- Aprotic solvents n° 1-12;

- Polar aprotic solvents n° 4, 8-12, a sub-group of the latter restricted to the most polar aprotic solvents ($\varepsilon > 7$,) for which dimerization is not expected;

- Protic solvents n° 13-16, 18, expected to inform on the role played by solvent-solute hydrogen bonding interactions on the solvatochromism.

IV.6.1.2 Kalmet-Taft correlation

The use of the Kamlet-Taft solvatochromic approach [121] provides an adequate way to ensure, within each set of solvents used for the determination of the dipole moments, whether solvent-solute interactions are mainly electrostatic or involve specific interactions. According to this approach, the solvent-dependent spectral shift can be linearly correlated with the empirical Kamlet-Taft solvatochromic parameters π^*, α, and β:

$$\nu = \nu_0 + p\pi^* + a\alpha + b\beta \qquad\qquad (III.10)$$

Where π^* is a measure of the nonspecific solvent polarity and polarizability, α and β characterize the solvent hydrogen bond donating and accepting properties, and p, a, and b are related to solute properties: dipole moment, ability to donate a hydrogen bond to the solvent and ability to accept a hydrogen bond/lone pair from the solvent, respectively. In practice, a set of solvent for which the p coefficient is higher than the a and b ones can be considered as having minor specific interactions with the solute.

For the three groups of solvents selected above the Kamlet-Taft correlation coefficients were determined for absorption and emission solvatochromic data, and the results of those six correlations are given in table IV.6. The correlations are somewhat disappointing since the coefficients a, b, and p are not so good at first glance, with for example a non negligible contribution obtained for coefficient a in aprotic solvents (absorption and fluorescence cases). Note that this result is a consequence that in the aprotic set only ACN and acetone have non-zero values for coefficient a and surprisingly solvatochromic data are correlated with coefficient a rather than coefficient p for these both solvents. Fortunately, the highest correlation coefficients are obtained for the polar aprotic set

(4, 8-12), which is relevant to a physical treatment of solvatochromism. This group of solvents can be considered as electrostatic, because p > a and b (even if a and b are still not negligible). As already discussed, the restricted set of solvent originated to the fact that SBPa is a tricky compounds with dimerization and specific interactions with protic solvent abilities. So, even if the limited number of solvents for each sets (N ≤ 6) does not allow a quantitative discussion of the numerical values of a, b, p an important qualitative information can be deduced from their signs. In the case of absorption, coefficients a and p are positive but b is negative, which is the hallmark of a zwitterionic structure in the ground state, whereas for fluorescence, the respective signs are reversed, indicating a moderate polar emitting species

Table IV.6. Dipole moments determined through solvatochromism methods for 3 groups of solvents together with the corresponding Kamlet-Taft correlations coefficients. The last column precise if the dipole moments are determined from a true minimum on 2D map (see text).

		Kamlet-Taft correlations					Innovative Solvatochromism treatment			
	Solvent Group	ν_0	a	b	p	R^2	μ_g	μ_e	$2\alpha/a^3$	True Minimum on 2D map?
Absorption Aprotic	[1-12]	22750 ± 666	9010 ± 2770	2666 ±797	-63 ± 1230	0.7304	0.38	-6.8	0.93	Yes
Polar Aprotic	[4, 8-12]	22437 ± 668	4191 ± 1880	-1628 ±1010	4428 ± 1410	0.9105	0.27 9.1	-6.5 -1.5	0.97 0	Yes No
Protic	[13-16,18]	24716 ± 755	963 ± 697	-1828 ± 558	2490 ± 504	0.8231	1.73	-0.61	0.97	Yes
Fluorescence Aprotic	[1-12]	14823 ± 143	-1103 ± 595	-369 ± 171	207 ± 264	0.8169	2.78	0	1.034	Yes
Polar Aprotic	[4, 8-12]	15021 ± 17	-484 ± 48	506 ± 26	-872 ± 36	0.9981	3.31	0	0.01	Yes
Protic	[13-16,18]	17186 ±1600	-3695 ± 1480	-153 ±1180	2527 ± 1070	0.8769	7.5	0.005	1.015	Yes

IV.6.2   Solvatochromic data treatment

The main goal of our innovative solvatochromic data treatment consists in the deduction of 4 dipole moments for the three relevant solvent groups chosen above, already tested with Kamlet-Taft correlation. Reviewing the solvatochromism theory is necessary to fully understand the innovative date treatment proposed in this manuscript and to focus on the important parameters for which a special care has to be taken.

IV.6.2.1 Theory of solvatochromism

According to the dielectric continuum formalism of Bilot and Kawski [122, 123], the energy of the transitions (absorption and emission) between the ground and the excited states of the free solute molecule (gas phase) is derived from quantum-mechanical first-order perturbation theory and the influence of solvation is introduced according to Onsager's model [33]. By taking into account the dimensionless polarizability[12] α of the solute and considering a solvent with dielectric constant ε and refractive index n, Bilot and Kawski define two relevant solvent functions:

$$g(n, \varepsilon, \alpha) = \frac{1}{1 - \alpha f(n_0^2)} \left[\frac{f(\varepsilon)}{1 - \alpha f(\varepsilon)} - \frac{f(n_0^2)}{1 - \alpha f(n_0^2)} \right] \qquad (IV.11)$$

$$h(n, \alpha) = \frac{2 - \alpha f(n_0^2)}{1 - \alpha f(n_0^2)} \left[\frac{f(n_0^2)}{1 - \alpha f(n_0^2)} \right] \qquad (IV.12)$$

where $f(x) = (x - 1)/(2x + 1)$. These two functions are involved in the first order expression of the difference of absorption/emission band maximum on going from the gas phase, $v_{Abs/Fluo}^{gas}$ to the solution, $v_{Abs/Fluo}^{sol}$, according to:

$$k\pi\varepsilon_0 hca_0^3 \left(v_{Abs/Fluo}^{sol} - v_{Abs/Fluo}^{gas} \right) = \vec{\mu}_{g/e}(\vec{\mu}_e - \vec{\mu}_g) g(n, \varepsilon, \alpha) - \frac{(\vec{\mu}_e)^2 - (\vec{\mu}_g)^2}{2} h(n, \alpha) \quad (IV.13)$$

where a_0 is the Onsager cavity radius and the subscripts g and e refer to the ground and excited states, respectively (the other constants having the usual meanings). For sake of simplicity this equation can be rewritten as

$$\left(v_{Abs/Fluo}^{sol} - v_{Abs/Fluo}^{gas} \right) = K_1 g(n, \varepsilon, \alpha) - K_2 h(n, \alpha) \qquad (III.14)$$

where K_1 has different values for absorption and emission while K_2 is the same. It is now obvious that with a non-linear fit of the solvatochromic data according to equation III.14, one can assess both coefficients K_1 and K_2. So, considering distinct treatment for absorption or emission solvatochromic data, the corresponding parameters K_1 and K_2 can be used to determine the dipole moments $\mu_g(S_0)$ and $\mu_e(S_2)$ on one hand (absorption data), and $\mu_g(S_0')$ and $\mu_e(S_1)$, on the other hand (emission data), according to:

---

[12] We will, after Bilot and Kawski, use dimensionless polarizability α, which can be derived from the solute polarizability α' as following: $\alpha = \frac{2\alpha'[Å^3]}{a^3}$, where a is Onsager cavity radius.

$$\begin{cases} \mu_g(S_0) = \dfrac{1}{\sqrt{4\pi\varepsilon_0 a^3}} \dfrac{K_1}{\sqrt{2(K_1 - K_2)}} & \text{(IV.15)} \\[3mm] \mu_e(S_2) = \dfrac{(cos\theta)^{-1}}{\sqrt{4\pi\varepsilon_0 a^3}} \dfrac{K_2}{\sqrt{2(K_1 - K_2)}} & \text{(IV.16)} \end{cases}$$

$$\begin{cases} \mu_g'(S_0') = \dfrac{1}{\sqrt{4\pi\varepsilon_0 a^3}} \dfrac{2K_2 - K_1}{\sqrt{2(K_1 - K_2)}} & \text{(IV.17)} \\[3mm] \mu_e(S_1) = \dfrac{(cos\theta)^{-1}}{\sqrt{4\pi\varepsilon_0 a^3}} \dfrac{K_1}{\sqrt{2(K_1 - K_2)}} & \text{(IV.18)} \end{cases}$$

where θ is the angle between the ground and excited states dipole moments considered in the above equations. At this point we have to choose reliable data treatment strategy.

IV.6.2.2   Innovative algorithm

The originality of the treatment proposed here originates from the combination of the following three aspects: i) absorption and emission solvatochromic data are considered separately and thus the four distinct dipole moments, $\mu_g(S_0)$, $\mu_e(S_2)$, $\mu_e(S_1)$ $\mu_g(S_0')$, can be evaluated. ii) the polarizability of the solute is explicitly included as an adjustable parameter with the approximation that it has the same value in the ground and excited states, i.e. $\alpha_g \approx \alpha_e = \alpha$; iii) the gas phase absorption/emission band maxima $v_{Abs/Fluo}^{gaz}$ are also considered as adjustable parameters.
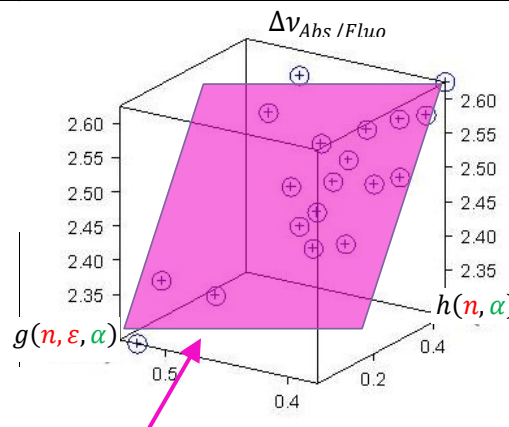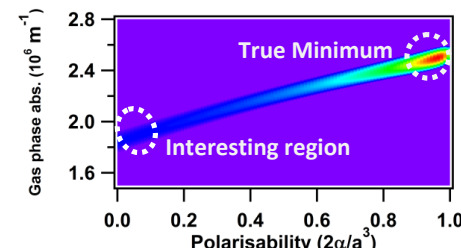
Solvatochromic Data Treatment Algorithm

GOAL= determinations of 2 dipole moments

3 inputs:	Set of solvent values: $\{n, \varepsilon\}$ Solvatochromic data: $\{\nu_{Abs}^{sol}\}$ or $\{\nu_{Fluo}^{sol}\}$
2 adjustable parameters:	ν_{Abs}^{gaz} or ν_{Fluo}^{gaz} (gas phase!) and polarizability α.

2 outputs:

$\mu_g(S_0)$, $\mu_e(S_2)$ (absorption) or

$\mu_e(S_1)$, $\mu_g(S_0')$ (emission)

STEP 1 — One chooses appropriate intervals for $[\nu_{Abs/fluo}^{gaz}]$ and $[\alpha]$.

STEP 2

a) For a pair of values $(\nu_{Abs/Fluo}^{gaz}; \alpha)$ one computes:
- $g(n, \varepsilon, \alpha)$
- $h(n, \alpha)$
- $\Delta\nu_{Abs/Fluo} = \nu_{Abs/Fluo}^{sol} - \nu_{Abs/Fluo}^{gaz}$

b) one plots 3D graph

$$\Delta\nu_{Abs/Fluo} = f[g(n, \varepsilon, \alpha), h(n, \alpha)]$$

c) Non-linear fit: $\Delta\nu_{abs/fluo} = K_1 g(n, \varepsilon, \alpha) - K_2 h(n, \alpha)$

$\Rightarrow$ **K_1, K_2 and χ^2 are stored**

operation a)-c) repeated until both $[\nu_{Abs/fluo}^{gaz}]$ and $[\alpha]$ are spanned

STEP 3

2D Map are plotted

$$\chi^2 = f(\nu_{Abs/Fluo}^{gaz}; \alpha)$$

$\Rightarrow$ identification of true minimum or other relevant points

STEP 4

For the selected points :
- **K_1, K_2**
- **Onsager radius=4.75 Å**
- **Phase θ=0 or π**

absorption

$$\mu_g(S_0) = \frac{1}{\sqrt{4\pi\varepsilon_0 a^3}} \frac{K_1}{\sqrt{2(K_1 - K_2)}}$$

$$\mu_e(S_2) = \frac{(cos\theta)^{-1}}{\sqrt{4\pi\varepsilon_0 a^3}} \frac{K_2}{\sqrt{2(K_1 - K_2)}}$$

emission

$$\mu_g'(S_0') = \frac{1}{\sqrt{4\pi\varepsilon_0 a^3}} \frac{2K_2 - K_1}{\sqrt{2(K_1 - K_2)}}$$

$$\mu_e(S_1) = \frac{(cos\theta)^{-1}}{\sqrt{4\pi\varepsilon_0 a^3}} \frac{K_1}{\sqrt{2(K_1 - K_2)}}$$

Figure IV.17 Solvatochromic data treatment algorithm for determination of dipole moments from stationary absorption and fluorescence data.

The inputs of our algorithm are the experimental solvatochromic data $\{v_{Abs}^{sol}\}$ or $\{v_{Fluo}^{sol}\}$ and the solvent properties n and ε while the adjustable parameters are polarizability α of the solute and the gas phase absorption/emission band maxima $v_{Abs}^{gaz}/v_{fluo}^{gaz}$. The main idea of this approach is based on the principle that the best set of $v_{Abs/Fluo}^{gaz}$ and α parameters should lead to the most accurate non-linear fit of the solvatochromic data according to eq III.14. Thus, we have imagined to plot in a 2D map the variation of the mean square coefficient χ^2 characterizing this non linear fit as a function of both the $v_{Abs/Fluo}^{gaz}$ and α values. Analyzing this 2D map should allow to visualize directly the optimum values of $v_{Abs/Fluo}^{gaz}$ and α. The algorithm core (double implementation structure), illustrated in figure IV.17, can be described as follows:

STEP 1: the experimental data $\{v_{Abs}^{sol}\}$ or $\{v_{Fluo}^{sol}\}$ measured for a given set of solvents $\{n, \varepsilon\}$ are selected. Appropriate intervals for the adjustable parameters $v_{Abs/Fluo}^{gaz}$ and α are chosen. The polarizability is scanned within the [0; 1.2] interval while v_{Abs}^{gaz} and v_{Fluo}^{gaz} are scanned within the [15000; 28000 cm^{-1}] and [10000; 17000 cm^{-1}] frequency intervals, respectively.

STEP 2:

   a) a pair of $v_{Abs/Fluo}^{gaz}$ and α values is implemented in the loop. The 2 functions $g(n, \varepsilon, \alpha)$ and $h(n, \alpha)$ (eqs. IV.11 and IV.12) and $\Delta v_{Abs/Fluo} = v_{Abs/Fluo}^{sol} - v_{Abs/Fluo}^{gaz}$ (left side of eq. III.14) are determined.

   b) Then the $\Delta v_{Abs/Fluo}$ values are plotted for all solvents as a function of $g(n, \varepsilon, \alpha)$ and $h(n, \alpha)$ in a 3D graph $\Delta v_{Abs/Fluo} = f[g(n, \varepsilon, \alpha), h(n, \alpha)]$.

   c) Non-linear fits of $\Delta v_{Abs/Fluo}$ by the equation plane $K_1 g(n, \varepsilon, \alpha) - K_2 h(n, \alpha)$ (eq. III.14) is performed and the fitted parameters K_1 and K_2 as well as χ^2 are stored.

Then the $v_{Abs/Fluo}^{gaz}$ and α values are incremented step by step within their respective intervals. For each set of values, the above operations a – c listed in step 2 are repeated until the overall chosen ranges are spanned by the procedure.

STEP 3: a 2D map of χ^2 as a function of the $v_{Abs/Fluo}^{gaz}$ and α values is built and its minimum value is detected. Alternatively, other interesting regions of the 2D map can be tested.

STEP 4: for the selected points chosen above, $\mu_g(S_0)$, $\mu_e(S_2)$ (abs) or $\mu_e(S_1)$ $\mu_g(S_0')$ (emiss) are computed from K_1 and K_2 according to eq.IV. 15-31 and eq IV. 17-33 after implementing an Onsager radius of 4.75 Å (DFT calculations) and a phase value $\theta = 0$ or π.
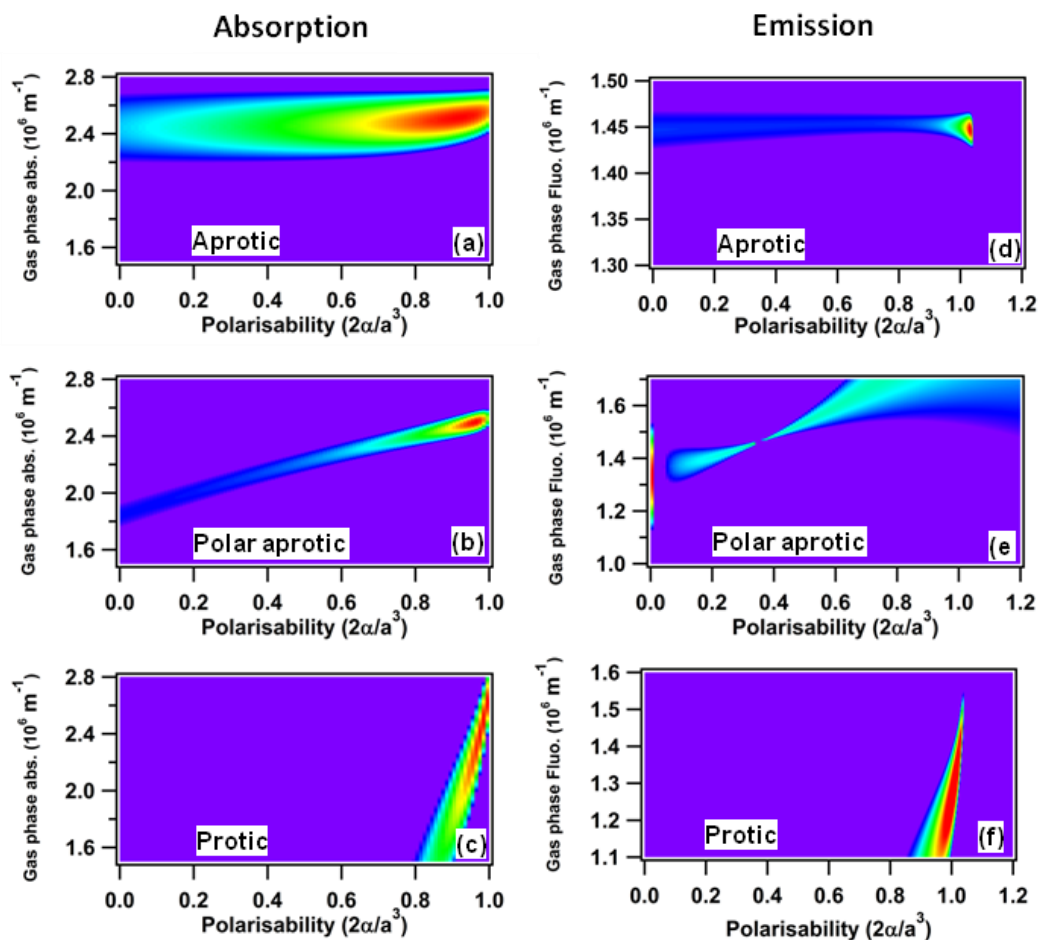
Figure IV.18 Maps of the χ^2 values deduced from the non linear fits of the 3D Solvatochromic data, $\nu_{abs/fluo} = \mathrm{f}[g(n, \varepsilon, \alpha),\ h(n, \alpha)]$, according to equation III.14 for absorption (a-c) and fluorescence (d-f). Three distinct sets of solvent were tested Aprotic, Polar Aprotic and Protic (see the text).

IV.6.2.3   Results and comparison with TDDFT values

We now apply, for each group of solvents, the detailed solvatochromic analysis described in section IV.6.2.2, which pays a special attention to the choice of the solute polarizability and gas phase transition energy values. A most interesting aspect of this approach is that it allows spanning a large interval of values for the polarizability as proposed recently by Krawczyk et al. [124], a point quite tricky for molecules having some zwitterionic character such as SBPa. In fact, while the polarizability can be easily evaluated for neutral molecules and commonly approximated to $\alpha \approx 1/2a_0$, it is hardly quantifiable for strongly polar, weakly polarizable molecules. Furthermore, apart from a recent paper by Renge et al. [107], there has never been any discussion in the literature about the importance of choosing with caution the $\nu_{Abs/Fluo}^{gaz}$ value (such a value is not easily accessible) within a solvatochromic approach that does not deal with stokes shift quantities.

Consider first the results obtained for the group of aprotic solvents. As seen in Figure IV.18a, the optimum χ^2 value related to the absorption data is found for $\alpha \approx 0.93$ and $\nu_{Abs}^{gaz} \approx 25000$ cm-1, which corresponds to dipole moments $\mu_g(S0) = 0.38$ D and $\mu_e(S2) = -6.8$ D. This result is totally irrational because, on one hand, the ν_{abs}^{gaz} value is manifestly too large compared to the 22400 cm^{-1} absorption maximum measured in nonpolar toluene, and, on the other hand, the 0.38 D dipole moment value determined for the ground state is in total disagreement with the experimental value (10.33 D). The unreliability of the solvatochromic analysis in aprotic solvents is also perceptible in the related Kamlet-Taft data (first line in table IV.6). Indeed, as already commented above, the much weaker value found for the polarity coefficient p compared to coefficients a and b seems to indicate a dominant contribution from specific interactions. A similar conclusion can be derived from the analysis based on the emission data (figure IV.18 and table IV.6). A possible explanation for this failure is that the solvatochromic analysis is invalidated due to partial aggregation of SBPa as dimers.

Table IV.7 Dipole moments of SBPa of various electronic states (see text): comparison between theoretical and experimental results including innovative data treatment presented.

		INDO/S		CIS	TDDFT PBE0/6-311G* (Vaccum)	Solvato-chromism[c]	Exp.
		HF/ 6-31G**	MP2/ 6-31G**	HF/ 6-31G**			
μ_g (D)	S_0	+10.27[a]	+10.14[a]	+10.50[a]	+8.2	+9.1	10.33[b]
	S_0'	-	-	-	+8.8	+3.3	-
μ_e (D)	S_1	-4.68[a]	-4.50[a]	-6.24[a]	-1.4	0	-
	S_2	-	-	-	+2.7	-1.5	-

[a] ref [18-20]; [b] ref [23]; [c] deduced from innovative solvatochromic data treatment.

To avoid the perturbing effect of dimerization, we consider now the solvent group restricted to the polar aprotic ones, in which aggregation of SBPa is assumed to be reduced. In this case, the Kamlet-Taft correlation leads to better results, with a prevailing p coefficient, although the a and b coefficients are still not negligible. The χ^2 map corresponding to this solvent group in figure IV.18b, established from the absorption data, shows a slight minimum in exactly the same region as for the previous group (figure IV.18a), which leads to an unrealistically weak $\mu_g(S_0)$ value. However the map presents also a well defined tail of χ^2 values only slightly higher than at the minimum, extending until $\alpha = 0$ for a value of $\nu_{abs}^{gaz} = 17200$ cm^{-1} that is reasonable. For this value of polarizability, the corresponding dipole moment predicted for the ground state,

$\mu_g(S_0) = 9.1$ D, is in quite good agreement with the experimental value and that obtained for the excited state is opposite and has a much weaker value, $\mu_e(S_2) = -1.5$ D, which is consistent with expectations. On the other hand, the excellent correlation results (0.9981) obtained for the emission data (figure IV.18f) confirms more decisively this result, with a p coefficient notably higher than the a and b coefficients and a χ^2 minimum clearly located at $\alpha = 0.01$. The two dipole moments related to this minimum, $\mu_e(S_1) = 0$ and $\mu_g(S_0') = 3.31$ D, fit perfectly within the range fixed by solvatochromism absorption results. The overall picture for the aprotic case is summarized in figure IV.19.

The case of the protic solvents is more difficult to analyze because of the presence of intermolecular solvent-solute hydrogen bonds (see figure IV.10). It is worth noting that the 2D χ^2 maps obtained from both the absorption and emission data (Figures IV.18c and IV.18g, respectively) have a quite similar shape with a minimum near $\alpha = 1$. Concerning the Kamlet-Taft analysis, the p and b coefficients have similar contributions if the correlation is done with the absorption data whereas the a coefficient dominates if the correlation refers to the emission data. Such a discrepancy brings serious doubts concerning the use of the Onsager model to analyze the solvatochromism of SBPa in protic solvents. For comparison with aprotic case, we displayed on figure IV.19 the four dipole moments found keeping in mind that the molecular species, and thus polarizability, are different for both case.
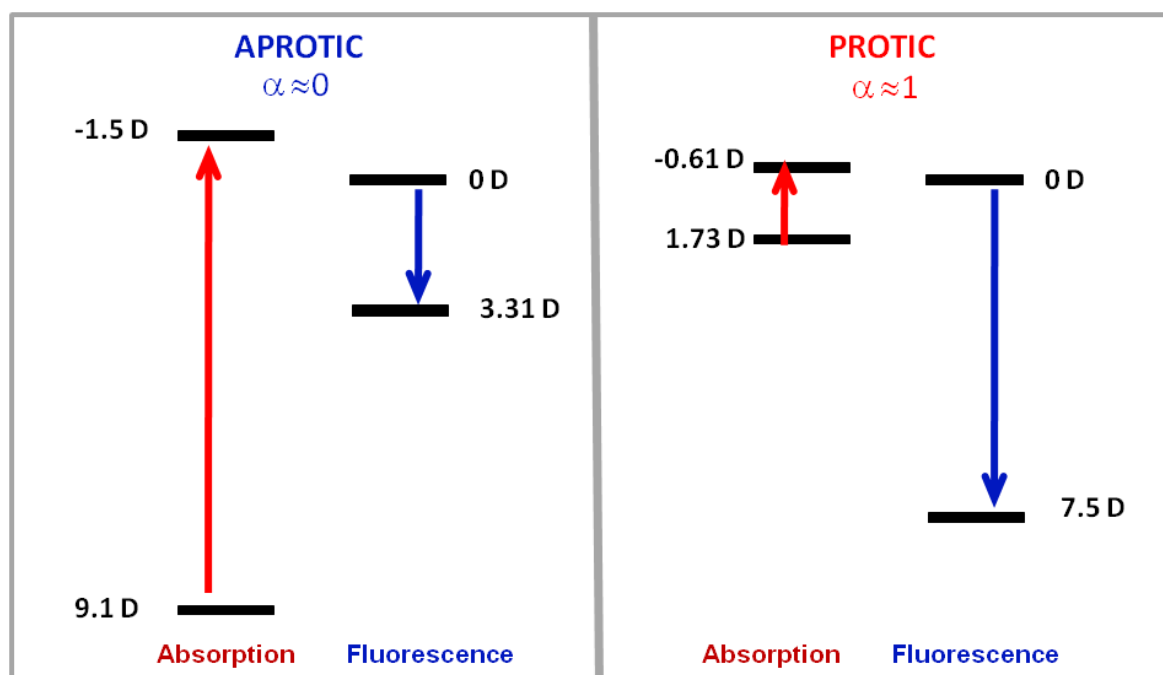
Figure IV.19 Dipole moments deduced from the solvatochromic analysis restricted to the set of polar or aprotic solvents.

To the best of our knowledge, this study is the first one to compare 4 experimental dipole moments with 4 corresponding theoretical values all gathered in table IV.7. Despite the numerous issues encountered with SBPa molecules (zwitterionic character, dimerization, and specific interactions) the confrontation experiment-theory is very encouraging. Indeed, as seen on table 4 we successfully recovered the ground state value +9.1 D than correlates well with TDDFT results (+8.2 D) or experimental conventional techniques (+10.33 D). For the excited states S_2(FC) and S_1(E) the results are excellent in absolute values but the sign is not well reproduced for absorption process. Unfortunately, by comparison with TDDFT, we failed to retrieve the dipole value of S'_0. This failure is probably due to: i) our difficulty to generate a good electrostatical solvent set; ii) the assumption on polarizabilities, $\alpha_g = \alpha_e$ that has to be invalid when reversion of dipole moment is obtained between excited and ground state.

IV.7   Conclusions

In this chapter, the detailed analysis of stationary spectroscopy as well as quantum mechanical calculations results obtained for the solvatochromic SBPa molecule was presented. As a first result, a photoinduced ICT transition has been identified through the observation of a strong negative solvatochromic absorption band and confirmed by conclusive application of the Weller equation. The solvatochromic data were analysed with different approaches.

First, applying a band shape analysis treatment based on the semiclassical Marcus theory, the values of reorganization energies and driving forces for 12 different solvents were evaluated. These later values are very important and will be used further in chapter V for determining the Marcus region concerned by excited state ICT reaction.
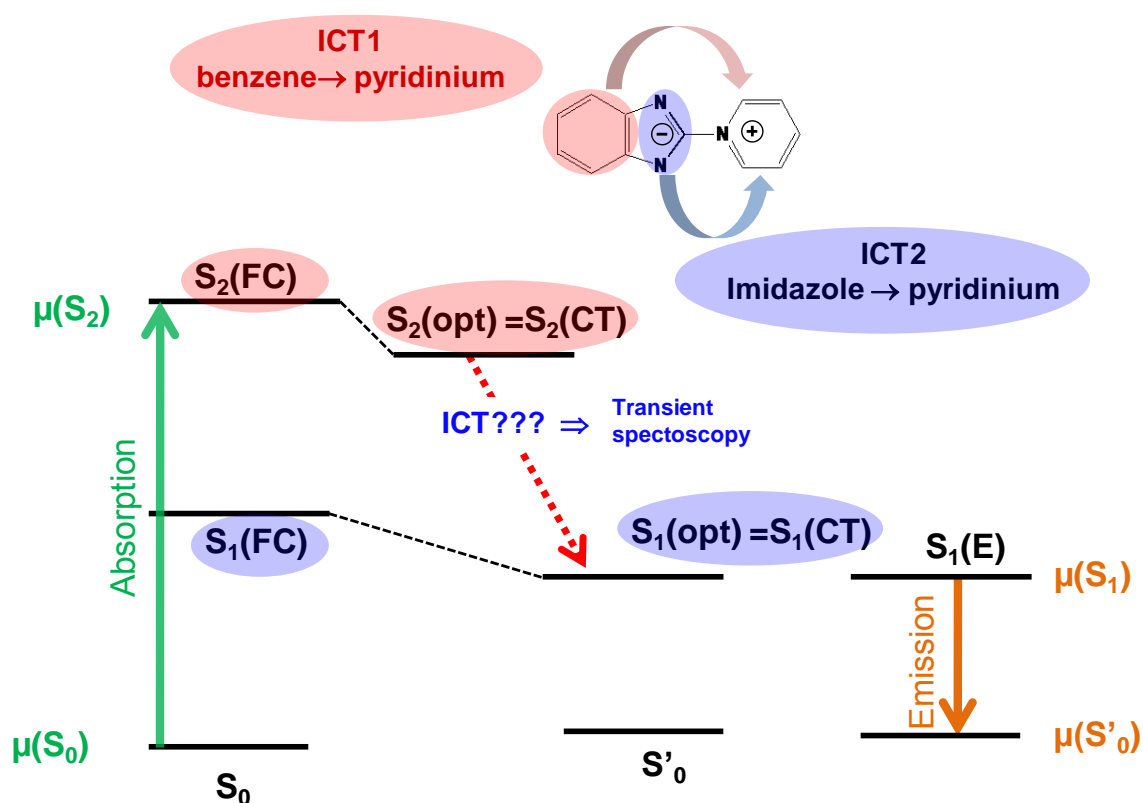
Figure IV.20. Representation of electronic states revealed by theory and experiment.

Using advanced PCM-TDDFT calculations, the solvatochromic absorption band has been attributed to a $S_0 \rightarrow S_2(FC)$ transition while the $S_0 \rightarrow S_1(FC)$ is forbidden due to symmetry restrictions. In a complementary way, a similar investigation of the fluorescence data revealed a non solvatochromic emission band not related to the S_2 state. Advanced LR-PCM-TDDFT geometry optimization from the Franck-Condon configurations $S_2(FC)$

and S_1(FC) allowed to calculate the corresponding relaxed configurations S_2(opt) and S_1(opt), respectively, and predict the associated emission wavelengths (vertical transitions). The most important states studied in this chapter are displayed in figure IV.20. Further, theory-experiment comparisons indicated that the non-solvatochromic emission band observed experimentally can be reasonably related to a transition from S_1(opt).

All the dipole moments of the different electronic states were determined by calculations; in parallel, we decided to develop a novel approach to obtain reliable experimental values of these dipole moments. This approach consists in performing with great caution the non-linear fit of the solvatochromic data according to equation III.14. To ensure that the considered solvent set is mainly electrostatic, Kamlet-Taft correlations were systematically performed. The new aspects of the approach was based on the fact that i) absorption and emission solvatochromic data were treated separately; ii) the solute polarizability α and gas phase absorption/.emission $\nu_{Abs/Fluo}^{gaz}$ were considered as adjustable parameters; and iii) the relevant regions that can give reliable dipole moments were visualized by plotting a 2D map $\chi^2 = f(\nu_{Abs/Fluo}^{gaz}, \alpha)$. As displayed in table IV.7, the results obtained are very encouraging as 3 of the 4 dipole moments deduced from this solvatochromic treatment are close to the TDDFT values. In the future, clear improvement could be obtained by selecting a still better solvent set (our best Kamlet-Taft correlation indicated non negligible contributions from specific interactions). On the other hand, concerning the theoretical model used for fitting the solvatochromic data, the approximation considering the same value in the ground and excited states for polarizabilities, i.e. $\alpha_g \approx \alpha_e$ is clearly problematic. We propose to reconsider eq. III.14 in order to go beyond the first order term and take into account the second order one (the Stark effect term, [26, 125, 126], to test separately the polarizability values of the ground and excited states.

In order to get a better knowledge of the CT states encountered in this chapter, we analysed the computed MK charges for the four electronic configurations, S_1(FC), S_2(FC), S_1(opt) and S_2(opt). All have been recognized as having CT character involving specific parts of the molecule. It is fundamental to remember that, for each one of the S_1 and S_2 states, the CT character is more or less pronounced between the FC and optimized geometries. For this reason, we used the following correspondence S_1(opt) $\Leftrightarrow$ S_1(CT) as well as S_2(opt) $\Leftrightarrow$ S_2(CT). In particular, the absorption transition $S_0 \rightarrow S_2$(FC) is found to

correspond to the transfer of less than 0.5|e| (depending on the solvent) from the benzene to the pyridinium part. Then, the internal relaxation process $S_2(CT) \rightarrow S_1(CT)$ is also found to have notable ICT character and to correspond to the transfer of less than 0.2|e| (depending on the solvent) from the imidazole to the pyridinium part. To complement this ensemble of steady-state spectroscopic measurements, we will now investigate the real-time dynamics of the ICT processes using time-resolved spectroscopic experiments with a special attention to the $S_2(CT) \rightarrow S_1(CT)$ transition predicted by calculations.

CHAPTER V

Transient absorption spectroscopy studies of SBPa.

V.1 Introduction

In chapter IV the steady-state optical properties of the SBPa molecule in various solvents were studied with the help of quantum chemical calculations. The lowest energy absorption band, characterized by a strong negative solvatochromism, was assigned to a $S_0 \rightarrow S_2(FC)$ transition with an expected high charge transfer (CT) character. For emission, an apparent non solvatochromic band was ascribed to a $S_1(E)$ state. To gain more information on these electronic states, stationary absorption and fluorescence results were compared to advanced PCM-TDDFT calculations. As a starting point, a quasi-planar geometry has been proposed for the ground state from NMR data and (PCM-)DFT calculations. The two lowest-lying singlet excited states have been investigated at both the Franck-Condon geometry corresponding to the vertical transition from S_0 and after full geometry optimization. The main characteristics predicted for the three most important configurations are:

$\underline{S_2(FC)}$ state: The Franck-Condon (vertical transition) configuration $S_2(FC)$ has a strongly pronounced CT character with a dipole moment difference $\Delta\mu$ relative to the ground state ranging from 6D (vacuum) to 14D (ACN) in agreement with the observed negative solvatochromism of the absorption band. In vacuum, this state arises from the transfer of 0.2|e| from the benzene to the pyridinium ring, the charge of the imidazole bridge being constant. Note that the lowest FC state, i.e., $S_1(FC)$, has a larger CT character but its photoexcitation is forbidden by selection rules (symmetry restriction).

$\underline{S_2(CT)}$ state: This state has been obtained after optimization of the $S_2(FC)$ geometry. Its CT character is similar in vacuum to that predicted in the FC region but decreases with increasing solvent polarity, *i.e.*, the solvent initiates some back electron transfer. As a consequence, the $S_2(FC) \rightarrow S_2(CT)$ relaxation leads to an expansion of the benzene and pyridinium rings together with a concomitant contraction of the central C-N bond.

$\underline{S_1(CT)}$ state: The $S_1(CT)$ state obtained through geometry optimization of $S_1(FC)$ presents different properties: i) the CT character is still more pronounced than for $S_2(CT)$, with a reversion of the dipole moment that reaches a final value around -1.4 D; ii) as compared to $S_2(CT)$, few geometry changes are noticed on the pyridinium part while the quinoid character of the benzene ring is modified. Because vertical optical transition to $S_1(FC)$ is not allowed, $S_2(CT) \rightarrow S_1(CT)$ internal conversion is expected to be the only

process to populate $S_1(CT)$. It leads to the transfer of 0.2|e| from the imidazole to the pyridinium part (vacuum case). For this reason, this process will be named as "ICT" in the following of this manuscript. At the present time, on the basis of only the comparison of emission-TDDFT data, the predicted $S_1(CT)$ could correspond to the observed emissive $S_1(E)$ state. We will see that this attribution will no longer hold with regard to the transient spectroscopy data.

Having obtained thoughtful characterization of electronic states, we still do not know the overall photophysical scheme that links all these excited states together and their related dynamics. In order to get some information on this aspect, we present in this chapter an investigation of the real-time photophysical relaxation processes following photoexcitation of SBPa by using the femtosecond transient absorption spectroscopy. Indeed, transient absorption spectroscopy can supply information about the kinetics of very fast processes [57]. It allows following in "real time" the evolution of reactions induced by photoexcitation and gives the opportunity to assess rate constants k_i for these reactions. Our objective is to try to characterize the different excited state configurations predicted above and determine their formation and decay kinetics to be able to propose a plausible photophysical scheme describing the SBPa relaxation route(s) after excitation. Special attention will be given to the following issues:

- ICT reaction: what are the electronic states involved in this process?

- back Electron Transfer (bET) reaction: which kind of deactivation route (s) the system will choose to return to the ground state?

- Competitive relaxation processes: besides the radiative deexcitation to the ground state, does it exist other competitive channels to the CT reaction like intersystem crossing (ISC) to the triplet state?

- Besides the mechanism of the ICT reaction, major questions have to be answered: does the molecular geometry change substantially in the ICT state? What is the role played by the solvent?

As already discussed in the introduction of this manuscript, these issues have been the object of a number of studies of photoinduced ICT reactions in various systems in the past. A brief summary of the question is given below.

The pNA and DMABN molecules represent two different and representative classes of ICT molecules with ICT characteristic times differing by one order of magnitude. For pNA in water, the FC state, solvated in less than ~100 fs, has already a well pronounced CT character proportional to the initial dihedral angle between the nitro and phenyl groups (a distribution of dihedral angle broadens the solvatochromic band). The ICT reaction takes places immediately, within ~120 fs, and actually consists in the stabilization of the overall charges by a twisting motion of the nitro group. However, this twisting motion leads the system toward a conical intersection that allows IC to a hot ground state within ~250 fs, followed by a biexponential relaxation (1 and 3 ps). As already mentioned, DMABN is characterized by longer characteristic times: an ICT occurring within 4 ps and back reaction within a few ns [47-51]. This is explained by the different natures of the ICT process in the two molecules: a $CT_1 \rightarrow CT_2$ transition in PNA and a well identified LE $\rightarrow$ CT transition in DMABN with a notable potential barrier.

Focusing our attention to the case of the pyridinium betaine family, only one study in solution (film and crystal as well) has been undertaken by Jursenas et al. [127] on the polar Indandione-1,3 Pyridinium Betaine, abbreviated **IPB** (see chart III.). Combining *ab initio* calculations and time-resolved absorption and fluorescence spectroscopy, this group found that: i) the solvatochromic band can be related to a transition involving $S_2(CT)$ and $S_1(LE)$ excited states; ii) the ICT process and energy transfer to the localized state are characterized by a 0.6 ps time constant; iii) the final decay kinetics of few tens of ps is insensitive to solvent polarity but sensitive to solvent viscosity.

Chart III.1 molecule Indandion-1,3 Pyridinium Betaine (IPB)
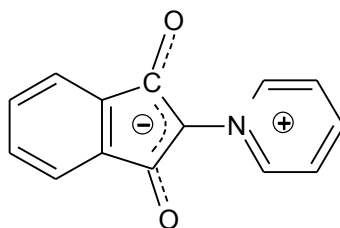
Geometry of excited states. Another important issue concerning ICT reactions is the knowledge of the excited CT state geometry. In fact, this question has been extensively studied during the last decades for DMABN molecule for which a twisted geometry of the ICT state (TICT) has been speculated with the discovery of the dual fluorescence. Furthermore, the observed sensitivity of the ICT characteristic time on solvent viscosity is

interpreted in different ways by the authors depending on the hypothesis made concerning the excited state geometry. Among all papers discussing the geometry of the CT state of DMABN [37, 128, 129], two main hypotheses are the most widely considered:

- **The ICT state is a Twisted Intramolecular Charge Transfer (TICT)**, in which the positively charged dimethylamino group is twisted with respect to the plane of the negatively charged benzonitrile moiety (zwitterionic configuration). Coulombic interactions between the unpaired electrons are minimized, which stabilizes the ICT state [37, 130]. This structure is supported by transient absorption [131] and transient Raman [128, 130] spectroscopy results and numerous quantum chemical calculations [132, 133]. The idea of TICT was born after the discovery of a dual fluorescence signal for DMABN [134]. Another confirmation that the ICT state is twisted was inferred from the dependence of its characteristic time on solvent viscosity [135].

- **The ICT state is a Planar Intramolecular Charge Transfer (PICT)**, meaning that the transfer of charge proceeds within the planar geometry of the ground state molecule. This hypothesis, defended essentially by Zachariasse and his group [136], takes into account the fact that the donor and acceptor parts of the molecule are strongly coupled in the CT state, which excludes a twisted geometry. This model assumes a small energy gap between the two lowest singlet excited states [37, 137]. Note that a recent CASSCF/CASPT2 study of Boggio-Pasqua et al. [137] concluded to a planar geometry of both the LE and CT excited states and described the ICT reaction as a non-adiabatic process occurring through a conical intersection for which a relevant reaction coordinate would be the quinoidality rather than the torsional angle [137].

Even if the subject has been studied by many groups for a long time, there are still discussions about details concerning the intramolecular charge transfer in this molecule. The persistently different opinions about this question point out for its complexity. In addition, very recently, it was proposed by Gustavsson et al. [51] that the emissive ICT state observed from time-resolved fluorescence measurements is different from the TICT sate observed in transient absorption measurements, which suggests an even more complex picture for the photophysics of DMABN.

Solvent controlled ICT process. One of the most difficult tasks to accomplish when studying ICT reactions concerns the role played by the solvent before, during, and after the CT process. Does the CT rate depend on solvent reorganization or does it occur before solvent reorganization? Obviously, both polarity (dipole-dipole interaction) but also viscosity (diffusion of the molecules) can influence the solvation processes of the CT and precursor states. These questions have been examined in the literature and, undeniably, the study of the intramolecular electron transfer reaction of bianthryl by Kang et al. has provided the most convincing evidence for a dynamical solvent controlled ICT process [99, 138]. Indeed, the average electron transfer time τ_{ET} and the average solvation time $\langle \tau_{solv} \rangle$[13] are close to equality in each polar solvent. It appears that the reaction coordinate for the S_1 state electron transfer in bianthryl is predominantly the solvent coordinate and the process is electronically adiabatic [99, 138] However, for most of the ICT molecules, such simple correlation does not hold and for this reason, Palit et al. [139] proposed to examine some power law correlation, i.e., $\tau_{ET} \sim \langle \tau_{solv} \rangle^{\alpha}$. Such complex dependency can be rationalized with the help of Sumi and Marcus's theory [93] (described in subsection III.2.2.5) and may indicate whether fluctuations in the intramolecular modes of the molecule are dominantly contributing to the reaction dynamics or whether the excited state solvation is the only contribution.

Besides the dependency on solvation time, Palit et al. have used the power law approach to derive the solvent viscosity dependency. By considering a Kramer's picture[14], for a barrier crossing process, the strength of the solvent viscosity dependence may be correlated to the height of the barrier. However, investigating separately the role of different solvent parameters can be misleading, since all solvent parameters influence each other. Extensive discussion can be found in reviews [140].

Solvent Polarity influence of ICT according to Marcus Theory. Studies of the polarity dependence of the CT characteristic time, combined with Marcus theory extensively presented in subsection III.2.2, can provide information on the adiabatic nature of the process, as well as on the Marcus region, normal or inverted, in which it takes place. Indeed, in the Marcus normal region, the barrier height to overpass is sensitive to solvent polarity while no such dependency is expected in the inverted region. Experimentally,

---

[13] More detailed description in subsection III.3.1
[14] More detailed description in subsection IV.3.2.1

increase of ICT characteristic time with solvent polarity within Marcus normal region was effectively observed for various systems [141, 142]. Similarly no such dependency was found experimentally in inverted region.

In this chapter, we will first describe in section V.2 the femtosecond transient absorption data of SBPa in ACN (representative example of aprotic solvent) and ethanol (example of protic solvent) by exciting the solvatochromic absorption band with 390 nm laser excitation. Then, to track the possible existence of pump energy dependent competitive processes, we will present additional data recorded with 266 nm excitation. Finally, to check if triplet state formation arises, data obtained for a bromine substituted molecule will be provided to detect whether a heavy atom effect is present or not. All these results together with advanced MCR-ALS analyses of the data will allow to derive a complete photophysical scheme for SBPa.

Next, in section V.3, the question of the dependency of both the CT and bET processes on the solvent properties will be investigated. Guided by the results of the previous chapter, a systematic distinction between protic and aprotic solvents will be made. Following the study done on bianthryl or neighbouring molecules [99], we will explore the dependencies on solvation time, polarity and viscosity and discuss the results within the photophysical framework proposed above. The difficulty will consist in detangling properly the contribution of each one of these solvent parameters.

Finally, the question of the real geometry of the excited states involved in the photophysics will be addressed, with a main interrogation: do we have a TICT process or not? The data obtained by femtosecond absorption spectroscopy for the parent SBPa molecule and for a pre-twisted derivative will be carefully analyzed and the differences and common spectro-kinetic features of the two molecules will be discussed. As we will see, an alternative mechanism leading to the final CT state will be revealed.

V.2 Ultrafast dynamics and evidence for an ICT process following excitation.

Because our first objective is to study the intramolecular CT process in the SBPa molecule and related processes, in the absence of any specific interaction with the solvent, ACN has been chosen as a reference solvent. Indeed, as demonstrated in chapter IV, neither dimerization nor solute-solvent hydrogen bonding arise in ACN, in contrast to what is observed in less polar aprotic or protic solvent. Moreover, ACN is a solvent of high polarity ($\varepsilon = 35.9$) which is favourable to charge transfer processes [143, 144]. Representative femtosecond transient absorption data after photoexcitation of SBPa in ACN will thus be described first (section V.2.1), the 390 nm excitation chosen for this study being in resonance with the peak of the $S_0 \rightarrow S_2$ absorption (solvatochromic band). An attribution of the electronic states responsible for the transient data and the underlying photophysical processes will be proposed (section V.2.2).

Then, these results will be refined by similar investigations of the SBPa ultrafast photophysics i) in the protic solvent ethanol, to evaluate the influence of hydrogen bonding (section V.2.3) and ii) upon 266 nm excitation, to find out whether additional/competitive pump energy dependent processes occur (section V.2.4.1); finally, iii) a comparative analysis of a bromine substituted SBPa molecule, in which enhancement of ISC through heavy atom effect is expected, was performed to investigate the possible triplet state formation (section V.2.4.2). [145]

V.2.1   Femtosecond transient absorption spectra of SBPa in ACN.

The time evolution of the femtosecond transient absorption spectra of SBPa in ACN is presented in figure V.1. The evolution of the signal was measured in the spectral range between 395 and 765 nm and in the temporal window between 0 and 500 ps for solutions of 5 x 10^{-4} M concentration. For clarity, we present the transient data in three parts according to three major dynamical events, qualified as "initial dynamics", "transitional dynamics" and "final dynamics" that appear with different time constants. All spectra were corrected for GVD effect.
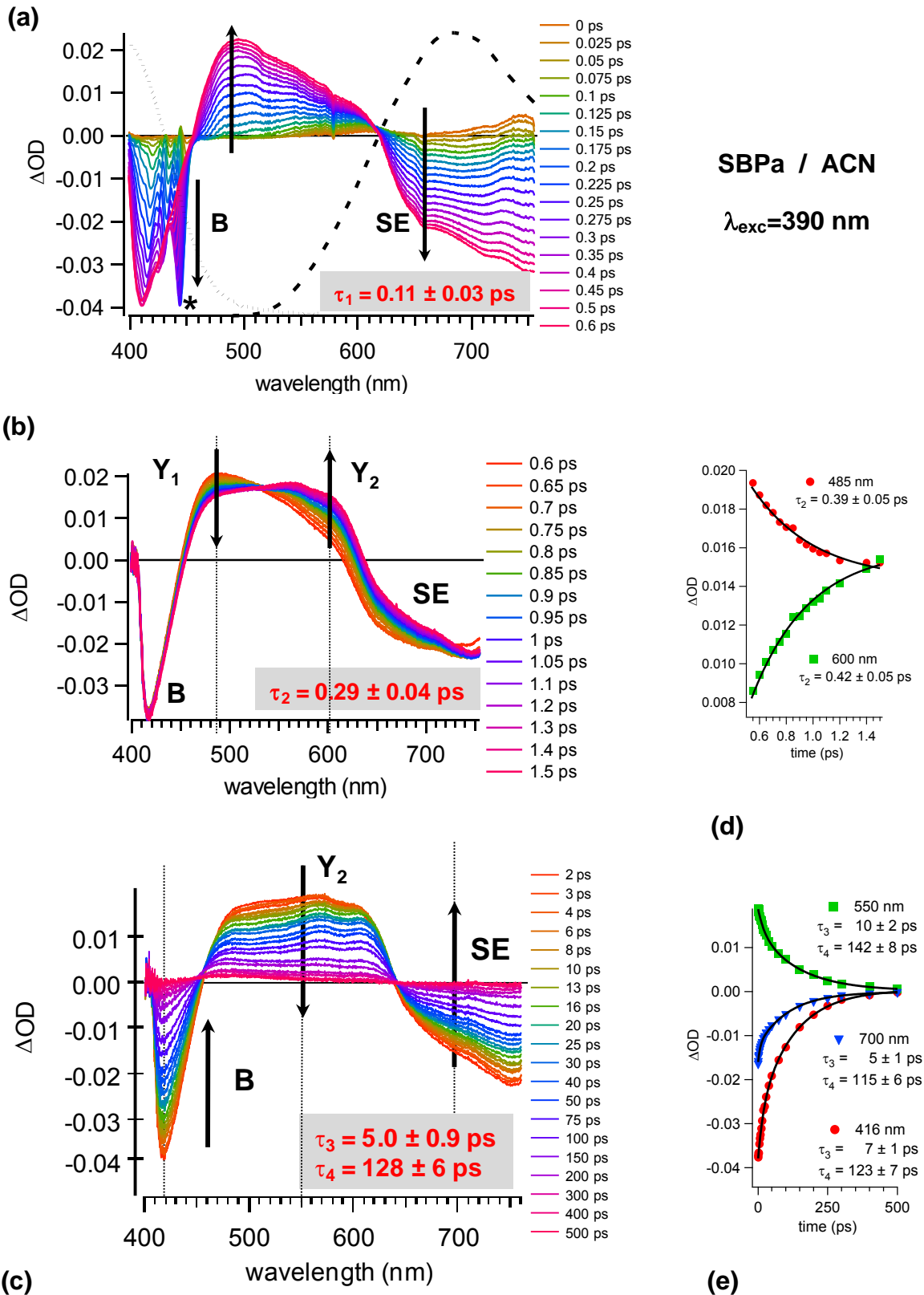
Figure V.1 Femtosecond transient absorption spectral evolution of SBPa in ACN following laser excitation at 390 nm, divided into three temporal windows: a) [-1 – 0.6 ps], b) [0.6 – 1.5 ps], c) [2 – 500 ps]. Characteristic times found using the global fitting method are indicated in red. Graphs d) and e) show typical kinetics for chosen wavelengths and their fits with mono-exponential and bi-exponential functions, respectively. The star indicate stimulated Raman pick of the solvent. Pump-probe correlation time: τ = 180 fs

Initial dynamics. In figure V.1a transient spectra for a temporal window [-1 – 0.6 ps] are shown. Just after excitation, the simultaneous growth of three bands can be observed. A first negative band between 400 and 450 nm, (truncated below 410 nm by the optical filter used to suppress pump perturbations) is easily recognized as a bleaching component (band **B**), as it corresponds approximately to the negative image of the absorption spectrum of SBPa (dotted trace in figure V.1a). A second negative band appears simultaneously between 610 and 760 nm and can be attributed to stimulated emission (band **SE**) because it corresponds to the position of the stationary fluorescence spectrum of SBPa in ACN (dashed trace in figure V.1a). As discussed in chapter IV, fluorescence originates from the $S_1(E)$ emissive state, thus it is natural to consider that the time evolution of the stimulated emission characterizes the $S_1(E)$ state dynamics. Further discussion of the relationship between the stimulated emission and this $S_1(E)$ state will be presented later in view of the results obtained in the protic solvent. Finally, a positive band, named as band $\mathbf{Y_1}$, located between 450 and 610 nm, is related with absorption of excited species. Note that two isosbestic points can be observed, one at 450 nm and the other one at 610 nm, confirming that all three signals appear simultaneously. The characteristic time τ_1 found for this initial dynamics, is $\tau_1 \sim 110$ fs while the global parameter τ for the GVD modified Gaussian pump-probe correlation time inside the global fitting function is optimum at $\tau \sim 180$ fs (see previous chapter). Note that all events shorter than the time resolution will appear as "instantaneous" within the same dynamics. For this reason, although appearing simultaneously, band SE and band Y1 can be related to different states providing that their relaxation dynamics are shorter than time resolution

Transitional dynamics. In figure V.1b transient absorption spectra for a temporal window between 0.6 and 1.5 ps are presented. The evolution shows the decrease of the $\mathbf{Y_1}$ band concomitant with the increase of a new transient absorption band peaking at ~570 nm – named as $\mathbf{Y_2}$ – with a clear isosbestic point in between, at 530 nm. During this process, the **SE** band remains mostly unchanged: it keeps nearly constant intensity and evolves only slightly in shape, which can be explained as the result of the appearance of the overlapping $\mathbf{Y_2}$ absorption. It seems that the **SE** band is not affected by the $\mathbf{Y_1} \rightarrow \mathbf{Y_2}$ process, i.e., the emissive $S_1(E)$ state population does not vary significantly during this process. In addition, there is no perceptible recovery of the ground state, as revealed by the stability of the bleach band **B** intensity. In other words, one can classified the $\mathbf{Y_1} \rightarrow \mathbf{Y_2}$ process as a reaction between two excited states arising independently of the formation of the $S_1(E)$

state. We will discuss this attribution later. The characteristic time found with the global fitting method for this process is $\tau_2 = 0.29 \pm 0.04$ ps. For illustration, single-exponential fittings at two characteristic wavelengths below and beyond the isosbestic point (485 and 600 nm respectively) are shown in figure V.1d, giving slightly overestimate characteristic times (0.39 and 0.42 ps respectively). This discrepancy arises from the fact that these two single-exponential fittings are restricted to the 0.6 – 1.5 ps time domain and are thus less accurate than the global fitting procedure takes into account all the kinetics in the 0–500 ps

Final dynamics. The spectral evolution in the temporal window [2 – 500 ps] is shown in figure V.1c. In this graph, the simultaneous fading of all bands – the negative bleach **B** and stimulated emission **SE** as well as the positive excited state absorption band **Y$_2$** – can be observed. This process was found to be double-exponential with characteristic times of $\tau_3 = 5.0 \pm 0.5$ ps and $\tau_4 = 128 \pm 6$ ps. A double-exponential function is always needed to describe the decay process at all wavelengths, as shown in graph V.1e. It is difficult to attribute now these two dynamics. One of them has to be the decay of the emissive $S_1(E)$ state responsible for the **SE** signal. As one can see, the **SE** signal is present almost until the end of the evolution and does not disappear definitively before 500 ps, which indicates that the decay of emissive $S_1(E)$ state can be correlated to the longer decay time ($\tau_4 = 128$ ps). As a matter of fact, the shorter decay time ($\tau_3 = 5.0$ ps) is likely related with the decay of the other excited state characterized by transient absorption **Y$_2$**. (Note that vibrational relaxation of the $S_1(E)$ state may bring a contribution to the overall decay process but no band shape evolutions is noticed). Finally, after 500 ps, a very weak residual positive transient band is still present with maximum near 450 nm. Further measurements allowing to identify this species will be discussed in section IV.2.5.

V.2.2　First identification of the photoinduced intermediates in ACN

Because of the complexity of the ultrafast processes involved in the ICT reaction, a first tentative attribution will help the reader to understand the photophysical mechanism in SBPa. We intend to recognize the electronic states responsible for the transient bands **SE**, **Y$_1$**, and **Y$_2$** and rationalize the four different times found with the global fitting method: $\tau_1 = 110$ fs, $\tau_2 = 0.29$ ps, $\tau_3 = 5.0$ ps, and $\tau_4 = 128$ ps. For this purpose, in the following discussion, three hypothetical reaction schemes presented in figure V.2 a, b, c respectively, will be successively examined. Those three schemes have been elaborated by taking into consideration the major results of the previous chapter and basic photochemical rules:

i) following the photoexcitation $S_0 \rightarrow S_2(FC)$, an ICT is spontaneously initiated

ii) two well defined CT states can be populated $S_1(CT)$ and/or $S_2(CT)$.

iii) An emissive singlet state $S_1(E)$ has to be taken into account. In contradiction with previous findings this state has to be distinct compare to $S_1(CT)$ or $S_2(CT)$. Indeed, a two exponential decay is reported (vibrational relaxation hypothesis has been discarded) pointing out the existence of two different states.

The schemes a and b explore the possibility for a final state being $S_1(CT)$ (Kasha's rule respected) while scheme c examines the possibility for an ICT giving rise to a final state being $S_2(CT)$ (Kasha's rule violation)

Intitial dynamics identification. First, the vertical pump excitation (red arrow in the figure V.2) reaches the Franck-Condon (FC) region of the absorbing excited state. As said ahead, our excitation at 390 nm is almost matching the maximum of the strong absorption of SBPa in ACN ascribed to $S_0 \rightarrow S_2(FC)$ transition. Consequently the $S_2(FC)$ state is populated at time zero. It is probable that internal conversion from $S_2(FC)$ to $S_1(E)$ occurs very rapidly within time τ_1. In this regard, in a first hypothesis, one can assume that the former transient absorption band $\mathbf{Y_1}$ appearing at short time (figure V.1a) characterizes the emitting $S_1(E)$ state. This is consistent with the simultaneous growth of the $\mathbf{Y_1}$ and $\mathbf{SE}$ components due to the fact that τ_1 is less than our temporal resolution. An alternative hypothesis is to consider the possibility that $S_2(FC)$ reacts as fast or faster than the $S_2(FC)$ $\rightarrow S_1(E)$ internal conversion and leads to the formation of an additional transient state in parallel to the emissive $S_1(E)$ state. In this case, the transient absorption band Y_1 appearing at short time τ_1 would result from the superimposition of two spectral components related to the emissive S_1 state and the new transient state formed in parallel. The analysis of the further evolution of the $\mathbf{SE}$ and $\mathbf{Y_1}$ bands will allow to discriminate between these two hypotheses.

The ICT dynamics identification. It has been speculated that the spectral evolution observed in figure V.1b between 0.6 and 1.5 ps, characterized by the concomitant decrease of band $\mathbf{Y_1}$ absorption in the blue region and increase of a new band $\mathbf{Y_2}$ in the red region, with a well defined isosbestic point, denotes a transition between two excited states. Such "excited states" reactions detected by ultrafast spectroscopy are often observed for CT molecules. We propose to assign this ultrafast process ($\tau_2 = 0.29$ ps) to a last stage of the

ICT process, (Precursor $\rightarrow$ CT) taking into consideration that excitation has already induced the first, instantaneous ICT process.

We are now concerned with an important point of our study, that is the identification of the precursor and final excited states that are involved in this final CT step and are responsible for the transient bands Y_1 and Y_2, respectively. At this stage, we can consider three possible schemes, one corresponding to the above first hypothesis that the Y_1 absorption characterizes only the emissive $S_1(E)$ state, and the two others originating from the second hypothesis that the Y_1 absorption characterizes both the $S_1(E)$ state and another state formed in parallel from the $S_2(FC)$ state (figure V.2):

- **Scheme 1:** the final step of the ICT process occurs at the S_1 level from the $S_1(E)$ state (Y_1 absorption) to a $S_1(CT)$ state (Y_2 absorption) that can be in equilibrium, by analogy with the DMABN mechanism. [37] In this case, the stimulated emission from $S_1(E)$ is expected to show the same decay kinetics as the absorption band Y_1 ($\tau_2 = 0.29$ ps), which manifestly is not the case since the **SE** band keeps a constant intensity during the ICT process. In other words, as already remarked, the reaction step occurring with time τ_2 involves two excited state species that evolve independently of the $S_1(E)$ state. We conclude that the final ICT process does not occur from the emissive $S_1(E)$ state, but from another excited configuration.

- **Scheme 2:** the ICT process occurs nonadiabatically from the relaxed minimum of the S_2 electronic state out of the FC region, already identified as $S_2(CT)$ state, to the $S_1(CT)$ state. In this assumption, the initial $S_2(FC)$ configuration undergoes ultrafast internal conversion to the $S_1(E)$ state in competition with its evolution toward the relaxed $S_2(CT)$ configuration. The Y_1 band is thus due to the superimposition of the $S_1(E)$ and $S_2(CT)$ absorption features and the Y_2 band characterizes the superimposition of the $S_1(E)$ and $S_1(CT)$ absorptions. If the $S_2(FC) \rightarrow S_2(CT)$ and $S_2(CT) \rightarrow S_1(CT)$ processes can be seen as the ultimate steps by which the ICT process is stabilized and completed, the $S_2(FC) \rightarrow S_1(E)$ process could correspond to a partial back electron transfer that is possible in the $S_2(FC)$ state because the geometry and solvent cage have not yet evolved to stabilize the photoinduced ICT configuration.

- **Scheme 3:** the CT process follows an adiabatic mechanism occurring not on the S_1 surface but rather on the S_2 surface. In this case, the precursor and final states of the reaction would involve different solvation states or different geometries of the S_2 potential surface. As in case 2, the **Y_1** and **Y_2** bands would still be due to the superimposition of absorption features from these states and the $S_1(E)$ state. This hypothesis can be ruled out from the fact that the 5 ps lifetime of the final CT excited state seems exceedingly long for a S_2 state and because the subsequent formation of the $S_1(CT)$ state is not observed (kasha rule violation are not frequently observed)
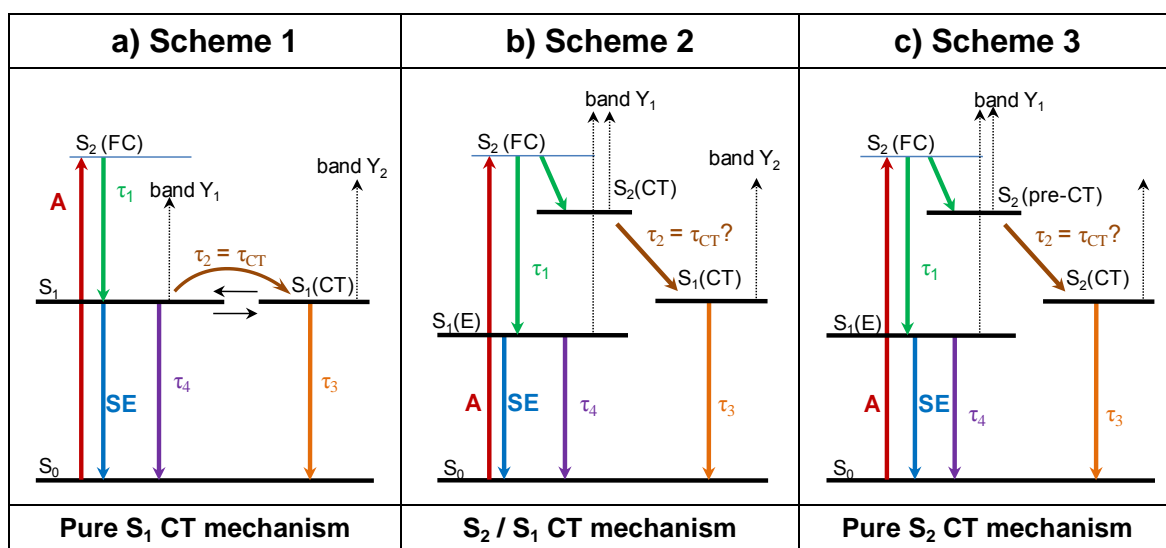
Figure V.2 Three schematic hypotheses proposed for the SBPa photophysics from the experimental femtosecond transient absorption data in ACN.

Post-ICT dynamics identification. For very long delays – between 2 and 500 ps – deactivation of all excited states takes place (see figure V.1c). This evolution was fitted with a double-exponential, meaning that at least two different states are contributing, as discussed above. The shorter characteristic time of $\tau_3 = 5.0$ ps can be tentatively ascribed to the deactivation of the $S_1(CT)$ state while the longer time of $\tau_4 = 128$ ps corresponds to the deactivation of the emissive S_1 state. More precisely, the deactivation of $S_1(E)$ proceeds via fluorescence but with very low efficiency ($\Phi_F \sim 0.001$), suggesting that IC has to be the main decay process for the $S_1(E)$ state. Because no emission is characterized from either $S_1(CT)$ or $S_2(CT)$, the corresponding fast decay of 5 ps is likely related with an IC process. Finally, regarding the spectrum at 500 ps in figure V.1c, one can notice a small residual absorption with maximum at 470 nm. This signal can indicate the existence of an additional decay pathway of $S_1(E)$ by intersystem crossing (ISC) to the triplet state. This point will be investigated in section V.2.4.2.

V.2.3   Femtosecond transient absorption signal of SBPa in EtOH.

After a detailed analysis of the femtosecond transient absorption data of SBPa in ACN, a photophysical scheme was retained, which assumes that: i) ultrafast relaxation of $S_2(FC)$ state populates both $S_2(CT)$ and the emissive $S_1(E)$ giving rise to "instantaneous" **SE**. ii) the ICT process between excited states has been recognized as the IC from the relaxed $S_2(CT)$ state to the $S_1(CT)$ state (figure V.2b).

Femtosecond transient absorption measurements were made for SBPa molecule in EtOH because from previous chapter hydrogen bonding effect has been evidenced during the analysis of solvatochromic absorption or emission (see figure IV.16). The obtained spectra, divided into four temporal windows, are presented in figure V.3 a) – d). The spectral evolution observed from 1.5 ps to 400 ps strongly resembles that previously found in ACN. In contrast, in the short-time domain (< 1.5 ps), notably different spectral features arise in EtOH likely related within hydrogen bonding effect.

Initial dynamics. The first signal appearing after photoexcitation between -1 and 0.3 ps in figure V.3a shows only negative components: a very strong and broad negative **SE** signal peaking around 480 nm combined with the bleaching band **B**. The fast appearing stimulated emission is totally different from that occurring from the $S_1(E)$ state in ACN (Figure V.1a). It can be supposed to come directly from the $S_2(FC)$ state.

After 300 fs (figure V.3b), an absorption band peaking around 460 nm begins to appear and grows in the time window [0.4 – 1.5 ps] with a time constant 120 fs (deconvoluted from pump-probe correlation width found at 150 fs). This absorption corresponds clearly to the Y_1 band seen in ACN. Simultaneously, the SE signal evolves into a new component with maximum at 640 nm. This SE band is approximately matching the broad steady-state emission although it is partially overlapping the **Y_1** absorption band, and thus is likely characterizing the $S_1(E)$ state. The apparent shift of the SE band in the 0.4 – 1.5 ps time range (characteristic time less than 100 fs) is either the result of the concomitant growth of the S_1 absorption band or a real shift reflecting the geometry/solvent cage relaxation, $S_2(FC) \rightarrow S_2(CT)$.
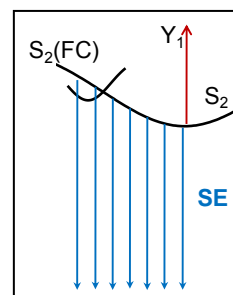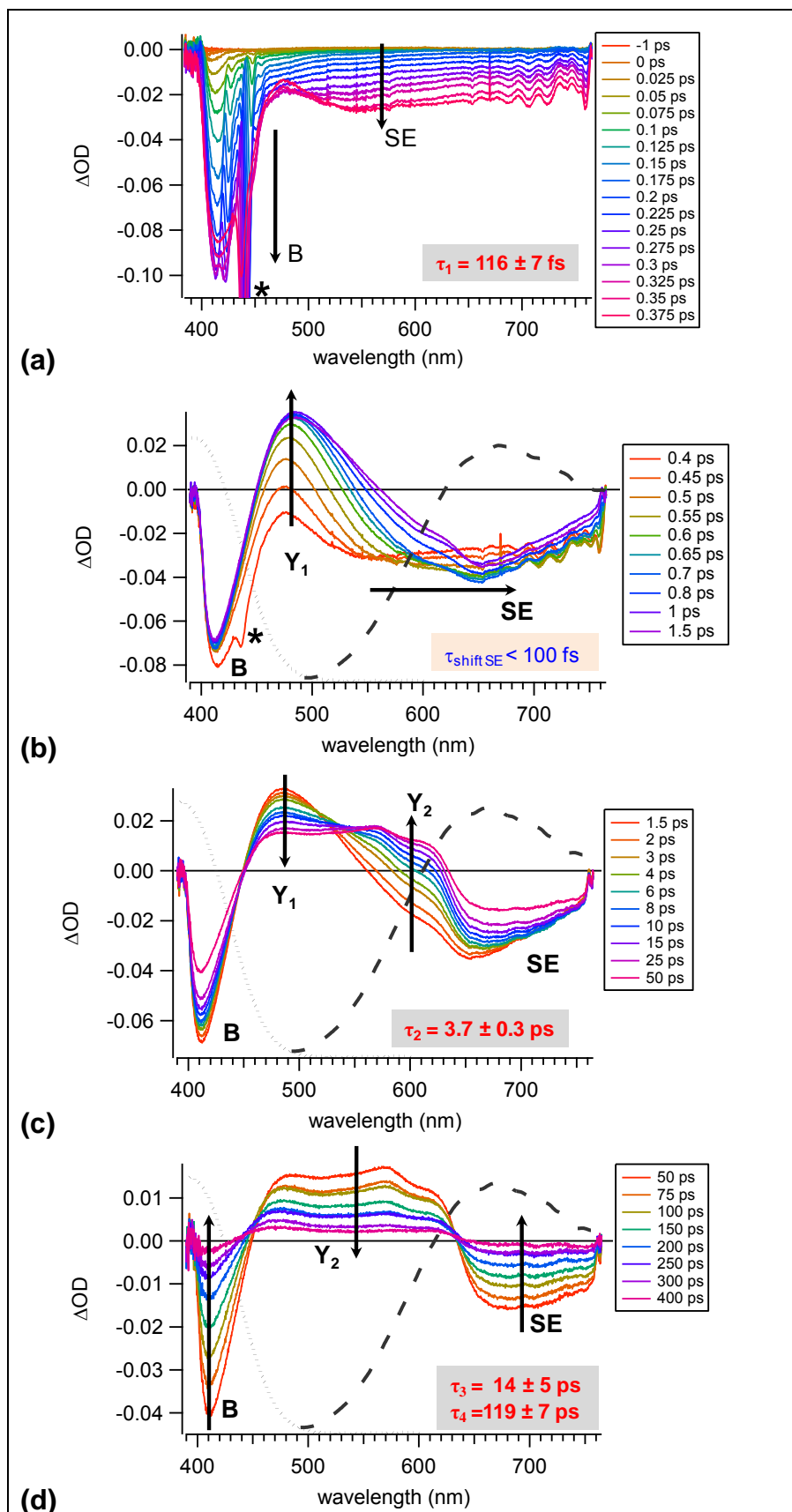
Figure V.3 Femtosecond transient absorption spectral evolution of SBPa in EtOH following 390 nm excitation. Transient data divided into four stages: a) growth of SE, b) growth of excited state absorption and apparent shift of SE, c) ICT evolution and d) decay of all signals. The star indicate stimulated Raman pick of the solvent. Pump-probe correlation time: τ = 190 fs

ICT dynamics. In figure V.3c between 1.5 and 50 ps, one recognizes an ICT dynamics manifestly similar to that measured in ACN in the 0.6 − 1.5 ps range (see figure V.1b), characterized by the decay of band $\mathbf{Y_1}$ concomitantly with the increase of a new band $\mathbf{Y_2}$. The characteristic time for this evolution is notably longer in EtOH (τ_2^{EtOH} = 3.7 ps) than in ACN (τ_2^{ACN} = 0.29 ps). During this process, as in ACN, the **SE** signal in the red region is affected by the increase of the overlapping $\mathbf{Y_2}$ absorption but does not disappear. This observation strongly suggests that the same relaxation scheme as that proposed in ACN arises in EtOH: after population of the $S_2(FC)$ charge transfer configuration, ultrafast internal conversion to the $S_1(E)$ state competes with the ultimate charge transfer steps $S_2(FC) \rightarrow S_2(CT) \rightarrow S_1(CT)$ by which the ICT process is completed.

Post-ICT dynamics. In Figure V.3d the constant decay of all signals is observed within the temporal window [30 − 400 ps], as in ACN (see figure V.1c). Two characteristic times are again found for this decay: τ_3 = 8 ps and τ_4 = 140 ps. They are thus attributed to the decay of the final $S_1(CT)$ and $S_1(E)$ states, respectively.

Apart an effect on characteristic time that will be discuss later, the most striking differences between ACN and EtOH is undeniably the initial dynamics revealed by **SE**. In aprotic case, only $S_1(E)$ gives rise to **SE** signal while this latter is noticed already from the FC region in EtOH. Considering that the efficiency of **SE** signal of any singlet states can be related with the degree of configuration mixing with the emissive singlet state $S_1(E)$, the presence of **SE** signal coming from FC singlet states is interpreted in term of electronic coupling $\hat{V}$ enhanced by solute-solvent hydrogen bonding, with a coupling term proportional to $\langle FC|\hat{V}|S_1(E)\rangle$. This proposition is consistent with a $S_1(E)$ having electronic density localized on imidazole part for which hydrogen bonds have been evidenced by DFT calculations. Indeed, one can expect than hydrogen bonds can stabilize the system for various electronic singlet states

V.2.4   Additional photophysical processes in SBPa

V.2.4.1   Excitation wavelength effect?

In order to investigate the possible existence of additional pump wavelength dependent processes competitive with the ICT reaction, femtosecond transient absorption experiments were made using excitation at 266 nm. From TDDFT results, such UV excitation corresponds to the S_5 state (H $\rightarrow$ L+1 transition, λ_{max} = 290 nm). The transient spectra

between 310 and 680 nm, divided into three time intervals (appearance, transitional evolution, and decay of the signal) – as it was done earlier for SBPa in ACN with excitation wavelength 390 nm – are shown in figure V.4 a – c.
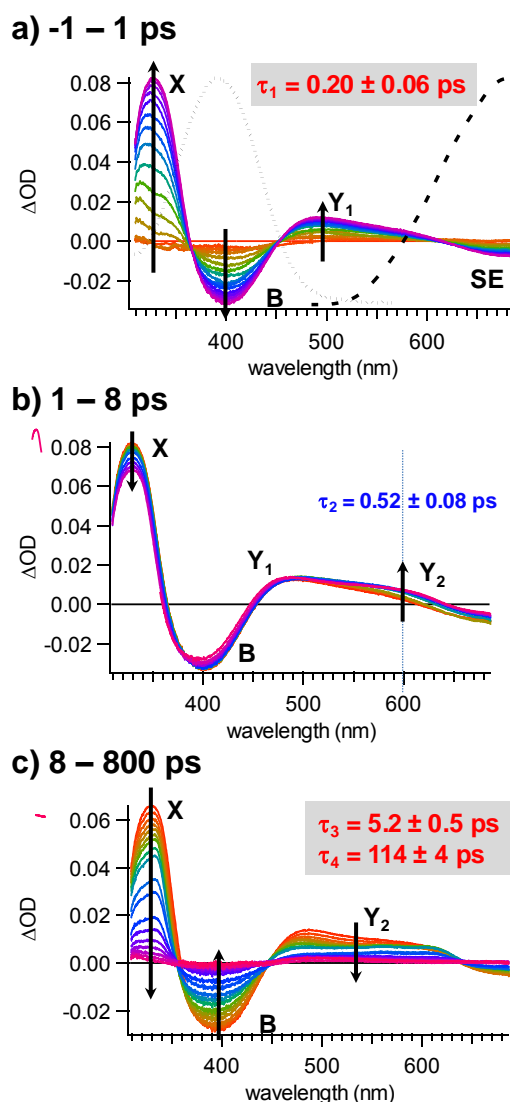
Figure V.4 Spectral evolution of the femtosecond transient absorption signal of SBPa in ACN with excitation wavelength 266 nm, divided into three temporal windows: a) -1 – 1 ps; b) 1 – 8 ps; and c) 8 – 800 ps. Pump-probe correlation time: τ = 270 fs

The first graph (figure V.4a) shows an evolution between -1 and 1 ps with the appearance of three types of bands. As for 390 nm excitation (figure V.1a), one can recognize the negative bleaching band (**B**) between 360 and 450 nm, with maximum at 390 nm – at the same position as the ground state absorption band. The stimulated emission (**SE**) band is also present, at wavelength longer than 610 nm. Within this time interval, one can also recognize the excited state absorption band **Y$_1$** between 360 and 610 nm (λ_{max} ~480 nm). In the blue part of the spectra, between 310 and 360 nm, a new excited state absorption band – named **X** – can be observed with a maximum at 330 nm.

This band was not registered in the 390 nm excitation experiment because the high energy edge of the detection spectral window was set at 400 nm. The characteristic time found for the appearance of all these spectral components is about $\tau_1 = 200$ fs deconvoluted from pump-probe correlation function $\tau = 185$ fs.

In figure V.4b, the growth of the $\mathbf{Y_2}$ excited state absorption band is shown within the temporal window [1 − 8 ps]. During this process no recovery of the ground state is noticed, the bleaching band being stable in intensity. This behaviour is similar to the CT evolution found for the 390 nm excitation experiment (see figure V.1b), however the isosbestic point between $\mathbf{Y_1}$ and $\mathbf{Y_2}$ bands is less clear, probably because stronger band shape distortion by cooling effect arises from the fact that higher excess of vibrational energy is deposited in the molecule at 266 nm compared to 390 nm excitation. Finally, partial decrease in intensity of band $\mathbf{X}$ is noticed.

Finally, the decay of all signals − negative bleaching $\mathbf{B}$ and stimulated emission $\mathbf{SE}$ as well as positive excited state absorption bands $\mathbf{Y_2}$ and $\mathbf{X}$ − occurs between 8 and 800 ps (figure V.4c) with two characteristic times of $\tau_3 = 5.2$ ps and $\tau_4 = 114$ ps, which are very close to those obtained for 390 nm excitation. Comparison of all characteristic times obtained for SBPa in ACN for the two different excitation wavelengths 266 and 390 nm is done in table V.1.

Table V.1 Comparison of the main characteristic times extracted from global analysis of the femtosecond transient absorption data recorded at two different excitation wavelengths: 266 nm and 390 nm.

Excitation wavelength	τ_1 (ps)	τ_2 (ps)	τ_3 (ps)	τ_4 (ps)
266 nm	0.20 ± 0.06	0.52 ± 0.08*	5.2 ± 0.5	114 ± 4
390 nm	0.11 ± 0.03	0.29 ± 0.04	5.0 ± 0.9	128 ± 6

* time constant found with single-exponential fitting of the 600 nm kinetics in the 1 − 8 ps time interval.

The variation of τ_1 from 110 fs at 390 nm to 200 fs at 266 nm can be interpreted by an energy gap law occurring on $S_n − S_2(CT)$ IC. However it parallels also the increase of the experimental time resolution resulting from a larger pump pulse using the laser third harmonic than the second harmonic.

The ICT characteristic time of $\tau_2 = 0.52$ ps (probably overestimated) measured at 266 nm is in the same order of magnitude as the 0.29 ps value found at 390 nm. As noted above, the amplitude of the spectral change related to the $\mathbf{Y_1} \rightarrow \mathbf{Y_2}$ evolution seems weaker at 266 nm than at 390 nm. Beside this difference in apparent efficiency, we can affirm that, from a qualitative point of view, the same evolution of transient absorption spectra was found exciting two different states.

V.2.4.2   Triplet state formation.

In the analysis of the femtosecond transient absorption spectra of SBPa in ACN, it was remarked that a residual low signal was remaining after 500 ps (see figure V.1c). Such long living signal can be due to the formation of a triplet T_1 state [146]. To confirm this hypothesis, a SBPa derivative substituted with two bromine atoms (see chart V.1) was studied with femtosecond transient absorption using a pump excitation at 390 nm. In fact, in such a molecule, it is well-known that a heavy atom effect[15] is expected to notably enhance the quantum yield of triplet state formation via intersystem crossing (ISC).

Chart V.1. Br_2SBPa
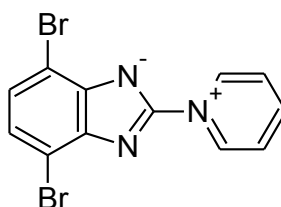
First, stationary absorption and fluorescence spectra were measured (see figure V.5a). The maximum of absorption band is found at 360 nm; fluorescence band maximum is found at 475 nm. The absorption transitions calculated by TDDFT agree quite well with the experimental data. The strongest oscillator strength was found for $S_0 \rightarrow S_2$ transition, as for the SBPa parent molecule.

The molecular orbitals calculated by DFT were also compared with those obtained for SBPa (see figure V.5b). Almost the same representations were found, however additional delocalization of the charge on the attached bromine atoms is noticed for Br_2SBPa. The same molecular orbitals (MO) are involved in the first two electronic transitions: $S_0 \rightarrow S_1$ corresponds to $H \rightarrow L$, while $S_0 \rightarrow S_2$ to $(H-1) \rightarrow L$ transitions. Therefore, it is reasonable to presume that the photophysics of SBPa and Br_2SBPa are comparable.

To detect the possible creation of triplet state in Br_2SBPa, a first femtosecond transient absorption experiment with 390 nm excitation was done (figure V.6). Within the temporal window of [0.8 – 500 ps], the evolution from a broad positive band centred near 480 nm to

---

[15] **Heavy atom effect** – the enhancement of a spin-forbidden process by the presence of an atom of high atomic number, which is either part of, or external to, the excited molecular entity. (IUPAC compendium of Chemical Terminology, 2nd edition, 2007. http://www.iupac.org/goldbook/H02756.pdf)

a new band with maximum near 450 nm can be observed with a characteristic time of $\tau_T =$ 31 ps. The final band, abbreviated as band T, is stable between 200 and 500 ps.
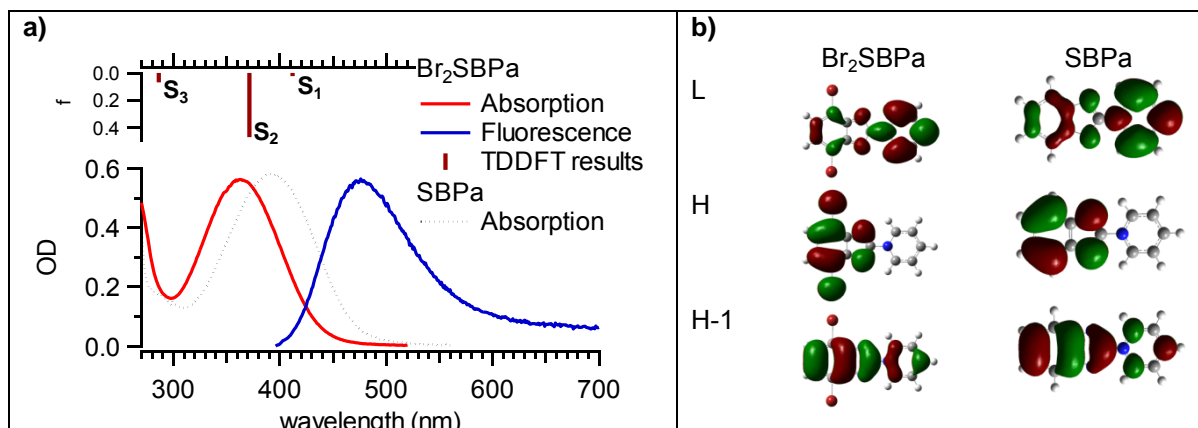
Figure. V.5 a) Stationary absorption and fluorescence spectra (solid lines) of Br_2SBPa in ACN as well as TDDFT transitions (sticks). The stationary absorption spectrum of SBPa in ACN is added for comparison (dashed line), b) Comparison of molecular orbitals (MOs) calculated using DFT with 6-311++g(d,p) basis and PBE0 functional for the Br_2SBPa and SBPa molecules.

To learn more about this state, Br_2SBPa molecule was then studied with nanosecond flash photolysis. The data (figure V.7) show essentially the decay of band **T**. It is monoexponential with a time constant of $\tau = 1.43$ µs in degassed ACN. Strong quenching by oxygen is observed (figure V.7b), which provides clear evidence for the assignment of the T band to the lowest triplet state T_1.
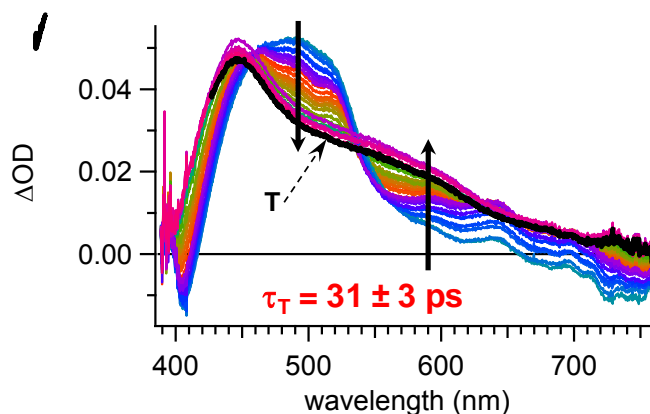
Figure V.6 Femtosecond transient absorption spectra of Br_2SBPa in ACN within the temporal window [0.8 – 500 ps] (the thick black line shows the final signal).

In figure V.6 the residual signal observed at the end of the femtosecond transient absorption evolution of Br_2SBPa (shown with thick black line) is compared with that obtained for SBPa (see figure V.8). As one can see, the maxima of excited state absorptions are not exactly at the same position because the bleaching band is red-shifted in SBPa compared to that in Br_2SBPa (see figure IV.6a) and can affect more deeply the

absorption band. However the general shapes of both signals are very similar and, by analogy with Br_2SBPa, we ascribe with certainty the residual spectrum observed at 500 ps for SBPa in ACN to the triplet T_1 state.
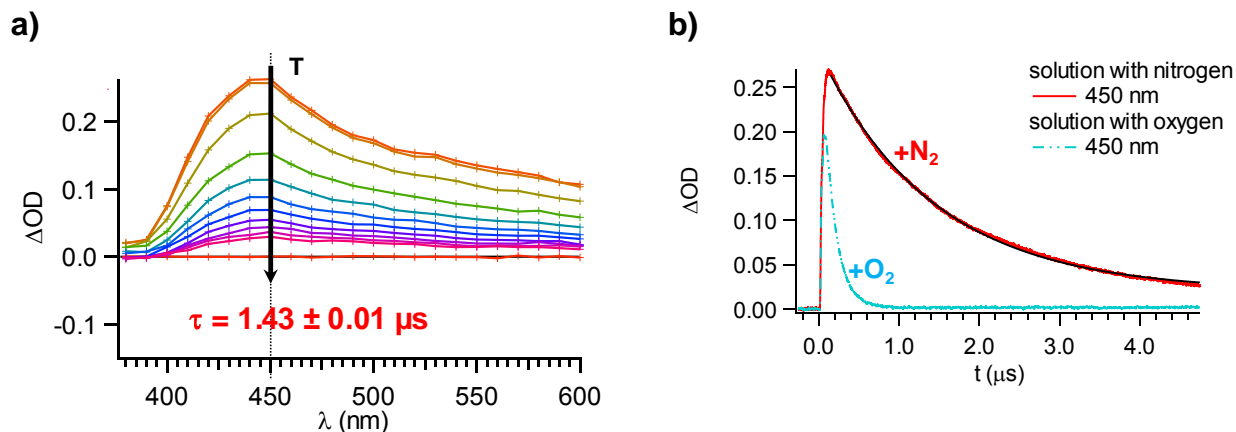
Figure **V.7** Nanosecond flash photolysis results for Br_2SBPa in ACN after 355 nm excitation a) 0-5 µs spectral evolution; b) decay kinetics measured at 450 nm for O_2 saturated and N_2 saturated solutions.

One more question concerns the identity of the singlet state which is the precursor of the triplet state. Two hypotheses can be considered, as two excited singlet states contribute to the final evolution of transient signal of SBPa:

- The $S_1(CT)$ state characterized by a decay time constant of $\tau_3 = 5$ ps

- The emissive $S_1(E)$ state characterized by a decay time constant of $\tau_4 = 128$ ps
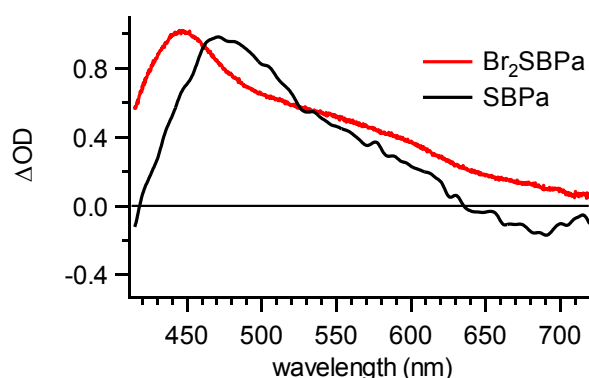
Figure V.8 Comparison of residual transient absorption spectra observed at times longer than 500 ps for SBPa and Br_2SBPa in ACN.

Since the heavy atom effect is expected to favour the ISC process, the triplet state formation is likely occurring with higher rate constant in SPBa than in Br_2SBPa. Therefore

a characteristic time higher than $\tau_T = 31$ ps can be assumed for the appearance time of T_1 in SPBa, which suggests strongly that the precursor of T_1 must be the $S_1(E)$ state.

In summary, it has been confirmed that the long-lived excited state absorption band T in the Br_2SBPa molecule characterizes the triplet state, as demonstrated by an undeniable oxygen quenching effect. By analogy, the similar 500 ps spectrum observed for SBPa is also assigned to the triplet state that arises probably from the $S_1(E)$ state.

V.2.5 Multivariate analysis of transient data: toward more mechanistic details.

At this point of the manuscript, we have already performed a quite good determination of the photophysical scheme of SBPa based partially on a global analysis of transient data. However, in our group laboratory, we have demonstrated since 2007 that combining advanced chemometrics tools and good noise/signal ratio transient data can allow for the characterization of transient species with minor spectral intensity or for unravelling different species with strong temporal and/or spectral overlap [63, 64, 147] The two approaches tentatively applied here (**MCR-ALS** and **HS-MCR)** are presented with all details in chapter II. They have been applied to the SBPa transient data in ACN (figure V.1) in order to confirm and eventually complete the previous findings obtained in this chapter. A 3D representation of these data is presented in figure V.10a.

The kinetic matrix (**D**) consists in 1340 wavelength values while the temporal window begins from 0.2 ps in order to reduce the GVD effect. Note that Raman stimulated picks have been removed previously to the treatment. The **MCR-ALS** procedure has been restricted to 4 transient components as suggested by the SVD decomposition [148]. Non-negativity and unimodality of the time-dependent concentration profiles were the two constraints applied during the MCR-ALS procedure. The four concentration profiles (**C**) labelled as **A,B,C**, and **D** and the corresponding pure component spectra (S^T) are displayed in figure V.10b and V.10c, respectively.
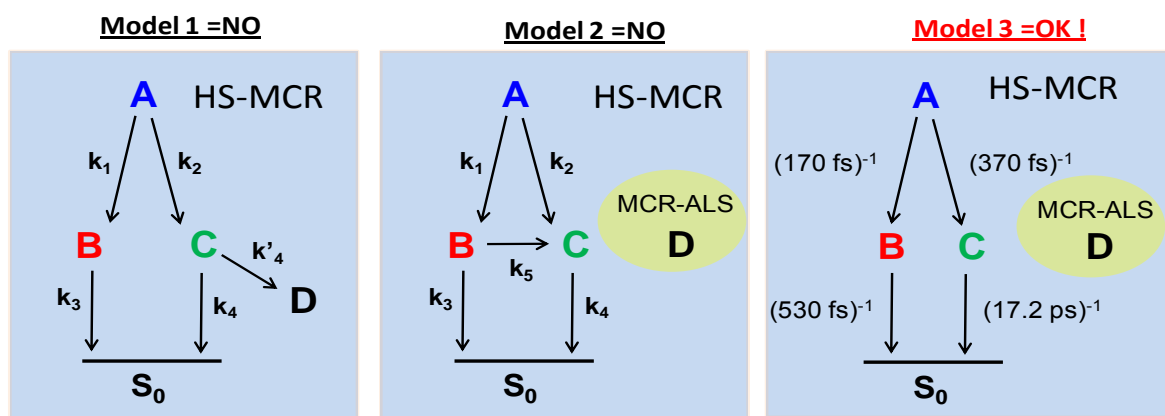
Figure V.9: the 3 models implemented on HS-MCR procedure.

The **HS-MCR** procedure allows implementation of kinetic models as constraints applied on the time-dependent concentration profiles during the ALS procedure. Different kinetic models were tested (Fig V.9). Unfortunately, none of the models including all the 4 components (see for instance model 1 in Fig V.9) provided reliable results (in practice, divergence of the fitting procedure occurs). This is a typical situation where we may benefit from the main advantage of the proposed HS-MCR procedure compared to the more classical global fitting procedure. In HS-MCR, some of the species can be described by kinetic (hard-model) constraints while others are kept outside of the kinetic model (only non-negativity and unimodality constraints are applied for these species see e.g. models 2 and 3). In this way, partial kinetic description of some events can still be obtained even in cases where the full kinetic description of all the processes is not possible. The results obtained for the kinetic profiles and associated transient spectra are indicated figures V.10d and V.10e, respectively. One can compare the HS-MCR results with previous findings and correlate the A and B components with bands Y_1 and Y_2 (on figure IV.1) due to the $S_2(CT)$ and $S_1(CT)$ states, respectively. The C component is rather related with $S_1(E)$ state as the **SE** is predominant compared to the bleaching band. The last D component is probably a linear combination of the triplet species and its precursor. We will discard this species contribution and focus on the remaining processes. The A $\rightarrow$ B process is clearly recognized has the ICT final process, with similar characteristic times found by HS-MCR (170 fs) and global fitting (240 fs). In addition, this result emphasizes for the possibility to produce the $S_1(E)$ state from $S_2(CT)$, i.e. a competitive channel with non negligible $(370\,\mathrm{fs})^{-1}$ rate. The IC from the $S_1(CT)$ state to the ground state is surprisingly fast, $(570\,\mathrm{fs})^{-1}$ opens the question for alternative decay channels via $S_1(E)$ states. Finally, the decay of $S_1(E)$ in this model neglects ISC to the triplet species in such a way that the rate

of (17.2 ps)$^{-1}$ can be considered has an estimation for the rates of the other processes (IC and fluorescence).

So, although encouraging **MCR-ALS** results have been obtained allowing exploring individual photophysical processes rather than deactivation of electronic state, in the future, more elaborated models have to be tested. A challenging model would be based on a two-channel reaction producing A/S$_2$(CT) and C/S$_1$(E) via a "transparent" precursor state, i.e. implemented on the procedure with a zero spectra as constraints.
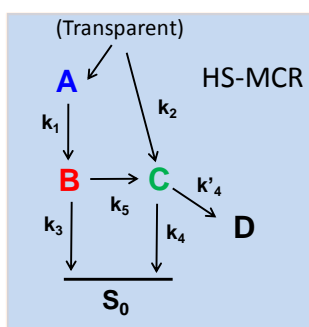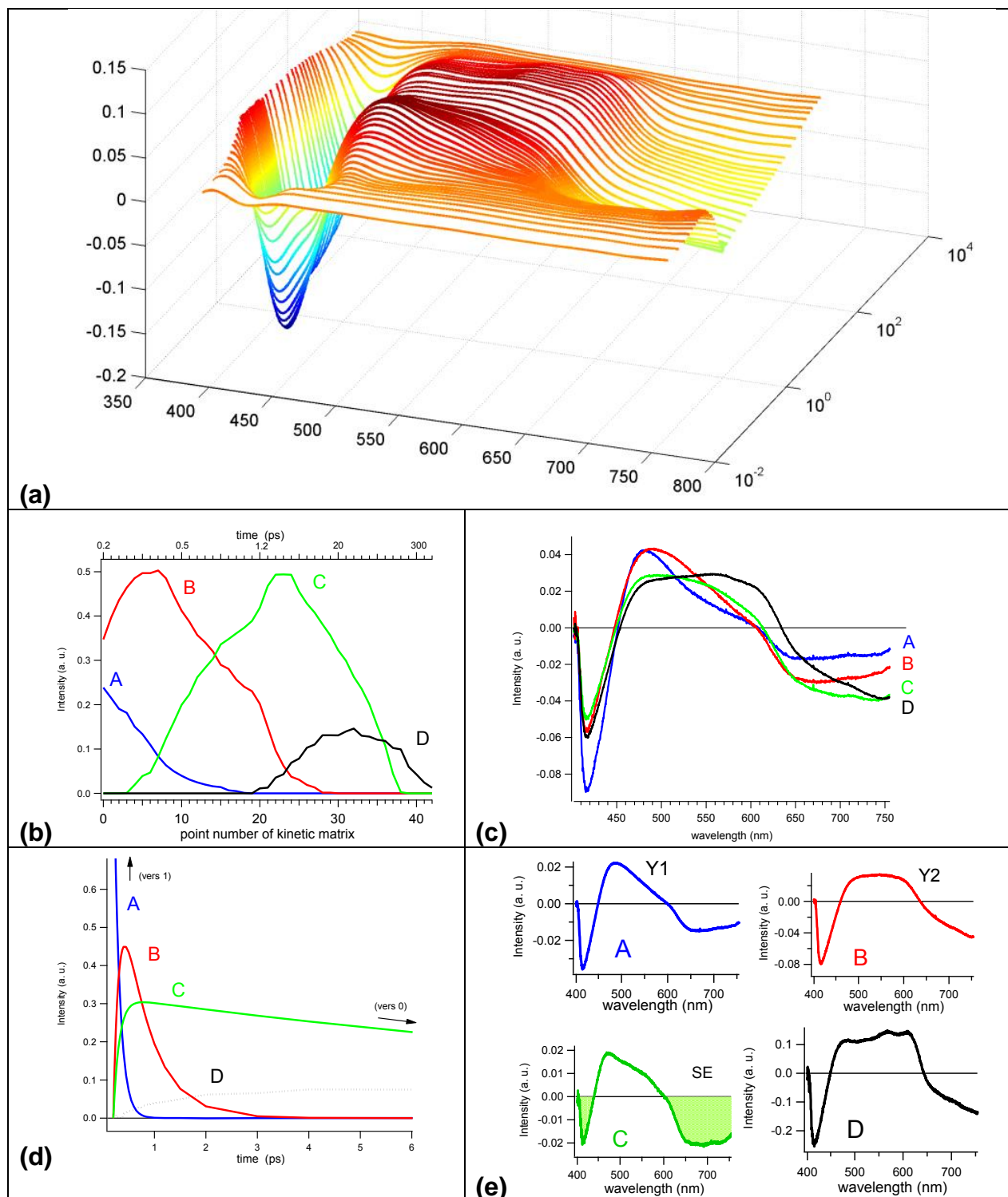
Figure V.10 3D representation of transient spectra for SBPa/ACN for 390 nm excitation (similar data as in Figure V.1) in the [0.2-500 ps] time window (a). **MCR-ALS** resolution of transient data: time-dependent concentration profiles A, B, C, and D obtained under non-negativity and unimodality constraints (b) and the corresponding transient spectra (c). **HS-MCR** resolution of transient data: time dependent concentration profiles obtained under hard-modeling kinetic constraint for A, B, C (see text) and non-negativity and unimodality constraints for D (d) and the corresponding transient spectra (e).

V.2.6   The overall photophysical scheme of SBPa.
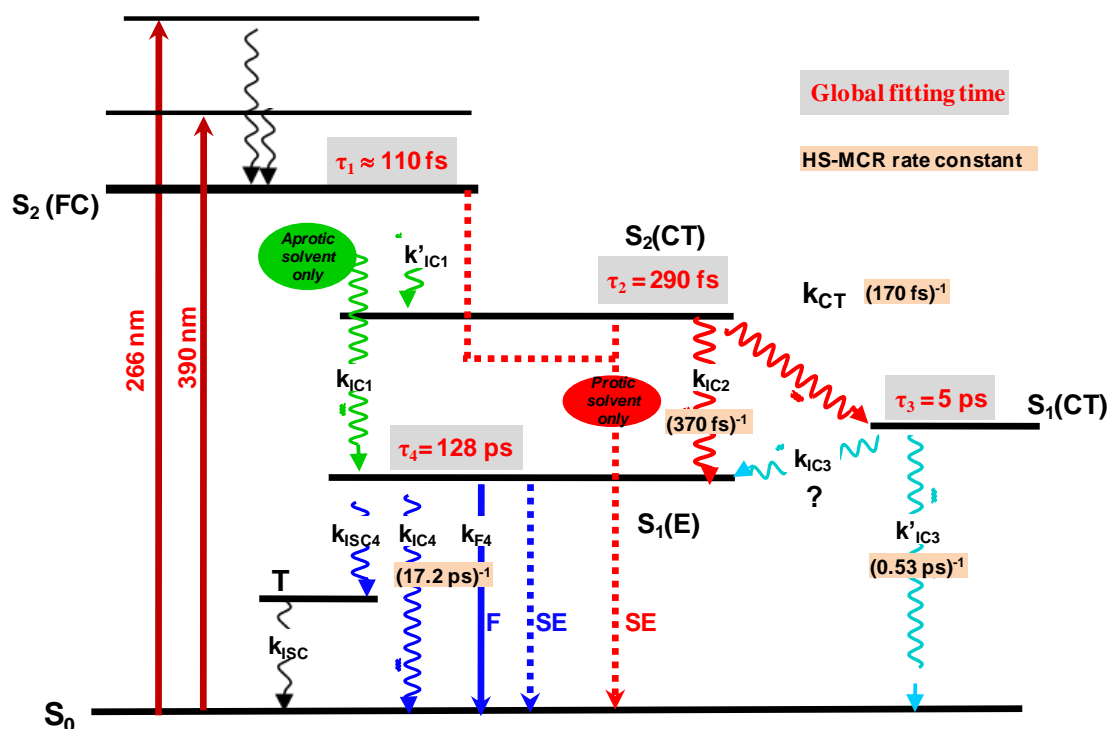
Figure **V.11** The photophysical scheme of SBPa molecule. The characteristic times are those obtained for ACN solvant.

A comprehensive picture of the SBPa photophysics has been derived along this chapter and the overall results are summarized in the qualitative Jabłoński diagram in figure V.11. First, it has been found that both excitations within the solvatochromic CT absorption band or well above this band lead to the population of the former reactive CT state in the FC region, the $S_2(FC)$. Unexpectedly, only in aprotic solvent, ultrafast IC to the emissive $S_1(E)$ state occurs probably faster than the 110 fs. So, an efficient conical intersection S_2/S_1 can be suggested. Reversely, protic solvent seems to quench this conical intersection channel while the SE from $S_1(E)$ state is supplemented by an ultrafast red shifting **SE** suggesting an ultrafast evolution along $S_2(FC)$ potential surface. It has been suggested an electronic coupling via solute-solvent hydrogen bonding between FC and emissive state.

In parallel, an ultrafast IC accounts for the population of $S_2(CT)$ from the FC region with a rate below $(110\,fs)^{-1}$. The final stage of the ICT reaction then proceeds that consists actually in an non-adiabatic transition between $S_2(CT)$ and $S_1(CT)$ with an ultrafast characteristic time ranging from 170 fs to 300 fs according to the HS-MCR and global fitting treatments, respectively. As seen with EtOH case, this time is sensitive to the solvent nature but this point will be studied hereafter. Note that this reaction scheme has

therefore some common points with that proposed by Zachariasse et al. for DMABN derivatives, which first correlate the occurrence of ICT process with the energy gap between S_2 and S_1 states [74, 149-151].

The deactivation pathways of $S_1(E)$ seems to be well understood as occurring mainly by emission and probably internal conversion. (The overall rate for both processes can be proposed with **HS-MCR** results). Additionally, it has been demonstrated that minor ISC process originates rather from $S_1(E)$ than $S_1(CT)$. Concerning the decay of $S_1(CT)$, the lack of emission together with a probable fast IC to the ground state (back electron transfer) account for its short lifetime.

If the photophysical scheme of SBPa is now quite well rationalized, further crucial points remain unexplained. Indeed, focusing on the ICT process itself, it is desired to identify the actual reaction coordinate that is involved in this ultrafast S_2/S_1 IC. So, is this last ICT step controlled by the solvent dynamics, as for the bianthryl molecule [99], by geometrical changes as for TICT compounds [37], or by both solvent and intramolecular changes as in the Sumi-Marcus theory? Similar questions can be address also for the back electron transfer decay processes.

In the following, we will perform a quite exhaustive femtosecond absorption study of the SBPa photophysics in a series of solvents of varying polarity and viscosity. Finally, concerning the question whether a large amplitude twist of the geometry arises during the ICT process in SBPa, we have investigated a substituted molecule in which a distorted "pre-twisted" conformation is imposed.

V.3 Dependence of the SBPa photophysical processes on the solvent properties.

V.3.1   Introduction

In the previous subsections, a detailed analysis of the femtosecond transient absorption spectra of SBPa in ACN and Ethanol was carried out. A hypothetical photophysical scheme was proposed (see figure V.11), including characteristic times for the different transition steps. Within this subsection, a comparison of the femtosecond transient absorption experimental spectra of SBPa in numerous solvents of different polarities and viscosities will be done. All the results are put together in table V.2. The main purpose are: i) to check if the proposed photophysical scheme is consistent with the observed solvent effects; ii) to understand the role played by the solvent in the CT dynamics and decay processes; iii) to track possible photoinduced changes of molecular geometry.

The role of the solvent reorganization which accompanies the formation of polar species in polar environment was introduced in 80's [96]. The best known example proving that charge transfer kinetics can be controlled by the dynamics of the solvent is related to the bianthryl molecule. Years of study of the photophysics of this molecule have shown that in polar solvents the characteristic time of the photoinduced CT process is proportional to the time of solvent reorganization (explained in more details later in chapter III) [152]. Processes limited by solvation are barrierless and can be described with only one reaction coordinate: the solvation.

However, not all ICT processes are solvent controlled. When the charge transfer process is combined with an intramolecular reorganization of the solute, like for example in the case of the formation of a twisted intramolecular charge transfer (TICT) state, the theories describing the process have to take into account two different reaction coordinates related to the solvation and intramolecular change, respectively. Sumi-Marcus and other, more recent, models show that the CT process does not have to be limited by the solvation time [94]. Nevertheless, other solvent properties, than solvation, can influence the CT process. If the reaction is accompanied by large amplitude geometrical changes of the molecule, such as an intramolecular twist between two parts of the molecule, it should be reflected by some solvent viscosity dependence of the characteristic time [37], as all movements of the solute are sensitive to frictions with the environment (solvent). Such dependency was

found for DMABN molecule and was considered as a confirmation for the existence of a TICT process in this molecule [135, 153, 154].

The influence of the different solvent effects on the ICT process is intricate because they can appear simultaneously and are interdependent. Within this part, the detailed analysis of the influence of different solvent parameters on the SBPa CT mechanism and characteristic times given in table V.2 will be presented.

V.3.2 Solvent influence on the ICT dynamics (τ_2) of SBPa

For all tested solvents the same type of femtosecond transient signals as those presented for the ACN representative case (section V.2.1) were found. In table V.2 are plotted the characteristic times obtained by fitting the kinetics with the global fitting method using the GVD correction function (equation II.19). The same four characteristic times are thus tabulated: τ_1 for appearance of the early transient signals, τ_2 for ICT process, τ_3 and τ_4 for the decay of S_1(CT) and S_1(E) respectively.

Table V.2. SBPa characteristic times (in ps) for: initial dynamics (τ_1), CT dynamics (τ_2) and Post-CT dynamics (τ_3 and τ_4), for different solvents, obtained from femtosecond transient absorption using 390 nm excitation wavelength. All time constants are obtained global fitting method using the GVD modified gaussian pump-probe correlation function (eq. II.19). Additionally, some characteristic solvent parameters are given: dielectric constant ε, viscosity η, and average solvation time <τ>$_{solv}$.

Solvent	ε^a	η (cP)	$<\tau>_{solv}^b$ (ps)	τ_1 (ps)	τ_2 (ps)	τ_3 (ps)	τ_4 (ps)
ACN	35.9	0.345	0.27	0.106±0.008	0.29±0.04	5.0±0.9	128±6
Butyronitrile	24.8	0.542	0.54	0.074±0.002	1.2±0.2	22±8	146±20
Octanenitrile	13.6	1.525	3.94	0.150±0.020	4.0±0.5	25±10	172±10
Decanenitrile	10.6	2.676	-		11±4^c	-	200±10^c
THF	7.58	0.575	0.94	0.170±0.050	0.4±0.1	2.6±0.3	134±8
Methyl Acetate	6.68	0.364	0.61	0.100±0.007	1.0±0.1	9±4	145±10
Ethyl Acetate	6.02	0.426	0.86	0.100±0.020	1.2±0.4	12±8	130±20
Methanol	32.7	0.593	5	0.120±0.090	0.3±0.1	3.4±0.4	109±10
TFE^c	26.1	1.995	-	0.140±0.020	1.7±0.4	8±2	140±30
Ethanol	24.6	1.2	16	0.116±0.007	3.7±0.3	14±5	119±7
2-Butanol	16.6	3.632	63	0.120±0.050	12±4	40±20	250±40
2-Pentanol	13.7	5.307	103	0.140±0.020	19±2		260±30

^{a} ref [98]; ^{b} determined from femtosecond transient absorption data for C153 (see appendix C). ^{c} due to the bad signal quality, fitted with single-exponential functions within suitable regions.

Time τ_1 corresponds to the ultrafast decay of S_2(FC) state but its determination after deconvolution is probably affected by the proximity with temporal resolution. As a confirmation, one notes in table V.2 that the value of time τ_1 is nearly insensitive to the solvent nature. In the following, we thus restrict the discussion of the solvent effects to the three other time constants, τ_2, τ_3, and τ_4. The influence of the different solvent properties,

the solvation time, polarity and viscosity, are interconnected in such a way that it can be difficult to differentiate their specific contribution to the solvent effect. The scheme given in figure V.12 helps to clarify this multiparameter problem. Indeed, we have seen that k_{CT} can depend on the solvation dynamics (bianthryl case) and on the solvent viscosity according to Kramers related theories. But the solvation dynamics itself depend on the diffusion of solvent molecules. Additionally, dependence with polarity is well introduced through the Marcus theory (see chapter III, equations III.11 and III.15).
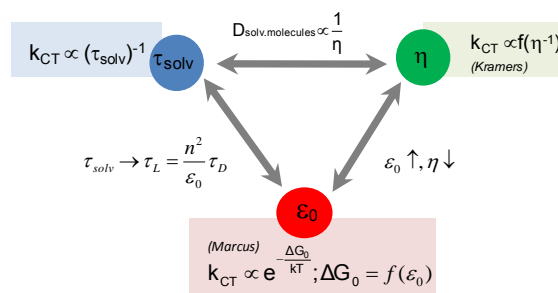
Figure V.12 Scheme illustrating the dependence of the different solvent parameters.

By definition, the value of the solvent polarity is included in the expression of the relaxation time which is a superior limit for $\langle \tau \rangle_{solv}$. However, an empirical relation indicates that, for a given family of solvents, the viscosity and polarity are roughly inversely proportional. For example, as illustrated in figure V.13 for SBPa in nitrile solvents, the same CT process is clearly observed in ACN and butyronitrile, with its characteristic isosbestic point, but the reaction rate is four times slower in the second case. Is this variation due to the much higher viscosity of BuCN compared to ACN, or to its lower polarity, or both?

In the following, we analyze in detail the dependency of the solvation time, polarity, and viscosity on the CT dynamics in SBPa. According to the results of chapter IV, a distinction between aprotic and protic solvent has to be made.
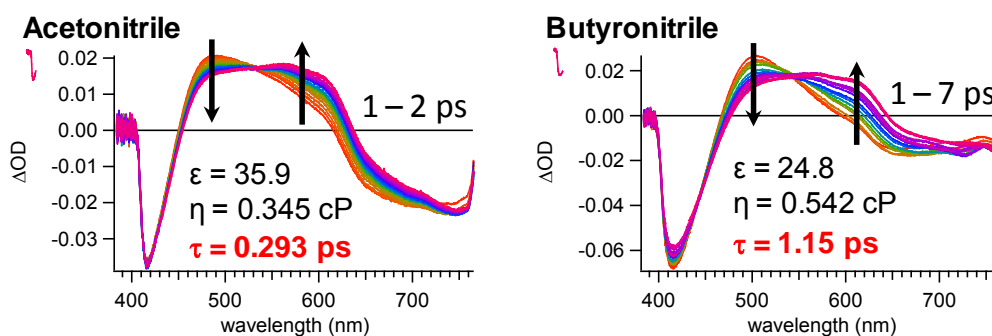
Figure V.13 Comparison of the final CT spectral evolution and characteristic times of SBPa in two solvents of different polarity and viscosity – ACN and butyronitrile.

Solvation time. First the dependency of τ_2 on the solvation time $\langle\tau\rangle_{solv}$ will be studied. Plots of τ_2 as a function of the solvation time for the aprotic and protic solvents are presented in parts a and b, respectively, of figure V.14, together with their linear correlation. For aprotic solvents, one can immediately notice a slope close to 1 with a small value at origin. In fact, as seen in Table IV.2, the τ_2 values match satisfactorily the solvent $\langle\tau\rangle_{solv}$ values. These observations indicate unambiguously that, for aprotic solvents, the CT process described by time τ_2 is controlled by the solvation dynamics as it is the case for bianthryl [99]. From a Marcus-Sumi picture, it means that the solvent reorganization energy λ_0 is higher than the intramolecular reorganization energy λ_i [93-95].
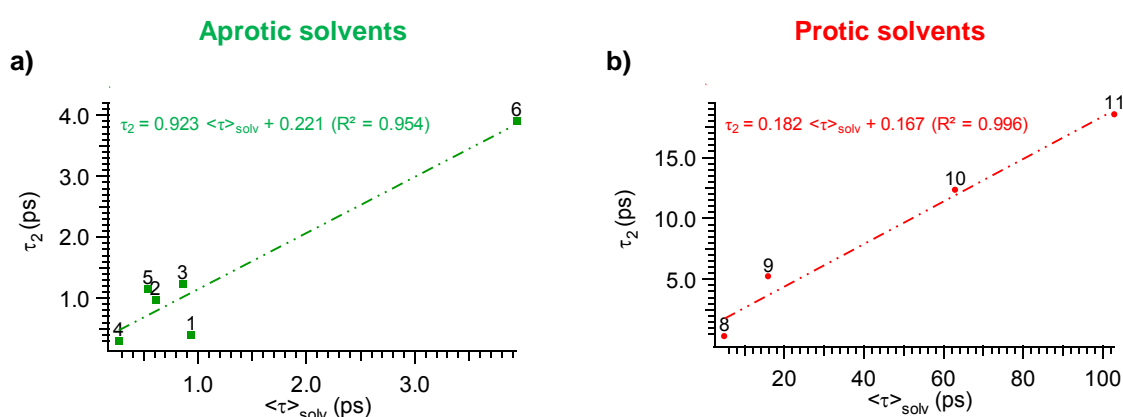
Figure V.14 Plots of the CT time constant τ_2 as a function of the average solvation time $\langle\tau\rangle_{solv}$ and best linear fits (dashed lines) for a) aprotic and b) protic solvents. (1 – THF, 2 – methyl acetate; 3 – ethyl acetate, 4 – ACN, 5 – butyronitrile, 6 – octanenitrile, 7 – decanenitrile, 8 – methanol, 9 – ethanol, 10 – 2-butanol, 11 – 2-pentanol).

On the other hand, for protic solvents, τ_2 is always smaller than $\langle\tau\rangle_{solv}$. The linear correlation is excellent ($R^2 = 0.996$) with a slope much smaller than 1, which suggests that the electrostatic solvation dynamics is clearly not the only parameter governing the CT process and hydrogen bonds are likely playing a special role in this case. Probably the intramolecular reorganization energy has a much higher value than the solvent reorganization energy, i.e. $\lambda_0 < \lambda_i$, in protic solvents. This result can be rationalized if one takes into account the fact that the hydrogen bonds network of protic solvents cannot reorganize so easily compared to aprotic solvents. Note that similar results have been reported by Varne et al concerning the charge transfer process in 1-(N,N-dimethylamino)-fluoren-9-one (1DMAF) [155].

In summary, the solvent reorganization dynamics around SBPa has significant influence on the final step of the ICT process, as evidenced by a clear dependence of τ_2 on the solvation time $\langle\tau\rangle_{solv}$ in both protic and aprotic solvents. However in aprotic solvent, the

CT dynamics seem to be solvent controlled ($\lambda_0 > \lambda_i$) as the order of magnitude of τ_2 and $\langle\tau\rangle_{solv}$ is the same. In protic solvents, the CT process is much faster than the solvent dynamics due to a higher contribution from intramolecular solute reorganization ($\lambda_0 < \lambda_i$).

Polarity. In figure V.15, the plot of τ_2 as a function of the dielectric constant (ε) for both protic and aprotic solvents is presented. At first glance, it is possible to find an excellent correlation for protic or alkylnitrile group. However, this apparent correlation is likely related to a viscosity change. Indeed, as indicated by the blue region in figure V.15, if the more viscous solvents ($\eta > 0.6$ cP) are excluded from this investigation, the dependency of the CT time constant on the polarity becomes very weak (slope = -0.017). We do not have a set of isoviscous solvents allowing to investigate the real effect of polarity for each group of solvent. However, by comparing protic and aprotic solvents, we observe a lack of polarity effect for the almost isoviscous THF/MeOH couple while a drastic viscosity effect is found for the isopolar decanitrile/2-pentanol couple. So, one concludes definitively for an unexpected non dependency of CT rate with the solvent polarity.

Reversely, considering the less polar aprotic solvents, the CT time seems to be correlated to ε rather than viscosity (compare ACN and MeAc for example). However, we discussed in chapter IV that dimerization of SBPa molecules can occur and may compete with ICT process leading to a decrease of CT rate. We will discuss this effect later.
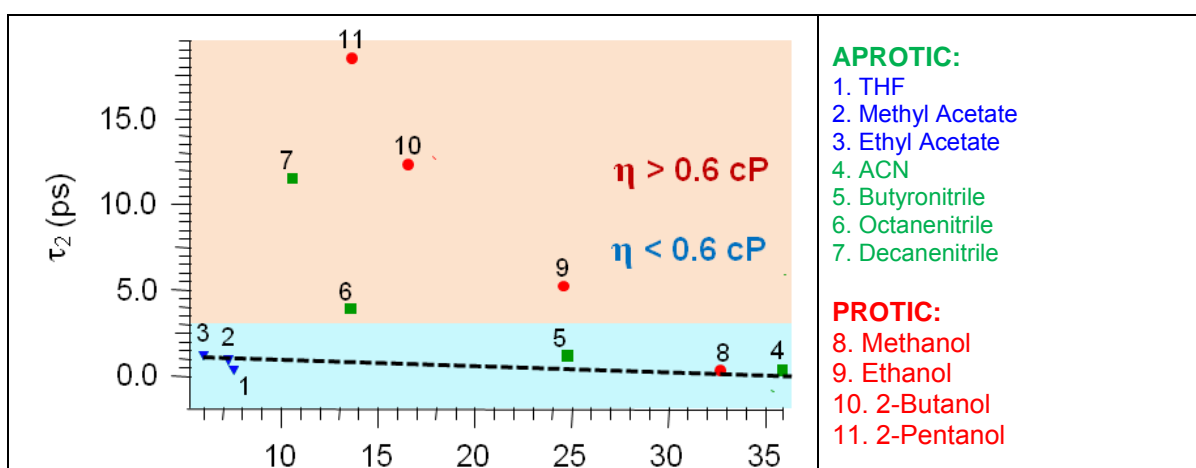
Figure V.15 Plot of the CT time constant τ_2 as a function of the dielectric constant (ε). The blue and red areas refer to solvents of viscosity below and beyond 0.6 cP, respectively.

To better understand why the CT kinetics ($1/\tau_2$) shows no dependency on solvent polarity, at least for moderate or high polar solvent, one can refer to the semi-classic Marcus theory [94] (described in more details in subsection III.2.2.3). In this approach, the

charge transfer rate shows no (or small) dependency on changes of solvent polarity in the inversed Marcus region, while the rate increases with increasing solvent polarity in the normal region. Thus, we suggest that the CT process in SBPa is more likely located in the Marcus inverted region.

To confirm this hypothesis, we plot in figure V.16 the logarithmic value of k_{CT}, approximated as $1/\tau_2$, as a function of the ΔG_0 values (Gibb Free Energy, see figure III.5) determined from the band shape analysis of the stationary absorption spectra in subsection IV.3.2 in the chapter IV. Immediately, one notes an excellent linear correlation for protic ($R^2 = 0.885$) and alkylnitrile groups ($R^2 = 0.999$). The slopes observed for these two groups of solvents are negative, which provides strong evidence that the ICT process of SBPa occurs in the Marcus inverted region. Note that this result is very important because only few examples of confirmed Marcus inverted region has been so far found in the literature [156, 157]. Furthermore, it means that the CT reaction is non-adiabatic process. One has to remember that band shape analysis is a controversial approach and, in order to further confirm results from the above analysis, the complementary electrochemical measurements in different solvents should be done in the future.
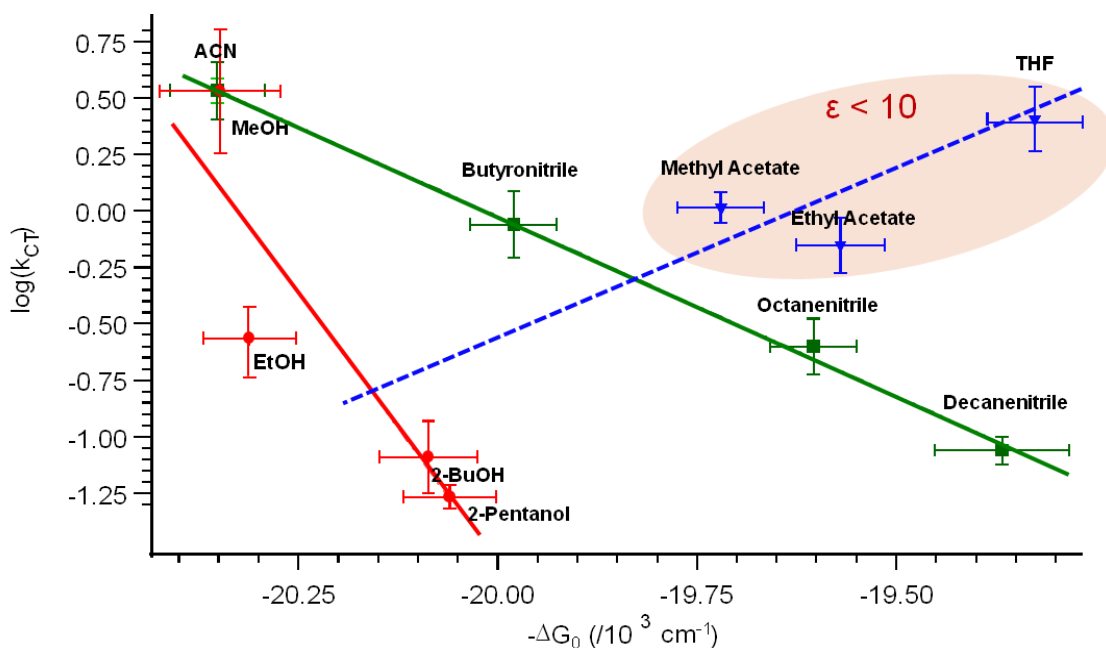
Figure **V.**16 Logarithm plot of the CT constant rate (k_{CT}~$1/\tau_2$ evaluated from transient absorption data) as a function of the Gibbs free energy ($-\Delta G_0$) deduced from bond shape analysis in chapter IV

At the opposite, the case of nonpolar aprotic solvents is different because a positive slope is found. A first explanation is based on the probable dimerization of SBPa in these

solvents that may affect both the k_{CT} and ΔG_0 values. However, the proportion of dimers (not detectable in absorption) is expected to not exceed few percents of the total population and thus cannot account totally for this result. Another explanation within the Marcus approach is to consider that the system corresponds to the normal region for sufficiently low polar solvents. It would imply a progressive switch from inverted to normal region by decreasing the polarity of the medium.

Viscosity. We already evoked the existence of a clear solvent viscosity dependency of k_{CT}. This is well apparent in figure V.17 a and b (logarithmic representations) for aprotic and protic solvents, respectively, which shows good linear correlation between the CT rate constant $1/\tau_2$ and η. At first glance, this suggests that the CT process can be related with some kind of large amplitude geometrical changes like internal torsion by analogy with the TICT transformation found in DMABN [153]. However, as already concluded from the nice correlation between τ_2 and the solvation time $\langle\tau\rangle_{solv}$, the CT process is most likely solvent controlled, at least in aprotic solvents. Two hypotheses then arise with regard to the observed dependency on viscosity:

- The viscosity sensitivity is only a secondary effect of the solvation time dependency since $\langle\tau\rangle_{solv} \propto D \propto 1/\eta$

- The viscosity sensitivity reflects a large amplitude geometrical change induced by the charge transfer in the molecule [153, 158]

To answer this question, different theoretical models of viscosity will be tested.

Application of the power law [100, 159], described earlier in the theoretical background subsection, did not succeed as expected. The values obtained for the α parameter (slope of the dependence of $\log(k_{CT})$ as a function of $\log(\eta)$ fitting function) are always higher than 1 ($\alpha = 1.45$ for aprotic solvents and 1.71 for protic solvents). Such high α values most probably do not only reflect friction effects but also the decrease of polarity that accompanies the increase of viscosity. A reliable determination of α would require a series of solvents with same polarity but different viscosities [160].

However, an alternative approach to the power law has been developed by Hara et al. for the study on 4,4'-diaminodiphenyl sulfone [161]. In this approach, the molecule was investigated by measuring the picosecond fluorescence lifetime as a function of the pressure in three linear alcohol solvents to verify the formation of TICT excited state. They

presented a model similar to that proposed by Marcus and Sumi, assuming the involvement of two reaction coordinates, one for the solvent relaxation and the other one for the nuclear motions. In the "low viscosity regime", where the solvent relaxation time is much faster than the intrinsic nuclear motion ($k_{CT} << \tau_L^{-1}$), the orientation of the solvent dipoles is fast enough to follow the changes of the charge distribution in the solute during the CT process. Conversely, in the "high viscosity regime" ($k_{CT} >> \tau_L^{-1}$), the orientation of the solvent dipoles does not change before the reaction is completed. In the intermediate solvent regime, $k_{CT} = f(\tau_L^{-1})$ and the CT process is purely solvent controlled. In order to describe the whole viscosity dependence of k_{CT}, the following formula can be used:

$$k_{CT} = \frac{C_1}{\eta} + \frac{C_2}{\eta^\alpha} \qquad\qquad (IV.1)$$

where C_1 and C_2 are viscosity independent constants. The first term indicates the viscosity dependence along the solvent coordinate (solvent relaxation) and the second term the dependence along the nuclear coordinate. The viscosity dependence is likely to saturate with increasing η, approaching a limiting value of $\alpha = 0.2$.
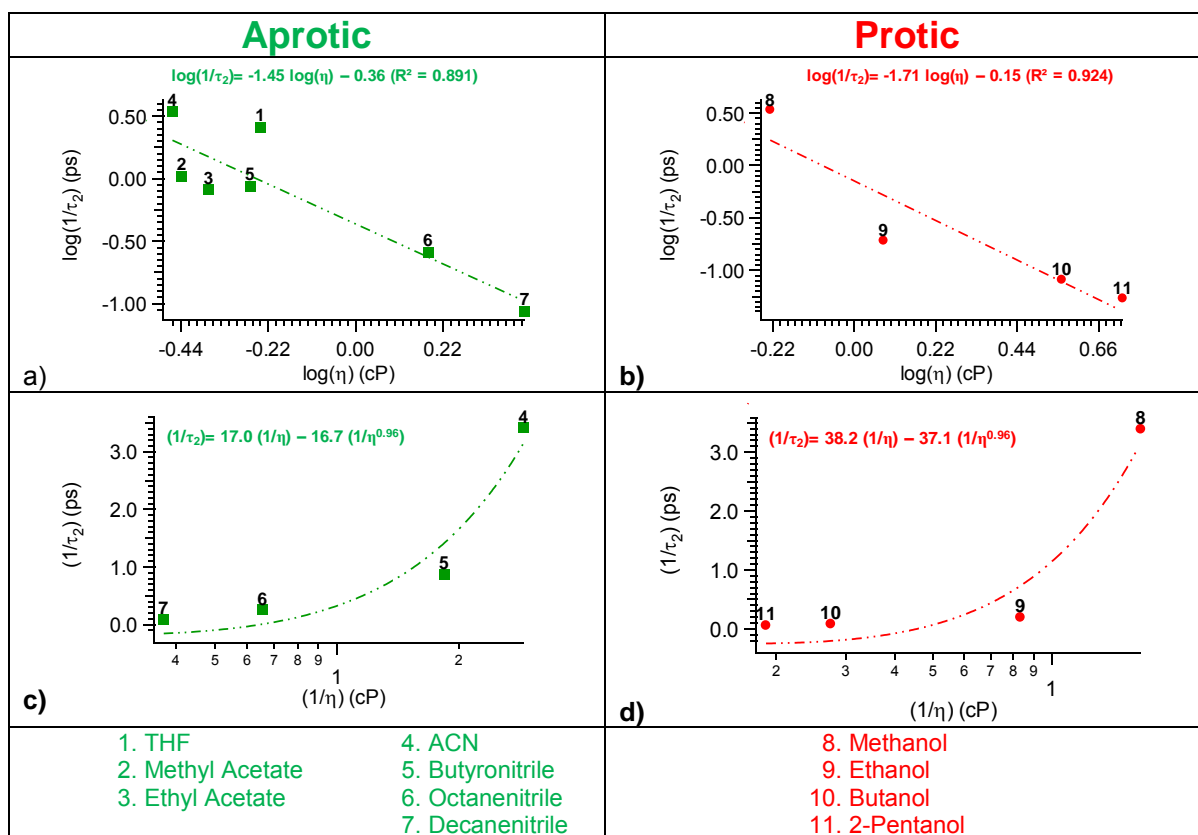

Figure V.17 plot of the CT rate constant $1/\tau_2$ as a function of the solvent viscosity η (logarithmic scale, upper graphs a and b) and of $1/\eta$ (lower graphs c and d) for the protic (right graphs) and aprotic (left graphs) solvents.

Applying this procedure to the SBPa molecule, a plot of the CT time constant $(1/\tau_2)$ as a function of the reversed viscosity $(1/\eta)$ is presented in figure V.17 c and d for aprotic and protic solvents, respectively. Even if the investigated viscosity range is very limited compared to that considered by Hara et al., it appears clearly that no viscosity effect due to intramolecular rearrangement of the solute form can be evidenced ($\alpha \rightarrow 1$ and $C_1 \approx C_2$).

In conclusion, regarding the solvent viscosity dependency of the CT process, we do not find any definite evidence that a significant intramolecular structural change takes place, while influence from solvation dynamics dependency is an averred fact. At this point of the manuscript, we thus have no evidence for a TICT process in SBPa.

V.3.3   Solvent influence on the excited state decay times τ_3 and τ_4.

The excited state decay process following the CT reaction was found to be double-exponential in most of the solvents (see table V.2) with characteristic times τ_3 and τ_4. The shorter one (τ_3) ranges from 2.6 ps in MeOH to 37 ps in 2-butanol. The longer one (τ_4) ranges from 109 ps in MeOH to 260 ps in 2-butanol. As discussed in the previous section, the longer decay time τ_4 was ascribed to the deactivation of $S_1(E)$ by IC, fluorescence and ISC. The shorter decay time τ_3 is rather ascribed to the decay of $S_1(CT)$ state by IC.

As it was done for time τ_2, the solvent dependence of times τ_3 and τ_4 will be investigated in order to learn more about the photophysical decays within the two excited states. First, the dependence on the solvent reorganization time will be studied; next, the influence of the polarity of the solvent will be discussed. At the end, the viscosity dependences will be investigated.

Solvation time. Following the study of Palit et al. [139] concerning LDS 821 dye, a double logarithmic plot of the characteristic times versus the solvation times is presented in figure V.18. First, one notes a satisfying correlation in the protic solvents while poor results are obtained for the aprotic ones. Both E and CT S_1 state decay processes in aprotic solvents seem to be weakly influenced by the solvent dynamics as suggested by the very small slopes of the fits and the low values of the correlation coefficient R^2 (0.426 and 0.791). In contrast, the IC process from $S_1(CT)$ in protic solvents is likely to be solvent controlled as the slope of the linear fit is close to unity. After the ICT process, the stability of the CT state is probably ensured by the hydrogen bond network.
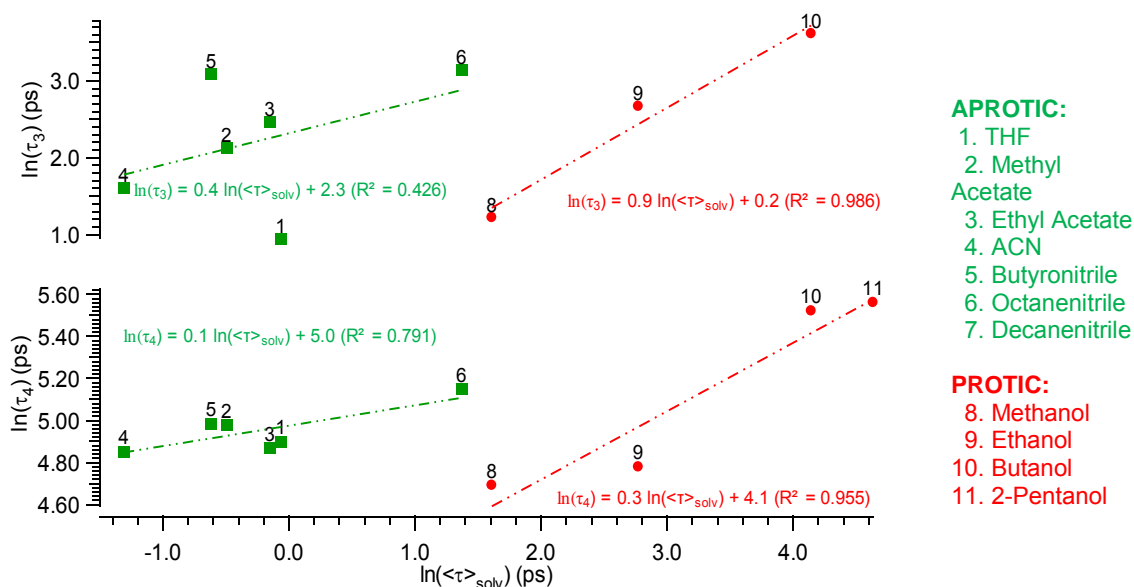
Figure V.18 Dependency of the decay time constants τ_3 (upper graph) and τ_4 (lower graph) of SBPa on the solvation time $\langle\tau\rangle_{solv}$ for aprotic and protic solvents (logarithmic values).

<u>Polarity dependence</u>. In figure V.19 are presented the dependences of τ_3 and τ_4 on the solvent dielectric constant (ε) together with the corresponding best linear fits determined separately for the protic solvents (in red), the polar aprotic solvents (in green), and the nonpolar aprotic solvents (in blue).
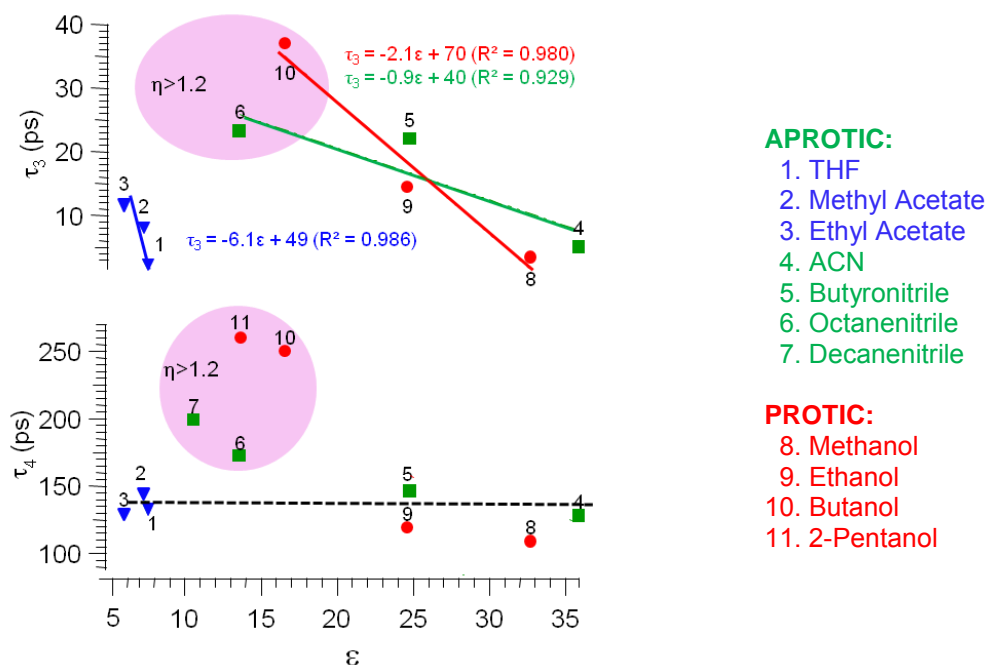
Figure V.19 Dependency of the characteristic decay times τ_3 (upper graph) and τ_4 (bottom graph) of SBPa on the dielectric constant (ε) for protic (in red), polar aprotic (in green), and nonpolar aprotic (in blue) solvents. Dashed lines represent linear fits using equations given in the graphs.

We first comment the case of τ_4 (bottom graph in figure V.19). At first glance, some dependency can be found for the protic and alkylnitrile groups. However, this dependency becomes insignificant if the viscous solvents are neglected. In fact, all weakly viscous solvents (# 1-5, 8, 9) lead to similar τ_4 values. This result is fully consistent with the absence of solvatochromic behaviour characterizing the emission from the $S_1(E)$ state: the energy level of this state is independent of the solvent polarity.

The case of τ_3 is intriguing because different dependency rules, discarding some viscosity influences, seem to apply for the protic (red points), polar (green points) and nonpolar (blue points) aprotic solvents, respectively. Even if some caution has to be taken with regard to the fact that each one of these subgroups includes very few experimental points, this last dependency appears consistent with the hypothesis of a normal Marcus regime suggested above. One might consider also that any polarity effects are observed for τ_3 which would be consistent with an energy level of $S_1(CT)$ not sensitive to polarity of surrounding medium (see previous chapter). Anyhow, the polarity dependence is not so clear and isoviscous series has to be investigate in the future to definitely find reliable explanation [162].

<u>Viscosity dependence.</u> The dependences of τ_3 and τ_4 on solvent viscosity (η) are plotted in figure V.20 a). As one can see, for each one of these time constant, the dependences found in the protic and aprotic solvents are similar. However the τ_4 decay time shows more linear dependences than τ_3 (as the corresponding R^2 fit parameters are higher).

To investigate more quantitatively the viscosity dependence of the decay times, the power law approach (eq. III.23 and III.24) described in the chapter III was tested. Plots of the logarithm values of the decay rate constants $1/\tau_3$ and $1/\tau_4$ as a function of the logarithm of reversed viscosity ($1/\eta$) are presented in figure V.20 b) for both protic and aprotic solvents. As one can see, the linear correlation of τ_3 is excellent for protic solvent ($R^2=0.969$) and moderate for aprotic solvents ($R^2=0.784$). However, both solvent groups give a slope close to 1 indicative, according to the power law, of a small activation barrier to be crossed (see Kramers picture, figure III.7) and thus a strong dependency of τ_3 on the solvent viscosity. One cannot exclude that this dependency is also a secondary effect of the solvent dynamics. Otherwise, this dependency is consistence with the existence of solute-solvent frictions in the back charge transfer process, the IC $S_1(CT) \rightarrow S_0$ leading to the recovery of starting molecule.

On the other hand, smaller slope values were found for τ_4. For protic solvents a value of 0.2 corresponds to a large barrier, which implies a weaker influence of solvent viscosity. This strong dependency seems to validate that the deactivation pathway of $S_1(E)$. For aprotic solvents, a slope of 0.5 is indicative of an effective (but moderate) barrier height, which suggests that, among the IC, ISC and fluorescence processes contributing to the decay of the $S_1(E)$ state, the latter is probably the minor deactivation pathway as two former ones (IC and ISC) are directly sensitive to solute-solvent frictions. Similarly, an activation barrier was also found for the decay of the localized excited state in the case of 1DMAF [155].
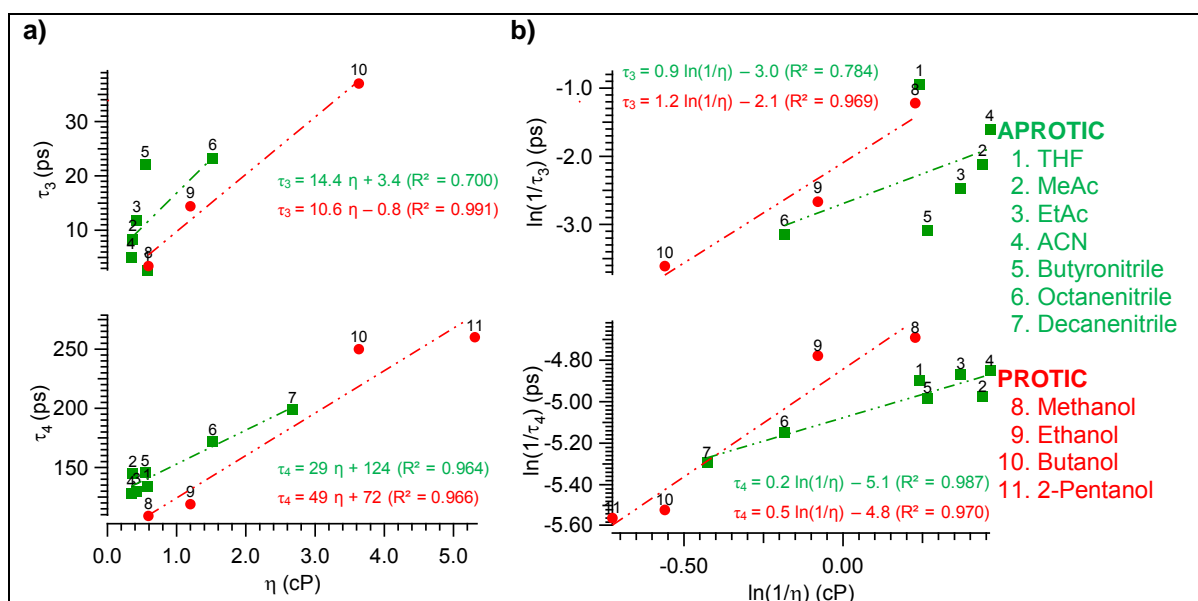
Figure V.20. (a) plots of the time constants τ_3 (upper graph) and τ_4 (lower graph) as a function of the solvent viscosity η and (b) Logarithm plots of the decay rate constants $1/\tau_3$ (upper graph) and $1/\tau_4$ (lower graph) as a function of the reversed viscosity ($1/\eta$). Best linear fits are represented with dotted dashed lines.

We summarized all solvent dependencies in table V.3 with a clear contribution from solvation dynamique, responsible for the apparent viscosity dependency. However, polarity dependence is more complicated and additional experiments (using isosviscous solvent set [162]) are required. Note that the theoretical $S_1(CT)$ dipole moment, as discussed in chapter IV, computed was found to be constant with solvent polarity (see table IV.4), this result would be consistent with lack of polarity dependency for τ_3 characteristic time.

Table **V.3** Dependences of ICT (τ_{CT}) and decay (τ_3, τ_4) characteristic times on solvent parameters.

	τ_{CT} ICT process	τ_3 IC from $S_1(CT)$	τ_4 deactivations of $S_1(E)$
$\langle\tau\rangle_{solv}$	YES	YES	YES
η	YES	YES	YES
ϵ	NO	Undefined	NO

V.4 Geometry of SBPa in the excited state: TICT or not?

In the previous section, a noticeable dependency of the SBPa final ICT step rate constant ($k_{CT}=1/\tau_2$) on the solvent viscosity has been observed and tentatively assumed to be a manifestation of the solvation dynamics dependency (sensitive to viscosity through solvent-solvent frictions) rather than of the existence of a large amplitude structural change yielding a TICT state (sensitive to solute-solvent frictions). Our attempt to better discriminate between these two possible explanations through the Harat et al. approach (equation IV.1) could not be fully validated due to the limited range of solvent viscosity employed. Similarly, regarding the bET (back electron transfer) process ($k_{bET}=1/\tau_3$), a dependency with viscosity has been established by applying the power law, which is possibly originating from a structural rearrangement of the solute upon recovering the starting geometry, but might also originate from the solvation dynamics, by analogy with other studies.

Finally, we found that the ICT dynamics is purely solvent controlled in aprotic solvents, suggesting that the solvation coordinate is the unique relevant one. In protic solvents, the ICT is faster than the solvent dynamics, which suggests that, according to the Sumi-Marcus theory, a second reaction coordinate other than solvation is involved. However, the latter is not necessarily a twist of the molecule.

Besides these experimental results, theoretical calculations presented in chapter IV have predicted planar configurations for SBPa in all the S_0, S_1 and S_2 electronic states, which apparently excludes the hypothesis that the torsion of dihedral angle can be a relevant molecular coordinate.

Chart V.2. TwSBPa
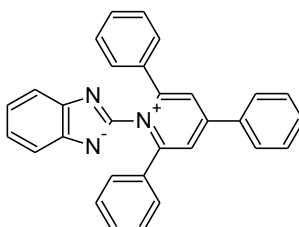
To definitively address the question of whether an intramolecular twist motion occurs during the ICT process in SBPa, we decided to investigate by ultrafast spectroscopy the photophysics of a pre-twisted SBPa molecule abbreviated as TwSBPa (chart V.2). In this

system, a twisted conformation of the ground state geometry is forced by the presence of phenyl groups attached to the pyridin ring in position α of pyridinium nitrogen

Previous stationary studies of this molecule were done by Alcalde et al. [23] The ground state geometry is characterized by a twist angle of about 84° [23]. However, in order to use TwSBPa as a model of twisted molecule for comparing the influence of the twist angle on the photophysics of SBPa, it must be ensured first that the electronic transitions are the same for both the planar and twisted molecules. In consequence, at the beginning of this subsection, stationary absorption as well as TDDFT calculation results for both molecules will be compared. Femtosecond transient data using 266 and 390 nm excitation will be then commented and compared to the results obtained for SBPa.

V.4.1 Stationary spectroscopic results and calculations on TwSBPa.

In figure V.21, a comparison of stationary absorption spectra of TwSBPa and SBPa is presented together with PCM-TDDFT calculation results. Note that no measurable steady-state emission could be detected for TwSBPa.
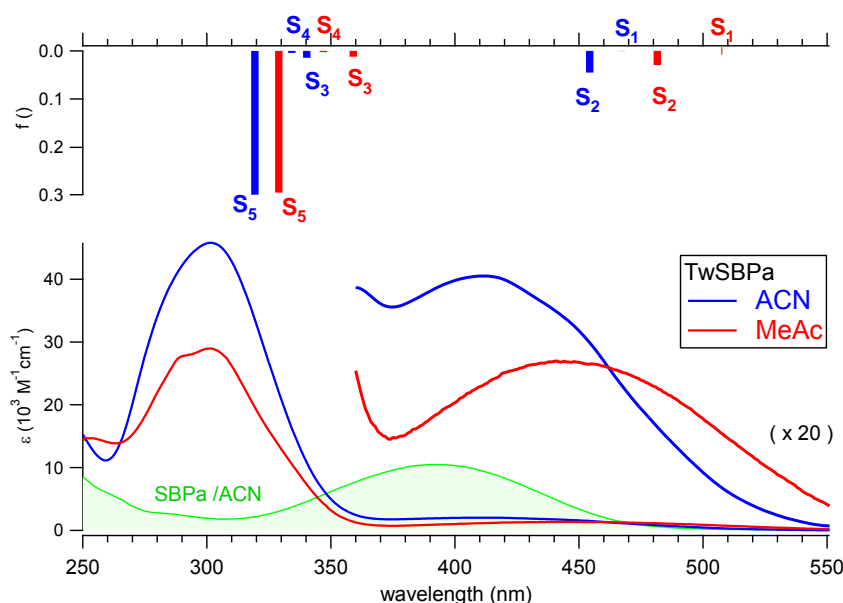
Figure V.21. Stationary absorption spectra of TwSBPa in ACN (blue) and MeAc (red) compared with SBPa in ACN (green). The inset shows an expansion of the 340-550 nm region. PCM-TDDFT position (PBE0-6-311++g(d,p)// PBE0-6-311++g(d,p)) and electronic oscillator strengths for vertical transitions up to S_5 are also given for TwSBPa (upper graph).

As one can see, the weak visible absorption band of TwSBPa, appearing between 375 and 500 nm, shows a negative solvatochromic effect on going from ACN to MeAc while

the stronger band near 300 nm is merely at the same position in these two solvents. As it was found for SBPa, PCM-TDDFT calculations with the PBE0 functional allow identifying the solvent sensitive band as the $S_0 \rightarrow S_2$ transition and reproducing satisfactorily the solvatochromic effect. In contrast, the $S_0 \rightarrow S_1$ oscillator strength is about zero. Apart a drastic diminution of its intensity compared to the CT band of SBPa (see later), one can conclude that the $S_0 \rightarrow S_2$ transition leads to similar solvatochromic bands in the planar and twisted molecules. (Note that the UV band is attributed to the $S_0 \rightarrow S_5$ transition).

Molecular orbitals of TwSBPa were also compared with those of SBPa in order to check if the orbitals involved in electronic transitions have the same configuration. As one can see in figure V.22, the general forms of these orbitals for both molecules are similar. For example the HOMO (H) and HOMO-1 orbitals are mostly localized in the betaine part whereas the LUMO (L) orbital is rather localized in the pyridinium moiety. However, the localized character of the H-1 and L orbitals appears notably more striking in TwSBPa than in SBPa. This increased localization effect is obviously resulting from a full electronic decoupling of the two moieties of the molecule when they are twisted relative to each other. The charge transfer nature of the $S_0 \rightarrow S_1$ and $S_0 \rightarrow S_2$ transitions is thus expected to be more complete in the twisted molecule.
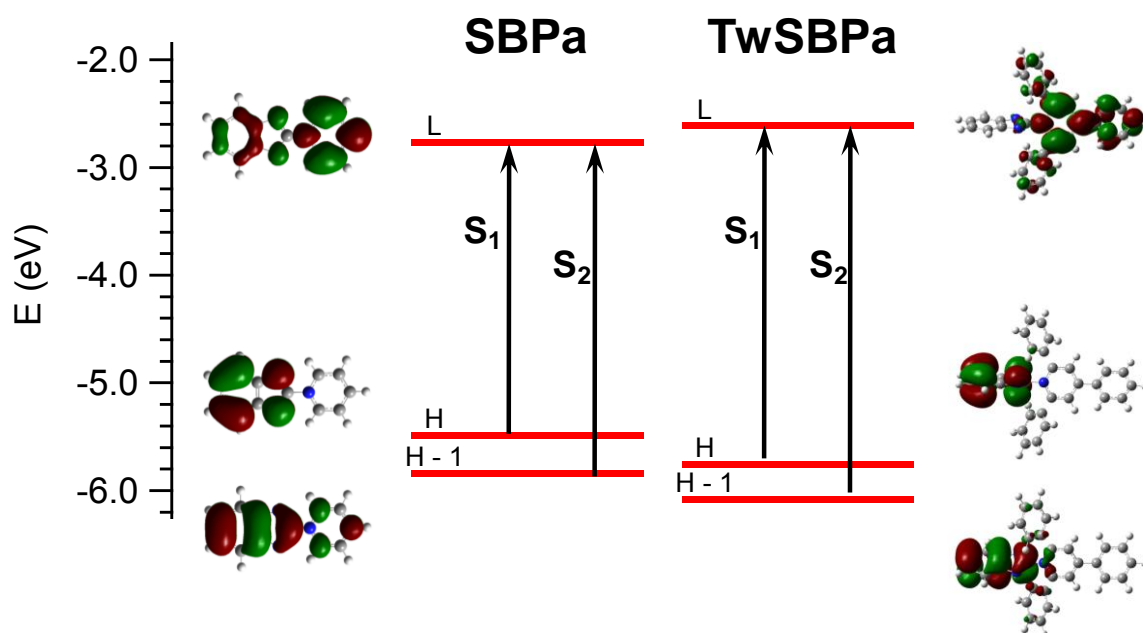
Figure V.22. Molecular orbitals representation of the H-1, H and L orbitals (PCM-DFT6-311++G(d,p) in ACN) for TwSBPa and SBPa molecules.

These calculations confirm that the first two electronic transitions of TwSBPa and SBPa involve the same orbitals: $S_0 \rightarrow S_1$ corresponds to transition H $\rightarrow$ L, and $S_0 \rightarrow S_2$ to transition H-1 $\rightarrow$ L. Moreover, the transition to the S_1 state is forbidden as its oscillator strength is very low (f = 0.001) in both molecules. Note that the drastic diminution of the $S_0 \rightarrow S_2$ CT band intensity in TwSBPa compared to SBPa can be rationalized in terms of cancellation of the $\langle H - 1 | L \rangle$ matrix element engaging the MO of the betaine part. Indeed, in SBPa, the H-1 and L orbitals have common electronic density on the two first phenyl carbon atoms of the betaine part, allowing notable FC overlap factor. This good overlap is considerably reduced due to the electronic decoupling effect in TwSBPa. Similarly, the absence of any measurable emission for TwSBPa is well explained by the total lack of overlap between the H and L orbitals involved in the $S_0 \leftrightarrow S_1$ transitions. Note also that the strongest intensity is predicted for transition n $\rightarrow \pi^*$ to the S_5 state (f = 0.293, orbitals: H-2 $\rightarrow$ L, which is a transition to S_3 state in the SBPa molecule).

Thus, even if additional delocalization of charge within the phenyl substituted pyridyl moiety and stronger electronic decoupling between the betaine and pyridyl parts arise in TwSBPa, one can safely assume similar photophysical properties in SBPa and TwSBPa.

V.4.2 Femtosecond transient absorption results for TwSBPa in ACN.

To investigate the role played by the dihedral angle between the pyridinium and betaine parts in the ICT mechanism, femtosecond transient absorption experiments were made for TwSBPa in ACN. Assuming no geometric influence during ICT process, the photophysics of the pre-twisted molecule has to be similar to those found for SBPa, i.e. transition S_2(CT)$\rightarrow$ S_1(CT) (time constant τ_2) is expected through the observation of transient band **Y_1/Y_2**, as well as a double-exponential decay process. Reversely, if the dihedral angle plays a role during the ICT process, knowing that TwSBPa cannot twist anymore due to steric hindrance, one can expect a novel photophysics to arise.

V.4.2.1 266 nm excitation experiment.

First, spectra recorded for TwSBPa in ACN using 266 nm excitation wavelength are presented in figure V.23 a – c. Similarities with SBPa results at 266 nm (figure V.4) are visible although fundamental differences in the kinetic evolution arise.

Initial dynamics. Figure V.23a shows the growth of a transient spectrum with two bands maximizing at 360 nm and 550 nm that resemble the transient bands **X** and **Y$_1$**, respectively, observed for SBPa upon 266 nm excitation (figure V.4). Mono-exponential fits at both wavelength gives a characteristic time of 0.20 ps, time close to experimental time resolution of the set-up. The differences with the SBPa evolution in this short time domain are the lack of **SE** signal and bleaching band in the case of TwSBPa, which is consistent with the extreme weakness of the visible absorption band, on one hand, and the nonemissive character of the S$_1$ state, on the other hand. A shift of band **Y$_1$** seems to arise in the first picosecond. This phenomenon will be discussed later.

CT dynamics. The evolution following 0.9 ps is similar to that found for SBPa upon 266 nm excitation (figure IV.5, b), with a small decrease of bands **X** and **Y$_1$** concomitantly with the increase of a new **Y$_2$** band and an isosbestic point in between at 470 nm. By analogy with SBPa, we assign this evolution to the existence of a final charge transfer step that stabilizes the ICT process, i.e. S$_2$(CT) $\rightarrow$ S$_1$(CT) Even if during this process only small variations of intensity are observed, the corresponding characteristic time of 0.22 ps is comparable to the 0.24 ps τ_2 value found for the ICT process in SBPa. Consequently, again by analogy with the reaction scheme proposed for SBPa, we ascribe the transient bands **X** and **Y$_1$** to S$_2$(CT) states and band **Y$_2$** to S$_1$(CT). At this point, we do not obtain any evidences for a contribution a second singlet state analog to S$_1$(E) states[16]. Observation of decay processes will help to clarify this point.

Post-CT dynamics. In figure V.23c, the complete decay of bands **X** and **Y$_2$** is observed between 1.5 and 150 ps. A double-exponential decay is found for band **X** at 360 nm, with characteristic times of 2.6 and 23 ps, while a single-exponential decay is found for band **Y$_2$** at 550 nm with 2.6 ps characteristic time. From comparison with SBPa results, we propose to ascribe the faster decay to the S$_1$(CT) state ($\tau_3 = 5$ ps for SBPa) and the longer one to the S$_1$(E) state decay. ($\tau_4 = 128$ ps for SBPa). Note the shortening of τ_4 parallels the disappearance of fluorescence

These results indicate that the last step of the ICT process observed in the planar SBPa molecule with a characteristic time τ_2, is still occurring for the highly pre-twisted TwSBPa molecule. This common behaviour of SBPa and TwSBPa suggests that the ICT process of time τ_2 does not characterize a twisting motion of the molecule skeleton, i.e., the charge transfer does not lead to a TICT state.

---

[16] Note that for sake of simplicity, we keep the notation S$_1$(E) even if emission is not reported anymore.
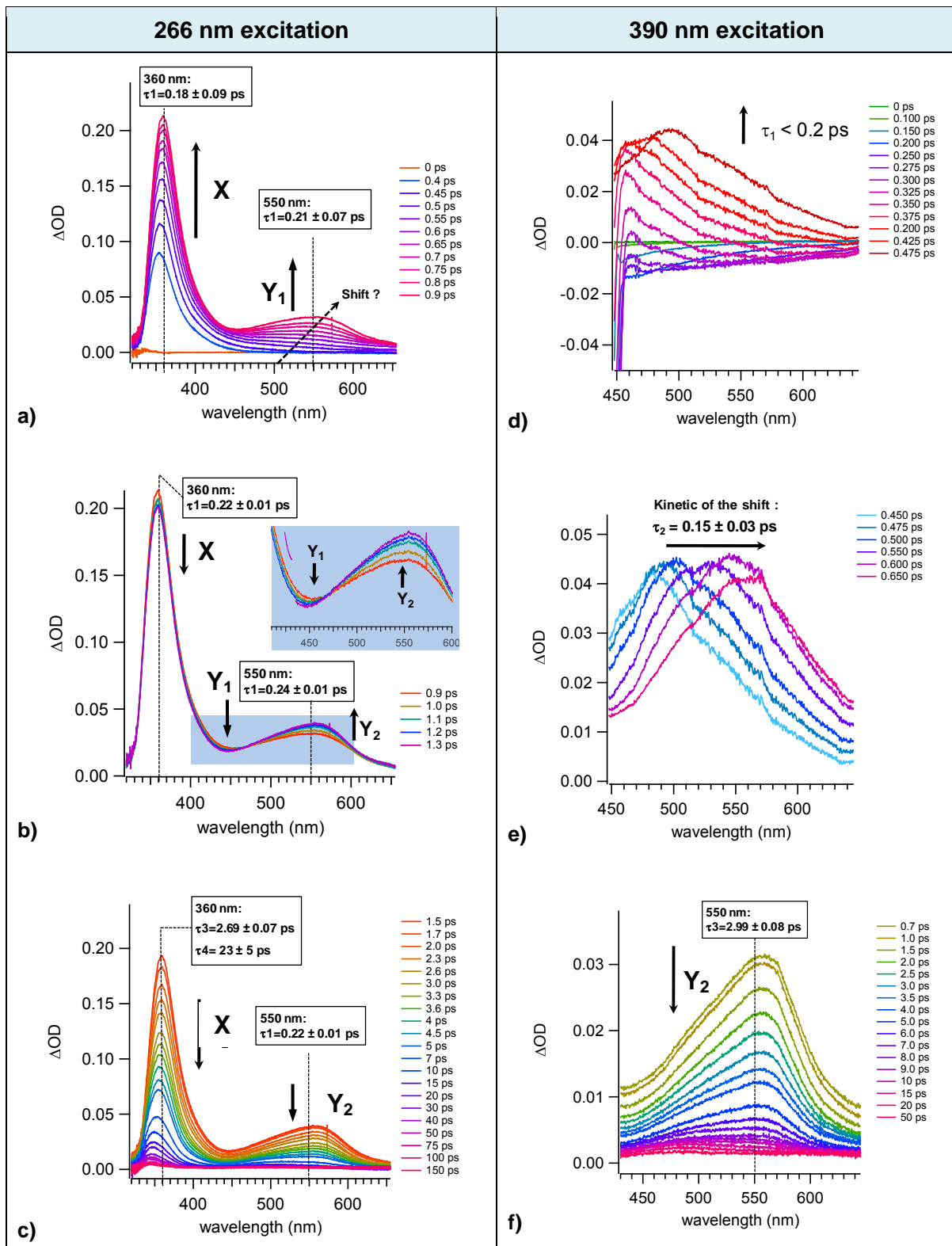
Figure V.23. Femtosecond transient absorption evolution of TwSBPa in ACN for two distinct laser excitations: 266 nm (left) and 390 nm (right). Characteristic times (mono/bi exponential fits at selected wavelength) are also given. Data are divided into three temporal windows: a) [0 – 0.9 ps], b) [0.9 – 1.3 ps] and c) [1.3 – 150 ps] for 266 nm excitation and d) [0– 0.47 ps], e) [0.45 – 0.65 ps] and f) [0.7 – 50 ps] for 390 nm excitation.

V.4.2.2   390 nm excitation experiment.

To complete the investigation of TwSBPa, the femtosecond absorption results using 390 nm excitation, divided into three temporal windows, are presented in figure V.23 d-f. By analogy with the above analysis of the spectral evolution recorded upon 266 nm excitation, we separate the discussion of spectra in figure V.23 d-f into three time periods. Additionally, the manifest band shift observed in the sub-picosecond time domain will be discussed.

initial dynamics. First, in figure V.23 d, the increase of an excited state absorption band peaking below 500 nm can be observed with a characteristic time limited by the time resolution of the experimental setup. Note that sharp and intense negative peaks around 450 nm are due to stimulated Raman scattering. As expected, there is no noticeable **SE** signal.

Transitional dynamics. In figure V.23 e, one can see the existence of a drastic spectral red-shift of the excited state absorption band from about 450 nm at t = 0.45 ps to 560 nm at t = 0.65 ps. The final position corresponds well to the 560 nm band Y_2 obtained with 266 nm excitation. It is therefore tempting to ascribe the 560 nm signal to S_1(CT). The characteristic time for this spectral shift (as measured by the time dependent position of the band maximum) was found to be $\tau_{sh} = 0.15$ ps. Such ultra fast evolution can indicate an evolution along an adiabatic curve, as it will be discussed in more details later. This new effect clearly observed for 390 nm excitation was probably spectrally overlapped upon 266 nm as suggested by the shift on figure V.23 a .

Final dynamics. Figure V.23f presents the constant decay of the excited state absorption band peaking at 560 nm with a single characteristic time $\tau_3 = 2.99$ ps. Again, one finds exactly the same spectral and kinetic evolution as that observed upon 266 nm excitation (compare with figure V.4 c). We definitively conclude that this transient signal is ascribed to S_1(CT). Note that, due to the above mentioned red-shift of the absorption, the second, longer decay time (as for band Y_1 in 266 nm excitation wavelength experiment) can be found only for kinetics at shorter wavelength.

In conclusion, exciting at 390 nm leads to an alternative route for producing the S_1(CT) species that is different from that arising by using 266 nm excitation. This new route involves a different precursor state PS that cannot be S_2(CT). Indeed, the "characteristic isosbestic point" observed in the spectral evolution induced by exciting at 266 nm is now substituted by an ultrafast band shift effect. In order to try to identify this novel mechanism, solvent effects have been studied and are presented below.

V.4.3 Solvent effect for TwSBPa: evidence for a novel photophysical mechanism.

To complete the photophysical analysis of TwSBPa, femtosecond transient absorption experiments were done in two other solvents, butyronitrile and methyl acetate, using 390 nm excitation. For the three solvents, the ultrafast shift of the excited state absorption band is presented in figure V.24. The time constant τ_{sh} associated to the shift as well as the mono-exponential absorption decay time of this band are given in table V.4 (together with relevant solvent parameters).

Table V.4 . Characteristic times associated to the spectral shift (τ_{sh}) and decay (τ_3) of the transient visible absorption band observed for TwSBPa following 390 nm excitation. Solvent parameters: ε, dielectric constant, n, refractive index, η, viscosity.

Solvent	ε	n	η (cP)	$\langle\tau\rangle_{solv}$ (ps)	τ_{sh} (ps)	τ_3 (ps)
ACN	35.9	1.344	0.345	0.27	0.15 ± 0.03	2.99 ± 0.08
Butyronitrile	24.8	1.382	0.542	0.54	0.25 ± 0.06	5.10 ± 0.30
Methyl Acetate	6.68	1.3589	0.364	0.61	0.44 ± 0.09	6.30 ± 0.70

Solvation time. First, it is clear that both τ_{sh} and τ_3 seem to be correlated with the solvation time. It is worth noting that the characteristic times of the shift are approximately two times shorter than $\langle\tau\rangle_{solv}$, meaning that the processes described with these times are faster than the dynamics of the surrounding solvent. One can then assume that the novel process PS $\rightarrow$ S_1(CT) does not depend only on the solvent reorganization and cannot be characterized as a "solvent controlled" process, as it was the case for SBPa in aprotic media. To rationalize this result, it is worth to remember that the two molecular moieties are well screened by the presence of the substituted phenyl rings from the influence of surrounding solvent. For both times τ_{sh} and τ_3, the observed dependency on the solvation time may also originate as a consequence of the polarity dependency.

a) Acetonitrile

ε = 35.9
0.375 – 0.65 ps

$\tau_{sh} = 0.15 \pm 0.03$ ps

b) Butyronitrile

ε = 24.8
0.45 – 0.75 ps

$\tau_{sh} = 0.25 \pm 0.06$ ps

c) Methyl acetate

ε = 6.68
0.5 – 0.85 ps

$\tau_{sh} = 0.44 \pm 0.09$ ps
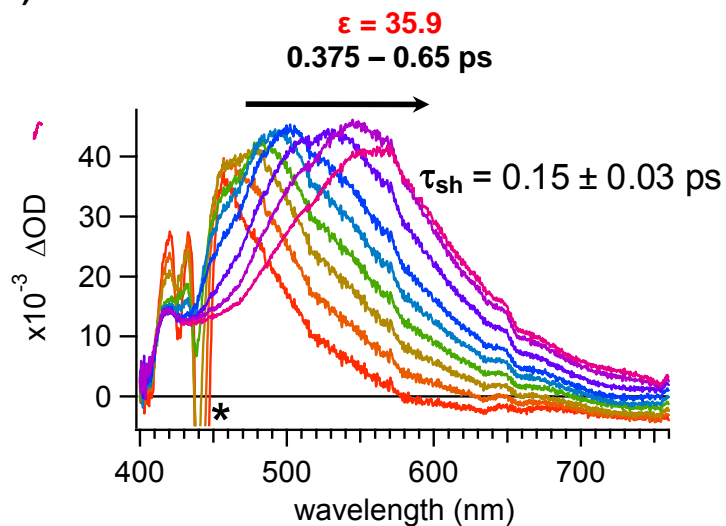
Figure **V.24** Spectral evolution of the excited state visible absorption band observed following 390 nm excitation of TwSBPa in solvents of different polarities: a) acetonitrile, b) butyronitrile and c) methyl acetate. The star indicate stimulated Raman pick of the solvent.

Polarity. Even with few points, manifest linear correlations of both times τ_3 and τ_{sh} on solvent polarity were found (R^2=0.999 and 0.907, respectively) (figure V.25 a and b). Note also that the solvent viscosity is clearly not correlated with any of these times. In fact, the polarity dependency is the key point to identify the novel mechanism occurring in TwSBPa upon 390 nm excitation.
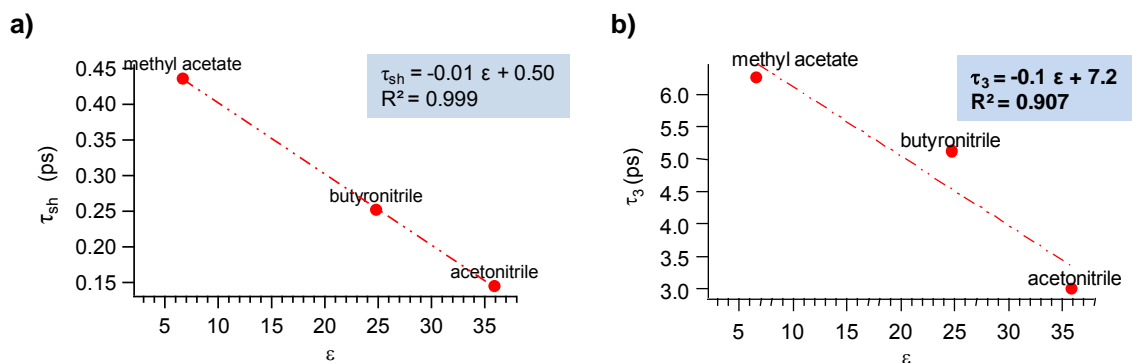
Figure V.25 Linear correlation of time constants τ_{sh} (a) and τ_3 (b) with the solvent polarity.

Identification of the novel mechanism.

At this point, the clear rationalization of the solvent effect concerning the novel mechanism leading to $S_1(CT)$ with the time constant τ_{sh} is not easily accessible and more data will be necessary. However, two important points can be commented. Concerning the disappearance of $S_2(CT) \rightarrow S_1(CT)$ in benefit to IS$\rightarrow S_1(CT)$, IS being a novel intermediate state, we saw in chapter IV that excited state crossing can occurs between S_1 and S_2 states when the system begin to evolve along the S_2 manifold. So by analogy with the parent molecule, one can assume that the ultra fast shift observed for TwSBPa is related with a population jumps from S_2 to S_1 potential curve via vibrational excited state, conical intersection.... Furthermore, dealing with solvatochromic states, one can suspect the solvent effect observed on τ_3 to be related with a the $S_1(CT)$-S_0 energy gap law operating on IC.

In the future, a final validation of this new mechanism will be done with the help of TDDFT excited state optimizations (optimized excited state nature, dipole moment, energy level...) as well as CASSCF/CAFPT2 calculations – the advanced technique to determine possible conical intersections between these excited states.

V.5 Conclusions

Combining the results obtained in this chapter with those of the previous one, we achieved a thorough characterization of the SBPa photophysics and related ICT processes. The Jablonski diagram in figure IV.20 has been completed by studies of the solvent effects and of model molecules. A final summary of the results is presented in figure V.26 adopting diabatic and adiabatic representations (see subsection III.2.2.1). The keypoint to understand the photophysics of SBPa was undeniably the two-step aspect of the photoinduced ICT process yielding the final S_1(CT) state. Indeed, considering the initial planar ground state molecule, light excitation of the solvatochromic transition $S_0 \rightarrow S_2$(FC) induces a first charge transfer from the benzene to the pyridinium ring, which results in a drastic dipole moment reduction (inversion can even be expected in polar solvents). An ultrafast relaxation of ~100 fs leads to the stabilization of this first CT state from its initial Franck-Condon geometry, i.e. S_2(FC) $\rightarrow$ S_2(CT), which is accompanied by a small reorganization of the electronic configuration (small charge fraction is transferred back). Note that according to TDDFT calculations, the dipole moment difference between these two configurations is not negligible (see table IV.4) and one could expect some polarity effect on the characteristic time τ_1 probed by ultrafast spectroscopy providing however a much better temporal resolution. A second ICT step then proceeds via S_2(CT) $\rightarrow$ S_1(CT) internal conversion, which corresponds to a CT from the imidazole part to the pryridinium ring. The characteristic time τ_2 for this reaction ranges between ~300 fs and 20 ps depending on the solvent nature because it is fully controlled by the solvent dynamics, at least for the aprotic solvent. In protic solvents, a more complicated situation arises probably due to the hydrogen bond network influencing the ICT process. After the study of the pretwisted TwSBPa molecule, we definitively excluded the hypothesis of TICT formation and confirmed that the observed viscosity and polarity dependency of τ_2 is related to the excited state solvation dynamics. As an interesting results, the final S_1(CT) dipole moment is independent of the solvent polarity (see table IV.4), which could explain the lack of clear polarity effect on the S_1(CT) lifetime τ_3. This point has to be clarified in the future by testing various iso-viscous solvents. Reversely, the viscosity dependency of this later time is easily rationalized in terms of solute-solvent frictions acting on the $S_1 \rightarrow S_0$ IC rate. In order to achieve the final rationalization of the ICT process and back reactions, a look on the qualitative non-adiabatic representation is instructive. Does the central reaction of the SBPa photophysics, S_2(CT) $\rightarrow$ S_1(CT), proceed through conical

intersections S_2/S_1? Answer to this question will require in the future advanced CASSCF/CASPT2 calculations [137] in order to determine the different possible points of S_2/S_1 conical intersections and the related molecular geometries. Concerning the deactivation process $S_1(CT) \rightarrow S_0$, if similar calculations could be undertaken for S_1/S_0 intersections, a complementary approach will be to compute the transition state between $S_1(CT)$ and S_0. It will be interesting to compare this result with the recent conclusions of Rettig et al. [35] reporting a twisted geometry of the Betaine-30 molecule.
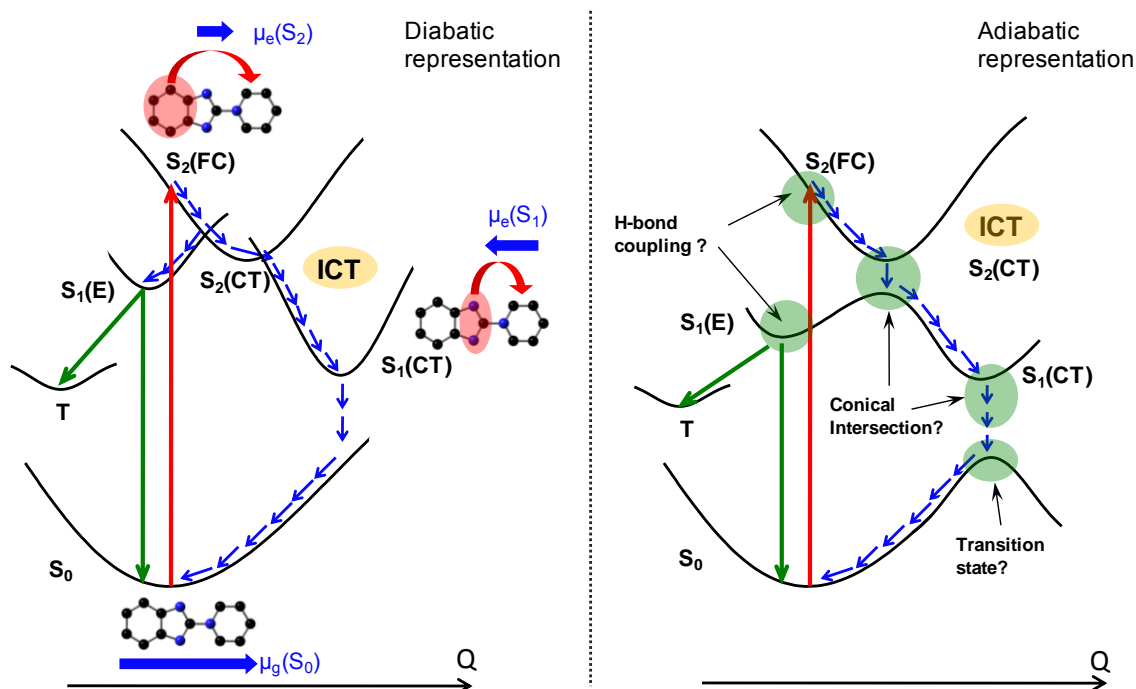
Figure **V.26** Possible photophysical schemes proposed for SBPa molecule

In parallel to the $S_2(CT) \rightarrow S_1(CT)$ ICT deactivation route, a competitive process has been found to occur from S_2, leading to the $S_1(E)$ state that is the only emissive state of SBPa (no dual fluorescence). Two opposite results have been obtained in this manuscript. In chapter IV, the $S_1(E)$ state was identified as $S_1(CT)$ (preliminary named as $S_1(opt)$) based on experiment-PCM-TDDFT comparison of the emission band positions. In this chapter, transient spectroscopy results have provided evidence that $S_1(CT)$ and $S_1(E)$ are two distinct states. A number of open questions concern this state. First, the mechanism of its production is not elucidated, as illustrated in figure V.26 and one can consider the possibility of two different non-adiabatic mechanisms $S_2(FC) \rightarrow S_1(E)$ or $S_2(CT) \rightarrow S_1(E)$. Second, knowing that $S_1(E)$ is the precursor of the triplet state, it would be instructive to perform some triplet calculation. Another interesting point to explore concerns the

transient **SE** signal observed from all FC singlet states in protic medium (see figure V.3) and not only from emissive state as in aprotic medium (see figure V.1). We emitted the hypothesis for a coupling induced by intramolecular hydrogen bonds between FC and emissive state. Based on this idea, the existence of $S_1(E)$ is perhaps related with the consideration of surrounding solvent. Consequently, in the near future, it will be interesting to perform TDDFT excited state optimization but including 2 or 4 explicit molecules of solvent in order to find a secondary minimum close to the minimum corresponding to $S_1(FC)$.

Having rationalized the photophysics of SBPa and especially the ICT processes governing the various dipole moment between $S_2(CT)$ and $S_1(CT)$, we will investigate structural effect focusing on the influence of substituting thiophenic groups on the acceptor part

CHAPTER VI

Studies of thiophene substituted SBPa molecules:

Th$_2$SBPa and Th$_4$SBPa.

VI.1 Introduction

In previous chapters, photoinduced ICT process in SBPa molecule was investigated and a complete photophysical scheme (see figure V.11) has been derived. It was discovered, that ICT process is largely initiated by excitation to S$_2$(CT) and is amplified in the S$_2$(CT) → S$_1$(CT) transition. This last process is most likely arising in the Marcus inverted region and is mainly controlled by the solvent dynamics in the case of aprotic solvents. No evidence of geometrical change toward a twisted form in the excited state was found from theoretical calculations nor from comparing the experimental femtosecond absorption data of SBPa and its twisted derivative, TwSBPa. The later molecule was shown to undergo two effective mechanisms: a non-adiabatic process involving a S$_2$/S$_1$ conical intersection and a direct adiabatic mechanism consisting in an evolution along the S$_1$(CT) potential curve. Besides ICT processes, population of an emissive S$_1$(E) state and consecutive weak triplet creation were evidenced.

As explained in the introduction, one of the interests for studying such ICT molecules is their potential ability to be used as photoswitches in organic conducting devices: in particular, by inserting SBPa within polythiophenic chains, one can expect to be able to control the electrical conduction by light irradiation via the ICT phenomenon. In this sense, two novel molecules, noted as Th$_2$SBPa and Th$_4$SBPa, were recently designed and synthesized in the group of Professor Jiro Abe through symmetric substitution of the SBPa betaine moiety by two thiophene or bithiophene units, respectively, in para position (see chart VI.1).

Chart VI.1. a) 4,7-Dithiophen-1H-benzimidazol-2èyl-pyridinium (Th$_2$SBPa); b) 4,7-Bis(2,2'-bithiophebe)-1H-benzimidazol-2èyl-pyridinium (Th$_4$SBPa)

a)

b)
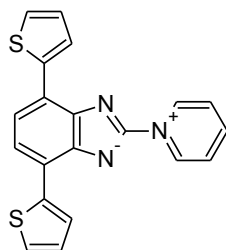
Th$_2$SBPa
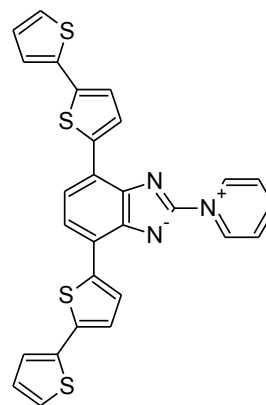
Th$_4$SBPa

It is highly desired to check if the photoinduced ICT processes remain unchanged in these substituted SBPa molecules. More precisely, we have to focus to following points concerning the Th_nSBPa molecules: i) is the non-adiabatic ICT $S_2(CT) \rightarrow S_1(CT)$ mechanism still the same compared to the parent molecule? is the competitive mechanism $S_2 \rightarrow S_1(E)$ also effective? As some energy transfer can be expected from the betaine to the thiophene groups, does this process compete efficiently with the SBPa ICT processes? What is the influence of the thiophenic chain length? Furthermore, with regard to the large steric occupancy of the thiophenic substituents, is the role played by the solvent dynamics still decisive?

In order to answer these questions, the photophysics of Th_2SBPa and Th_4SBPa will be investigated in this chapter. However, because the own oligothiophenic photophysics is likely contributing to the photoinduced properties of Th_2SBPa and Th_4SBPa, it appears adequate to remind in a first section the main literature data about α-oligothiophenes (noted nT, where n is the number of thiophene units). In the second section, as it was done previously for SBPa molecule, the stationary absorption and PCM-TDDFT calculations results obtained for Th_2SBPa and Th_4SBPa will be presented. Finally, transient absorption results will be discussed and compared with those obtained for the parent molecule.
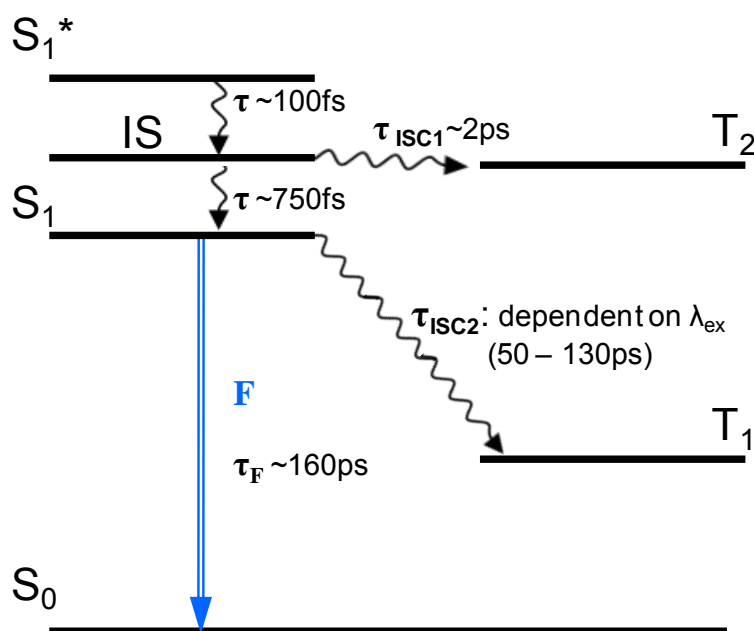
Figure VI.1 Photophysical scheme of terthiophene 3T.[163-166]

VI.1.1   Photophysics of oligothiophenes

First studies of the absorption spectra of oligothiophenes were presented by Sease and Zechmeister in 1947 [167]. They discovered that increasing the number of thiophene rings in the chain induces a batochromic shift of the lowest energy absorption band while the position of the second absorption band remains unchanged ($\sim$ 250 nm): for instance, the terthiophene (3T) molecule absorbs at 354 nm [168] whereas 5T absorbs at 417 nm [168].
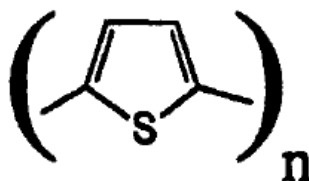
Scheme VI.2. α-oligothiophene (nT)

During the 1980's and 90's nanosecond transient absorption data on different oligothiophenes (nT) were reported [169, 170]. At this time, the excited triplet state was characterized with a lifetime of tens microseconds. The $T_1 \rightarrow T_n$ absorption spectra of 3T and 5T present one band peaking near 460 and 630 nm, respectively [169]. In parallel, fluorescence measurements [171] showed that when the number of thiophene rings increases, the quantum yield of triplet formation decreases and the quantum yield of fluorescence increases. Femtosecond time-resolved studies of nT were also carried out [166]. The $S_1 \rightarrow S_n$ absorption spectrum of 3T displays a sharp band at 600 nm, that reported for 5T a broad band covering the entire red region above 580 nm and peaking around 845 nm.

Finally, from the beginning of our century, Rentsch et al. [165] characterized by femtosecond transient absorption the intersystem crossing (ISC) dynamics in some oligothiophenes. The kinetics of triplet state formation included two characteristic times, one rather short (2 ps) and the second one in the $50 - 120$ ps domain depending on the excitation wavelength [164]. These time constants characterize the ISC from the vibrationally excited S_1 state, close in energy to the upper triplet state T_2, and the vibrationally relaxed S_1 state, respectively, both having possibly different geometry. A general photophysical scheme for terthiophene is presented in figure VI.1.

VI.2 Stationary results for thiophene substituted molecules.

As before for SBPa, stationary absorption measurements on Th$_2$SBPa and Th$_4$SBPa were done in three solvents of different polarities in order to check the presence of a solvatochromic band as found for the SBPa parent molecule. Additionally, PCM-TDDFT calculations were performed to interpret the optical transitions observed for both molecules in terms of molecular orbitals.

Table **VI.1.** PCM-TDDFT assignments of the absorption spectra of TH$_2$SBPa and TH$_4$SBPa in three solvents.

		Toluene			THF			ACN		
		Excit.	λ (nm)	f	Excit.	λ (nm)	f	Excit.	λ (nm)	f
Th$_2$SBPa	S$_1$	H→L (0.693)	670	0.053	H→L (0.692)	576	0.075	H→L (0.961)	543	0.088
	S$_2$	H-1→L (0.659) H→L+1 (-0.118)	458	0.465	H-1→L (0.668)	420	0.448	H-1→L (0.669)	405	0.436
	S$_3$	H→L+1 (0.694) H-1→L (0.101)	401	0.074	H→L+1 (0.658)	368	0.922	H→L+1 (0.658)	366	0.887
	S$_4$	H→L+2 (0.660)	371	0.974	H→L+2 (0.695)	360	0.056	H→L+2 (0.699)	344	0.051
Th$_4$SBPa	S$_1$	H→L (0.691)	740	0.132	H→L (0.690)	644	0.206	H→L (0.688)	612	0.258
	S$_2$	H-1→L (0.668) H-2→L (0.143)	484	0.1658	H-1→L (0.201) H→L+1 (0.636)	448	1.393	H→L+1 (0.668)	447	1.458
	S$_3$	H→L+1 (0.667)	452	1.614	H-1→L (0.634) H-2→L (0.157) H→L+1 (-0.202)	400	0.280	H-1→L (0.667) H-2→L (0.164)	435	0.136
	S$_4$	H-2→L (0.561) H-1→L (-0.188) H→L+2 (-0.351) H→L+3 (0.103)	432	0.112	H-2→L (0.621) H-1→L (-0.202) H→L+2 (0.130) H→L+3 (0.191)	383	0.152	H-2→L (0.608) H-1→L (-0.195) H→L+3 (0.263)	389	0.136

VI.2.1 Th$_2$SBPa: evidence for a CT band.

The stationary absorption spectra of Th$_2$SBPa in three solvents of different polarities – ACN (ε = 35.9), THF (ε = 7.58) and toluene (ε = 2.38) – are presented in figure VI.2a together with the corresponding PCM-TDDFT (PCM-TD-PBE0/6-311++G(d,p)//PBE0/6-311G) wavelengths and oscillator strength using the same colour code. In figure VI.2b are displayed the PCM-DFT energy diagram, MO contour plots from (HOMO-2) to (LUMO+2), and TDDFT vertical transitions (some of them involve various MO excitations). The main MO excitations (up to 10%) contributing to the four lowest $S_0 \to S_n$ transitions are listed in Table VI.1. In this table and in figure VI.2b, notable similarities with SBPa can be found (see figure IV.12): the S_1 state was found to be related to the

HOMO → LUMO transition (green arrows in the diagram) and the S$_2$ state to the HOMO-1 → LUMO transition (blue arrows in the scheme). For toluene this last transition is not pure. It is fundamental to notice that the orbitals involved in the transitions are almost exactly the same as for the SBPa molecule except for a minor additional electronic delocalization on the thiophene rings in Th$_2$SBPa. Therefore, it can be concluded safely that the electronic nature of the transitions is comparable in the two molecules.

As one can see on figure VI.2a, the solvatochromic band in the 400 − 450 nm range, already observed for SBPa, is still present upon thiophenic substitution. Its position is almost the same in both molecules for a given solvent: 390 nm for SBPa and 397 nm for Th$_2$SBPa in ACN. Similarly, the overall shift of the band maximum from ACN to toluene is also quite similar: 2754 cm^{-1} for Th$_2$SBPa and 3023 cm^{-1} for SBPa. As expected, the energy calculated by TDDFT for the S$_0$ → S$_2$ transition is again in excellent accordance with the position of this band in the experimental spectra. From a MO point of view (figure VI.2b), the negative solvatochromism comes from HOMO stabilization and LUMO destabilization, i.e. increasing HOMO-LUMO energy gap with polarity. In conclusion, the negative solvatochromic band, strictly similar to that observed for the parent molecule, is related to the S$_2$(CT) state and seems to be insensitive to thiophenic substitution (this point will reveal important when considering the case of Th$_4$SBPa later).

The comparison of Th$_2$SBPa with its parent molecule points also to some noticeable differences. Indeed, unlike for SBPa, a novel solvatochromic "tail" is present as a broad and weak shoulder at longer wavelengths than the S$_0$ → S$_2$ band. It is lying in the 450 − 600 and 500 − 650 nm regions in ACN and toluene, respectively. From the TDDFT results, this tail is safely attributed to the S$_1$(CT) state that was a dark state in the parent SBPa molecule (the symmetry restrictions occurring for SBPa are no longer valid in the substituted derivative).

Another noticeable difference with SBPa is the presence of an intense non-solvatochromic band peaking at 350 nm. The position of this band is very similar to stationary absorption spectrum of the terthiophene (3T) molecule (354 nm [168]), suggesting a transition localized in the thiophene-phenyl-thiophene moiety (denoted as thiophenic system in the following).

a)
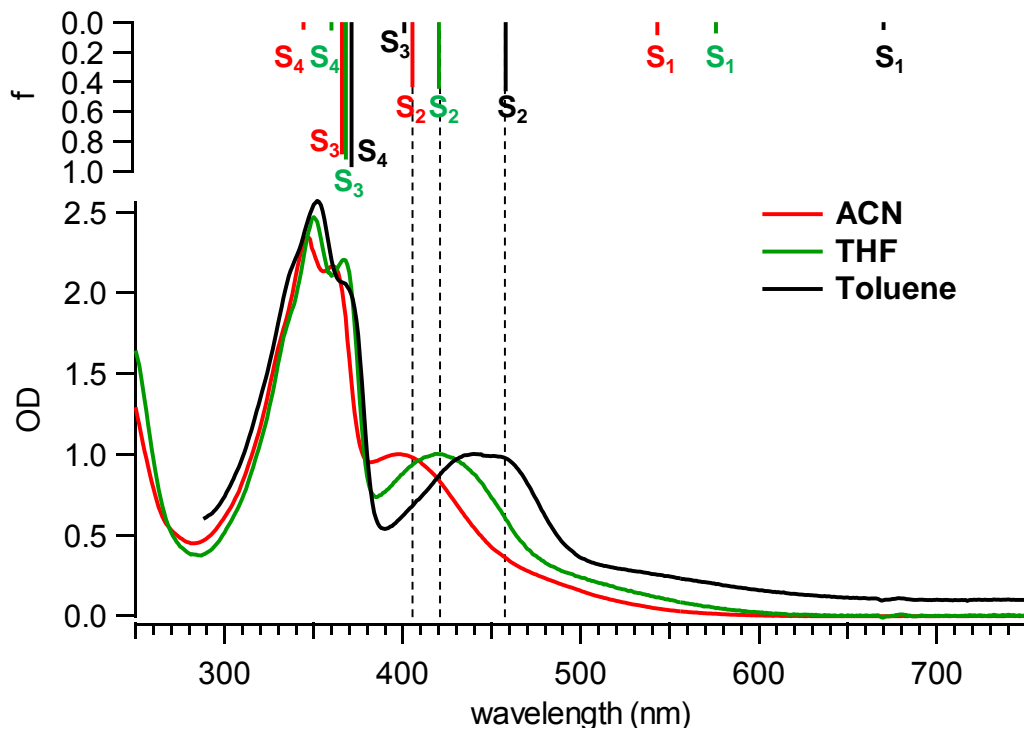
b)

Figure VI.2 Absorption characteristics of Th$_2$SBPa: a) stationary absorption spectra and PCM-TDDFT transitions in three solvents of different polarity; b) PCM-DFT energy diagram and representation of the orbitals involved in the four lowest energy transitions.

a)

b)

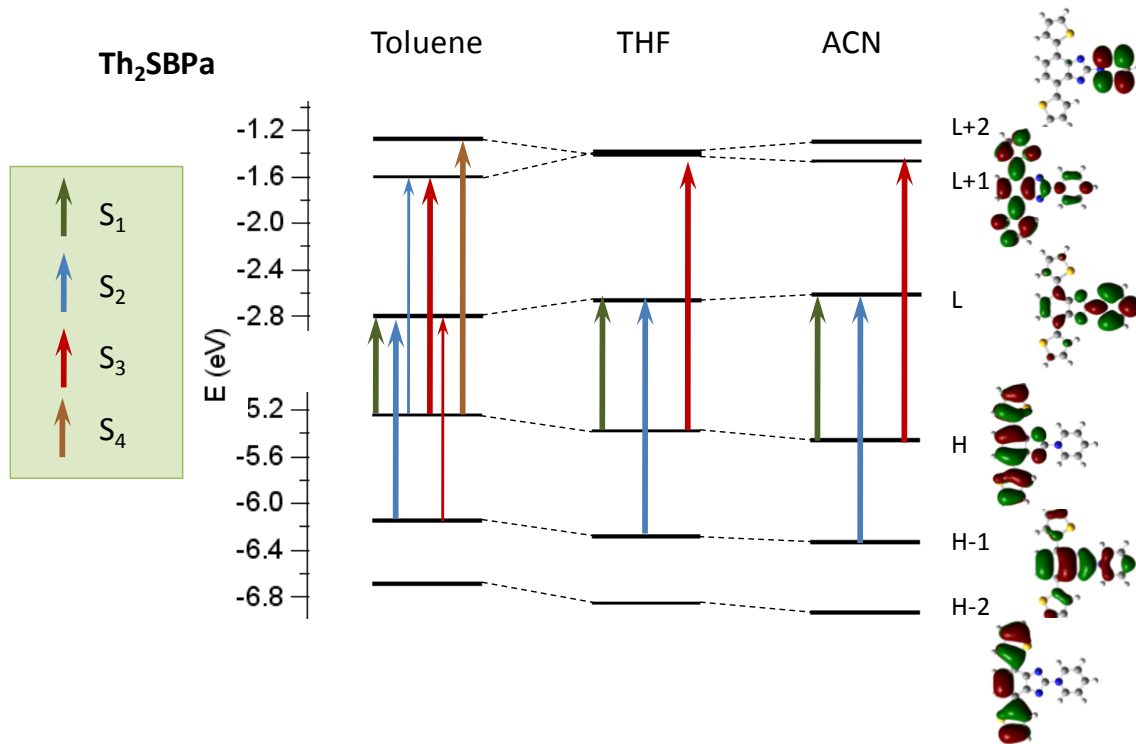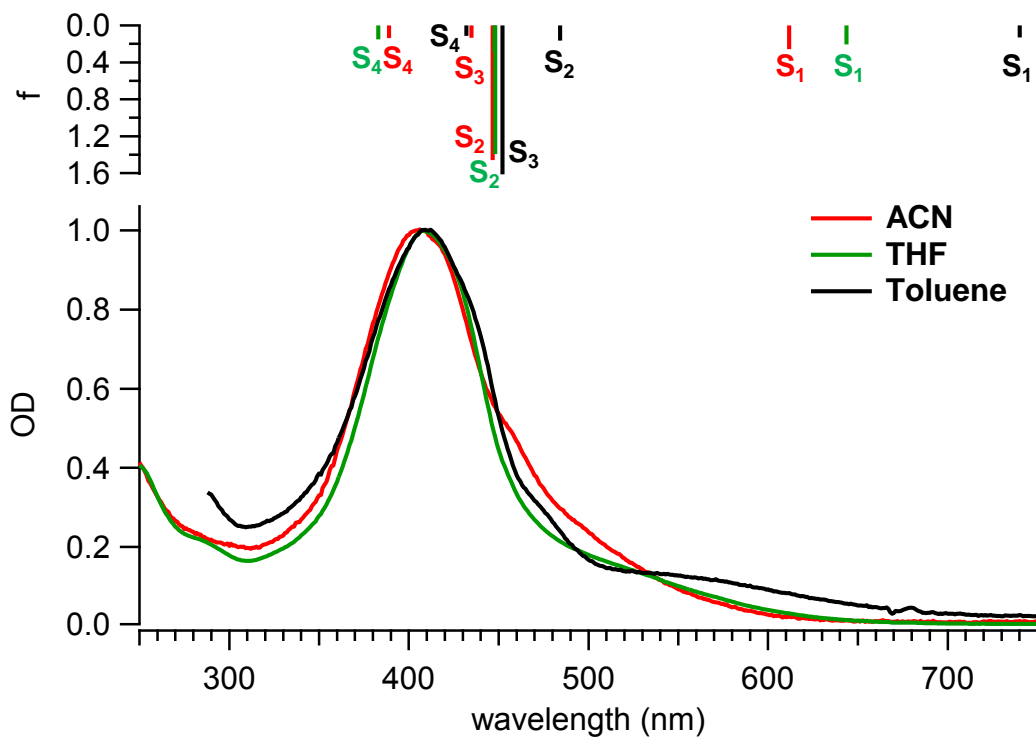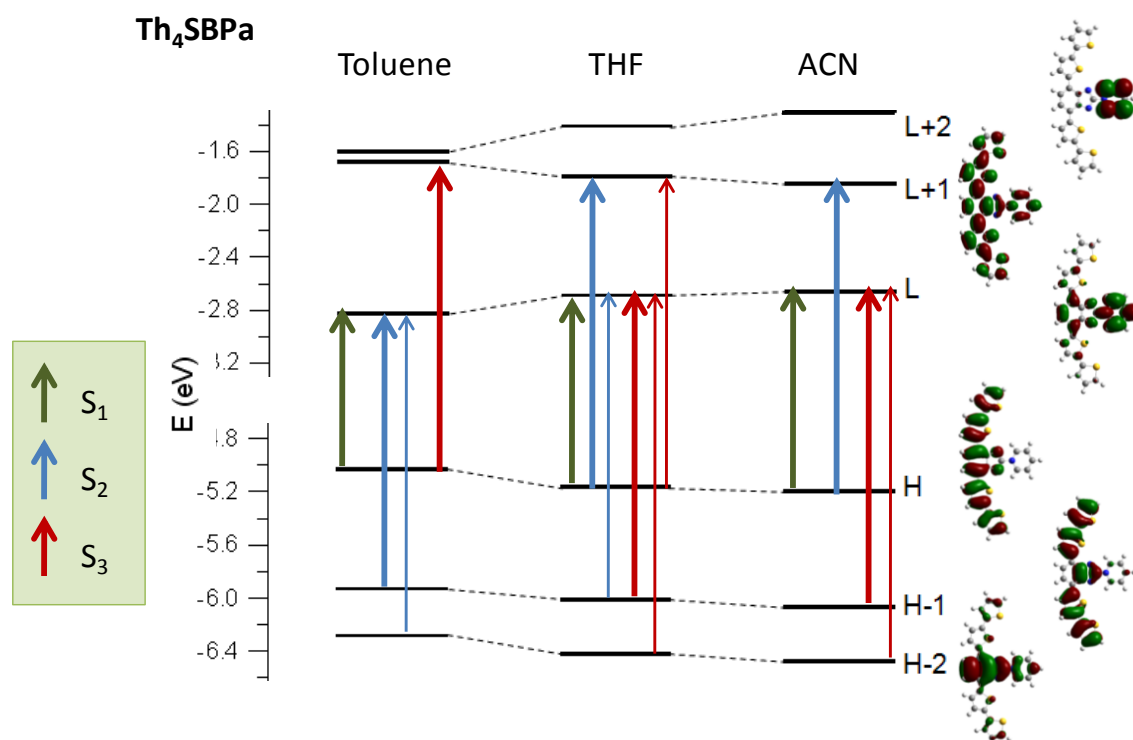**Figure VI.3** Absorption characteristics of Th$_4$SBPa: a) stationary absorption spectra and PCM-TDDFT transitions in three solvents of different polarity; b) PCM-DFT energy diagram and representation of the orbitals involved in the four lowest energy transitions.

As a confirmation, excellent accordance is found with the predicted TDDFT $S_0 \rightarrow S_3$ (ACN and THF) or $S_0 \rightarrow S_4$ (toluene) transitions that correspond in fact to a H $\rightarrow$ L+1 ($\pi\pi^*$) excitation engaging mainly the thiophenic π system, as seen in the MO diagram of figure VI.2b (note that the L+1 and L+2 orbitals are inverted in toluene compared to the two other solvents).

In Summary, the Th_2SBPa molecule is characterized by a strong, non solvatochromic $S_0 \rightarrow S_3(\pi$-$\pi^*)$ absorption band localized in the thiophene-phenyl-thiophene group, a $S_0 \rightarrow S_2(CT)$ band of medium intensity showing negative solvatochromism, and a weak shoulder corresponding to $S_0 \rightarrow S_1(CT)$, also undergoing negative solvatochromism.

VI.2.2 Th_4SBPa: lack of CT band

In figure VI.3a are presented the stationary absorption spectra of Th_4SBPa in three different solvents together with the corresponding PCM-TDDFT transitions with the same level of calculation as for Th_2SBPa (see also table VI.1). The related PCM-DFT energy diagram and representation of the involved MOs are displayed on figure VI.3b, where the excitations contributing to the transitions (three first singlet states) are also shown.

At first glance, unlike the Th_2SBPa and SBPa cases, no well-defined band showing a characteristic solvatochromic effect can be distinguished. However, a broad and weak absorption tail extending far in the red region and displaying some solvatochromic behaviour, already observed in the bithiophenic molecule, is still present. It is attributed on the basis of the TDDFT calculation to the $S_0 \rightarrow S_1(CT)$ transition. As previously found for Th_2SBPa and SBPa, the S_1 state is thus due to the HOMO $\rightarrow$ LUMO transition (green arrows in figure VI.3b).

In addition to this weak $S_0 \rightarrow S_1(CT)$ transition, an intense band peaking at 410 nm is noticed, which does not show any solvatochromism. It is fundamental to notice that the band maximum is almost at the same position as the lowest energy absorption of the 5T molecule (417 nm [168]), suggesting a localization of the excitation in the bithiophene-phenyl-bithiophene chain. In fact, according to the TDDFT calculation (see figure VI.3b), this band is easily recognized as due to the $S_0 \rightarrow S_2$ absorption in ACN and THF and $S_0 \rightarrow S_3$ absorption in toluene, which arise mainly from a H $\rightarrow$ L+1 ($\pi\pi^*$) excitation localized in the thiophenic system. The nature of this transition is thus strictly similar to that observed at $\sim$350 nm for Th_2SBPa.

At this point, one wonders if the CT solvatochromic band is really missing or if it is just hidden by the intense $S_0 \rightarrow S_{2(3)}(\pi\pi^*)$ absorption. Indeed, in the analysis of the Th_2SBPa data, we observed that the main $S_0 \rightarrow S_2(CT)$ band was insensitive to the substitution by thiophenic groups. The presence of this CT transition can thus also be expected on the one hand around 400 nm in Th_4SBPa. On the other hand following the analogy with 5T molecule a strong $\pi\pi^*$ absorption band is expected also at the same position [168]. Comparing now the energy diagrams in figure VI.3b, it reveals that, the H-1 orbital related with solvatochromic band in the case of SBPa and Th_2SBPa is correlated with the H-2 orbital in the case of Th_4SBPa. As a consequence it suggests that the characteristic CT transition corresponds to a $S_0 \rightarrow S_4(CT)$ rather than $S_0 \rightarrow S_2(CT)$ transition (see table V.1) and is thus somewhat shifted to higher energy. As we will see later, femtosecond experiments will be decisive to determine if the CT state is populated in the case of Th_4SBPa.

In summary, stationary absorption experiments together with theoretical calculations have shown that, after substitution of two thiophenic rings to the SBPa parent molecule, the transition showing the characteristic solvatochromic behaviour is still present as the main absorption in the visible region, which allows us to expect unchanged ICT processes upon photoexcitation within this transition ($\sim$400 nm). However, an additional strong $\pi\pi^*$ UV absorption of the thiophene-phenyl-thiophene chain might induce some novel photophysical processes upon excitation below 400 nm. On the other hand, increasing the size of the substituted groups to bithiophenic units seems to drastically weaken or totally suppress the solvatochromic CT band in favour of the thiophenic chain absorption.

In the following, in subsection VI.3, we will first study the transient spactroscopy of Th_2SBPa upon excitation i) near 400 nm, i.e., in resonance with the $S_0 \rightarrow S_2(CT)$ transition; ii) near 500 nm as an attempt to directly excite the $S_1(CT)$ state; iii) well below 350 nm (266 nm excitation) as an attempt to identify the influence of populating the $S_3(\pi\pi^*)$ state. Furthermore, repeating experiments in different solvents will allow estimating the role of the solvent in the photophysics and discussing whether large-amplitude geometrical changes arise. In subsection VI.4, the photophysics of Th_4SBPa will be reviewed by using 390 and 266 nm pump excitations. Finally, conclusions about ability of such thiophene substituted SBPa molecules to be used as photo-switches will be discussed.

VI.3   Transient absorption spectroscopy of Th_2SBPa

The analysis of the Th_2SBPa stationary absorption data revealed the presence of three different, well separated states:

- $S_2(CT)$ for which similar ultrafast CT dynamics as for the parent SBPa molecule can be expected upon 390 nm excitation

- $S_1(CT)$ for which the adiabatic mechanism evidenced in the case of TwSBPa can be expected upon red-shifted excitation

- $S_3(\pi,\pi^*)$ for which deactivation pathways engaging mostly the thiophenic groups can be expected upon UV excitation.

Consequently, in the following we will report transient absorption results using different excitation wavelengths with the final goal to explore all possible deactivation pathways of Th_2SBPa following excitation.

VI.3.1   390 nm excitation of the $S_2(CT)$ state

Similarly to the previous chapter, femtosecond transient absorption data using 390 nm excitation adjusted near the $S_2(CT)$ absorption band maximum (420 nm in THF, figure VI.2a) will be analysed first. Because the best quality data were obtained in THF, this solvent is chosen as a representative case and the related results are presented before all. Then these data will be compared with those obtained in various solvents to investigate the influence of the environment on the photoreactivity. As it will be shown, a similar behaviour as that previously discussed for SBPa was found; therefore the presentation of the transient absorption spectra is similarly divided into three temporal windows.

VI.3.1.1   Photophysics of Th_2SBPa in THF.

Figure VI.4a – c presents the time evolution in the femto-picosecond time domain of the transient absorption spectra of Th_2SBPa in THF following excitation at 390 nm.

<u>Initial dynamics.</u> Between -1 and 0.6 ps, (figure VI.4a), the appearance of an excited state absorption band named $\mathbf{Y_1}$ with a maximum near 520 nm can be observed, together with that of the negative bleach band **B**. The characteristic time found for this process is τ_1 = 106 fs. This first spectrum is very similar to that observed previously for SBPa within the same temporal window (see figure V.1a). For this reason and because the 390 nm

excitation is in resonance with the $S_0 \rightarrow S_2$ charge-transfer transition, this spectrum is likely attributable to the $S_2(CT)$ state. The fact that no stimulated emission (**SE**) signal is present for Th_2SBPa is consistent with the lack of stationary emission.

CT dynamics. Figure VI.4b shows a decrease of band $\mathbf{Y_1}$ concomitantly with the growth of a new band $\mathbf{Y_2}$ with maximum near 590 nm, within the temporal window [0.65 – 1.5 ps] with a characteristic time of $\tau_2 =$590 fs. A clear isosbestic point is present at ~520 nm during this evolution, whereas no recovery of the ground state occurs (**B** band stable in time). Almost exactly the same spectral evolution was found for SBPa molecule (see figure V.1b) allowing to immediately assign the $\mathbf{Y_1} \rightarrow \mathbf{Y_2}$ process to the already encountered $S_2(CT) \rightarrow S_1(CT)$ ultrafast ICT process. Besides spectral similarities with the parent SBPa molecule, the characteristic times related to this process are also similar: 0.59 ps for Th_2SBPa in THF and 0.4 ps for SBPa in the same solvent.

Post-CT dynamics. The decay of all signals (excited state absorption band $\mathbf{Y_2}$ and bleach **B**) takes place between 1.5 and 100 ps and is presented in figure VI.4c. Surprisingly, this process was found to be mono-exponential and not double-exponential as observed for SBPa. The characteristic time of $\tau_3 = 7.6$ ps of this decay is undeniably more similar to the SBPa decay component ascribed to the $S_1(CT)$ state depopulation (2.6 ps) rather than to that associated to the $S_1(E)$ state depopulation (134 ps). As a consequence, we assigned the 7.6 ps kinetics to the $S_1(CT)$ decay by internal conversion to the ground state. After 100 ps there is still a very weak residual signal which can indicate some negligible creation of a triplet state (in the following, we will ignore the ISC process).

In summary, after 390 nm excitation within the $S_0 \rightarrow S_2(CT)$ absorption, the main photophysical mechanism found for Th_2SBPa is nearly similar to that observed for the parent SBPa molecule: after excitation, the initial Franck-Condon configuration $S_2(FC)$ evolves in less than 100 fs to the relaxed $S_2(CT)$ state and further ICT evolution proceeds with the $S_2(CT) \rightarrow S_1(CT)$ internal conversion within less than 600 fs in THF without any population of an emissive $S_1(E)$ state. Finally, the latter state relaxes in 7.6 ps mainly through internal conversion to the ground state (accompanied with negligible ISC process). Therefore, after symmetrical substitution of two thiophene rings to the SBPa molecule, the ICT mechanism remains unchanged. It is now interesting to check if the CT characteristic time follows the same dependences on environment properties as in the parent molecule.
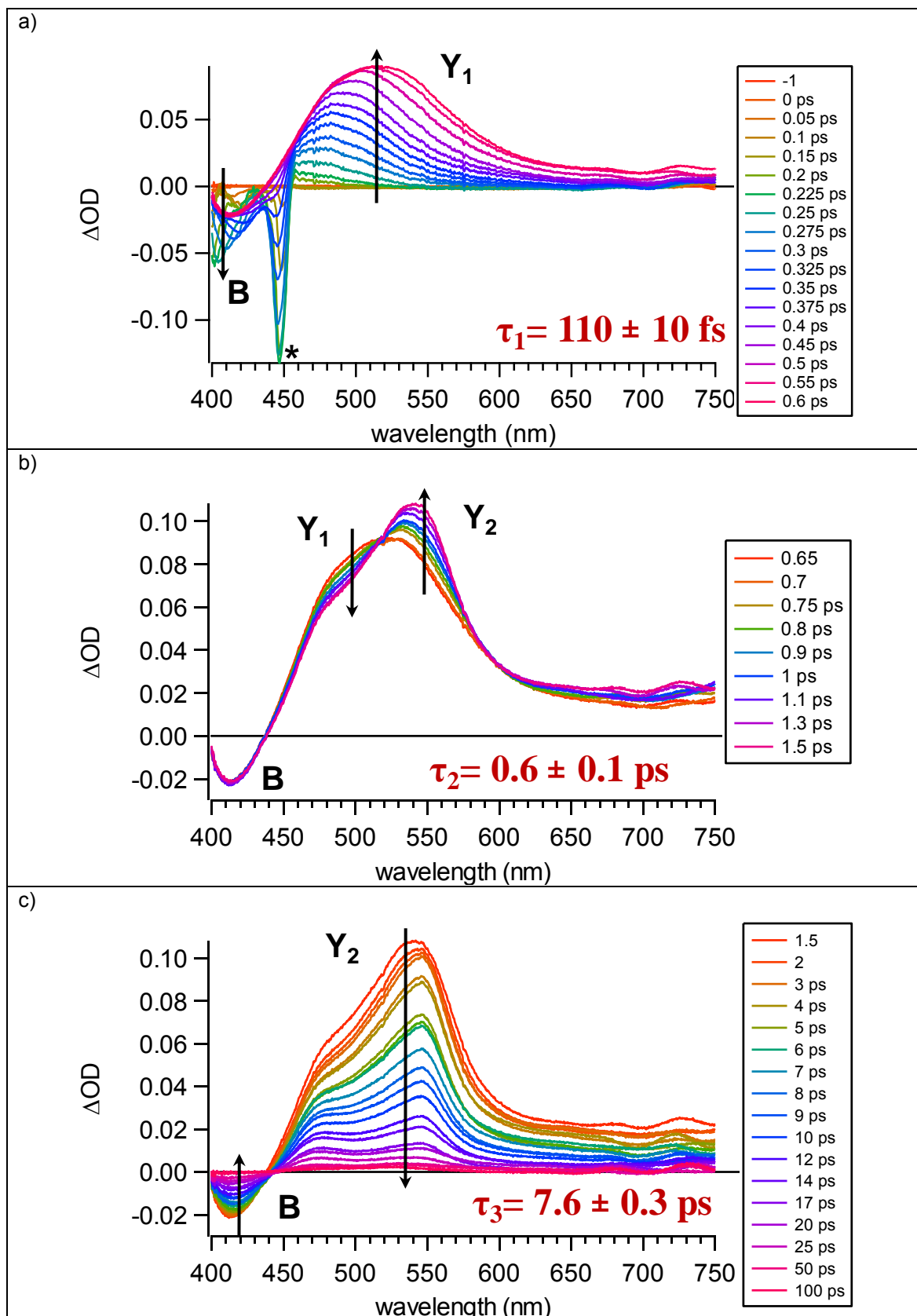
Figure VI.4 Femtosecond transient absorption spectra following 390 nm excitation of Th$_2$SBPa in THF in three temporal windows: a) -1 – 0.6 ps; b) 0.65 – 1.5 ps and c) 1.5 – 100 ps. All characteristic times are obtained with global fitting method. The star indicate stimulated Raman pick of the solvent. Pump-probe correlation time: τ = 190 fs

VI.3.1.2 Solvent dependency of the Th$_2$SBPa CT characteristic time τ_2

As it was done for the parent molecule, Th$_2$SBPa transient absorption spectra were measured in different solvents in order to check the influence of the environment on the photophysics. All characteristic times obtained by global fitting are gathered in table VI.2 together with some solvent parameters: dielectric constant, viscosity and average solvation time. As observed in figure VI.5 for three typical solvents, the characteristic ICT evolution (concomitant decrease of band **Y$_1$** and rise of band **Y$_2$** with clear isosbestic point in between) was found whatever the viscosity or polarity of the solvent. We analyze first the dependency of the corresponding characteristic time τ_2 on the solvent properties by analogy with the results obtained above for SBPa.
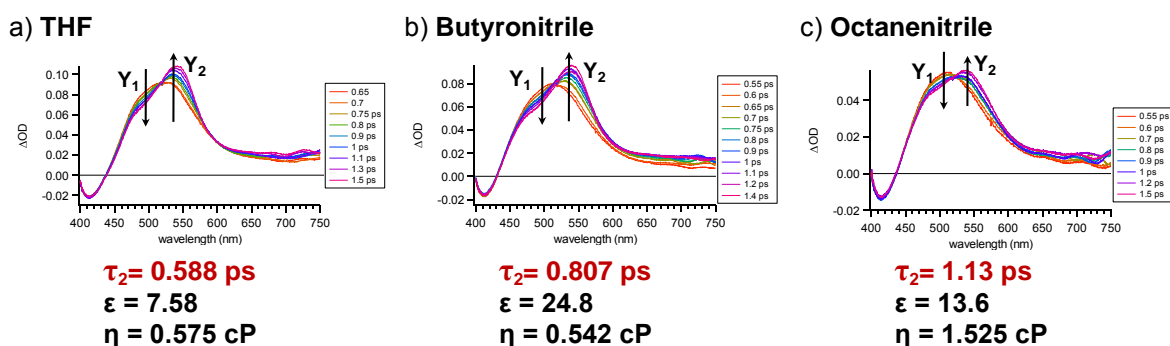
Figure VI.5 Femtosecond transient absorption spectra showing the ICT evolution for Th$_2$SBPa in a) THF (temporal window [0.65 – 1.5 ps]), b) butyronitrile (temporal window [0.55 – 1.4 ps]) and c) octanenitrile (temporal window [0.55 – 1.5 ps])

Dependency of τ_2 on the solvation time. In figure VI.6a, the dependency of the ICT characteristic time τ_2 on the solvation time is shown together with its linear fit (green line). For comparison, the corresponding fit previously obtained for SBPa is also displayed (pink line). As only one protic solvent was studied for Th$_2$SBPa (methanol), it was not taken into consideration in this analysis. As one can see, the correlation for Th$_2$SBPa is much less convincing than it was for the parent molecule. The conclusion in chapter V that the ICT process in SBPa is purely controlled by the solvent (slope ~0.92) seems to be no longer true for Th$_2$SBPa (slope ~0.16). Note however that the correlation parameter (R^2) is very small, mostly due to the bad octanenitrile point. Anyhow, considering that the correlation is really reduced, the following interpretation can be proposed: besides the solvent coordinate, a second reaction coordinate is required to describe the ICT process in the case of Th$_2$SBPa according to Sumi-Marcus theory [94]. Note that similar result was obtained for TwSBPa molecule.

Dependency of τ_2 on the solvent viscosity. In figure VI.6b, a correlation of the ICT characteristic time τ_2 on the solvent viscosity is presented (green line) together with that previously established for SBPa (pink line). Again much weaker relationship was found for the thiophenic compound, the slope of the linear correlation being reduced by one order of magnitude. This apparent weak solvent viscosity dependency is likely to be only a reflection of the weak solvation time dependency reported just above.

Dependency of τ_2 on the solvent polarity. In figure VI.6c, the dependency of the ICT characteristic time τ_2 on the solvent polarity parameter (dielectric constant) is presented together with the corresponding SBPa results. Both molecules show quite similar behaviour, i.e., a very weak solvent polarity dependency. By analogy one can predict that the ICT process arises within the Marcus inverted region for Th$_2$SBPa as for SBPa. This conclusion is consistent with the previous observation that thiophenic substitution on the SBPa skeleton has almost no influence on the S$_2$(CT) and S$_1$(CT) energy levels involved in the ICT process.

Table VI.2. Characteristic times found by global fitting from the femtosecond transient absorption data of Th$_2$SBPa in different solvents and at different excitation wavelengths. Additionally, solvent parameters: dielectric constant (ε), viscosity (η) and solvation time ($<\tau>_{solv}$) are given.

Solvent	ε[a]	η (cP)	$<\tau>_{solv}$[b] (ps)	τ_{grwoth} (ps)	τ_2 (ps)	τ_3 (ps)	τ_4 (ps)
LASIR – 390 nm excitation							
ACN	35.9	0.345	0.27	0.073±0.002	0.3±0.1	3.1±0.1	
Butyronitrile	24.8	0.542	0.54	0.102±0.001	0.8±0.1	5.9±0.2	
Octanenitrile	13.6	1.525	3.94	0.111±0.002	1.1±0.2	13.8±0.5	
THF	7.58	0.575	0.94	0.106±0.004	0.7±0.1	7.6±0.3	
Ethyl Acetate	6.02	0.426	0.86	0.106±0.004	1.0±0.2	7.3±0.3	
Methanol	32.7	0.593	5	0.089±0.002	0.4±0.1	4.9±0.1	
LASIR – 266 nm excitation							
ACN	35.9	0.345	0.27	0.158±0.003	a	1.9±0.1	28 ± 2 160 ± 20
Leuven – 495 nm excitation							
THF	7.58	0.575	0.94	0.105±0.010	0.7±0.2	7.5±5.0	
Octanenitrile	13.6	1.525	3.94	0.104±0.013	1.7±0.6	10.5±5.0	

[a]Not observed (see text)
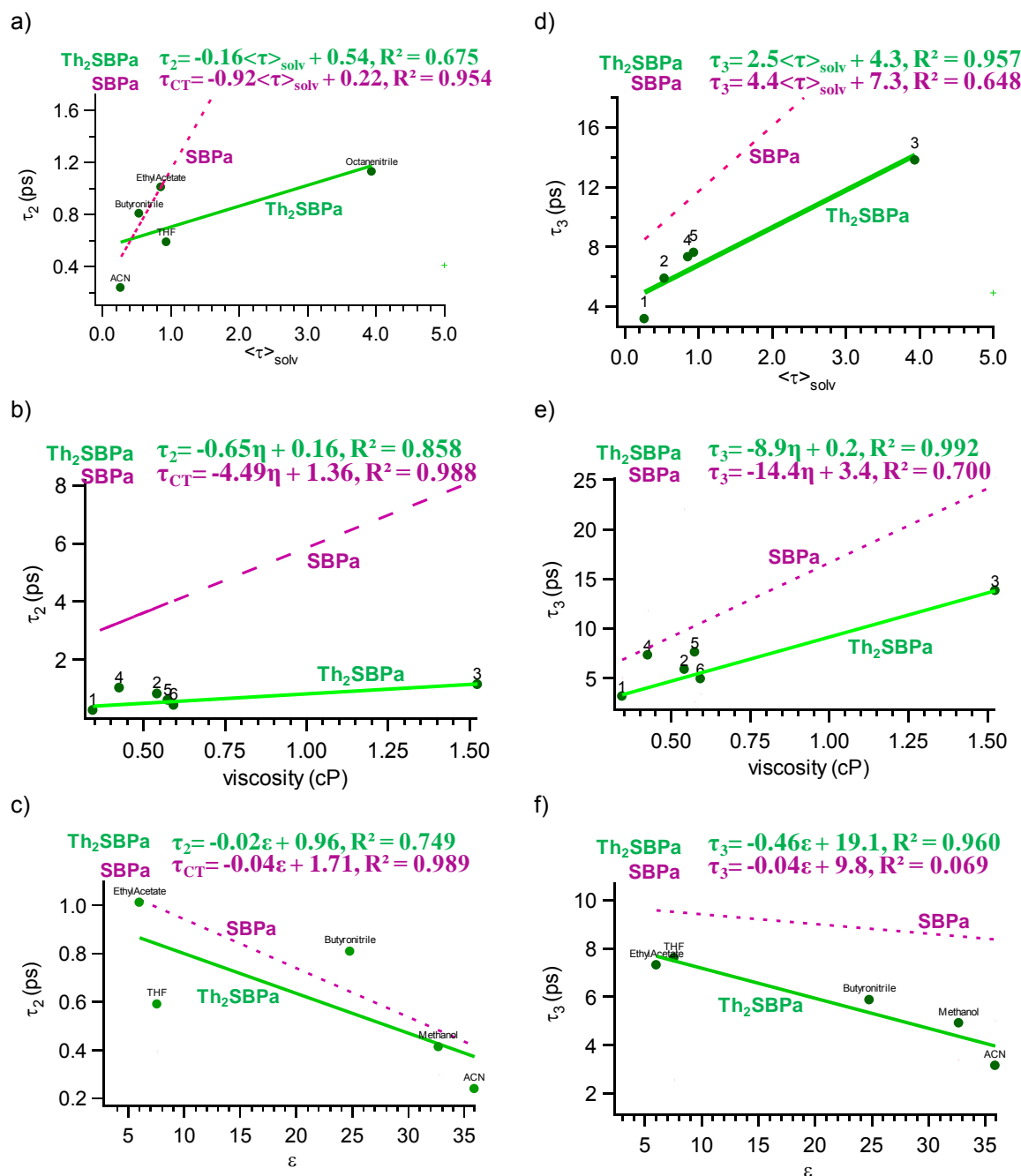
Figure VI.6. Plots of the Th$_2$SBPa time constants τ_2 (S$_2 \rightarrow$ S$_1$ ICT process) and τ_3 (S$_1$(CT) lifetime) measured upon 390 nm excitation as a function of a) and d) the solvation time; b) and e) the solvent viscosity; and c) and f) the solvent polarity.

VI.3.1.3   Solvent dependency of the Th$_2$SBPa decay time τ_3

Figure VI.6 d-f presents linear correlations (green lines) of decay time τ_3 on the solvation time, solvent viscosity, and solvent polarity. Similar correlations made in the previous chapter for the parent SBPa molecule are also shown to facilitate the comparison (pink lines). One should remind that this time characterizes the internal conversion from S$_1$(CT) to the ground state, which corresponds thus to an intramolecular back charge transfer.

183

Dependency of τ_3 on the solvation time. As shown in figure VI.6d, a quite good accordance with the results obtained for SBPa is found, the slope of the linear correlation being only two times smaller for the thiophenic molecule. Moreover, the quality of the correlation ($R^2=0.957$) is significantly higher compared to that of the parent molecule. It is attempting to consider than a lower $S_1(CT)$ dipole moment in Th_2SBPa compare to the parent molecule could be responsible for lower necessity of solvation. This would be consistent also with some screening effect induces by large thiophene groups (larger Onsager cavity radius).

Dependency of τ_3 on the solvent viscosity. Again, as seen in figure VI.6e, a better correlation with viscosity is found for Th_2SBPa decay time τ_3, than it was for the parent molecule ($R^2=0.992$). Moreover, the slope of the fit is again almost half that found for SBPa, which brings the strong evidence that the viscosity dependency is only a reflection of the solvation time dependency, and thus no large-amplitude geometrical change arises in the excited state.

Dependency of τ_3 on the solvent polarity. Figure VI.6f shows the dependency of the decay time τ_3 on the solvent polarity. Surprisingly, nearly ten times higher dependency was found for Th_2SBPa than for the parent molecule and the correlation coefficient is excellent ($R^2=0.992$). The data for the parent molecule were not straightforwardly interpreted: a partition between weakly and highly polar aprotic solvents was necessary (see figure V.19) due to either dimerization or inverted/normal Marcus regime competition. Possible equilibrium between $S_1(E)$ and $S_1(CT)$ was also suggested. For the thiophenic analogue, the observed strong dependency with polarity is likely interpreted as a clear manifestation of the $S_1(CT)$-S_0 energy gap law. As the energy gap is controlled by the molecule solvatochromism, the internal conversion rate is a function of the gap size and thus of the solvent polarity. Similar results were found for the twisted molecule TwSBPa (see figure V.25b).

In summary, using a 390 nm excitation that matches the maximum of the solvatochromic band, almost the same transient absorption evolution has been observed for Th_2SBPa as for the parent SBPa molecule. The only difference is the fact that no evidence for population of a $S_1(E)$ state was found. But, undeniably, the most important process of intramolecular charge transfer $S_2(CT) \to S_1(CT)$ is still present in the thiophene substituted molecule. Since from stationary absorption spectra a weak $S_0 \to S_1(CT)$ state absorption

was observed for Th_2SBPa, it is interesting to check if it is possible to populate directly the $S_1(CT)$ state, without passing by the S_2 state. Such non-adiabatic mechanism has been found for TwSBPa. In this regard, femtosecond transient absorption experiments using an excitation wavelength at 495 nm – close to S_1 absorption – will be now discussed.

VI.3.2   495 nm excitation – attempt to excite the $S_1(CT)$ state

The oscillator strength of the $S_0 \rightarrow S_1$ transition is much weaker than for the $S_0 \rightarrow S_2$ transition, but it is still stronger than in the SBPa molecule. Direct excitation of the $S_1(CT)$ state using 495 nm excitation was not possible with our experimental set-up and was performed at the Katholieke Universiteit of Leuven in collaboration with Eduard Fron[17].

Figure VI.7 b and d shows kinetics recorded upon 495 nm excitation for Th_2SBPa in THF and octanenitrile, respectively. Two probe wavelengths at 510 nm (red trace) and 550 nm (blue trace) were monitored, which are lying just below and beyond the $\mathbf{Y_1 \rightarrow Y_2}$ isosbestic point (see figure VI.4b) and characterize the $\mathbf{Y_1}$ and $\mathbf{Y_2}$ band maxima, respectively. To facilitate the comparison, similar data recorded upon 390 nm excitation are also displayed (figures VI.7 a and c).

All kinetics were fitted using global fitting method and for all of them three characteristic times were found. The first time is the same (within matching errors) for both solvents and wavelengths, and corresponds to the time resolution of the used setup. The third characteristic time is hard to estimate accurately in the 495 nm experiment since only a short time delay window has been monitored. However, for each solvent, approximately similar τ_3 values are found at both pump excitations. The most striking and valuable conclusion from this experiment comes from comparison of the ICT characteristic time τ_2. For each solvent, very close τ_2 values are found at both excitation wavelengths, 0.69 and 0.7 ps in THF and 1.3 and 1.7 ps in octanenitrile. We conclude that, surprisingly, similar photophysics is achieved at both excitations. This observation implies that the S_2 state is populated in both cases. As a matter of facts, due to the notable overlap between the $S_0 \rightarrow S_2$ and $S_0 \rightarrow S_1$ bands, the intensity of the $S_0 \rightarrow S_2$ is not negligible at 495 nm. Therefore we must admit that this longer excitation wavelength still reaches dominantly the S_2 potential curve.

---

[17] Parameters of the experimental setup: resolution of 100 fs, pump/probe wavelengths tunable between 350 and 1000 nm, sensitivity up to 0.0001 change in optical density.
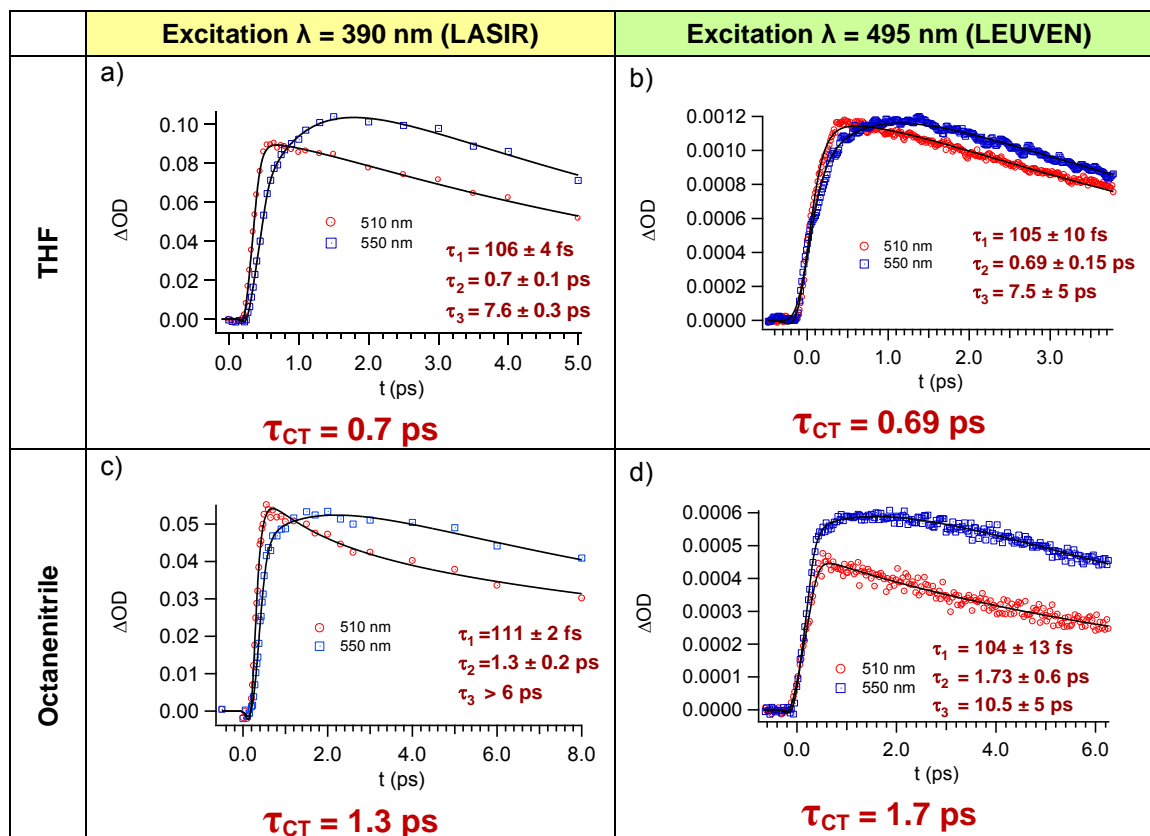
Figure VI.7 Kinetics of femtosecond transient absorption of Th$_2$SBPa for two different solvents and excitation wavelengths: a) THF, λ_{ex} = 390 nm; b) THF, λ_{ex} = 495 nm, (in Leuven); c) octanenitrile, λ_{ex} = 390 nm; d) octanenitrile, λ_{ex} = 495 nm (in Leuven)

So, in conclusion, we failed by using 495 nm excitation to detect the direct ICT mechanism by exciting directly the S$_1$(CT) state although it was well characterized with its solvatochromic long tail. In the future, we propose to use still lower excitation energy, around 550 nm, where only the S$_0 \rightarrow$ S$_1$ transition has significant contribution.

VI.3.3   266 nm excitation of the S$_3$($\pi\pi^*$) state

We now try to check if the ICT process still happens upon excitation within the strong $\pi\pi^*$ transition localized in the thiophene-phenyl-thiophene part of the molecule. In order to observe the photophysics while this state is excited, additional femtosecond transient absorption experiments using 266 nm excitation wavelength were done.

In figure VI.8 a – d, the time evolution of the transient absorption spectra within the 320 – 760 nm spectral range after excitation at 266 nm is presented. For clarity, the data are divided into four temporal windows. The stationary absorption spectrum of Th$_2$SBPa and its fluorescence spectrum upon 266 nm excitation are added in figure VI.8e in order to help the comprehension of these complicated transient data.

Stationary Spectra (figure VI.8e). The absorption spectrum has been well commented previously (subsection VI.2.1). The observed λ_{max} ~340 and 360 nm ($S_0 \rightarrow S_3$ $\pi\pi^*$ transition) and ~400 nm ($S_0 \rightarrow S_2$ ICT transition) are indicated by green solid-line. Whereas no fluorescence could be detected upon excitation of Th_2SBPa at 390 nm, a strong emission spectrum peaking at 410 nm is induced at 266 nm. For comparison, the emission spectra of terthiophene (3T) and SBPa are presented as well. One notices immediately the similarity of the Th_2SBPa and 3T emission spectra whereas the Th_2SBPa and SBPa spectra are highly different. The Th_2SBPa emission seems to be the mirror image of the $S_0 \rightarrow S_3$ absorption band, which suggests that the Th_2SBPa emission has $\pi\pi^*$ character [163, 172] and is localized on the thiophene-phenyl-thiophene chain. These results and the fact that no emission signal is detected for 390 nm excitation confirms that the $S_3(\pi\pi^*)$ state (i) is the emissive state or its direct precursor and (ii) does not relax entirely to the $S_2(CT)$ and $S_1(CT)$ states. As a consequence, during transient absorption experiments upon 266 nm excitation one can thus expect to detect additional transient species compare to 390 nm excitation.

First temporal window [-1 – 1.5 ps] (figure VI.8a) In this time domain, a spectrum showing both negative component below 430 nm and a positive absorption above 430 nm is growing with a time constant of τ_1=160 fs (pump-probe correlation time τ = 290 fs) The negative signal presents two features between 320 and 430 nm. Its shape is clearly the opposite of the steady-state absorption spectrum, which allows to assign it to a bleach signal **B**. The negative band peaking at 400 nm corresponds also to the position of the emission and is probably a combination of bleaching and stimulated emission components (**B+SE**). Besides this negative signal, an excited state absorption band labelled as **W_0** can be observed between 430 and 670 nm.

Even if we did not observe the characteristic band **Y_1/Y_2** evolution like the 390 nm excitation case (figure VI.4b), we emit the hypothesis that ICT reaction has already occurred within τ_1=160 fs. Indeed, it is worth to notice that this early spectrum **W_0** resembles that observed at 1.5 ps upon 390 nm excitation. In particular, striking similarity is noticed between the absorption band W_0 and the **Y_2** band ($S_1(CT)$ absorption) present in the 1.5 ps spectrum recorded with 390 nm excitation (figure VI.4b).
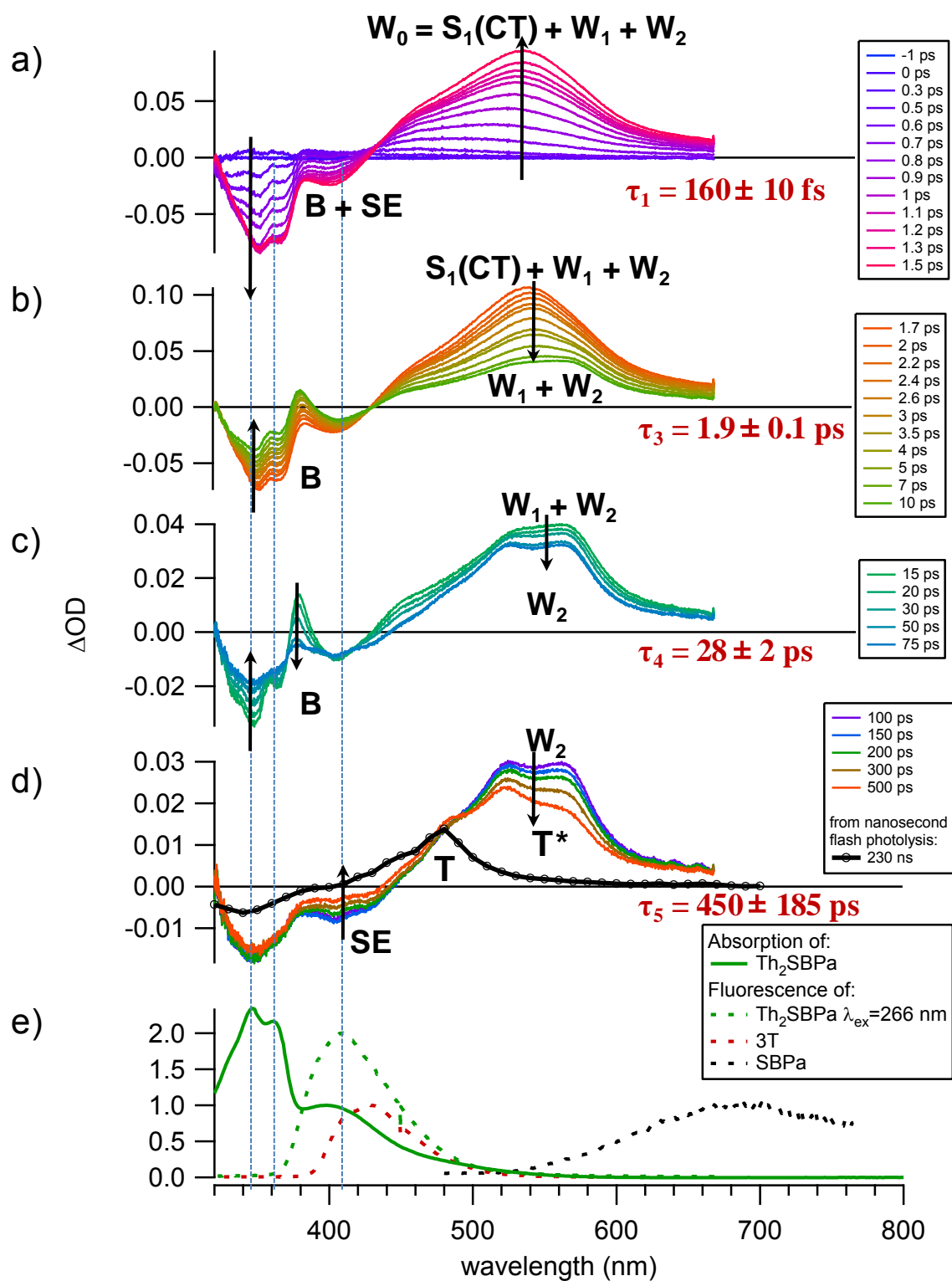
Figure VI.8 Femtosecond transient absorption spectra of Th2SBPa in ACN after excitation with 266 nm pulse, divided into four temporal windows: (a) -1 – 1.5 ps, (b) 1.7 – 10 ps, (c) 15 – 75 ps, and (d) 100 – 500 ps; (e) stationary absorption and fluorescence spectra of Th_2SBPa and emission spectra of terthiophene (3T) and SBPa (pump-probe correlation time τ = 290 fs).

When these two bands are normalized (figure VI.9), one can see that their maximum is at the same position, but the band width is much broader at 266 nm than at 390 nm excitation. Therefore, the ICT dynamics (band **Y$_1$/Y$_2$** evolution) might be hidden by some overlapping signal coming from additional internal conversion from higher excited state occurring with close characteristic time (see also discussion in section V.2.4). It is thus conceivable that band **W$_0$** is a sum of a S$_1$(CT) absorption contribution and additional signals. In particular, in the hypothesis that the 400 nm negative band is partly due to stimulated emission, the **W$_0$** absorption band must include some contribution related to the emissive excited state.

We need to take a little anticipation and to note that compare to 390 nm excitation, two additional decays are reported (without any additional growing signal). So, one can make the hypothesis of parallel population of three states: S$_1$(CT) state and two additional states giving birth of two transient bands, abbreviated as **W$_1$** and **W$_2$**, are responsible for red and blue wings of band **W$_0$**. By sake of simplicity, one can resume the situation like: **W$_0$=S$_1$(CT) + W$_1$+ W$_2$**
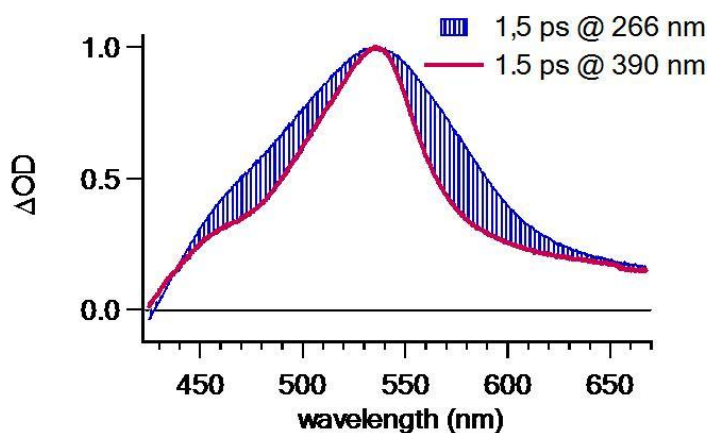
Figure VI.9 Comparison of transient absorption signals at 1.5 ps for Th$_2$SBPa in ACN at two different wavelengths of excitation: 390 nm (in pink) and 266 nm (in blue).

Second temporal window [1.7 – 10 ps] (figure VI.8b). Within this temporal window a mono-exponential decay of the **W$_0$** positive band proceeds until 10 ps concomitantly with a decrease of the negative bands (both features), with an isosbestic point at ~420 nm. This evolution can be safely explained as a recovery of the ground state. This decay can be compared to that observed for band Y$_2$ in the transient spectrum of Th$_2$SBPa following 390 nm excitation (see fig VI.4c for the THF solvent) and the characteristic time measured for this process (1.9 ps) is somewhat analogous to the 3 ps value found in the 390 nm

experiment in ACN. We thus propose to assign the 1.9 ps kinetics to the decay of the contribution to the W_0 band due to the $S_1(CT)$ state, i.e., to the internal conversion process, $S_1(CT) \rightarrow S_0$. However, whereas upon 390 nm excitation all transient signals disappear completely during this process, at 266 nm excitation a residual transient spectrum is still present at the end of the decay as well in the bleach/**SE** region as in the absorption region. This confirms the existence of different spectral components contributing to the W_0 absorption. The residual absorption comprises two maxima at 525 and 560 nm.

Third temporal window [15 – 75 ps] (figure VI.8c). This time domain is characterized by a complex spectral evolution arising with a single-exponential kinetics of time constant 28 ps estimated from global fitting analysis. During this evolution, the main absorption band in the 480 – 600 nm range does not change markedly. More perceptible spectra evolution is noticed for the sharp peak at 380 nm which reveals the decay of a broad absorption component. Simultaneous decay of the bleach signal in the same region leads to a complex spectral change with at least 2 isosbestic points. This indicates that at least two different absorption components contributed to the 15 ps trace: the above broad absorption decaying in 28 ps, designed as W_1 in Fig. V.8, and the spectrum remaining after 75 ps, designed as W_2.

In order to assign the W_1 and W_2 species, it is worth to remind that neither of them is formed upon excitation at 390 nm. Both of them should thus arise specifically from the excitation of a state that cannot be populated with longer excitation wavelength than 266 nm, such as the $S_3(\pi\pi^*)$ state localized in the thiophene-phenyl-thiophene group or another close-lying upper excited state. Even if definite attribution cannot be achieved, it appears relevant to note that the 28 ps decay time found for species W_1 is very close to the 23 ps decay of the $S_1(E)$ state in TwSBPa (Chap. IV.4.2). As discussed earlier for TwSBPa, emission is not possible due to electronic decoupling of the pyridine and betaine parts. Several similarities can be found for the TwSBPa and Th_2SBPa molecules: a lack of both stationary emission from $S_1(E)$ as well as corresponding **SE** (in the red region) and a decaying process with similar characteristic time. Based on these analogies, we propose that, for Th_2SBPa, the decay of 28 ps related with W_1 species may describe $S_1(E) \rightarrow S_0$ internal conversion. One has to still identify the W_2 species.

Fourth temporal window [100 – 500 ps] (figure VI.8d) The last event probed in this experiment occurs with a characteristic time of 450 ps. It shows the decay of the last

transient absorption band, **W$_2$**, with a concomitant diminution of the negative signal around 400 nm. However, no significant decay of the bleach band at 340 nm is observed during this process. This observation indicates that the 450 ps kinetics does not correspond to a ground state recovery process. The decrease of the 400 nm negative signal can thus be ascribed to a decay of the stimulated emission present at this wavelength, which means a depopulation of the emissive excited state. Accordingly, the absorption band W$_2$ is likely characterizing this emissive excited singlet state, which has been identified as a $\pi\pi^*$ state localized in the thiophenic system on the basis of an emission similar to that of 3T. The decrease of the 400 nm negative signal can also be due, in part, to the rise of a transient absorption in the same region. Such an assumption is consistent with the observation that the decay of the W$_2$ is more pronounced in its red part than in the blue part. An isosbestic point is indeed present at 490 nm.

Although the 450 ps kinetics is not fully achieved at a delay of 500 ps, it is thus clear that it corresponds to the decay of the emissive $\pi\pi^*$ excited singlet state (component **W$_2$**) to yield a new transient species absorbing in the 400-540 nm domain. An assignment of this species to an excited triplet state T$_1$ can be envisaged. In order to confirm this hypothesis, we undertook flash photolysis measurements to characterize the triplet state absorption of Th$_2$SBPa. A long-lived transient spectrum observed in degassed solution, strongly quenched in presence of oxygen, was indeed ascribed to the T$_1 \rightarrow$ T$_n$ absorption. For comparison, an illustration of this triplet state spectrum recorded at a delay of 230 ns is shown in figure V.8d. This spectrum presents, in addition to a bleach component around 440 nm, a transient absorption band peaking at 480 nm which resembles the 460 nm T$_1 \rightarrow$ T$_n$ absorption of 3T [169] and agrees nicely with the spectrum expected to arise from the decay of the Th$_2$SBPa $\pi\pi^*$ excited singlet state. We thus conclude that, indeed, the 450 ps kinetics is due to the ISC process S$_1(\pi\pi^*) \rightarrow$ T$_1(\pi\pi^*)$ mostly localized in the thiophene-phenyl-thiophene group. Note that the strong ISC quantum yield reported for the 3T molecule ($\Phi_T = 0.90$ in ACN [168]), is consistent with an efficient triplet creation in Th$_2$SBPa as well as the small ground state recovery observed from S$_1$.

In conclusion, the photophysics of Th$_2$SBPa after 266 nm excitation is clearly more complex than with 390 nm excitation. As summarized in the overall photophysical scheme displayed in figure VI.10, it appears to result from a combination of the intrinsic photophysics of SBPa on one hand and the typical photophysics of terthiophene on the other hand.
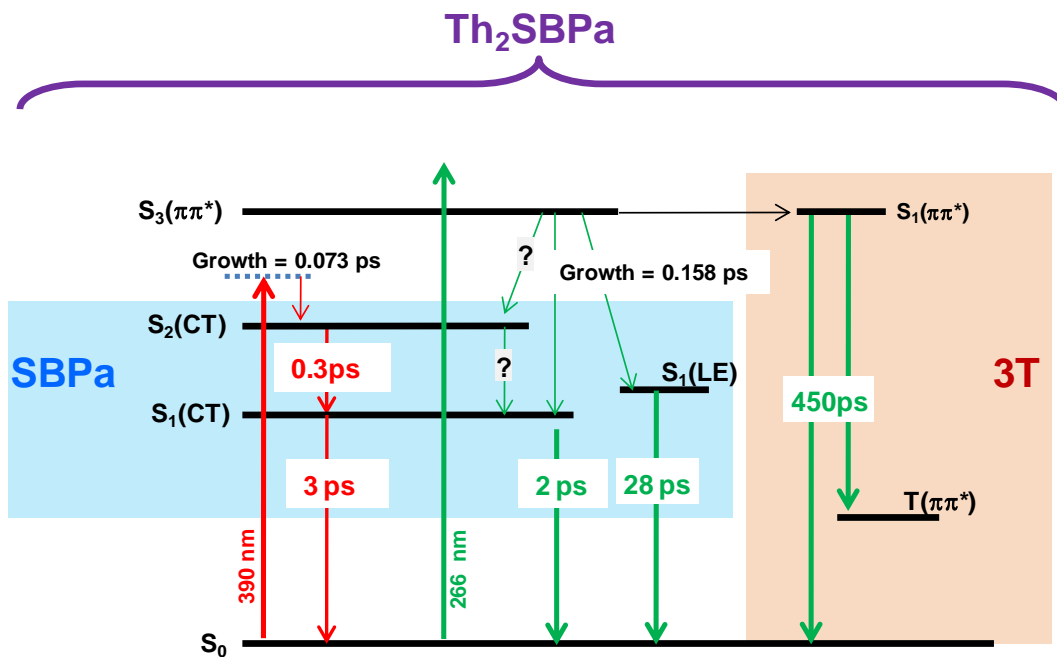
Figure VI.10 Photophysical scheme of Th2SBPa

It is still not established whether the $S_1(CT)$ state is populated directly from the $S_3(\pi, \pi^*)$ state, or via the $S_2(CT)$ state followed by $S_2(CT) \rightarrow S_1(CT)$ transition. In order to answer this question in the future, one can envisage to apply CASSCF calculations looking for possible conical intersection between $S_3(\pi, \pi^*)$ and $S_1(CT)$ states. Advanced HS-MCR analysis can also supply additional information. Note that both processes have to be considered as competitive processes.

VI.4   Transient absorption spectroscopy of Th$_4$SBPa

As discussed in subsection VI.2.2, Th$_4$SBPa seems to not show solvatochromic properties, apart from the weak $S_0 \rightarrow S_1$ transition. It was found that the S_2 state, which for SBPa and Th$_2$SBPa molecules was identified as a CT state, became for Th$_4$SBPa a $\pi\pi^*$ state with strong intensity. In fact, as discussed earlier, the missing CT state is correlated with the S_4 electronic state rather than the S_2 state, the former having energy just above the latter. Therefore even if stationary results show no evidence for the existence of a CT state in Th$_4$SBPa, it is still possible that the strong $\pi\pi^*$ absorption band overlaps and covers the weaker solvatochromic band. To check this hypothesis femtosecond transient absorption experiments for two different excitation wavelengths, 390 and 266 nm, were done.

With anticipation, it is fundamental to note here two decisive points: i) 390 nm and 266 nm excitations gave almost the same transient data (for this reason we will only show the latter case); ii) Th$_4$SBPa and Th$_2$SBPa transient data seem to be composed of the same temporal events. Accordingly, to facilitate the comparison, we will systematically adopt the same transient band notations for the Th$_4$SBPa data as for the Th$_2$SBPa ones (bands **W$_0$**, **W$_1$**, **W$_2$** and **T**).

VI.4.1   266 nm excitation

Figure VI.11 a – d show the spectral evolution of the Th$_4$SBPa transient absorption signal between 320 and 660 nm after excitation at 266 nm. As previously done for Th$_2$SBPa, these data are divided into four temporal windows for clarity. Additionally, stationary absorption and fluorescence spectra of Th$_4$SBPa in ACN are shown in part e of figure VI.11.

Sationary Results. (figure VI.11e) As discussed in subsection VI.2.2, the absorption spectrum of Th$_4$SBPa is dominated by the intense $S_0 \rightarrow S_2(\pi,\pi^*)$ transition peaking at 410 nm, localized in the thiophenic system, equivalent to the 350 nm $S_0 \rightarrow S_3(\pi,\pi^*)$ transition of Th$_2$SBPa. The emission spectrum shows one band in the 430-600 nm region with two vibronic features indicated by dashed lines at 470 and 490 nm. Similarities with 5T molecule indicate that such emission is related with $S_1(\pi\pi^*)$ state of the thiophenic system[171].

First temporal window [-1 – 1.6 ps]. (figure VI.11a) The early dynamics with a characteristic time of 250 fs is dominated by the fast appearance of an excited state absorption band W_0 with a maximum at 650 nm and negative band **(B + SE)** with two features peaking near 410 nm and less clearly 480 nm. The 410 nm component corresponds undeniably to the stationary absorption spectrum and is thus ascribed to bleaching. The second negative shoulder at 490 nm is likely to correspond to the emission spectrum and is thus ascribed to **SE** process. The lack of vibrational structure in the **SE** signal can be explained by the fact that, at early time, the emissive state is populated in a vibrationally hot, unrelaxed conformation. Band W_0 is thus certainly ascribable, at least in part, to the emissive excited singlet state. However, as it will be seen below, the decay of band W_0 is complex and arises via at least three steps, which indicates that, as for Th_4SBPa, various transient species are contributing to the spectrum.

Second temporal window [1.8 – 4 ps]. (figure VI.11b) In this time domain, partial diminution of both the bleach and W_0 absorption signals can be observed with a time constant of 2 ps. During this evolution, an isosbestic point is visible at 490 nm. By analogy with the Th_2SBPa molecule which presented a similar evolution (time constant 1.9 ps), we propose to tentatively ascribe this first event to the $S_1(CT) \rightarrow S_0$ internal conversion responsible for the ground state recovery

Third temporal window [5 – 100 ps] (figure VI.11c). This evolution presents a further decrease of the bleach band concomitantly with an apparent increase of the **SE** signal with a characteristic time of 16 ps. In the same time, the **SE** band vibronic structure becomes more pronounced. The increase of the **SE** band is probably resulting from the decay of a positive transient absorption band present in the same spectral region, $\sim$430-550 nm. This evolution is somewhat comparable to the 28 ps dynamics observed for Th_2SBPa upon 266 nm excitation (see figure VI.8c) and can be ascribed, by analogy, to the decay of a $S_1(E)$ state by internal conversion to the ground state. As for Th_2SBPa, the $S_1(E)$ absorption contribution can be named as W_1. After this decay, the residual transient absoption at 100 ps is certainly due to the emissive $\pi\pi^*$ excited singlet state for which spectral contribution is noticed W_2.
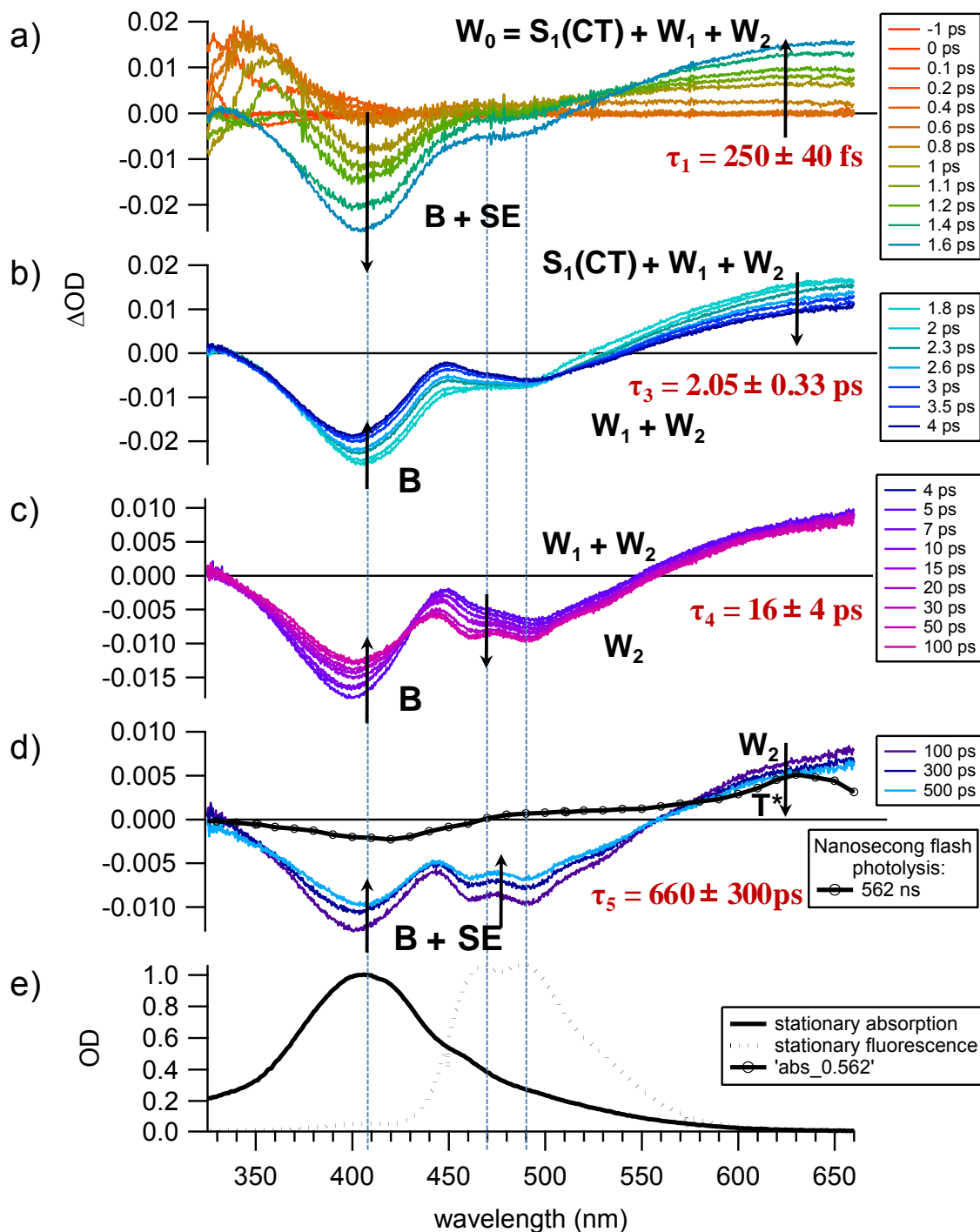
Figure VI.11 Femtosecond transient absorption spectra of Th$_4$SBPa in ACN after 266 nm excitation, divided into four temporal windows: a) -1 – 1.6 ps, b) 1.8 – 4 ps, c) 4 – 100 ps, and d) 100 – 500 ps; (e) stationary absorption and fluorescence spectra of Th$_4$SBPa. Pump-probe correlation time: τ = 400 fs

Fourth temporal window [100 - 500 ps] (figure VI.11d) Finally, after 100 ps, the evolution shows the concomitant decrease of all transient signals with a time constant of 660 ps, which is likely characterizing the decay of the emissive excited state. With nanosecond flash photolysis, using 355 nm excitation, a long-lived transient spectrum is observed (562 ns thick black trace in fig. V.11d) and characterized as the triplet state species on the basis of a strong oxygen quenching effect (triplet state lifetime: $\tau_T = 5.9$ µs). The decay of the emissive excited singlet state can be thus be ascribed to ISC process, i.e. $S_1(\pi\pi^*) \rightarrow T(\pi\pi^*)$ with also a non negligible IC process $S_1(\pi\pi^*) \rightarrow S_0$ accounting for the ground state recovery.

In summary, the characteristic times as well as the spectral evolutions measured for Th$_4$SBPa are very similar to those found for Th$_2$SBPa. Even if the main ICT process is not directly evidenced trough a **Y$_1$/Y$_2$** spectral exchange as in SBPa, its existence in Th$_2$SBPa and Th$_4$SBPa is suggested to be related to the observed 2 ps dynamics. So, despites the lack of clear solvatochromic band, the ICT reaction is still possible for Th$_4$SBPa molecule while excited with 266 nm or 390 nm excitation wavelengths.

VI.5   Conclusion
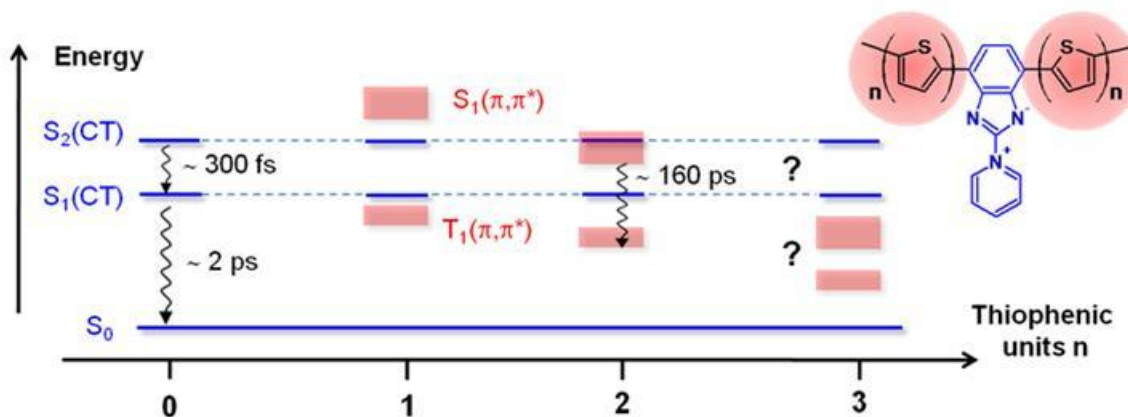
Figure **VI.12**. Illustration of photophysical evolution for (Th)$_n$SBPa for n = [0, 3]

The main results of this chapter are illustrated in figure VI.12 that synthesizes the influence of adding thiophenic groups of different lengths to the parent SBPa skeleton on the photophysical properties.

First, we found that the overall photophysics of betaine pyridinium molecules bearing two thiophenic groups substituted in symmetric position can be interpreted by considering that these entities involve two orthogonal systems:

- a first "CT system" corresponding to the parent molecule SBPa.

- a second oligothiophenic-like system including the two thiophenic groups and the central benzene ring.

This partition is justified by several concordant results. The thiophenic system has been evidenced by the various similarities between Th$_2$SBPa and 3T, on one hand, as well as Th$_4$SBPa and 5T, on the other hand, regarding the $\pi\pi^*$ absorption and emission band position and the triplet-triplet spectral shape. This result is of great importance because it means that conduction of π electrons is feasible in the ground state.

Concerning the "CT system", it has been found that, in SBPa and Th$_2$SBPa, the solvatochromic transition shows almost the same absorption maximum as well as a similar solvatochromic behaviour. The femtosecond experiment have demonstrated unambiguously that the S$_2$(CT) $\rightarrow$ S$_1$(CT) process extensively studied in the previous chapter in the case of SBPa still occurs for Th$_2$SBPa. Concerning Th$_4$SBPa the situation is

more complex because the two systems arise at the same energy level impeding the possibility to detect either the solvatochromic band (stationary measurements) or the characteristic $S_2(CT)$-$S_1(CT)$ transient signal with femtosecond measurements. At the present time, we obtained quite serious evidence for the production of $S_1(CT)$ but the hypothesis of an alternative mechanism like $S(\pi,\pi^*)\rightarrow S_1(CT)$ has to be seriously considered in the future. Another important question will concern the Th_6SBPa molecule: it will be decisive to study this molecule check if $S_2(CT)\rightarrow S_1(CT)$ process occurs.
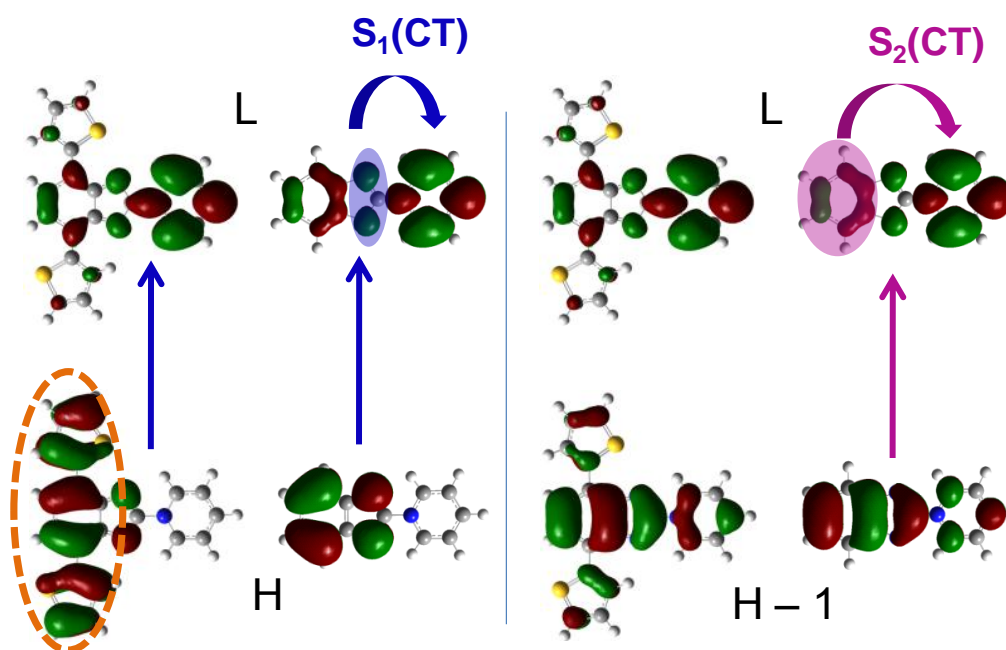
Figure **VI.13**. $S_1(CT)$ and $S_2(CT)$ MO representation for the SBPa and Th_2SBPa molecules

As a final conclusion we compare SBPa and Th_2SBPa molecular orbitals to highlight an unexpected result. In the parent molecule, the $S_2(CT)$ state arises from an ICT from the benzene ring of the betaine donor moiety to the pyridinium acceptor part of the molecule. Thus, in Th_2SBPa, one could expect that the delocalized Thiophen-Benzene-Thiophen π-system would be engaged in this $S_0 \rightarrow S_2(FC)$ excitation as well. Instead, as clearly shown by the HOMO orbital, this π-system is engaged in $S_0 \rightarrow S_1(FC)$ excitation that corresponds in the parent molecule to CT from the imidazole to the pyridinium part. In the future, because these compounds have been tailored for photoconductivity purposes, it appears highly desirable to overcome the negative results of subsection VI.3.2 to finally succeed to excite directly the $S_1(CT)$ state as we succeeded before for TwSBPa. To reach this goal, the use of an excitation wavelength far from the $S_2(CT)$ band position will be necessary. It will require completing our laser system by an OPA module able to provide a fully accordable excitation.

CHAPTER VII

Conclusions

The study of the photophysics of SBPa parent molecule and thiophenic analogs Th$_2$SBPa and Th$_4$SBPa, first dedicated to understand the ICT processes in donor-acceptor compounds, have led actually to plenty of results of fundamental interest. From the first evidence of a possible photoinduced ICT transition from the observation of a negative solvatochromism effect together with its corroboration using the Weller's concept - the combination of various techniques have been the key to unravel a succession of elementary ultrafast processes occurring in these betaine molecules upon excitation. Indeed, the complementarity between advanced PCM-TDDFT, stationary (absorption, emission, ^{1}H-NMR) and time-resolved (femtosecond and nanosecond transient absorption) spectroscopies has allowed us to get the major information concerning the photophysical properties. More particularly, an innovative treatment of the solvatochromism observed experimentally from stationary spectroscopy, on one hand, and the global fitting analysis, with the help of MCR-ALS approach, of the time-resolved spectroscopic data, on the other hand, have been helpful to reach a very detailed and comprehensive interpretation of the experimental results.

Indeed, by tracking an ICT reaction for the SBPa molecule, we found that the overall ICT process involves two distinct ICT steps well localized in specific parts of the molecule. The excitation of the solvatochromic transition, i.e., $S_0 \rightarrow S_2(FC)$, induces a first charge transfer from the benzene to the pyridinium ring, which results in a drastic dipole moment reduction (inversion can even be expected in polar solvent). A second ICT step then arises with the non-adiabatic internal conversion process, $S_2(CT) \rightarrow S_1(CT)$, the charge being transferred from the imidazole to the pyridinium part. Apart the CT processes, the population of an emissive state $S_1(E)$ state with possible CT character predicted by LR-PCM-TDDFT calculations has to be considered as a competitive (and not desired for applications) channel.

In the future, the study of the $S_0 \rightarrow S_2(FC)$ absorption transition together with the $S_1(E) \rightarrow S'_0$ emission transition has to be continued through the innovative solvatochromic data treatment presented in this manuscript. To the best of our knowledge, our study is the first one to present a comparison of 4 dipole moments $\mu_g(S_0)$, $\mu_e(S_2)$, $\mu_e(S_1)$ and $\mu_g(S_0')$ with *ab initio* calculations. The already good experiment-theory accordance obtained will be improved by a better choice of solvent set avoiding the presence of specific interaction or dimerization effects. A better improvement will consist in considering the second order

term of the theoretical solvatochromic expression allowing to overcome the problematic hypothesis $\alpha_g \approx \alpha_e$. To unify both approaches, it will be interesting in the future to perform within a similar group of solvents, the band shape analysis from which the dipole moments can be deduced as well and the innovative data treatment. Actually, the precise determination of dipole moments is merely important considering that Professor Abe group is developing efforts to link the SBPa units with photochromic molecules (see chart 4 in the introduction). By the way, the study of such molecules will be initiated.

Considering the dynamics of the ICT process, we found that, following vertical photoexcitation to the charge transfer, Franck-Condon configuration $S_2(FC)$, an ultrafast relaxation of ~100 fs leads to the stabilization of the CT state, i.e. $S_2(FC) \rightarrow S_2(CT)$, which is accompanied by some electronic reorganization (partial back charge transfer). To gain more detailed insight into this earlier process, it would be desirable to use experimental techniques with better temporal resolution or smaller GVD effect, such as transient absorption in liquid jet or time-resolved photoelectron spectroscopy in gas phase. The following photophysical event was shown to be the internal conversion process, $S_2(CT) \rightarrow S_1(CT)$. The characteristic time for this further ICT process ranges between ~300 fs and 20 ps depending on the solvent nature because it is fully controlled by the solvent dynamics, at least for the aprotic solvents. In protic solvents, a more complicated situation arises probably due to the presence of the hydrogen bond network affecting the ICT process. Anyhow, in both cases this ICT reaction proceeds in the inverted Marcus region. Finally, the hypothesis that this reaction leads to a twisted (TICT) state has been definitively excluded. In the future, the search for new insights on the mechanistic route leading to $S_1(CT)$ population (competing with $S_1(E)$ population) will motivate further advanced CASSCF/CASPT2 calculations. Another challenging subject will be the rationalization of the special effects observed in protic solvents compared to aprotic ones, such as the specific solvatochromic transition moment of absorption, the specific solvatochromic emission wavelength, the ultrafast transient stimulated emission observed from the FC region...etc. LR-PCM-TDDFT excited state optimization including 2 or 4 explicit protic molecules will be undeniably an interesting approach.

To initiate structural effect on the previous results, influence of adding more and more long thiophenic chains substituted to SBPa have been investigated with the photophysical study of Th$_2$SBPa and Th$_4$SBPa. We found that the overall photophysics of these thiophenic analogues can be surprisingly interpreted as the sum of the intrinsic

photophysics of two orthogonal systems: i) that related to the SBPa moiety, with the excited state ICT process $S_2(CT) \rightarrow S_1(CT)$ occurring with similar characteristic time as in the parent molecule; ii) the photophysics of the Th-Bz-Th or Th_2-Bz-Th_2 chains, which mimics the deactivation pathway of the corresponding oligothiophenes 3T or 5T, respectively. Among the two ICT processes reported for SBPa, the orbitals localized on the Th-Bz-Th or Th_2-Bz-Th_2 chains are not engaged in the initial $S_0 \rightarrow S_2(CT)$ transition but contribute to the subsequent ICT process $S_2(CT) \rightarrow S_1(CT)$. This result is of fundamental importance considering the possible application of these molecules for optoelectronic devices. In the future, ultrafast time-resolved studies of the photophysics of larger oligomers (Th_6SBPa) in solution or electropolymer films ($Th_mSBPa)_n$ will be a nice achievement of this study.

Appendix

A. Choice of relevant functional for (TD)DFT calculations

In general, for CT molecules, the post Hartree-Fock calculations methods are recommended [53] but they are also computationally expensive. On the other hand, calculations based on DFT, which are less time consuming, depend mainly on the choice of the functional. This choice can be made by comparing absorption spectra with PCM-TD-DFT vertical transitions calculations. By performing calculations with different solvents, this choice can be refined by a good reproduction of the experimental solvatochromism.

For SBPa molecule, we aim to determine the best functional among four functionals with different percentage of exact exchange: B3LYP (20%) [173], PBE0 (25%), BMK (42%) [174] and BHandHLYP (50 %) [175]. The best functional is the one that reproduces quantitatively the solvatochromic absorption tendency of SBPa molecule reported in figure A.1. The maximum absorption band increases with the solvent polarity: ACN – λ_{max}=389 nm, THF – λ_{max}= 419 nm and toluene – λ_{max}=438 nm.

To achieve our goal, we have first optimized the ground state geometry of SBPa in the vacuum for the four tested functionals using 6-311++g(d,p) basis set. Next, for all functionals, we have calculated the vertical excitations to the first two excited states S_1(FC) and S_2(FC) including solvent with PCM model and using the same basis as for the optimization. Finally, we have compared the calculated transition positions with experimental data as shown in figure A1 and table A.1. As one can see in figure A.1, all four functional give a satisfactory solvatochromism behaviour for both transitions i.e. S_0(FC) to S_1(FC) and S_2(FC) states. Furthermore, for the PBE0, B3LYP and BMK functionals, it turns out that the transition to the S_2 state has the strongest oscillator strength, while the transition to S_1 is much weaker (forbidden due to selection rule). Only one functional – BHandHLYP – gives inversed results. Therefore, we can safely assume that solvatochromic absorption band of SBPa is due to $S_0 \rightarrow S_2$ transition and we discard the results obtained with the BHandHLYP functional.

To choose between the three remaining functionals we compare carefully the results for the three different solvents. In table A.1, wavelengths of the most intense transitions safely ascribed to experimental band are tabulated. It appears clearly, that the best accordance between experiment and theoretical calculations was achieved for the PBE0 functional for all solvents. Undeniably, PBE0 is the best functional for SBPa molecule, therefore within this thesis this functional will be used for all types of DFT calculations.

a)

b)

c)
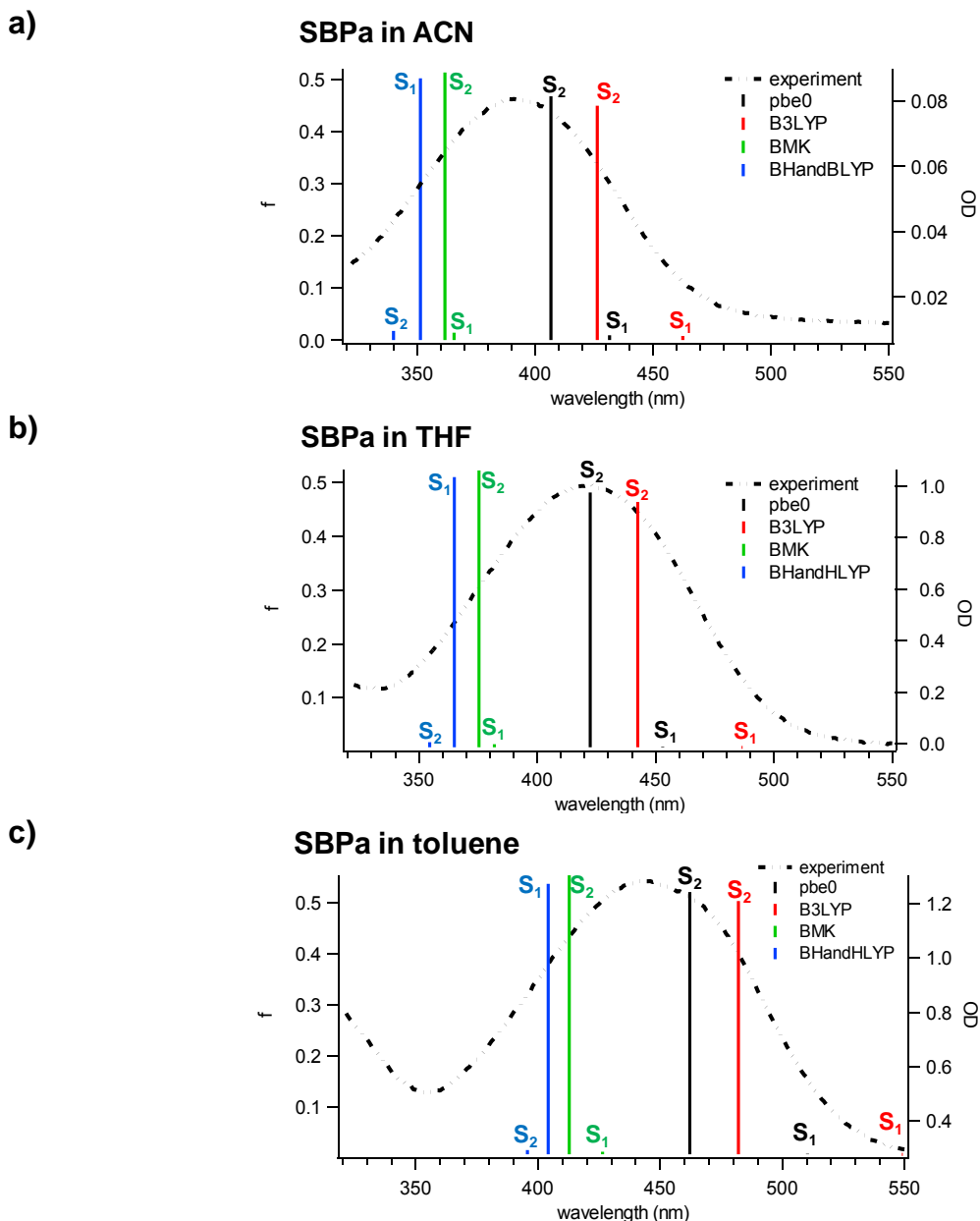
Figure A.1. Stationary absorption spectra and corresponding PCM-TDDFT wavelengths and oscillator strengths for $S_0 \rightarrow S_1$ and $S_0 \rightarrow S_2$ transitions using 6-311++g(d,p) basis and four functionals: PBE0 (black), B3LYP (red), BMK (green) and BHandHLYP (blue) in three different solvents: a) ACN, b) THF and c) toluene.

Table A.1. PCM TDDFT wavelength (nm) transitions for PBE0, B3LYP, BMK and BHandHLYP functionals (in black) and absolute differences with experimental values added in green. Only the most intense transitions between $S_0 \rightarrow S_1$ and $S_0 \rightarrow S_2$ best reproducing experimental data are chosen. (the best values are marked in red)

	ACN		THF		Toluene	
	λ_{max}	$\Delta\lambda$ exp-theory	λ_{max}	$\Delta\lambda$ exp-theory	λ_{max}	$\Delta\lambda$ exp-theory
Exp	**389**		**419**		**438**	
PBE0	407 (S_2)	**18**	422 (S_2)	**3**	462 (S_2)	**24**
B3LYP	426 (S_2)	37	443 (S_2)	24	482 (S_2)	44
BMK	362 (S_2)	27	375 (S_2)	44	413 (S_2)	25
BHandHLYP	351 (S_1)	38	365 (S_1)	54	404 (S_1)	34

B. Symmetry restrictions upon $S_0 \rightarrow S_1 / S_2$ transitions

Using DFT calculations, representations of SBPa orbitals involved in the two electronic transitions $S_0 \rightarrow S_1$ and $S_0 \rightarrow S_2$ are presented in figure B.1a. The corresponding irreductible representations are presented in figure B.1b considering C_{2v} and C_2 symmetry point group.

a) **b)**
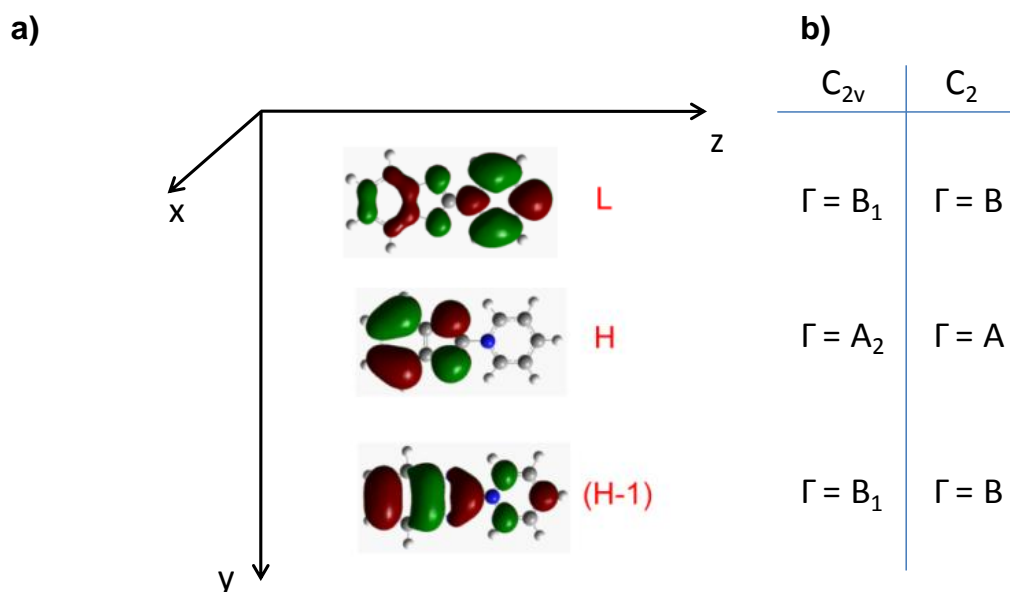
Figure B.1. a) Representation of molecular orbitals involved into electronic transitions to two first excited states in Cartesian coordinate system. b) Irreducible representations (Γ) of all three orbitals for two symmetry groups: C_{2v} and C_2.

To determine which transitions is more likely to occur according to dipole moments directions, we compute for each components of the dipole moments, the direct product

$$\Gamma_{\text{transition}} = \Gamma_{HOMO/HOMO-1} \otimes \Gamma_\mu \otimes \Gamma_{LUMO}$$

and the final results are gathered in tables B.1a for C_{2v} group and B.1b for C_2 group. Only the A_1 character for C_{2v} group (or A character for the C_2 group) indicates an allowed transition in given dipole direction. As one can see the only electronic transition possible for SBPa along main axis of the molecule (z) is for H-1 $\rightarrow$ L transition, i.e. for $S_0 \rightarrow S_2$ transition explaining furthermore the so weak $S_0 \rightarrow S_1$ transitions.

Table B.1. Irreducible representations of transitions for SBPa for a) C_{2v} and b) C_2 symmetry groups.

a)

C_{2v}	μ_x	μ_y	μ_z
H $\rightarrow$ L	A_2	A_1	B_2
H-1 $\rightarrow$ L	B_1	B_2	A_1

b)

C_2	$\mu_{x/y}$	μ_z
H $\rightarrow$ L	A	B
H-1 $\rightarrow$ L	B	A

C. Evaluation of solvation time.

Since the solvation dynamics of the dipolar solutes is expected to be important in determining the kinetics of charge transfer reactions, an accurate knowledge of the solvation time is of high priority. For this reason, Maroncelli et al. [98] have investigated the dynamics of solvation of coumarin 153 in 24 common solvents by time-dependent emission spectroscopy. As the solvation is expected to occur in a very short time scale at room temperature (~1 ps in usual solvents), subpicosecond experimental time resolution is needed.

Upon pulse laser excitation of the solute in an exited electronic state, a new charge distribution is instantaneously created in the solute. The solvent reequilibration to this new electronic state stabilizes the later, which reduces the energy gap with the ground state. This solvation process can thus be monitored by measuring the time-dependent red-shift of the emission band. The dynamics of reorganization of the solvent depends mainly on its viscosity and polarity. The main difference between different solvents lies in the extent of the frequency shift and its temporal characteristics. Therefore the position of the time-resolved emission band has to be plotted function of time and fitted with a multi-exponential function, from which an average solvation time can be defined as:

$$\langle \tau_{solv} \rangle = \sum_i a_i \tau_i \qquad (B.1)$$

Where $\sum_i a_i = 1$.

We aim to evaluate solvation times for solvents used in femtosecond transient absorption experiment within this thesis, as not all of them were studied by Maroncelli's group, and some values cannot be found in the literature. By analogy with previous studies, we decided to use the coumarin 153 as a solvation dynamics probe. In order to get some points of comparison, we repeated measurements in some solvents already studied by Maroncelli and then we investigated the unknown solvents. As in our laboratory we do not have access to time-resolved emission data, we decided to use the femtosecond transient absorption experiment and track the expected shift of the stimulated emission signal.

First, to ensure that we obtain reliable results we first applied our procedure to ACN, a representative solvent already tested by Maroncelli et al. Moreover, the group velocity dispersion (GVD) effect needed to be corrected as it can distort the values of ulatrafast solvation times (we did not applied our fitting function to stay close to the Maroncelli conditions)

Figure C.1. a) Transient stimulated emission spectra of coumarin 153 in ACN using 390 nm excitation, for early delay times in range [-1 – 10 ps]; b) band shift kinetics fitted with the y(t) function.

Figure C.1a shows the transient absorption spectra of coumarin 153 in ACN using 390 nm excitation for early delay times in range [-1 – 10 ps]. It shows a broad stimulated emission (SE) signal in spectral range between 435 and 700 nm with shifting maximum position in time from 475 nm to 560 nm. We plotted the peak position as a function of the delay time and fitted it with a double-exponential function (see figure C.1b). Higher or smaller exponential functions do not give satisfying fit results. Applying the fit results to equation C.1, we calculated a $\langle \tau_{solv} \rangle$ value of 0.267 ps for aceonitrile, which is in excellent agreement with the value of 0.26 ps reported by Maroncelli and co-workers and validates our method for estimating the $\langle \tau_{solv} \rangle$ from the stimulated emission signal.
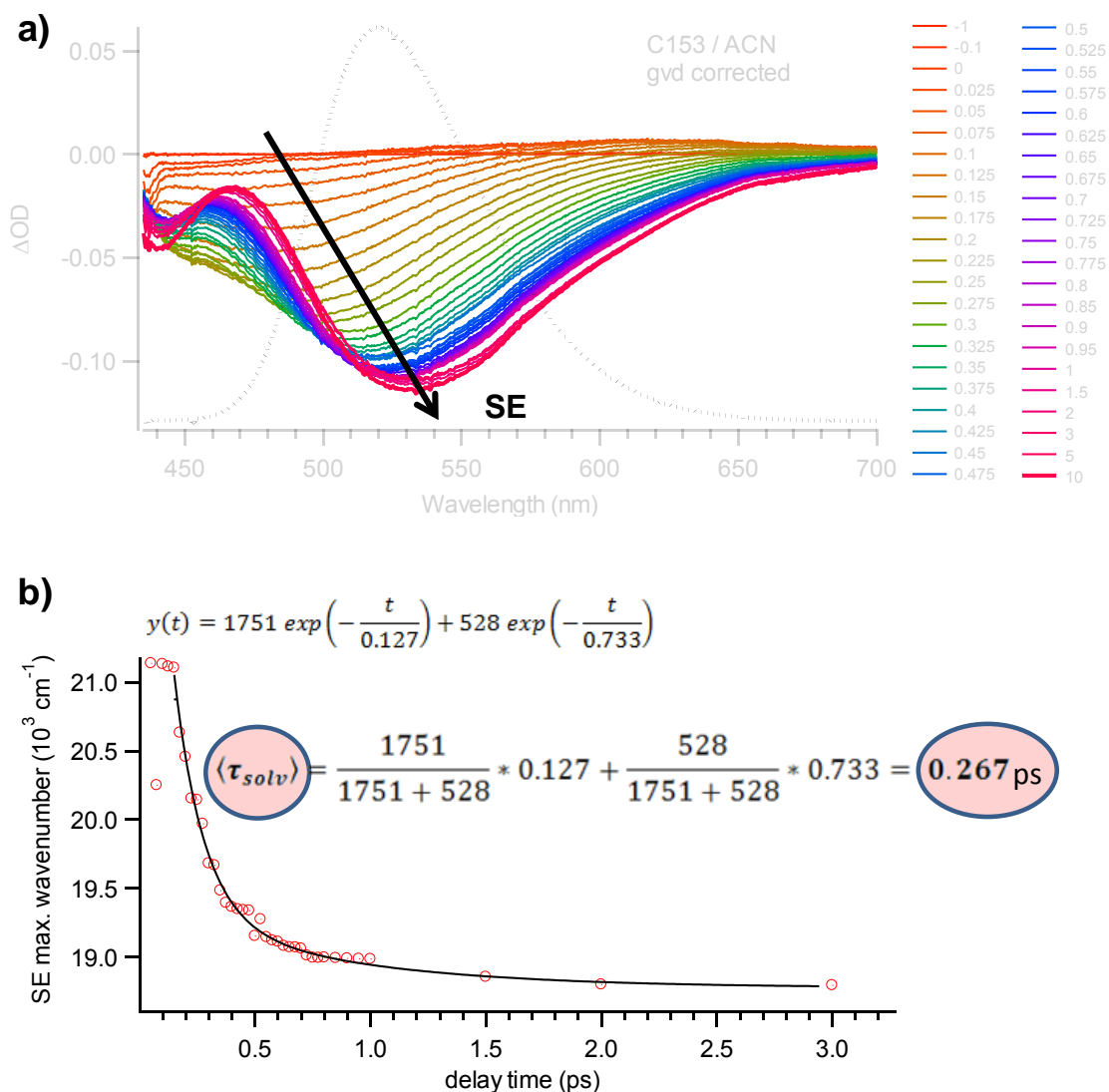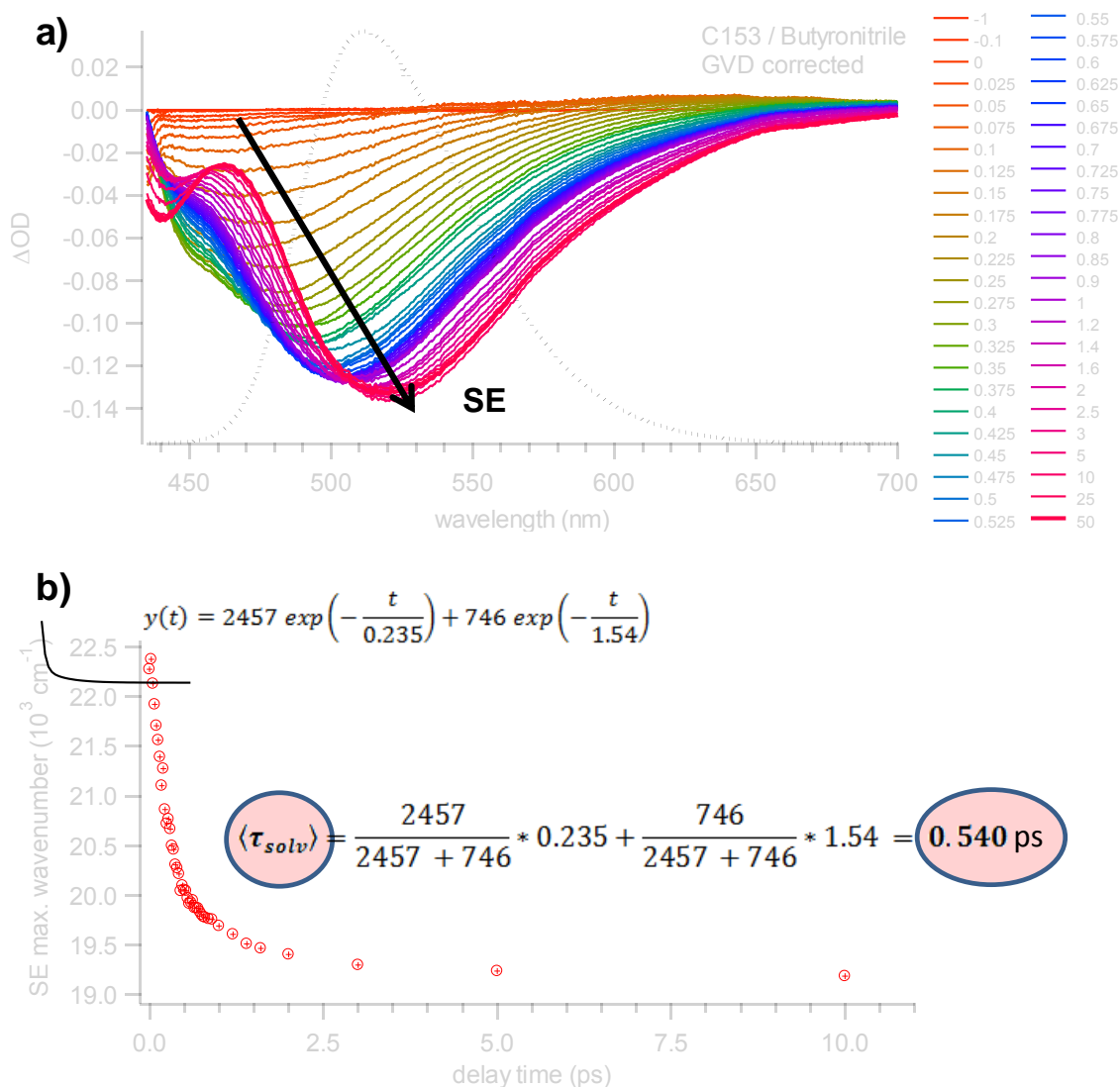
Figure C.2. a) Transient stimulated emission spectra of coumarin 153 in butyronitrile using 390 nm excitation, for early delay times in range [-1 – 50 ps]; b) band shift kinetics fitted with the y(t) function.

In figure C.2 a similar example of treatment is shown for the butyronitrile solvent (more viscous than ACN and not studied by Maroncelli and co-workers). A more extended temporal window [-1 – 50 ps] was necessary to follow the whole evolution, revealing a longer solvation dynamics of coumarin 153 in this solvent. Fitting the kinetics of the SE band shift (see figure C.2b) with a double-exponential function led to an average time of 0.54 ps, a time longer than in the case of ACN as expected. The same procedure was systematically used to evaluate the $\langle \tau_{solv} \rangle$ values for all solvents used in this thesis, the values being gathered in table V.2.

Bibliography

1. M.M. Russew and S. Hecht, *Photoswitches: From Molecules to Materials.* Advanced Materials. **22**(31): p. 3348-3360.
2. T. Nakahira, *Photofunctional polymers.* Journal of Synthetic Organic Chemistry Japan, 1984. **42**(11): p. 968-978.
3. T. Hasobe, *Supramolecular nanoarchitectures for light energy conversion.* Physical Chemistry Chemical Physics. **12**(1): p. 44-57.
4. J. Clark and G. Lanzani, *Organic photonics for communications.* Nature Photonics. **4**(7): p. 438-446.
5. B.L. Feringa, ed. *Molecular Switches*. 2001, Wiley-VCH: Weinheim
6. M. Irie, ed. *Photoreactive Materials for Ultrahigh-Density Optical Memory*. 1994, Elsevier: Amsterdam
7. V. Ramamurthy, ed. *Photochemistry in Organized and Constrained Media*. 1991, VCH: New York
8. J.C. Crano and R.J. Guglielmetti, eds. *Topics in Applied Chemistry, Organic Photochromic and Thermochromic Compounds*. 1999, Plenum Press: New York.
9. H. Durr and H. Bouas-Laurent, eds. *Photochromism. Molecules and Systems*. 2003, Elsevier: Amsterdam
10. A.P.d. Silva, ed. *Part one: Molecular-Level Electronics*. Electron Transfer in Chemistry, ed. V. Balzani. Vol. 5. 2001, WILEY-VCH Verlag GmbH: Weinheim.
11. E. Markava, D. Gustina, I. Muzikante, L. Gerca, M. Rutkis and E. Fonavs, *Photochromism of some azobenzene derivatives in thin films as a function of the chemical properties of the molecule.* Molecular Crystals and Liquid Crystals, 2001. **355**: p. 381-400.
12. B. Moine, G. Buntinx, O. Poizat, M. Frigoli, C. Moustrou and A. Samat, *Transient absorption investigation of the photophysical properties of thiophene linked [2H]-chromenes.* Molecular Crystals and Liquid Crystals, 2005. **431**: p. 363-368.
13. B. Moine, J. Rehault, S. Aloïse, J.C. Micheau, C. Moustrou, A. Samat, O. Poizat and G. Buntinx, *Transient absorption studies of the photochromic behavior of 3H-naphtho[2,1-b]pyrans linked to thiophene oligomers via an acetylenic junction.* Journal of Physical Chemistry A, 2008. **112**(21): p. 4719-4726.
14. S. Aloïse, M. Sliwa, Z. Pawlowska, J. Rehault, J. Dubois, O. Poizat, G. Buntinx, A. Perrier, F. Maurel, S. Yamaguchi and M. Takeshita, *Bridged Photochromic Diarylethenes Investigated by Ultrafast Absorption Spectroscopy: Evidence for Two Distinct Photocyclization Pathways.* Journal of the American Chemical Society, 2010. **132**(21): p. 7379-7390.
15. S. Aloïse, J. Rehault, B. Moine, O. Poizat, G. Buntinx, V. Lokshin, M. Vales and A. Samat, *Photochromism of photoenolizable ketones in quinoline and 1,8-naphthyridine series studied by time-resolved absorption spectroscopy.* Journal of Physical Chemistry A, 2007. **111**(10): p. 1737-1745.
16. M. Sliwa, N. Mouton, C. Ruckebusch, S. Aloïse, O. Poizat, G. Buntinx, R. Metivier, K. Nakatani, H. Masuhara and T. Asahi, *Comparative Investigation of Ultrafast Photoinduced Processes in Salicylidene-Aminopyridine in Solution and Solid State.* Journal of Physical Chemistry C, 2009. **113**(27): p. 11959-11968.
17. S. Mukamel, *Principles of nonlinear optical spectroscopy.* 1995, Oxford: Oxford University Press, Inc.
18. J. Abe, N. Nemoto, Y. Nagase and Y. Shirai, *Ab initio MO investigations of moleculer structures in the ground and first excited states of heterocyclic pyridinium betaine.* Chemical Physics Letters, 1996. **261**: p. 18-22.

19. J. Abe and Y. Shirai, *Heterocyclic Betaines Exhibiting Extremely Large First Hyperpolarizability: Ab Initio and INDO/S Calculations.* Journal of American Chemical Society, 1996. **118**: p. 4705-4706.

20. J. Abe, Y. Shirai, N. Nemoto, F. Miyata and Y. Nagase, *Heterocyclic Pyridinium Betaines, A New Class of Second-Order Nonlinear Optical Materials: Combined Theoretical and Experimental Investigation of First-Order Hyperpolarizability through ab Initio, INDO/S, and Hyper-Rayleigh Scattering.* Journal of Physical Chemistry B, 1997. **101**: p. 576-582.

21. J. Abe, Y. Shirai, N. Nemoto and Y. Nagase, *Manipulation of Dipole Moment and Hyperpolarizability Based on Heterocyclic Pyridinium Betaine Structures: Ab Initio and INDO/S MO Calculations.* Journal of Physical Chemistry B, 1997. **101**: p. 1910-1915.

22. G.V. Boyd, *An aza-analogue of N-pyridinium cyclopentadienide.* Tetrahedron Letters, 1966. **29**: p. 3369-3371.

23. E. Alcalde, I. Dinares, J. Elguero, J.-P. Fayet, M.-C. Vertut, C. Miravitlles and E. Molins, *Azinium Azolate Inner Salts: Synthesis and Structural Studies.* Journal of Organc Chemistry, 1987. **52**: p. 5009-5015.

24. K. Iwasaki, A. Kimoto, S.I. Naya, F. Iwahori and J. Abe, *Synthesis and properties of optically functionalized polythiophene having porphyrin side-chain.* Synthetic Metals, 2009. **159**(9-10): p. 880-884.

25. J. Abe, N. Nemoto, Y. Nagase and Y. Shirai, *Novel concept for non-destructive readout method for photochromic rewriteable memory devices.* Chemical Physics Letters, 1997. **276**(5-6): p. 450-454.

26. P. Suppan, *Solvatochromic shifts - the influence of the medium on the energy of electronic states.* Journal of Photochemistry and Photobiology A - Chemistry, 1990. **50**(3): p. 293-330.

27. C. Reichardt, *Solvatochromic Dyes as Solvent Polarity Indicators.* Chemical Reviews, 1994. **94**: p. 2319-2358.

28. C. Reichardt, *Solvents and Solvent effects in Organic Chemistry.* 2003: Wiley-VCH.

29. N. Mataga, Y. Kaifu and M. Koizumi, *Solvent effects upon fluorescence spectra and the dipolemoments of excited molecules.* Bulletin of the Chemical Society of Japan, 1956. **29**(4): p. 465-470.

30. E. Lippert, Z. Naturforsh, 1955. **109**: p. 571.

31. E. Lippert, Ber. Bunsenges, 1957. **61**: p. 962.

32. N. Mataga, Y. Kaifu and M. Koizumi, *The solvent effect on fluorescence spectrum - change of solute-solvent interaction during the lifetime of excited solute molecule.* Bulletin of the Chemical Society of Japan, 1955. **28**(9): p. 690-691.

33. L. Onsager, *Electric moments of molecules in liquids.* Journal of the American Chemical Society, 1936. **58**: p. 1486-1493.

34. C. Reichardt, *Pyridinium-N-phenolate betaine dyes as empirical indicators of solvent polarity: Some new findings.* Pure and Applied Chemistry, 2008. **80**(7): p. 1415-1432.

35. V. Kharlanov and W. Rettig, *Experimental and Theoretical Study of Excited-State Structure and Relaxation Processes of Betaine-30 and of Pyridinium Model Compounds.* Journal of Physical Chemistry A, 2009. **113**(40): p. 10693-10703.

36. S.R. Mente and M. Maroncelli, *Computer simulations of the solvatochromism of betaine-30.* Journal of Physical Chemistry B, 1999. **103**(36): p. 7704-7719.

37. Z.R. Grabowski, K. Rotkiewicz and W. Rettig, *Structural changes accompanying intramolecular electron transfer: Focus on twisted intramolecular charge-transfer states and structures.* Chemical Reviews, 2003. **103**(10): p. 3899-4031.

38. S.A. Kovalenko, N. Eilers-Konig, T.A. Senyushkina and N.P. Ernsting, *Charge transfer and solvation of betaine-30 in polar solvents - A femtosecond broadband transient absorption study.* Journal of Physical Chemistry A, 2001. **105**(20): p. 4834-4843.

39. N.E. Levinger, A.E. Johnson, G.C. Walker and P.F. Barbara, *specific excitation of the solvent coordinate in the S3 - S1 and S1 - S0 radiationless decay of the betaines.* Chemical Physics Letters, 1992. **196**(1-2): p. 159-165.

40. P.J. Reid and P.F. Barbara, *Dynamic solvent effect on betaine-30 electron-transfer kinetics in alcohols.* Journal of Physical Chemistry, 1995. **99**(11): p. 3554-3565.

41. E. Akesson, A.E. Johnson, N.E. Levinger, G.C. Walker, T.P. Dubruil and P.F. Barbara, *Temperature-Dependence of the Inverted Regime Electron-Transfer Kinetics of Betaine-30 and the Role of Molecular-Modes.* Journal of Chemical Physics, 1992. **96**(10): p. 7859-7862.

42. P.J. Reid, S. Alex, W. Jarzeba, R.E. Schlief, A.E. Johnson and P.F. Barbara, *Evidence for intermolecular hydrogen-bond rearrangement in the electron-transfer dynamics of betaine-30 in n-butanol.* Chemical Physics Letters, 1994. **229**(1-2): p. 93-100.

43. M.C. Beard, G.M. Turner and C.A. Schmuttenmaer, *Measuring intramolecular charge transfer via coherent generation of THz radiation.* Journal of Physical Chemistry A, 2002. **106**(6): p. 878-883.

44. M.C. Beard, G.M. Turner and C.A. Schmuttenmaer, *Measurement of electromagnetic radiation emitted during rapid intramolecular electron transfer.* Journal of the American Chemical Society, 2000. **122**(46): p. 11541-11542.

45. V.M. Farztdinov, R. Schanz, S.A. Kovalenko and N.P. Ernsting, *Relaxation of optically excited p-nitroaniline: Semiempirical quantum-chemical calculations compared to femtosecond experimental results.* Journal of Physical Chemistry A, 2000. **104**(49): p. 11486-11496.

46. S.A. Kovalenko, R. Schanz, V.M. Farztdinov, H. Hennig and N.P. Ernsting, *Femtosecond relaxation of photoexcited para-nitroaniline: solvation, charge transfer, internal conversion and cooling.* Chemical Physics Letters, 2000. **323**(3-4): p. 312-322.

47. S.I. Druzhinin, S.R. Dubbaka, P. Knochel, S.A. Kovalenko, P. Mayer, T. Senyushkina and K.A. Zachariasse, *Ultrafast intramolecular charge transfer with strongly twisted aminobenzonitriles: 4-(Di-tert-butylamino)benzonitrile and 3-(Di-tert-butylamino)benzonitrile.* Journal of Physical Chemistry A, 2008. **112**(13): p. 2749-2761.

48. S.I. Druzhinin, N.P. Ernsting, S.A. Kovalenko, L.W. Lustres, T.A. Senyushkina and K.A. Zachariasse, *Dynamics of ultrafast intramolecular charge transfer with 4-(dimethylamino)benzonitrile in acetonitrile.* Journal of Physical Chemistry A, 2006. **110**(9): p. 2955-2969.

49. C. Chudoba, A. Kummrow, J. Dreyer, J. Stenger, E.T.J. Nibbering, T. Elsaesser and K.A. Zachariasse, *Excited state structure of 4-(dimethylamino)benzonitrile studied by femtosecond mid-infrared spectroscopy and ab initio calculations.* Chemical Physics Letters, 1999. **309**(5-6): p. 357-363.

50. J.-K. Lee, T. Fujiwara, W.G. Kofron, M.Z. Zgierski and E.C. Lim, *The low-lying pisigma* state and its role in the intramolecular charge transfer of aminobenzonitriles and aminobenzethyne.* J Chem Phys, 2008. **128**(16): p. 164512.

51. T. Gustavsson, P.B. Coto, L. Serrano-Andres, T. Fujiwara and E.C. Lim, *Do fluorescence and transient absorption probe the same intramolecular charge transfer state of 4-(dimethylamino)benzonitrile?* Journal of Chemical Physics, 2009. **131**(3): p. 4.

52. J. Tomasi, B. Mennucci and R. Cammi, *Quantum mechanical continuum solvation models.* Chemical Reviews, 2005. **105**(8): p. 2999-3093.

53. L.C. Dias, R. Custodio and F.B.T. Pessine, *Theoretical studies of Nile Red by ab initio and semiempirical methods.* Chemical Physics Letters, 1999. **302**(5-6): p. 505-510.

54. G. Scalmani, M.J. Frisch, B. Mennucci, J. Tomasi, R. Cammi and V. Barone, *Geometries and properties of excited states in the gas phase and in solution: Theory and application of a time-dependent density functional theory polarizable continuum model.* Journal of Chemical Physics, 2006. **124**(9): p. 15.

55. G. Buntinx, R. Naskrecki and O. Poizat, *Subpicosecond Transient Absorption Analysis of the Photophysics of 2,2'-Bipyridine and 4,4'-Bipyridine in Solution.* Journal of Physical Chemistry, 1996. **100**: p. 19380 - 19388.

56. D. Eimerl, L. Davis, S. Velsko, E.K. Graham and A. Zalkin, *Optical, mechanical, and thermal properties of barium borate.* Journal of Applied Physics, 1987. **62**(5): p. 1968 - 1983.

57. R. Naskrecki, *Femtosekundowa spektroskopia absorpcji przejsciowej.* 2000.

58. T. Nakayama, Y. Amijima, K. Ibuki and K. Hamanoue, *Construction of a subpicosecond double-beam laser photolysis system utilizing a femtosecond Ti:sapphire amplifiers (a regenerative amplifier and two double passed linear amplifiers), and measurements of the transient absorption spectra by a pump-probe method.* Rev. Sci. Instrum., 1997. **68**(12): p. 4364 - 4371.

59. M. Ziolek, M. Lorenc, R. Naskrecki, J. Karolczak, J. Kubicki and A. Maciejewski, *Artifacts in femtosecond transient absorption spectroscopy.* Applied Physics B, 2002. **74**: p. 19 - 27.

60. M. Ziolek, M. Lorenc and R. Naskrecki, *Determination of the temporal response function in femtosecond pump-probe systems.* Appl. Phys. B, 2001. **72**: p. 843 - 847.

61. I.H.M. van Stokkum, D.S. Larsen and R. van Grondelle, *Global and target analysis of time-resolved spectra.* Biochimica Et Biophysica Acta-Bioenergetics, 2004. **1657**(2-3): p. 82-104.

62. I.H.M. van Stokkum, D.S. Larsen and R. van Grondelle, *Global and target analysis of time-resolved spectra (vol 1658, pg 82, 2004).* Biochimica Et Biophysica Acta-Bioenergetics, 2004. **1658**(3): p. 262-262.

63. S. Aloïse, C. Ruckebusch, L. Blanchet, J. Rehault, G. Buntinx and J.P. Huvenne, *The benzophenone S-1(n,pi*) -> T-1(n,pi*) states intersystem crossing reinvestigated by ultrafast absorption spectroscopy and multivariate curve resolution.* Journal of Physical Chemistry A, 2008. **112**(2): p. 224-231.

64. C. Ruckebusch, S. Aloïse, L. Blanchet, J.P. Huvenne and G. Buntinx, *Reliable multivariate curve resolution of femtosecond transient absorption spectra.* Chemometrics and Intelligent Laboratory Systems, 2008. **91**(1): p. 17-27.

65. J. von Frese, S.A. Kovalenko and N.P. Ernsting, *Interactive curve resolution by using latent projections in polar coordinates.* Journal of Chemometrics, 2007. **21**(1-2): p. 2-9.

66. R. Tauler, *Multivariate curve resolution applied to second order data.* Chemometrics and Intelligent Laboratory Systems, 1995. **30**(1): p. 133-146.

67. A. de Juan, M. Maeder, M. Martinez and R. Tauler, *Combining hard- and soft-modelling to solve kinetic problems.* Chemometrics and Intelligent Laboratory Systems, 2000. **54**(2): p. 123-141.

68. D. Jacquemin, E.A. Perpete, I. Ciofini and C. Adamo, *Accurate Simulation of Optical Properties in Dyes.* Accounts of Chemical Research, 2009. **42**(2): p. 326-334.

69. M. Caricato, B. Mennucci, J. Tomasi, F. Ingrosso, R. Cammi, S. Corni and G. Scalmani, *Formation and relaxation of excited states in solution: A new time dependent polarizable continuum model based on time dependent density functional theory.* Journal of Chemical Physics, 2006. **124**(12).

70. B. Mennucci, C. Cappelli, C.A. Guido, R. Camlmi and J. Tomasi, *Structures and Properties of Electronically Excited Chromophores in Solution from the Polarizable Continuum Model Coupled to the Time-Dependent Density Functional Theory.* Journal of Physical Chemistry A, 2009. **113**(13): p. 3009-3020.

71. B.H. Besler, K.M. Merz and P.A. Kollman, *Atomic charges derived from semiempirical methods.* Journal of Computational Chemistry, 1990. **11**(4): p. 431-439.

72. R.A. Marcus, *Electron Transfer Reactions in Chemistry*. 1992, Nobel Lecture.

73. J. Mattay, ed. *Part one: Organic molecules*. Electron Transfer in Chemistry, ed. V. Balzani. Vol. 2. 2001, WILEY-VCH Verlag GmbH: Weinheim.

74. K.A. Zachariasse, S.I. Druzhinin, V.A. Galievsky, S. Kovalenko, T.A. Senyushkina, P. Mayer, M. Noltemeyer, M. Boggio-Pasqua and M.A. Robb, *Counterintuitive Absence of an Excited-State Intramolecular Charge Transfer Reaction with 2,4,6-Tricyanoanilines. Experimental and Computational Results.* Journal of Physical Chemistry A, 2009. **113**(12): p. 2693-2710.

75. J.P. Malval, J.P. Morand, R. Lapouyade, W. Rettig, G. Jonusauskas, J. Oberle, C. Trieflinger and J. Daub, *Structural modelling of optical and electrochemical properties of 4-aminodiphenylamines - optoelectronic studies on a polyaniline repeating unit.* Photochemical & Photobiological Sciences, 2004. **3**(10): p. 939-948.

76. R.A. Marcus, *On the theory of oxidation-reduction reactions involving electron transfer .1.* Journal of Chemical Physics, 1956. **24**(5): p. 966-978.

77. N.S. Hush, *Adiabatic rate processes at electrodes .1. energy-charge relationships.* Journal of Chemical Physics, 1958. **28**(5): p. 962-972.

78. P. Suppan, *Chemistry and Light*. 1994, Cambridge: The Royal Society of Chemistry.

79. P.Y. Chen and T.J. Meyer, *Medium effects on charge transfer in metal complexes.* Chemical Reviews, 1998. **98**(4): p. 1439-1477.

80. K. Yoshihara, *Ultrafast intermolecular electron transfer in solution*, in *Electron Transfer-from Isolated Molecules to Biomolecules, Pt 2*. 1999, John Wiley & Sons Inc: New York. p. 371-402.

81. R.A. Marcus, *On theory of electron-transfer reactions .6. unified treatment for homogeneous and electrode reactions.* Journal of Chemical Physics, 1965. **43**(2): p. 679-&.

82. R.A. Marcus, *Theory of oxidation-reduction reactions involving electron transfer .5. comparison and properties of electrochemical and chemical rate constants.* Journal of Physical Chemistry, 1963. **67**(4): p. 853-&.

83. R.A. Marcus, *Theory of oxidation-reduction reactions involving electron transfer .4. a statistical-mechanical basis for treating contributions from solvent, ligands, and inert salt.* Discussions of the Faraday Society, 1960(29): p. 21-31.

84. R.A. Marcus, *Theory of oxidation-reduction reactions involving electron transfer .2. applications to data on the rates of isotopic exchange reactions.* Journal of Chemical Physics, 1957. **26**(4): p. 867-871.

85. G.J. Kavarnos, *Fundamentals of Photoinduced Electron Transfer*. 1993, New York: VCH Publishers, Inc.

86. V.G. Levich and R.R. Dogonadze, *Theory of non-radiation electron transitions from ion to ion in solutions.* Doklady Akademii Nauk Sssr, 1959. **124**(1): p. 123-126.

87. R.A. Marcus, *Nonadiabatic processes involving quantum-like and classical-like coordinates with applications to nonadiabatic electron transfers.* Journal of Chemical Physics, 1984. **81**(10): p. 4494-4500.

88. D.M. Guldi and K.D. Asmus, *Electron transfer from C-76 (C-2 nu') and C-78 (D-2) to radical cations of various arenes: Evidence for the Marcus inverted region (vol 119, pg 5744, 1997).* Journal of the American Chemical Society, 1997. **119**(40): p. 9588-9588.

89. N. Mataga, T. Asahi, Y. Kanda, T. Okada and T. Kakitani, *The bell-shaped energy-gap dependence of the charge recombination reaction of geminate radical ion-pairs produced by fluorescence quenching reaction in acetonitrile solution.* Chemical Physics, 1988. **127**(1-3): p. 249-261.

90. M.R. Wasielewski, M.P. Niemczyk, W.A. Svec and E.B. Pewitt, *Dependence of rate constants for photoinduced charge separation and dark charge recombination on the free-energy of reaction in restricted-distance porphyrin quinone molecules.* Journal of the American Chemical Society, 1985. **107**(4): p. 1080-1082.

91. N.R. Banerji, *Photoinduced electron transfer. From a fundamental understanding to potential applications*. 2009, Université de Genève: Genève.

92. I. Rips and J. Jortner, *Dynamic solvent effects on outer-sphere electron-transfer.* Journal of Chemical Physics, 1987. **87**(4): p. 2090-2104.

93. W. Nadler and R.A. Marcus, *Dynamic effects in electron-transfer reactions .2. numerical-solution.* Journal of Chemical Physics, 1987. **86**(7): p. 3906-3924.

94. H. Sumi and R.A. Marcus, *Dynamic effects in electron-transfer reactions.* Journal of Chemical Physics, 1986. **84**(9): p. 4894-4914.

95. H. Sumi and R.A. Marcus, *Dielectric-relaxation and intramolecular electron transfers.* Journal of Chemical Physics, 1986. **84**(8): p. 4272-4276.

96. L.D. Zusman, *Outer-sphere electron-transfer in polar-solvents.* Chemical Physics, 1980. **49**(2): p. 295-304.

97. J.D. Simon, *Time-resolved studies of solvation in polar media.* Accounts of Chemical Research, 1988. **21**(3): p. 128-134.

98. M.L. Horng, J.A. Gardecki, A. Papazyan and M. Maroncelli, *Subpicosecond measurements of polar solvation dynamics - coumarin-153 revisited.* Journal of Physical Chemistry, 1995. **99**(48): p. 17311-17337.

99. T.J. Kang, W. Jarzeba, P.F. Barbara and T. Fonseca, *A photodynamical model for the excited-state electron-transfer of bianthryl and related molecules.* Chemical Physics, 1990. **149**(1-2): p. 81-95.

100. J. Waluk, *Conformational analysis of molecules in excited state*. 2000, New York: WILEY-VCH.

101. H.A. Kramers, *Brownian motion in a field of force and the diffusion model of chemical reactions.* Physica, 1940. **7**: p. 284-304.

102. R.F. Grote and J.T. Hynes, *The stable states picture of chemical-reactions .2. rate constants for condensed and gas-phase reaction models.* Journal of Chemical Physics, 1980. **73**(6): p. 2715-2732.

103.   N.G. Bakhshiev, *New version of the semiempirical theory of the effect of the dielectric properties of individual solvents on the shift of the absorption spectra of solutions.* Journal of Optical Technology, 2001. **68**(3): p. 184-188.

104.   P. Suppan and N. Ghoneim, *Solvatochromism.* RSC, 1997.

105.   R. Kanya and Y. Ohshima, *Determination of dipole moment change on the electronic excitation of isolated Coumarin 153 by pendular-state spectroscopy.* Chemical Physics Letters, 2003. **370**(1-2): p. 211-217.

106.   I. Renge, *Excited-state polarizability and gas phase frequency of the solvatochromic polarity indicator E-T(30).* Chemical Physics Letters, 2008. **459**(1-6): p. 124-128.

107.   I. Renge, *Nonlinear Polarization of Solvatochromic Betaine 30.* Journal of Physical Chemistry A, 2010. **114**(21): p. 6250-6254.

108.   A. Kawski, *Progress in Photochemistry and Photophysics, Volume V*, ed. J.F. Rabek. 1992: CRC Press.

109.   R.A. Marcus, *On theory of shifts and broadening of electronic spectra of polar solutes in polar media.* Journal of Chemical Physics, 1965. **43**(4): p. 1261-+.

110.   A. Kapturkiewicz and J. Nowacki, *Properties of the intramolecular excited charge-transfer states of carlbazol-9-yl derivatives of aromatic ketones.* Journal of Physical Chemistry A, 1999. **103**(41): p. 8145-8155.

111.   Y. Marcus, *The Properties of Solvents*. II ed. Wiley Series in Solution Chemistry, ed. P.G.T. Fogg. 1999, Chichester: John Wiley & Sons Ltd.

112.   T. Hirsch, H. Port, H.C. Wolf, B. Miehlich and F. Effenberger, *Intramolecular charge separation and transition state dynamics in anthracene/pyridinium supermolecules.* Journal of Physical Chemistry B, 1997. **101**(23): p. 4525-4535.

113.   Y. Zeng and M.B. Zimmt, *Symmetry effects on electron-transfer reactions - temperature-dependence as a diagnostic-tool.* Journal of Physical Chemistry, 1992. **96**(21): p. 8395-8403.

114.   J. Cortes, H. Heitele and J. Jortner, *Band-shape analysis of the charge-transfer fluorescence in barrelene-based electron donor-acceptor compounds.* Journal of Physical Chemistry, 1994. **98**(10): p. 2527-2536.

115.   R.A. Marcus, *Relation between charge-transfer absorption and fluorescence-spectra and the inverted region.* Journal of Physical Chemistry, 1989. **93**(8): p. 3078-3086.

116.   I. Dinares, C. Jaime and E. Alcalde, *MM2 calculations with atomic point charges modelling AM1 energy surfaces.* Journal of Molecular Structure, 1993. **291**: p. 105-121.

117.   E.G. McRae and M. Kasha, *Enhancement of phosphorescence ability upon aggregation of dye molecules.* Journal of Chemical Physics, 1958. **28**(4): p. 721-722.

118.   M.L. Horng and E.L. Quitevis, *Visible absorption spectroscopy and structure of cyanine dimers in aqueous solution - An experiment for physical chemistry.* Journal of Chemical Education, 2000. **77**(5): p. 637-639.

119.   C.J. Cramer, *Essentials Of Computational Chemistry: Theories And Models*. 2nd Revised edition ed. 2004, West Sussex: John Wiley & Sons Ltd.

120.   G.A. Jeffrey, *An introduction to hydrogen Bonding*. 1997, New York: Oxford University:.

121.   M.J. Kamlet, J.-L.M. Abboud, M.H. Abraham and R.W. Taft, *Linear solvation Energy Relationships. 23. A Comprehensive Collection of the Solvatochromic Parameters, π* α and β, and Some Methods for Simplifying the Generalized Solvatochromic Equation.* Journal of Organc Chemistry, 1983. **48**: p. 2877-2887.

122. L. Bilot and A. Kawski, *Zur theorie des einflusses von losungsmitteln auf die elektroenspektren der molekule.* Zeitschrift Fur Naturforschung Part a-Astrophysik Physik Und Physikalische Chemie, 1962. **A 17**(7): p. 621-&.

123. L. Bilot and A. Kawski, *Der einfluss des losungsmittels auf die elektronenspektren lumineszierender molekule.* Zeitschrift Fur Naturforschung Part a-Astrophysik Physik Und Physikalische Chemie, 1963. **A 18**(1): p. 10-&.

124. S. Krawczyk, B. Jazurek, R. Luchowski and D. Wiacek, *Electroabsorption spectra of carotenoid isomers: Conformational modulation of polarizability vs. induced dipole moments.* Chemical Physics, 2006. **326**(2-3): p. 465-470.

125. E.C. Lim, ed. *Excited states.* Vol. 1. 1974, Academic Press, Inc.: London. 129-230.

126. N. Mataga and T. Kubota, *Molecular interactions and electronic spectra.* 1970, New York: Marcel Dekker.

127. S. Jursenas, V. Kovalevskij, V. Gulbinas, A. Gruodis, G. Kodis, I. Muzikante, T. Gustavsson, J.C. Mialocq and L. Valkunas, *Excitation dynamics in solutions, films and crystals of indandione-1,3 pyridinium betaine.* Molecular Crystals and Liquid Crystals, 2001. **355**: p. 105-125.

128. W.M. Kwok, C. Ma, D. Phillips, P. Matousek, A.W. Parker and M. Towrie, *Picosecond time-resolved study of 4-dimethylaminobenzonitrile in polar and nonpolar solvents.* Journal of Physical Chemistry A, 2000. **104**(18): p. 4188-4197.

129. H. Okamoto, *Picosecond transient infrared spectrum of 4-(dimethylamino)benzonitrile in the fingerprint region.* Journal of Physical Chemistry A, 2000. **104**(18): p. 4182-4187.

130. W.M. Kwok, C. Ma, M.W. George, D.C. Grills, P. Matousek, A.W. Parker, D. Phillips, W.T. Toner and M. Towrie, *Further time-resolved spectroscopic investigations on the intramolecular charge transfer state of 4-dimethylaminobenzonitrile (DMABN) and its derivatives, 4-diethylaminobenzonitrile (DEABN) and 4-dimethylamino-3,5-dimethylbenzonitrile (TMABN).* Physical Chemistry Chemical Physics, 2003. **5**(6): p. 1043-1050.

131. T. Okada, M. Uesugi, G. Kohler, K. Rechthaler, K. Rotkiewicz, W. Rettig and G. Grabner, *Time-resolved spectroscopy of DMABN and its cage derivatives 6-cyanobenzquinuclidine (CBQ) and benzquinuclidine (BQ).* Chemical Physics, 1999. **241**(3): p. 327-337.

132. A.L. Sobolewski and W. Domcke, *Charge transfer in aminobenzonitriles: Do they twist?* Chemical Physics Letters, 1996. **250**(3-4): p. 428-436.

133. A.B.J. Parusel, W. Rettig and W. Sudholt, *A comparative theoretical study on DMABN: Significance of excited state optimized geometries and direct comparison of methodologies.* Journal of Physical Chemistry A, 2002. **106**(5): p. 804-815.

134. K. Rotkiewicz, K.H. Grellmann and Z.R. Grabowski, *Reinterpretation of the anomalus fluorescence of p-N,N-dimethylamino-benzonitrile.* Chemical Physics Letters, 1973. **19**(3): p. 315-318.

135. W. Rettig, *External and internalparameters affecting the dual fluorescence of p-Cyano-Dialkylanilines.* Journal of Luminescence, 1980. **26**: p. 21-46.

136. K.A. Zachariasse, S.I. Druzhinin, W. Bosch and R. Machinek, *Intramolecular charge transfer with the planarized 4-aminobenzonitrile 1-tert-butyl-6-cyano-1,2,3,4-tetrahydroquinoline (NTC6).* Journal of the American Chemical Society, 2004. **126**(6): p. 1705-1715.

137. I. Gomez, M. Reguero, M. Boggio-Pasqua and M.A. Robb, *Intramolecular charge transfer in 4-aminobenzonitriles does not necessarily need the twist.* Journal of the American Chemical Society, 2005. **127**(19): p. 7119-7129.

138.   T.J. Kang, M.A. Kahlow, D. Giser, S. Swallen, V. Nagarajan, W. Jarzeba and P.F. Barbara, *Dynamic solvent effects in the electron-transfer kinetics of S-1 bianthryls.* Journal of Physical Chemistry, 1988. **92**(23): p. 6800-6807.

139.   D.K. Palit, A.K. Singh, A.C. Bhasikuttan and J.P. Mittal, *Relaxation dynamics in the excited states of LDS-821 in solution.* Journal of Physical Chemistry A, 2001. **105**(26): p. 6294-6304.

140.   M.J. Weaver and G.E. McManis, *Dynamic solvent effects on electron-transfer processes - recent progress and perspectives.* Accounts of Chemical Research, 1990. **23**(9): p. 294-300.

141.   M.R. Wasielewski, *Photoinduced electron-transfer in supramolecular systems for artificial photosynthesis.* Chemical Reviews, 1992. **92**(3): p. 435-461.

142.   T. Asahi, M. Ohkohchi, R. Matsusaka, N. Mataga, R.P. Zhang, A. Osuka and K. Maruyama, *Intramolecular Photoinduced Charge Separation and Charge Recombination of the Product Ion-Pair States of a Series of Fixed-Distance Dyads of Porphyrins and Quinones - Energy-Gap and Temperature Dependences of the Rate Constants.* Journal of the American Chemical Society, 1993. **115**(13): p. 5665-5674.

143.   V.A. Galievsky and K.A. Zachariasse, *Intramolecular charge transfer with N,N-Dialkyl-4-(trifluoromethyl)anilines and 4-(dimethylamino)benzonitrile in polar solvents. Investigation of the excitation wavelength dependence of the reaction pathway.* Acta Physica Polonica A, 2007. **112**: p. S39-S56.

144.   T. Fonseca, H.J. Kim and J.T. Hynes, *Twisted intramolecular charge-transfer dynamics in polar-solvents.* Journal of Photochemistry and Photobiology a-Chemistry, 1994. **82**(1-3): p. 67-79.

145.   N.J. Turro, *Modern molecular photochemistry.* 1978, Menlo Park, California: The Benjamin/Cummings Publishing Co., Inc.

146.   A.M. Sarker, Y. Kaneko, P.M. Lahti and F.E. Karasz, *Excited states of bromine-substituted distyrylbenzenes: Models for conjugated polymer emission.* Journal of Physical Chemistry A, 2003. **107**(34): p. 6533-6537.

147.   M. Sliwa, N. Mouton, C. Ruckebusch, L. Poisson, A. Idrissi, S. Aloïse, L. Potier, J. Dubois, O. Poizata and G. Buntinx, *Investigation of ultrafast photoinduced processes for salicylidene aniline in solution and gas phase: toward a general photo-dynamical scheme.* Photochemical & Photobiological Sciences. **9**(5): p. 661-669.

148.   M. Maeder and Y.-M. Neuhold, *Practical Data Analysis in Chemistry.* Data Handling in Science and Technology. 2007, Amsterdam: Elsevier B.V.

149.   K.A. Zachariasse, *Comment on "Pseudo-Jahn-Teller and TICT-models: a photophysical comparison of meta-and para-DMABN derivatives" [Chem. Phys. Lett. 305(1999)8] - The PICT model for dual fluorescence of aminobenzonitriles.* Chemical Physics Letters, 2000. **320**(1-2): p. 8-13.

150.   K.A. Zachariasse, S.I. Druzhinin, S.A. Kovalenko and T. Senyushkina, *Intramolecular charge transfer of 4-(dimethylamino)benzonitrile probed by time-resolved fluorescence and transient absorption: No evidence for two ICT states and a pisigma(*) reaction intermediate.* J Chem Phys, 2009. **131**(22): p. 224313.

151.   K.A. Zachariasse, S.I. Druzhinin, P. Mayer, S.A. Kovalenko and T. Senyushkina, *Decay times of 4-(dimethylamino)benzonitrile in acetonitrile and conclusions on entropy of activation.* Chemical Physics Letters, 2009. **484**(1-3): p. 28-32.

152.   M.L. Horng, J.A. Gardecki, A. Papazyan and M. M., *Subpicosecond Measurements of Polar Solvation Dynamics: Coumarin 153 Revisited.* Journal of Physical Chemistry, 1995. **99**: p. 17311-17337.

153. D. Braun and W. Rettig, *Kinetic-studies of twisted intramolecular charge-transfer in highly viscous solvents as a function of pressure and temperature.* Chemical Physics, 1994. **180**(2-3): p. 231-238.

154. A. Pigliucci, E. Vauthey and W. Rettig, *Entropic effects in excited state CT reactions.* Chemical Physics Letters, 2009. **469**(1-3): p. 115-120.

155. M. Varne, V. Samant, J.A. Mondal, S.K. Nayak, H.N. Ghosh and D.K. Palit, *Ultrafast Relaxation Dynamics of the Excited States of 1-Amino- and 1-(N,N-Dimethylamino)-fluoren-9-ones.* Chemphyschem, 2009. **10**(17): p. 2979-2994.

156. N. Mataga, H. Chosrowjan, S. Taniguchi, Y. Shibata, N. Yoshida, A. Osuka, T. Kikuzawa and T. Okada, *Ultrafast charge separation from the S-2 excited state of directly linked porphyrin-imide dyads: First unequivocal observation of the whole bell-shaped energy-gap law and its solvent dependencies.* Journal of Physical Chemistry A, 2002. **106**(51): p. 12191-12201.

157. E.H.A. Beckers, S.C.J. Meskers, A. Schenning, Z.J. Chen, F. Wurthner and R.A.J. Janssen, *Charge separation and recombination in photoexcited oligo(p-phenylene vinylene): Perylene bisimide arrays close to the marcus inverted region.* Journal of Physical Chemistry A, 2004. **108**(34): p. 6933-6937.

158. J.A. Mondal, M. Sarkar, A. Samanta, H.N. Ghosh and D.K. Palit, *Charge-transfer-induced twisting of the nitro group.* Journal of Physical Chemistry A, 2007. **111**(28): p. 6122-6126.

159. J.A. Mondal, H.N. Ghosh, T.K. Ghanty, T. Mukherjee and D.K. Palit, *Twisting dynamics in the excited singlet state of Michler's ketone.* Journal of Physical Chemistry A, 2006. **110**(10): p. 3432-3446.

160. I. Petkova, G. Dobrikov, N. Banerji, G. Duvanel, R. Perez, V. Dimitrov, P. Nikolov and E. Vauthey, *Tuning the Excited-State Dynamics of GFP-Inspired Imidazolone Derivatives.* Journal of Physical Chemistry A, 2010. **114**(1): p. 10-20.

161. K. Hara, D.S. Bulgarevich and O. Kajimoto, *Pressure tuning of solvent viscosity for the formation of twisted intramolecular charge-transfer state in 4,4'-diaminodiphenyl sulfone in alcohol solution.* Journal of Chemical Physics, 1996. **104**(23): p. 9431-9436.

162. T.O. Harju, J.E.I. KorppiTommola, A.H. Huizer and C. Varma, *Barrier crossing reaction of electronically excited DBMBF(2) in n-nitriles: The role of solvent polarity on activation energy.* Journal of Physical Chemistry, 1996. **100**(9): p. 3592-3600.

163. J.P. Yang, W. Paa and S. Rentsch, *Femtosecond investigations of photophysics of ultrafast intersystem crossing in terthiophene by wavelength dependent excitation.* Chemical Physics Letters, 2000. **320**(5-6): p. 665-672.

164. J.P. Yang, W. Paa and S. Rentsch, *Size dependent ultrafast dynamics of oligothiophenes with 1-4 monomer units.* Synthetic Metals, 1999. **101**(1-3): p. 624-625.

165. S. Rentsch, J.P. Yang, W. Paa, E. Birckner, J. Schiedt and R. Weinkauf, *Size dependence of triplet and singlet states of alpha-oligothiophenes.* Physical Chemistry Chemical Physics, 1999. **1**(8): p. 1707-1714.

166. D.V. Lap, D. Grebner and S. Rentsch, *Femtosecond time-resolved spectroscopic studies on thiophene oligomers.* Journal of Physical Chemistry A, 1997. **101**(2): p. 107-112.

167. J.W. Sease and L. Zechmeister, *Chromatographic and spectral characteristics of some polythienyls.* Journal of the American Chemical Society, 1947. **69**(2): p. 270-273.

168.   R.S. Becker, J.S. deMelo, A.L. Macanita and F. Elisei, *Comprehensive evaluation of the absorption, photophysical, energy transfer, structural, and theoretical properties of alpha-oligothiophenes with one to seven rings.* Journal of Physical Chemistry, 1996. **100**(48): p. 18683-18695.

169.   C.H. Evans and J.C. Scaiano, *Photochemical generation of radical cations from alpha-terthienyl and related thiophenes - kinetic-behavior and magnetic-field effects on radical-ion pairs in micellar solution.* Journal of the American Chemical Society, 1990. **112**(7): p. 2694-2701.

170.   V. Wintgens, P. Valat and F. Garnier, *Photochemical generation of radical cations from thiophene oligomers.* Journal of Physical Chemistry, 1994. **98**(1): p. 228-232.

171.   R.S. Becker, J.S. Demelo, A.L. Macanita and F. Elisei, *Comprehensive investigation of the solution photophysics and theoretical aspects of oligothiophenes of 1-7 rings.* Pure and Applied Chemistry, 1995. **67**(1): p. 9-16.

172.   R. Weinkauf, L. Lehr, E.W. Schlag, S. Salzmann and C.M. Marian, *Ultrafast dynamics in thiophene investigated by femtosecond pump probe photoelectron spectroscopy and theory.* Physical Chemistry Chemical Physics, 2008. **10**(3): p. 393-404.

173.   A.D. Becke, *Density-functional thermochemistry .3. the role of exact exchange.* Journal of Chemical Physics, 1993. **98**(7): p. 5648-5652.

174.   A.D. Boese and J.M.L. Martin, *Development of density functionals for thermochemical kinetics.* Journal of Chemical Physics, 2004. **121**(8): p. 3405-3416.

175.   A.D. Becke, *A new mixing of hartree-fock and local density-functional theories.* Journal of Chemical Physics, 1993. **98**(2): p. 1372-1377.

The photophysics of pyridinium betaines studied by ultrafast transient absorption spectroscopy: focus on the photoinduced intramolecular charge transfer process.

Abstract: This work deals with the photophysics in solution of Pyridinium betaine, 2-Pyridin-1-yl-1H-benzimidazole (SBPa), and 2 derivatives substituted by thiophene groups. It is based on a combination of steady-state and time-resolved absorption spectroscopic measurements supported by PCM-(TD)DFT calculations.

SBPa was found to undergo intramolecular charge transfer (ICT) process upon light excitation with a drastic change in dipole moment. Stationary absorption/emission and TDDFT results revealed a strongly solvatochromic $S_0 \rightarrow S_2(CT)$ absorption contrasting with weakly solvatochromic $S_1 \rightarrow S_0$ emission. Band shape analysis and innovative solvatochromic data treatment considering protic and aprotic solvents separately led to a detailed knowledge of the solvent effects and allowed estimating four relevant dipole moments.

From femtosecond transient absorption experiments, the photophysics of SBPa could be discussed in terms of two distinct CT states and a photophysical scheme was proposed: in parallel to the ultrafast production of the emissive S_1 state, an ultrafast ICT process occurs from the initially populated $S_2(CT)$ state to a new charge transfer $S_1(CT)$ state, reaction ranging from 0.3–12 ps depending on the solvent. Examining solvent effects, we found that the ICT process arises in the Marcus inverted region and is purely solvent controlled in aprotic media. Comparison with pre-twisted model molecule has excluded possibility of geometrical changes during ICT.

Similar study of the mono- and bi-thiophene substituted SBPa molecules revealed that the ICT process is still present but occurs in competition with a decay route involving the π-electron system localized in the thiophenic groups.

Keywords: pyridinium betaine, photoinduced charge transfer, solvatochromism, band shape analysis, solvation dynamics, Marcus inverted region, UV-vis femtosecond spectroscopy, PCM-DFT, PCM-TDDFT.

Etude par spectroscopie d'absorption transitoire ultrarapide de la photophysique de pyridinium betaines, en particulier du processus de photo-transfert de charge intramoléculaire.

Résumé: Ce travail concerne la photophysique en solution de la Pyridinium betaine, 2-Pyridin-1-yl-1H-benzimidazole (SBPa), et de 2 dérivés substitués par des groupes thiophéniques. Il repose sur un ensemble de mesures par spectroscopies stationnaires et résolue en temps, complétées par des calculs PCM-(TD)DFT.

Les données d'absorption/émission/TDDFT révèlent pour SBPa une transition de transfert de charge intramoléculaire (ICT) $S_0 \rightarrow S_2(CT)$ fortement solvatochrome (forte variation de moment dipolaire), et une émission $S_1 \rightarrow S_0$ peu solvatochrome. L'analyse des formes de bandes et du solvatochromisme (solvant protiques/aprotiques traités séparément), a conduit à une évaluation pertinente de 4 moments dipolaires.

A partir de mesures d'absorption femtoseconde, un schéma photophysique de SBPa a pu être établi, mettant en jeu 2 états CT distincts : parallèlement à la formation d'un état S_1 fluorescent, un état $S_2(CT)$ provenant de la relaxation de la zone de Franck-Condon subit un processus ICT de 0.3-20 ps en fonction du solvant pour aboutir à 2nd état de transfert de charge $S_1(CT)$. Les effets de solvants suggèrent que ce processus a lieu dans la région inverse de Marcus et est contrôlé par la dynamique du solvant (cas aprotique). La comparaison de ces résultats avec une molécule modèle non-plane a permis d'exclure définitivement l'hypothèse d'un changement de géométrie durant l'ICT.

L'étude analogue des molécules substituées par des groupes mono et bi-thiophéniques montre que le processus de transfert de charge est préservé mais entre en compétition avec une autre voie de désactivation photophysique parallèle impliquant spécifiquement le système π localisé sur les substituants thiophéniques.

Mots-clés: pyridinium betaine, transfert de charge photoinduit, solvatochromisme, dynamique de solvatation, région inverse de Marcus, spectroscopie UV-vis femtoseconde, PCM-DFT, PCM-TDDFT.